Matthieu Sala

Quantum Dynamics and Laser Control for Photochemistry

Springer Theses

Recognizing Outstanding Ph.D. Research

Aims and Scope

The series "Springer Theses" brings together a selection of the very best Ph.D. theses from around the world and across the physical sciences. Nominated and endorsed by two recognized specialists, each published volume has been selected for its scientific excellence and the high impact of its contents for the pertinent field of research. For greater accessibility to non-specialists, the published versions include an extended introduction, as well as a foreword by the student's supervisor explaining the special relevance of the work for the field. As a whole, the series will provide a valuable resource both for newcomers to the research fields described, and for other scientists seeking detailed background information on special questions. Finally, it provides an accredited documentation of the valuable contributions made by today's younger generation of scientists.

Theses are accepted into the series by invited nomination only and must fulfill all of the following criteria

- They must be written in good English.
- The topic should fall within the confines of Chemistry, Physics, Earth Sciences, Engineering and related interdisciplinary fields such as Materials, Nanoscience, Chemical Engineering, Complex Systems and Biophysics.
- The work reported in the thesis must represent a significant scientific advance.
- If the thesis includes previously published material, permission to reproduce this must be gained from the respective copyright holder.
- They must have been examined and passed during the 12 months prior to nomination.
- Each thesis should include a foreword by the supervisor outlining the significance of its content.
- The theses should have a clearly defined structure including an introduction accessible to scientists not expert in that particular field.

More information about this series at http://www.springer.com/series/8790

Matthieu Sala

Quantum Dynamics and Laser Control for Photochemistry

Doctoral Thesis accepted by
Université de Bourgogne Franche-Comté, Dijon, France

Springer

Author
Dr. Matthieu Sala
Laboratoire Interdisciplinaire Carnot de
  Bourgogne
Université de Bourgogne Franche-Comté
Dijon
France

Supervisors
Prof. Stéphane Guérin
Laboratoire Interdisciplinaire Carnot de
  Bourgogne
Université de Bourgogne Franche-Comté
Dijon
France

Prof. Fabien Gatti
Institut Charles GERHARDT—CNRS 5253
Université Montpellier 2
Montpellier
France

Parts of this thesis have been published in the following journal articles:

- M. Sala, F. Gatti, D. Lauvergnat and H.-D. Meyer, "Effect of the overall rotation on the cis-trans isomerization of HONO induced by an external field", *Phys. Chem. Chem. Phys.* **14**, 3791 (2012)

- M. Sala, S. Guérin, F. Gatti, R. Marquardt and H.-D. Meyer, "Laser-induced enhancement of tunneling in NHD_2", *J. Chem. Phys.* **136**, 194308 (2012)

- M. Sala, O. M. Kirkby, S. Guérin and H. H. Fielding, "New insight into the potential energy landscape and relaxation pathways of photoexcited aniline from CASSCF and XMCQDPT2 electronic structure calculations", *Phys. Chem. Chem. Phys.* **16**, 3122 (2014)

- M. Sala, M. Saab, B. Lasorne, F. Gatti and S. Guérin, "Laser control of the radiationless decay in pyrazine using the dynamic Stark effect", *J. Chem. Phys.* **140**, 194309 (2014)

- M. Sala, B. Lasorne, F. Gatti and S. Guérin, "The role of the low-lying dark $n\pi^*$ states on the photophysics of pyrazine: a quantum dynamics study", *Phys. Chem. Chem. Phys.* **16**, 15957 (2014)

- M. Saab, M. Sala, S. Guérin, B. Lasorne and F. Gatti, "Full dimensional control of the radiationless decay in pyrazine using the dynamic Stark effect", *J. Chem. Phys.* **141**, 134114 (2014)

- M. Sala, F. Gatti and S. Guérin, "Coherent destruction of tunneling in a six-dimensional model of NHD_2: a computational study using the multi-configuration time-dependent Hartree method", *J. Chem. Phys.* **141**, 164326 (2014)

- O. M. Kirkby, M. Sala, G. Balerdi, S. Guérin, R. de Nalda, L. Bañares, N. Kaltsoyannis and H. H. Fielding, "Comparing the electronic relaxation dynamics of aniline and d_7-aniline following excitation in the 273–238 nm region", *Phys. Chem. Chem. Phys.* **17**, 16270 (2015)

- M. Sala, S. Guérin and F. Gatti, "Quantum dynamics of the photostability of pyrazine", *Phys. Chem. Chem. Phys.* **17**, 29518 (2015)

Supervisors' Foreword

With the advent of femtosecond laser pulses in the 1990s, real-time imaging of ultrafast molecular phenomena has become possible. They are now used in a systematic manner in pump-probe experiments to map out, in real time, nuclear motion in molecules. In the past two decades, tremendous progress has been achieved on the experimental front with the possibility to align molecules with lasers and the production of attosecond pulses. In particular, the high-harmonic generation technique that is responsible for the formation of attosecond laser pulses has been exploited to image the faster electronic motion. In this context, it becomes conceivable to create a new chemistry where all the different motions (rotational, nuclear and electronic) in a molecular process could be manipulated and controlled by laser pulses. The stakes are high and pose further substantial requirements on the development of suitable theoretical methods. In addition, one important challenge is to transfer to chemistry techniques (experimental and theoretical) that have been developed mainly by physicists and for problems in physics.

The central subject of the present thesis is the theoretical description of ultrafast dynamical processes in molecular systems of chemical interest and their control by laser pulses. This work, performed in collaboration with experimentalists, can be considered as a decisive step to link and apply quantum physics to chemistry by transferring concepts developed in physics to chemistry such as "wavepackets" or "light dressed states." This is highlighted in Part II, where Dr. M. Sala exploits the "adiabatic Floquet theory" to rationalize the control of several molecular processes. When a molecular system is isolated, its quantum behavior can be described in terms of eigenstates and wavepackets featuring linear combinations of the eigenstates. However, when the system is in interaction with a time-dependent external field, the situation is completely different as the eigenstates are modified by the external fields. The adiabatic Floquet theory provides a quantum mechanical framework for the description of the interaction of quantum systems with light. More precisely, a description in terms of Floquet states or "light dressed states," i.e., quantum states similar to eigenstates that additionally include rigorous quantum-mechanical treatment of the mean frequency of the external fields (like in

the approach of "dressed atoms" in atomic physics). The laser parameters varying slowly in time with respect to the mean frequency (such as the envelope of the pulse and the chirp of the frequency) feature dynamical modification of the Floquet states, topologically represented as dressed surfaces in the parameter space. With adiabatic arguments, one can then characterize the quantum dynamics as trajectories in the parameter space.

Dr. M. Sala's Ph.D. encompasses cutting-edge methods not only for the rigorous description of the interaction of light and matter at the molecular level but also in quantum chemistry and molecular quantum dynamics. Indeed, one important aspect of his work was the exploration of potential energy landscapes for electronic excited states in organic molecules in the vicinity of so-called "conical intersections." At a conical intersection, the potential energy surfaces belonging to different electronic states become degenerate and the Born–Oppenheimer approximation, that separates the nuclear and electronic motions, fails: a nonadiabatic transfer from one electronic state to another can occur. From ab initio electronic structure calculations, Dr. M. Sala could build model Hamiltonians that can be used to solve, in a second step, the Schrödinger equation for the nuclei. For the latter step, he developed his own codes for low-dimensional simulations and exploited the Heidelberg Multi-Configuration Time-Dependent Hartree (MCTDH) package otherwise. The MCTDH approach is an efficient tool to solve both the time-dependent and time-independent Schrödinger for relatively large systems. Finally, Dr. M. Sala has highlighted general strategies for the coherent control of strong quantum effects involving the nuclei in chemical process: tunneling and strong nonadiabatic processes.

Altogether, this doctoral thesis lays out important foundations for the quantum mechanical treatment of molecular processes that we anticipate to be very useful in the context of applications of ultrafast laser pulses to chemistry. To conclude, we were impressed by the level of autonomy of Dr. M. Sala and his strong ability to take initiative at all the stages of his Ph.D. work.

Prof. Fabien Gatti
Prof. Stéphane Guérin

Acknowledgments

First of all, I am grateful to my supervisor Stéphane Guérin for guiding me through this thesis. His enthusiasm, his encouragement, the constant help and support he provided me with, and the trust he put in me has been instrumental in my development as a scientist. I have learned a lot from him, through numerous hours spent in his office discussing technical details or future projects. I also thank Stéphane for having given me the opportunity to spend six months in the group of Helen Fielding in London, in the middle of this thesis. Finally, I thank him for the wonderful dinner parties at his house with all the colleagues of our team, for the incredible food and wines I had the chance to taste, and the friendly and humorous atmosphere.

I wish to acknowledge Fabien Gatti, who introduced me to research during my master's thesis. His enthusiasm, his energy, and his passion for research are a source of inspiration for me. He has kept a constant interest in my work and has always been available for discussions, providing me with help and support, and giving me many useful advices. Nothing of what is written in this thesis would have happened without him.

I would like to thank Hans-Rudolf Jauslin, head of the quantum and nonlinear dynamics team, for giving me the opportunity to work in such a nice and stimulating environment. I also thank Claude Leroy, Yevgenya Pashayan-Leroy, Dominique Sugny, Vincent Boudon, Béatrice Bussery-Honvault, and Pascal Honvault, who I had the chance to get to know during this thesis, and who greatly contributed to the nice work environment of the first floor of the "Aile de Physique."

I acknowledge Helen Fielding for having made me feel so welcome in her group at the Chemistry Department of University College London, from March to August 2012. This research stay was a great opportunity for me to learn about the experimental point of view on molecular photodynamics. Thanks to her, my stay in London was a rich and rewarding experience. I also thank the students of the Fielding group, Roman Spesyvtsev, Oliver Kirkby, Ciaran Mooney, and Garikoitz Balerdi, who all contributed greatly in making this experience so enjoyable for me.

This thesis has been the opportunity to teach in chemistry and physics lab classes. I thank Frédéric Demoisson, Christine Gautheron-Geraci, Jean Suisse,

Olivier Politano, Kammal Hammani, and Eric Finot, who provided me with instruction and guidance, and contributed to make this experience pleasant and rewarding for me.

I thank the many Ph.D. students and postdocs I had the chance to rub shoulders with during this thesis. Marc Lapert, Élie Assémat, Ghassen Dridi, Vahe Hakobyan, Yulia Kalugina, Leo Van Damme, Rajagopala Rao Tammineni, Chanda-Malis Ouk, Maud Louviot, Hrant Hakhumyan, Anna Fomchenko, Ara Tonoyan, Rafayel Mirzoyan, Benjamin Rousseaux, David Dzsotjan, Anahit Gogyan, Mariam Gevorgyan, Levon Chakhmakhchyan, Mamadou Ndong, and all those who I forget (sorry for that !), for sharing their experience with me, for giving me valuable advice, for the many discussions on scientific problems from which many ideas came out, for the good times during coffee breaks, the blobby volley tournaments, the great parties, and much more. They all contributed to this work in their own way.

I would like to have a thought for my family, which always supported and encouraged me.

Finally, during this thesis, I had the chance to meet my loving partner Frédérique, and to become the father of a beautiful little girl, Charlotte. They bring me more joy and happiness than I could ever have imagined. I would like to thank them for just being there.

<div align="right">Matthieu Sala</div>

Contents

Chapter 1
General Introduction

Light induced chemical transformations, called photochemical reactions, are ubiquitous in nature. These processes are initiated by the absorption of a photon, that promotes the molecule into an excited state, where the reaction takes place. Important examples of photochemical reactions occurring in nature are the photolysis of ozone and molecular oxygen in the stratosphere [1–3], the initial steps of the processes of photosynthesis [4, 5] or of vision [6–9]. In addition, photochemical processes lie at the heart of important emerging technologies, such as 3D optical memories based on photoswitching molecular materials [10], Organic Light-Emitting Diodes (OLED) [11, 12] or organic photovoltaics [13–16]. For these reasons, a detailed understanding of photochemical processes at the molecular level is a major goal of modern physical chemistry.

Thanks to the development of powerful experimental techniques, tremendous progress in the understanding of photochemical processes have been made in the last few decades. The 1999 Nobel prize in chemistry was awarded to Ahmed Zewail for his seminal work on time-resolved spectroscopy of molecular processes on a femtosecond time scale [17–20]. The characteristic time scale of the vibrational motion of the nuclei in molecule being of the order of the hundred of femtoseconds, experiments with a time resolution of the same order of magnitude or less are able to probe the elementary steps (bond breaking, isomerizations, …) of photochemical reactions. Time-resolved spectroscopic techniques consist in making sequential spectroscopic measurements on a system during a dynamical process, allowing one to record the frames of a "movie" of a chemical transformation. In these techniques, the system is irradiated by two laser pulses delayed in time with respect to each other. The first laser pulse, called pump pulse, triggers a dynamical process via photoexcitation. The second laser pulse, called probe pulse, is then used to monitor the system during its evolution. Different probe techniques are available, such as transient absorption, laser induced fluorescence or photoelectron spectroscopy. This procedure is repeated with different delay times between the two laser pulses, yielding time-resolved spectroscopic data.

Since the first experiments on the I-CN [21] bond cleavage and the wavepacket oscillations between the ionic and covalent potentials in the photodissociation of NaI [22, 23], pump-probe techniques have been applied to a wide range of important photochemical processes. However, the data obtained from such experiments are often difficult to interpret and theoretical modeling is needed to get further insight into the excited state dynamics of the systems of interest at the atomistic level. In this context, the development of efficient and accurate computational methods for the description of ground and excited electronic states of mid-size molecular systems in a balanced way [24, 25], has greatly facilitated the theoretical study of photochemical processes.

During the same period, it became more and more evident that strong non-adiabatic effects, occurring at regions of degeneracy between electronic states, called conical intersections [26, 27], play an important role in a great number of cases. In such situations, associated with a breakdown of the Born–Oppenheimer approximation, the electronic and nuclear motions are strongly coupled, giving rise to non-radiative population transfers between electronic states, i.e population transfers that occur because of the coupling of the electronic and nuclear motions rather than the coupling with the electromagnetic field (Fig. 1.1).

Depending on their position and energetics with respect to the Franck–Condon region of the excited state potential energy surface (the region occupied by the wavepacket on the excited state potential energy surface immediately after a vertical photoexcitation), conical intersections can mediate ultrafast internal conversion processes from the excited state to the photoproducts on the ground state. A systematic exploration of the excited state potential energy surfaces, and their conical intersections with the ground state potential energy surfaces, of the basic organic chromophores using multi-configuration self-consistent field calculations, has been launched in the nineties in the groups of Robb, Bernardi and Olivucci [28, 29]. In most cases, these studies revealed the existence of low-lying conical intersections between the first excited state and the ground state, at geometries consistent with the observed photoproducts. This findings supported the hypothesis that low-lying

Fig. 1.1 Schematic view of an ultrafast radiationless decay process through a conical intersection
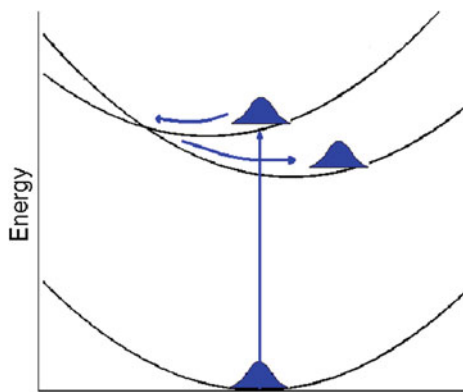
conical intersections are ubiquitous in organic molecules, and act as key mechanistic features in organic photochemistry, similarly to the transition state in thermal reactions occurring on the ground electronic state.

Often, the relaxation of a molecule to its ground electronic state via a conical intersection is associated with a competition between two situations. The molecule can reach a region of the ground state potential energy surface corresponding to a different isomer, or to a repulsive part resulting in a bond breaking process. This situation is called photoreactivity. But the molecule can also reach the ground state potential energy surface in the region of its equilibrium geometry. This situation is called photostability. The competition between photoreactivity and photostability (Fig. 1.2) is directly related to the topography of the potential energy surfaces around the conical intersection [30–32].

The notion of photostability is very important in the field of molecular biology. The molecular "building blocks of life", such as the DNA bases or the amino acids, often absorb in the ultra violet (UV) region of the electromagnetic spectrum. A UV photon carries an energy which is of the same order of magnitude as the binding energy associated with the weakest bonds of these molecules. Therefore, UV light is potentially harmful for these compounds and, by extension, for life. This is, however, in contradiction with the exceptional photostability observed experimentally for these molecules and their complexes. A large number of theoretical and experimental investigations, performed over the last two decades, have established that this exceptional photostability is related with the existence of conical intersections providing extremely efficient radiationless decay channels leading the molecules back to their ground state [33–37].

Nevertheless, although the characterization of the topography of potential energy surfaces using electronic structure calculations often provides a qualitative understanding of the mechanisms of photochemical transformations, a deeper insight into such processes often requires simulating the dynamics of the nuclei. For instance, it is known that the existence of conical intersections is often reflected in the absorption
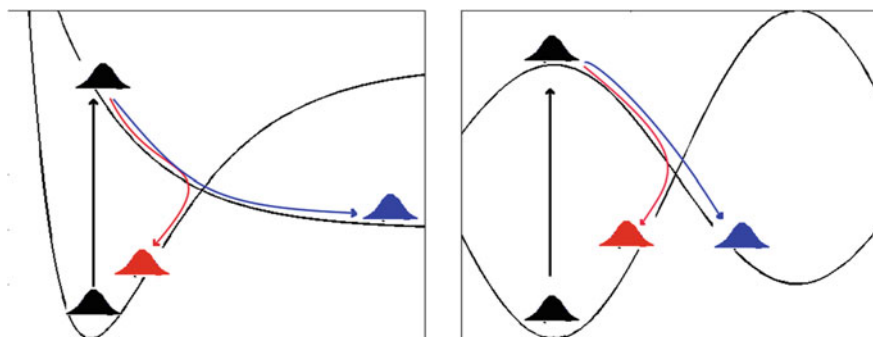
Fig. 1.2 Illustration of the competition between photostability (featured in *red*) and photoreactivity (featured in *blue*) in two different situations: a non-adiabatic photodissociation process (*left panel*) and a non-adiabatic photoisomerization process (*right panel*)

Fig. 1.3 Structure of the
butatriene molecule
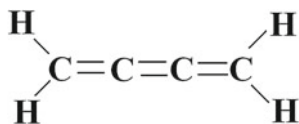
spectra through the presence of unexpected bands or of bands presenting an unusually complicated and broad profile. An interesting and historically important example is provided by the photoelectron spectrum of the butatriene molecule (see Fig. 1.3).

Despite the fact that butatriene is a quite exotic molecule, it has attracted a considerable attention in the spectroscopy community in the 70 s because of the unusual structure of its photoelectron spectrum in the region between 9 and 11 eV [38]. It was known that the butatriene radical cation has only two electronic states in this energy range, corresponding to the bands centered around 9.3 and 10.0 eV (bands noted 1 and 2 in the left panel of Fig. 1.4). However, the photoelectron spectrum presents a third, broad feature (noted 1′ in the left panel of Fig. 1.4) between these two bands that cannot be directly assigned to a given electronic state, and was termed the "mystery band". It was shown later by Cederbaum et al. [39] that this "mystery band" was a direct signature of the existence of a strong vibronic coupling between the two lowest excited electronic states of the cation, manifested by a conical intersection of the two corresponding potential energy surfaces. They constructed a model potential including the two most important vibrational modes and taking into account the vibronic couplings and could reproduce the photoelectron spectrum, including the "mystery band", as seen in Fig. 1.4. Since then, thanks to the enormous progress made in the methodology of molecular quantum dynamics calculations, absorption and photoelectron spectra of molecular systems of increasing complexity showing signatures of strong vibronic couplings have been simulated (see e.g. Chap. 7 in ref. [26] and Chap. 6 in ref. [27]).

Beyond the computation of spectra, the simulation of the dynamics of the nuclei has proven to be necessary for a proper understanding of a number of photochemical processes. Indeed, in most systems, the excited state dynamics is governed by the competition between several dynamical processes including several electronic states. These processes can correspond to channels with similar energies and in this case, it is difficult to predict the dynamics of the molecule using only the static information that can be obtained from electronic structure calculations. However, the simulation of such photochemical processes, which often involve large amplitude nuclear motions and complicated potential energy surfaces, using quantum dynamics techniques, remains a formidable challenge from the numerical point of view. For this reason, a variety of computational techniques based on a mixed quantum-classical formalism have been developed and used to study the excited state dynamics of mid-size molecular systems such as, for instance, the DNA bases [40–42]. The most popular family of such techniques is the trajectory surface-hopping method (see Chaps. 11–13 in ref. [27] and references therein). Other important methods in this category are the ab initio multiple spawning method (see Chap. 9 in ref. [27] and references therein) or the methods based on the Herman-Kluk semi-classical propagator combined with
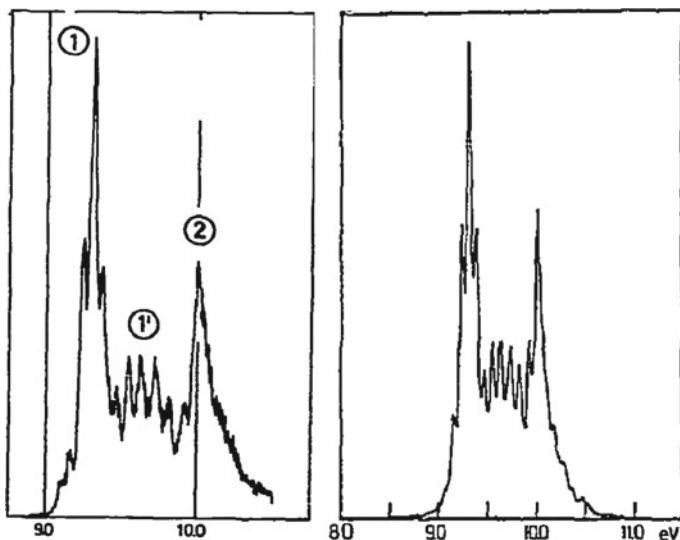
Fig. 1.4 Experimental [38] (*left panel*) and computed [39] (*right panel*) photoelectron spectrum of butatriene. Both figures are reproduced with permission from Elsevier

the initial-value representation (see Chap. 15 in ref. [26] and references therein). Nevertheless, the dynamics of the nuclei of molecular systems can be affected by strong quantum effects such as tunneling over potential energy barriers or interference effects. And, more importantly, internal conversion processes occurring in the vicinity of conical intersections are inherently quantum effects. Therefore, the development of simulation techniques fully based on a quantum mechanical description of the dynamics of the nuclei and which can be applied to complex photochemical processes is an active area of research.

The emergence of femtosecond laser technologies not only revolutionized our understanding of elementary photochemical processes. It also opened new possibilities in the way we can control the motion and the transformations of atomic and molecular systems. The manipulation of quantum systems using tailored light sources has potential applications in a large variety of domains such as optics, information processing, spectroscopic and imaging techniques, molecular electronics or chemical dynamics.

Generally speaking, quantum control consists in finding a way of inducing a partial or complete population transfer, in a controlled way, between an initial state and a final state (the initial and final states can be single eigenstates or superpositions of such eigenstates). A number of techniques allowing one to induce a complete population transfer between single eigenstates exist, such as the π-pulse techniques or the schemes based on adiabatic passage [43–45]. In addition, a number of extensions of these methods to the case of superpositions of eigenstates have been proposed [46–50].

Beyond these general schemes, methods specifically tailored for the control of molecular systems have been developed [51]. Brumer and Shapiro proposed to use simultaneously two laser fields with frequencies ω_1 and $\omega_n = n\omega_1$ that couple a bound state to a continuum. The final product can be controlled by modulating the relative phase and amplitude between the two laser fields [52]. This control scenario, often called "coherent control", has been used, e.g., for the control of photodissociation processes [53], the discrimination of enantiomers [54] or the photocurrent directionality in semiconductors [55]. This strategy has been implemented experimentally in a number of situations (see [56] and references therein). Tannor, Kosloff and Rice proposed a strategy relying on the manipulation of the time delay between two short laser pulses [57, 58]. A first laser pulse creates a wavepacket on an excited state potential energy surface. When the wavepacket reaches a configuration of interest for the outcome of the reaction on the ground state, the second laser pulse is used to bring the system back to the ground electronic state. This scheme is called pump-dump scheme. Another strategy relies on a specific preparation of the initial state of the system. For instance, it is known that molecules in excited vibrational states can have different reactivities than their ground vibrational state counterpart. This has been shown experimentally for prototypical systems relevant to non-adiabatic photodissociation [59], atom-molecule [60], or molecule-surface [61] reactive scattering. More recently, the use of a strong non-resonant laser pulse, acting on the molecule through the Stark effect, has been shown experimentally [62–64] and theoretically [65, 66], to provide another way of manipulating the outcome of non-adiabatic photodissociation processes.

The strategies mentioned above use rather simple laser pulse temporal shapes. The control is achieved by a proper choice of a few laser parameters such as the intensity, frequency, pulse duration, relative phase or time delay between two pulses. The variation of these parameters offers a sufficient flexibility to achieve a significant degree of control in relatively simple systems. In addition, a proper choice of the parameters can be guided by intuition, or by a systematic mapping of the few parameters. A different strategy implies a numerical optimization of the electric field required to guide the system towards a predefined objective. This is the basis of the optimal control [67, 68] and local control [69] techniques. These techniques have the advantage of being applicable, in principle, to complex systems for which intuition is of little help. However, because of their high computational cost, the applicability of these methods to the control of polyatomic molecules often enforces the use of simplified models. Nevertheless, general control strategies can be obtained from such studies and tested on more sophisticated models.

While most of the schemes described above have been demonstrated experimentally, a robust and efficient control of molecular processes is often difficult to achieve experimentally. In this context, the inclusion of robustness in optimal control theory to achieve such a robust and efficient control currently represents a very active field of research [70]. One of the main difficulties is that the interaction of a laser field with a sample of molecules is necessarily averaged with respect to the random orientation of the individual molecules of the sample. To overcome this issue, several

techniques to control the alignment and the orientation of molecular samples have been developed [71].

This thesis is split into two main parts. Part I is devoted to theoretical studies of the photochemistry of simple aromatic molecules.

In Chap. 2, the basic concepts relevant for the description of photochemical processes are presented. The molecular Schrödinger equation and the Born–Oppenheimer approximation are first introduced. Then, the notions of vibronic coupling and conical intersection are discussed and the diabatic representation for the electronic states is introduced. Finally, a review of the methodology used in this thesis for molecular electronic structure calculations, and their use in the exploration of potential energy surfaces, is presented.

Chapter 3 presents the results of a theoretical study of the photochemistry of aniline. The purpose of this work, initiated during a six-month fellowship in the group of Helen Fielding in the Chemistry Department of University College London, was to use electronic structure calculations to explore the potential energy surfaces of the low-lying electronic states of aniline in order to help in the interpretation of the time-resolved photoelectron imaging experiments performed in the Fielding group. After an introduction, in which the knowledge obtained from previous studies of the photochemistry of aniline and other simple benzene derivatives is reviewed, our results concerning the key structures and decay pathways of the molecule on the potential energy surfaces of the low-lying electronic states relevant for its photochemistry are presented and discussed in relation with the experimental results obtained in the Fielding group.

The methodology of molecular quantum dynamics applied to non-adiabatic systems is presented from a time-dependent perspective in Chap. 4. The representation of the molecular Hamiltonian is first discussed, with a focus on the choice of the coordinates to parametrize the nuclear motion and on the discrete variable representation. The multi-configuration time-dependent Hartree (MCTDH) method for the solution of the time-dependent Schrödinger equation is then presented. The chapter ends with a presentation of the vibronic coupling model of Köppel, Domcke and Cederbaum and the methodology used in the calculation of absorption spectra.

Finally, in Chap. 5 which closes Part I, an application of the tools introduced in Chaps. 2 and 4 to a quantum dynamical investigation of the photophysics of pyrazine is presented. This work focuses on the role of the low-lying dark $n\pi^*$ states in the non-adiabatic dynamics of the molecule after photoexcitation. Multi-reference electronic structure calculations are used to design a vibronic couping model Hamiltonian, including the four lowest electronic states and the sixteen most important vibrational modes. This model is then used to simulate the absorption spectrum and the ultrafast decay dynamics of the molecule using the MCTDH method.

Part II is devoted to the laser control of unimolecular processes. The general object of the research presented in this Part was to combine the theoretical tools for the computation of the electronic structure and nuclear quantum dynamics of molecular systems presented in Part I with the methodology of the laser control of quantum systems in order to address the problem of the quantum control by laser fields of polyatomic molecular systems.

In Chap. 6, the theoretical tools for the laser control of quantum systems used in this thesis are presented. The main approximations usually invoked in the theoretical description of the interaction of molecular systems with laser fields of wavelengths ranging from the mid-infrared to the ultraviolet regions of the electromagnetic spectrum, are first presented. The most basic features of the laser control of population inversion processes between quantum states are then presented in the framework of the two-level system in the resonant wave approximation. An effective Hamiltonian operator describing the interaction of a molecular system with a strong non-resonant laser pulse, useful in the theoretical study of laser control schemes based on the dynamic Stark effect, is then introduced. Finally, a detailed description of the Floquet theory, and its adiabatic extension, providing a general and rigorous theoretical framework for the description of the interaction of molecular systems with pulsed laser fields with slowly varying envelope and frequency is presented.

Chapter 7 presents a study of the laser control of the ultrafast radiationless decay of pyrazine using a control scheme based on the dynamic Stark effect. In this study, a simple model including the two lowest-lying bright excited electronic states and the four most important vibrational modes is used. This model is simpler than the model used in Chap. 5 and therefore is not expected to account for the full complexity of the non-adiabatic dynamics of photoexcited pyrazine. However, the results presented in this chapter are of general relevance for the study of the laser control of non-adiabatic systems. After a presentation of the model, the effect of the Stark shifts on the topography of the relevant potential energy surfaces is analysed and the mechanism of the control scheme proposed is presented from the adiabatic point of view. We then present our results and show that a strong non-resonant laser pulse can be used to trap the wavepacket in the upper electronic state, and therefore suppress the radiationless decay of the molecule for a time much larger than the natural decay time of this process. We then compare our control mechanism to previous works on the laser control of the non-adiabatic dynamics of pyrazine in which different control schemes were considered, and the merits and drawbacks of the control scheme proposed in this chapter are highlighted.

Chapter 8, which closes Part II, presents a study of the laser control of the tunneling dynamics in a model of the NHD_2 molecule including its six vibrational degrees of freedom. The aim of this work was to assess the applicability of well established control mechanisms, previously applied to simple one-dimensional double-well potential models, to a more complex system. Both the enhancement of tunneling, i.e the acceleration of the tunneling dynamics induced by a resonant laser pulse, and the coherent destruction of tunneling, which implies the freezing of the tunneling dynamics as long as the laser field is on, are investigated. For this purpose, a hierarchy of effective models of increasing complexity are considered. Simple few-level models are first used to analyse the general features of the proposed control mechanisms. Then, an effective model Hamiltonian expressed in the basis of the vibrational eigenstates of the molecule lying under a given energy threshold is used to investigate in details the effect of the parameters of the laser fields on the efficiency of the control. Finally, MCTDH calculations using the exact vibrational Hamiltonian are performed to confirm the validity of this effective model.

Finally, Chap. 9 concludes this thesis.

References

1. H.S. Johnston, Annu. Rev. Phys. Chem. **43**, 1 (1992)
2. A.R. Ravishankara, G. Hancock, M. Kawasaki, Y. Matsumi, Science **280**, 60 (1998)
3. SYu. Grebenshchikov, Z.-W. Qu, H. Zhu, R. Schinke, Phys. Chem. Chem. Phys. **9**, 2044 (2007)
4. B.R. Green, W.W. Parsons, *Light-Harvesting Antennas in Photosynthesis* (Kluwer, Dordrecht, 2003)
5. Y.C. Cheng, G.R. Fleming, Annu. Rev. Phys. Chem. **60**, 241 (2009)
6. G. Wald, Science **162**, 230 (1968)
7. R.A. Mathies, C.H. Brito Cruz, W.T. Pollard and C.V. Shank, Science **240**, 777 (1988)
8. L.M. Frutos, T. Andruniow, F. Santoro, N. Ferre, M. Olivucci, Proc. Natl. Acad. Sci. USA **104**, 7764 (2007)
9. D. Polli, P. Altoè, O. Weingart, K.M. Spillane, C. Manzoni, D. Brida, G. Tomasello, G. Orlandi, P. Kukura, R.A. Mathies, M. Garavelli, G. Cerullo, Nature **467**, 440 (2010)
10. D.A. Parthenopoulos, P.M. Rentzepis, Science **245**, 843 (1989)
11. J.H. Burroughes, D.D.C. Bradley, A.R. Burn, R.N. Marks, K. Mackey, R.H. Friend, A.B. Holmes, Nature **347**, 539 (1990)
12. Z. Shuai, Q. Peng, Phys. Rep. **537**, 123 (2014)
13. G. Yu, J. Gao, J.C. Hummelen, F. Wudl, A.J. Heeger, Science **270**, 1789 (1995)
14. C.J. Brabec, Sol. Energy Mat. Sol. Cells **83**, 273 (2004)
15. J.-L. Brédas, D. Beljonne, V. Coropceanu, J. Cornil, Chem. Rev. **104**, 4971 (2004)
16. S. Günes, H. Neugebauer, N.S. Sariciftci, Chem. Rev. **107**, 1324 (2007)
17. M.J. Rosker, M. Dantus, A.H. Zewail, Science **241**, 1200 (1988)
18. A.H. Zewail, Science **242**, 1645 (1988)
19. A.H. Zewail, Femtochemistry—Ultrafast Dynamics of the Chemical Bond, Vols. I and II, (World Scientific, New Jersey, 1994)
20. A.H. Zewail, Angew. Chem. Int. Ed. **39**, 2586 (2000)
21. M. Dantus, M.J. Rosker, A.H. Zewail, J. Chem. Phys. **89**, 6128 (1988)
22. T.S. Rose, M.J. Rosker, A.H. Zewail, J. Chem. Phys. **88**, 6672 (1988)
23. V. Engel, H. Metiu, R. Almeida, R. Marcus, A.H. Zewail, Chem. Phys. Lett. **152**, 1 (1988)
24. P.G. Szalay, T. Müller, G. Gidofalvi, H. Lischka, R. Shepard, Chem. Rev. **112**, 108 (2012)
25. L. González, D. Escudero, L. Serrano-Andrés, Chem. Phys. Chem. **13**, 28 (2012)
26. W. Domcke, D.R. Yarkony, H. Köppel, *Conical Intersections, Electronic Strucutre, Dynamics and Spectroscopy* (World Scientific, New Jersey, 2004)
27. W. Domcke, D.R. Yarkony, H. Köppel, *Conical Intersections, Theory, Computation and Experiment* (World Scientific, New Jersey, 2011)
28. F. Bernardi, M. Olivucci, M.A. Robb, Chem. Soc. Rev. **25**, 321 (1996)
29. M.A. Robb, M. Garavelli, M. Olivucci, F. Bernardi, Rev. Comp. Chem. **15**, 87 (2000)
30. G.J. Atchity, S.S. Xantheas, K. Ruedenberg, J. Chem. Phys. **95**, 1862 (1991)
31. B. Lasorne, M.J. Bearpark, M.A. Robb, G.A. Worth, J. Chem. Phys. **112**, 13017 (2008)
32. D. Mendive-Tapia, B. Lasorne, G.A. Worth, M.J. Bearpark, M.A. Robb, Phys. Chem. Chem. Phys. **12**, 15725 (2010)
33. C.E. Crespo-Hernández, B. Cohen, P.M. Hare, B. Kohler, Chem. Rev. **104**, 1977 (2004)
34. H. Kang, K.T. Lee, B. Jung, Y.J. Ko, S.K. Kim, J. Am. Chem. Soc. **124**, 12958 (2002)
35. D. Shemesh, C. Hättig, W. Domcke, Chem. Phys. Lett. **482**, 38 (2009)
36. D. Shemesh, A.L. Sobolewski, W. Domcke, Phys. Chem. Chem. Phys. **12**, 4899 (2010)
37. W. Domcke, A.L. Sobolewski, Nature Chem. **5**, 257 (2013)
38. F. Brogli, E. Heilbronner, E. Kloster-Jensen, A. Schmelzer, A.S. Manocha, J.A. Pople, L. Radom, Chem. Phys. **4**, 107 (1974)
39. L.S. Cederbaum, W. Domcke, H. Köppel, W. von Niessen, Chem. Phys. **26**, 169 (1977)
40. H.R. Hudock, T.J. Martínez, Chem. Phys. Chem. **9**, 2486 (2008)
41. Z. Lan, E. Fabiano, W. Thiel, J. Phys. Chem. B **113**, 3548 (2009)
42. M. Barbatti, A.J.A. Aquino, J.J. Szymczak, D. Nachtigallová, P. Hobza, H. Lischka, Proc. Natl. Acad. Sci. USA, **107**, 21453 (2010)

43. B.W. Shore, *Manipulating Quantum Structures Using Laser Pulses* (Cambridge University Press, Cambrigde, 2011)
44. N.V. Vitanov, T. Halfmann, B.W. Shore, K. Bergmann, Annu. Rev. Phys. Chem. **52**, 763 (2001)
45. K. Bergmann, H. Theuer, B.W. Shore, Rev. Mod. Phys. **70**, 1003 (1998)
46. R. Unanyan, M. Fleischhauer, B.W. Shore, K. Bergmann, Opt. Commun. **155**, 144 (1998)
47. L.P. Yatsenko, N.V. Vitanov, B.W. Shore, T. Rickes, K. Bergmann, Opt. Commun. **204**, 413 (2002)
48. N. Sangouard, S. Guérin, L.P. Yatsenko, T. Halfmann, Phys. Rev. A **70**, 013415 (2004)
49. P. Král, Z. Amitay, M. Shapiro, Phys. Rev. Lett. **89**, 063002 (2002)
50. I. Thanopulos, P. Král, M. Shapiro, Phys. Rev. Lett. **92**, 113003 (2004)
51. S.A. Rice, M. Zhao, *Optical Control of Molecular Dynamics* (Wiley, New York, 2000)
52. M. Shapiro, P. Brumer, *Principles of the Quantum Control of Molecular Processes* (John Wiley and Sons, Hoboken, 2003)
53. P. Brumer, M. Shapiro, Chem. Phys. Lett. **126**, 541 (1986)
54. M. Shapiro, E. Frishmann, P. Brumer, Phys. Rev. Lett. **84**, 1669 (2000)
55. G. Kurizki, M. Shapiro, P. Brumer, Phys. Rev. B **39**, 3435(R) (1989)
56. P. Král, I. Thanopulos, M. Shapiro, Rev. Mod. Phys. **79**, 53 (2007)
57. D.J. Tannor, S.A. Rice, J. Chem. Phys. **83**, 5013 (1985)
58. D.J. Tannor, R. Kosloff, S.A. Rice, J. Chem. Phys. **85**, 5805 (1986)
59. A. Bach, J.M. Hutchison, R.J. Holiday, F.F. Crim, J. Phys. Chem. A **107**, 10490 (2003)
60. S. Yan, Y.-T. Wu, B. Zhang, X.-F. Yue, K. Liu, Science **316**, 1723 (2007)
61. R. Beck, P. Maroni, D.C. Papageorgopoulos, T.T. Dang, M.P. Schmid, T.R. Rizzo, Science **302**, 98–100 (2003)
62. B.J. Sussman, M.Y. Ivanov, A. Stolow, Phys. Rev. A **71**, 051401(R) (2005)
63. B.J. Sussman, D. Townsend, M.Y. Ivanov, A. Stolow, Science **314**, 278 (2006)
64. M.E. Corrales, J. González-Vázquez, G. Balerdi, I.R. Solá, R. de Nalda, L. Bañares, Nature Chem. **6**, 785 (2014)
65. C. Sanz-Sanz, G.W. Richings, G.A. Worth, Faraday Discuss. **153**, 275 (2011)
66. G.W. Richhings, G.A. Worth, J. Phys. Chem. A **116**, 11228 (2012)
67. A.P. Peirce, M.A. Dahler, H. Rabitz, Phys. Rev. A **37**, 4950 (1988)
68. R. Kosloff, S.A. Rice, P. Gaspard, S. Tersigni, D.J. Tannor, Chem. Phys. **139**, 201 (1989)
69. V. Engel, C. Meier, D.J. Tannor, Adv. Chem. Phys. **141**, 21 (2009)
70. D. Daems, A. Ruschhaupt, D. Sugny, S. Guérin, Phys. Rev. Lett. **111**, 050404 (2013)
71. H. Stapelfeldt, T. Seideman, Rev. Mod. Phys. **75**, 543 (2003)

Part I
Theoretical Studies in Photophysics and Photochemistry: Applications to Aniline and Pyrazine

Chapter 2
Basic Concepts and Methodology

In this chapter, the main concepts relevant for the theoretical study of elementary photochemical processes are briefly reviewed. The notions of vibronic coupling and conical intersection are first introduced. The main basic tools from the molecular electronic structure theory and their use for the exploration of potential energy surfaces are then presented.

2.1 The Molecular Schrödinger Equation

2.1.1 The Molecular Hamiltonian Operator

The Hamiltonian operator $H(\boldsymbol{r}, \boldsymbol{R})$ of a molecule composed of N_{nu} nuclei and N_{el} electrons is the sum of a nuclear kinetic energy operator (KEO) $T_{nu}(\boldsymbol{R})$, an electronic KEO $T_{el}(\boldsymbol{r})$ and a potential energy operator $V(\boldsymbol{r}, \boldsymbol{R})$ that describes the Coulombic interaction between the different particles. Here, $\boldsymbol{r}$ and $\boldsymbol{R}$ denote vectors collecting all the electron and nuclear coordinates respectively. The KEOs read

$$T_{nu}(\boldsymbol{R}) = -\sum_{\alpha}^{N_{nu}} \frac{\hbar^2}{2M_{\alpha}} \boldsymbol{\nabla}_{\alpha} . \boldsymbol{\nabla}_{\alpha} \tag{2.1}$$

$$T_{el}(\boldsymbol{r}) = -\sum_{i}^{N_{el}} \frac{\hbar^2}{2m_e} \boldsymbol{\nabla}_{i} . \boldsymbol{\nabla}_{i} \tag{2.2}$$

where m_e is the mass of the electron, M_{α} is the mass of the αth nucleus and $\boldsymbol{\nabla}_i$ ($\boldsymbol{\nabla}_{\alpha}$) is a vector operator containing the derivative operators with respect to the coordinates of the ith electron (αth nucleus) as elements, i.e $\boldsymbol{\nabla}_i = \left(\frac{\partial}{\partial x_i}, \frac{\partial}{\partial y_i}, \frac{\partial}{\partial z_i} \right)$ in Cartesian coordinates. The potential operator is the sum of an electron–electron repulsion operator, a nucleus–nucleus repulsion operator and an electron–nucleus

attraction operator

$$V(\boldsymbol{r}, \boldsymbol{R}) = \sum_{i}^{N_{el}} \sum_{j>i}^{N_{el}} \frac{e^2}{4\pi\varepsilon_0 |\boldsymbol{r}_j - \boldsymbol{r}_i|} + \sum_{\alpha}^{N_{nu}} \sum_{\beta>\alpha}^{N_{nu}} \frac{Z_\alpha Z_\beta e^2}{4\pi\varepsilon_0 |\boldsymbol{R}_\alpha - \boldsymbol{R}_\beta|} - \sum_{\alpha}^{N_{nu}} \sum_{i}^{N_{el}} \frac{Z_\alpha e^2}{4\pi\varepsilon_0 |\boldsymbol{R}_\alpha - \boldsymbol{r}_i|},$$
(2.3)

where Z_α is the charge of the αth nucleus, e is the electron charge, $\boldsymbol{r}_i$ and $\boldsymbol{R}_\alpha$ are the position vectors of the ith electron and αth nucleus, respectively.

The quantum mechanical description of a molecule requires the solution of the time-dependent Schrödinger equation (TDSE) associated with the Hamiltonian operator $H(\boldsymbol{r}, \boldsymbol{R}) = T_{nu}(\boldsymbol{R}) + T_{el}(\boldsymbol{r}) + V(\boldsymbol{r}, \boldsymbol{R})$ described above

$$H(\boldsymbol{r}, \boldsymbol{R})\Psi(\boldsymbol{r}, \boldsymbol{R}, t) = i\hbar \frac{\partial}{\partial t} \Psi(\boldsymbol{r}, \boldsymbol{R}, t).$$
(2.4)

Because the motions of the various particles are correlated through the potential terms of Eq. (2.3), the direct integration of the molecular Schrödinger equation is an extremely difficult task that is only possible, in practice, for the simplest atomic and molecular systems.

2.1.2 The Born–Oppenheimer Approximation

The above problem can be simplified by separating the fast electronic motion from the slow nuclear motion. One first defines an electronic Hamiltonian, also called clamped nucleus Hamiltonian $H_{el}(\boldsymbol{r}; \boldsymbol{R}) = T_{el}(\boldsymbol{r}) + V(\boldsymbol{r}; \boldsymbol{R})$. This electronic Hamiltonian acts in the electronic space and depends parametrically on the nuclear coordinates $\boldsymbol{R}$, as indicated by the semicolon in the coordinate dependence of the operators. The eigenfunctions and eigenvalues of the associated time-independent Schrödinger equation (TISE)

$$H_{el}(\boldsymbol{r}; \boldsymbol{R})\phi_n(\boldsymbol{r}; \boldsymbol{R}) = V_n(\boldsymbol{R})\phi_n(\boldsymbol{r}; \boldsymbol{R})$$
(2.5)

are the electronic adiabatic energies and eigenfunctions. The set of eigenfunctions $\{\phi_n(\boldsymbol{r}; \boldsymbol{R})\}$ satisfies the usual orthonormality relation

$$\langle \phi_m | \phi_n \rangle = \int \phi_m^*(\boldsymbol{r}; \boldsymbol{R}) \phi_n(\boldsymbol{r}; \boldsymbol{R}) d\boldsymbol{r} = \delta_{mn}.$$
(2.6)

The molecular wavefunction $\Psi(\boldsymbol{r}, \boldsymbol{R}, t)$ of Eq. (2.4) can be expanded in the basis of the electronic eigenfunctions

$$\Psi(\boldsymbol{r}, \boldsymbol{R}, t) = \sum_{n} \chi_n(\boldsymbol{R}, t) \phi_n(\boldsymbol{r}; \boldsymbol{R}).$$
(2.7)

The exact molecular TDSE then reads

$$T_{nu} \sum_n \chi_n(\boldsymbol{R}, t)\phi_n(\boldsymbol{r}; \boldsymbol{R}) + H_{el} \sum_n \chi_n(\boldsymbol{R}, t)\phi_n(\boldsymbol{r}; \boldsymbol{R}) = i\hbar \frac{\partial}{\partial t} \sum_n \chi_n(\boldsymbol{R}, t)\phi_n(\boldsymbol{r}; \boldsymbol{R}).$$

(2.8)

Let us, for simplicity, rewrite the nuclear kinetic energy operator in terms of mass-weighted rectilinear coordinates (defined as the rectilinear coordinates multiplied by the square root of the mass of the nucleus) $T_{nu} = -\frac{\hbar^2}{2}\boldsymbol{\nabla}_R.\boldsymbol{\nabla}_R$. The first term of the last equation can now be developed

$$T_{nu} \sum_n \chi_n(\boldsymbol{R}, t)\phi_n(\boldsymbol{r}; \boldsymbol{R}) = \sum_n [\chi_n(\boldsymbol{R}, t)T_{nu}\phi_n(\boldsymbol{r}; \boldsymbol{R}) + \phi_n(\boldsymbol{r}; \boldsymbol{R})T_{nu}\chi_n(\boldsymbol{R}, t)$$
$$- \hbar^2\boldsymbol{\nabla}_R\phi_n(\boldsymbol{r}; \boldsymbol{R}).\boldsymbol{\nabla}_R\chi_n(\boldsymbol{R}, t)].$$

(2.9)

Inserting Eq. (2.9) in Eq. (2.8), multiplying from the left by $\phi_m^*(\boldsymbol{r}; \boldsymbol{R})$ and integrating over the electronic coordinates, one obtains

$$[T_{nu} + V_m(\boldsymbol{R})]\chi_m(\boldsymbol{R}, t) + \sum_n \Lambda_{mn}\chi_n(\boldsymbol{R}, t) = i\hbar\frac{\partial}{\partial t}\chi_m(\boldsymbol{R}, t).$$

(2.10)

This last equation shows that the nuclear motion of the molecule obeys an infinite set of coupled differential equations. The so-called *non-adiabatic couplings* Λ_{mn} describe the dynamical interaction between the electronic and nuclear motions [1–3]. They are given by

$$\Lambda_{mn} = \boldsymbol{F}_{mn}.\boldsymbol{\nabla}_R + G_{mn}$$

(2.11)

where $\boldsymbol{F}_{mn} = -\hbar^2\langle\phi_m|\boldsymbol{\nabla}_R\phi_n\rangle$ is a non-adiabatic *derivative coupling vector* element and $G_{mn} = \langle\phi_m|T_{nu}|\phi_n\rangle = -\frac{\hbar^2}{2}\langle\phi_m|\nabla_R^2\phi_n\rangle$ is an element of the non-adiabatic *scalar couplings*. The derivative coupling vector matrix $\boldsymbol{F}$ is antihermitian, i.e $\boldsymbol{F}^\dagger = -\boldsymbol{F}$. If the adiabatic electronic wavefunctions $\phi_n(\boldsymbol{r}; \boldsymbol{R})$ are chosen to be real, then the diagonal elements of $\boldsymbol{F}$ vanish.

The Born–Oppenheimer approximation [4, 5] consists in neglecting the non-adiabatic couplings. This approximation relies on the very different masses of the electron and nuclei. Indeed, the proton, which is the lightest atomic nucleus, is roughly 1836 times heavier than the electron. Therefore the electron velocity is much higher than that of the nuclei and the fast electrons adjust instantaneously to the slow motion of the nuclei. Within this approximation, no transition between different adiabatic electronic states can be induced by the nuclear motion and in this case, the total molecular wavefunction can be written as

$$\Psi(\boldsymbol{r}, \boldsymbol{R}, t) = \chi(\boldsymbol{R}, t)\phi(\boldsymbol{r}; \boldsymbol{R}),$$

(2.12)

which leads to

$$[T_{nu} + V(\boldsymbol{R}) + \Lambda]\chi(\boldsymbol{R}, t) = i\hbar\frac{\partial}{\partial t}\chi(\boldsymbol{R}, t).$$

(2.13)

Equation (2.13) constitutes the Born–Oppenheimer approximation. When the electronic adiabatic wavefunctions are chosen real, the non-adiabatic term simply reads $\Lambda = G = \langle \phi | T_{nu} | \phi \rangle$. Usually, Λ is very small and Eq. (2.13) is only used if very high accuracy is sought. Neglecting Λ leads to the so-called adiabatic approximation

$$[T_{nu} + V(\boldsymbol{R})] \chi(\boldsymbol{R}, t) = i\hbar \frac{\partial}{\partial t} \chi(\boldsymbol{R}, t). \tag{2.14}$$

Below, we show that the validity of the adiabatic approximation is directly related to the energy separation between the different electronic states. To this purpose, a useful expression for the derivative coupling vectors $\boldsymbol{F}_{mn}$ can be derived. It follows directly from the electronic TISE

$$\langle \phi_m | H_{el} | \phi_n \rangle = V_n(\boldsymbol{R}) \delta_{mn}. \tag{2.15}$$

Applying the nuclear gradient on both sides, one obtains

$$\boldsymbol{\nabla}_{\boldsymbol{R}} \langle \phi_m | H_{el} | \phi_n \rangle = \boldsymbol{\nabla}_{\boldsymbol{R}} V_n(\boldsymbol{R}) \delta_{mn}. \tag{2.16}$$

Let us develop the left hand side of this last equation

$$\boldsymbol{\nabla}_{\boldsymbol{R}} \langle \phi_m | H_{el} | \phi_n \rangle = \langle \boldsymbol{\nabla}_{\boldsymbol{R}} \phi_m | H_{el} | \phi_n \rangle + \langle \phi_m | (\boldsymbol{\nabla}_{\boldsymbol{R}} H_{el}) | \phi_n \rangle + \langle \phi_m | H_{el} | \boldsymbol{\nabla}_{\boldsymbol{R}} \phi_n \rangle$$
$$= (V_m(\boldsymbol{R}) - V_n(\boldsymbol{R})) \langle \phi_m | \boldsymbol{\nabla}_{\boldsymbol{R}} \phi_n \rangle + \langle \phi_m | (\boldsymbol{\nabla}_{\boldsymbol{R}} H_{el}) | \phi_n \rangle. \tag{2.17}$$

From the last two equations, one finally obtains

$$\boldsymbol{F}_{mn} = \frac{\langle \phi_m | (\boldsymbol{\nabla}_{\boldsymbol{R}} H_{el}) | \phi_n \rangle - \boldsymbol{\nabla}_{\boldsymbol{R}} V_n(\boldsymbol{R}) \delta_{mn}}{V_n(\boldsymbol{R}) - V_m(\boldsymbol{R})}. \tag{2.18}$$

For $m = n$, we have seen above that by choosing the $\phi_n(\boldsymbol{r}; \boldsymbol{R})$ real, the $\boldsymbol{F}_{nn}$ term vanishes. For $m \neq n$,

$$\boldsymbol{F}_{mn} = \frac{\langle \phi_m | (\boldsymbol{\nabla}_{\boldsymbol{R}} H_{el}) | \phi_n \rangle}{V_n(\boldsymbol{R}) - V_m(\boldsymbol{R})}. \tag{2.19}$$

This last equation shows that the magnitude of the non-adiabatic coupling vector depends on the energy separation between the different electronic states. They become large when different electronic states become close in energy. In particular, the non-adiabatic coupling vector diverges in the situation where two or more electronic states are degenerate. This particular situation is called a *conical intersection*, and leads to a breakdown of the adiabatic approximation near the degeneracy.

2.2 Vibronic Coupling

2.2.1 The Group Born–Oppenheimer Approximation

As seen in the previous section, the separability of the electronic and nuclear motions rests both on the large difference between the masses of electrons and nuclei and on a sufficient energetic separation between the electronic states. When electronic states become close in energy, the corresponding non-adiabatic coupling matrix elements become large and the Born–Oppenheimer approximation breaks down. However, in such situations, one is usually interested in a few electronic states and the couplings between them. Therefore one can consider a block of electronic states inside of which the non-adiabatic couplings are taken into account, and neglect the couplings between the states of interest and the other states. Considering a block of N_{st} states of interest, the set of equations of motion for the nuclei of Eq. (2.10) reduces to

$$[T_{nu} + V_m(\boldsymbol{R})] \chi_m(\boldsymbol{R}, t) + \sum_{n}^{N_{st}} \Lambda_{mn} \chi_n(\boldsymbol{R}, t) = i\hbar \frac{\partial}{\partial t} \chi_m(\boldsymbol{R}, t), \qquad (2.20)$$

where the indices n and m span the group of states of interest. Obviously, as for the original Born–Oppenheimer approximation, this partitioning of the space of the electronic states is only valid if the energy separation between the electronic states of interest and the higher electronic states is sufficient. This approximation is known as the group Born–Oppenheimer approximation [3].

2.2.2 The Diabatic Representation

Although the group Born–Oppenheimer approximation greatly simplifies the description of molecular systems with strong vibronic interactions between low-lying electronic states, Eq. (2.20) is still difficult to handle when the electronic states are nearly degenerate because of the divergence of the derivative couplings $\boldsymbol{F}_{mn}$, and of the topography of the adiabatic potential energy surfaces (PESs), which are difficult to represent by simple mathematical expressions. Therefore, in general, a more convenient representation of the electronic states, called *diabatic representation*, is used in quantum dynamical investigations. The diabatic representation is constructed such as to provide smooth potential energy and coupling surfaces. The diabatic basis is obtained through a unitary transformation

$$\phi^d(r; \boldsymbol{R}) = \boldsymbol{S}(\boldsymbol{R})\phi(r; \boldsymbol{R}), \qquad (2.21)$$

where $\phi = (\phi_1, \phi_2, \ldots, \phi_{N_{st}})^T$ and similarly $\phi^d = (\phi_1^d, \phi_2^d, \ldots, \phi_{N_{st}}^d)^T$, such that the derivative couplings in the new representation are zero

$$\boldsymbol{F}_{mn}^{d} = \langle \phi_m^d | \boldsymbol{\nabla}_R \phi_n^d \rangle = 0. \tag{2.22}$$

The diabatic derivative coupling matrix can be expressed in the adiabatic representation as

$$\boldsymbol{F}^d = \boldsymbol{S}^\dagger \boldsymbol{F} \boldsymbol{S} + \boldsymbol{S}^\dagger \boldsymbol{\nabla} \boldsymbol{S} \tag{2.23}$$

with $\boldsymbol{F} = [F_{mn}]$. It follows immediately that the unitary transformation that fulfills $\boldsymbol{F}^d = 0$ satisfies the following equation:

$$\boldsymbol{F}\boldsymbol{S} + \boldsymbol{\nabla}\boldsymbol{S} = 0. \tag{2.24}$$

Unfortunately, in the general case of a polyatomic molecule, the last equation only has a solution if the complete set of adiabatic electronic states is considered. Therefore, in practice, a strict diabatic basis does not exist and one usually searches a quasidiabatic representation that makes the derivative couplings small enough to be safely neglected. Several methods have been proposed to obtain a quasidiabatic representation from ab initio computed data in the adiabatic representation. These methods, which are reviewed in the Chap. 4 of Ref. [6], can be classified into three classes, depending on the type of data used to construct the quasidiabatic representation. The first class contains derivative-based methods, which use ab initio computed derivative couplings to integrate directly Eq. (2.24). These methods require the computation of the derivative couplings over extended portions of the geometry space and are therefore computationally expansive. The second class contains property-based methods, which attempt to reduce the configurational change of the electronic wavefunctions upon geometry changes to determine the transformation matrix $\boldsymbol{S}$. Since smoother electronic states yield smoother properties, this can also be achieved by enforcing the smoothness of electronic properties, such as, for instance, the dipole moment. The last class contains energy-based methods, which use only ab initio computed electronic energies.

Assuming that a suitable quasidiabatic representation has been derived, the TDSE in the diabatic representation can be written in matrix form as

$$[T_{nu}\boldsymbol{I} + \boldsymbol{W}(\boldsymbol{R})]\boldsymbol{\chi}^d(\boldsymbol{R}, t) = i\hbar\frac{\partial}{\partial t}\boldsymbol{\chi}^d(\boldsymbol{R}, t), \tag{2.25}$$

where

$$\boldsymbol{\chi}^d(\boldsymbol{R}, t) = \boldsymbol{S}(\boldsymbol{R})\boldsymbol{\chi}(\boldsymbol{R}, t), \tag{2.26}$$

is the vector of the diabatic nuclear wavefunction components and

$$\boldsymbol{W}(\boldsymbol{R}) = \boldsymbol{S}^\dagger(\boldsymbol{R})\boldsymbol{V}(\boldsymbol{R})\boldsymbol{S}(\boldsymbol{R}) \tag{2.27}$$

is the matrix of the diabatic potentials with

$$W_{mn} = \langle \phi_m^d | H_{el} | \phi_n^d \rangle. \tag{2.28}$$

We note that the diabatic electronic states are no longer eigenstates of the electronic Schrödinger equation, which means that the diabatic potential matrix is not diagonal. This transformed nuclear TDSE has a much more appealing form than the original nuclear TDSE in the adiabatic representation of Eq. (2.20) because the couplings between the different diabatic electronic states now appear in the diabatic potential matrix $W(R)$ that contains only local, i.e scalar, operators. In addition, in practice, the diabatic potential and coupling surfaces have a much simpler topography than their adiabatic counterparts.

2.2.3 Conical Intersections

The diabatic representation can now be used to characterize the topography of the PESs at the vicinity of conical intersections. We first expand the diabatic potential energy matrix elements as Taylor expansions around a reference geometry R_0

$$W(R) = W^{(0)} + W^{(1)} + W^{(2)} + \cdots. \tag{2.29}$$

It is assumed that the diabatic representation has been constructed such that, at this point, the adiabatic and diabatic representations are identical. This is always possible since Eq. (2.24) defines the transformation $S(R)$ up to a constant unitary transformation. In other words, if the matrix $S(R)$ satisfies Eq. (2.24), the matrix $TS(R)$, where T does not depends on R, also does. Therefore, by choosing $T = S^\dagger(R_0)$, the adiabatic and diabatic representations are identical at R_0. This point can be the ground state equilibrium geometry, a point of electronic degeneracy, or any other point of interest. The zeroth order diabatic potential matrix is simply the diagonal matrix of the adiabatic energies

$$W_{ij}^{(0)} = \langle \phi_i | H_{el} | \phi_j \rangle \big|_{R_0} = V_i(R_0)\delta_{ij}. \tag{2.30}$$

The first order potential matrix can be expressed in the adiabatic basis at R_0 as

$$W_{ij}^{(1)}(R) = \left[\langle \phi_i | \nabla_R H_{el} | \phi_j \rangle \big|_{R_0} \right]^T (R - R_0). \tag{2.31}$$

For diagonal elements, this leads to

$$\begin{aligned} W_{ii}^{(1)}(R) &= \left[\langle \phi_i | \nabla_R H_{el} | \phi_i \rangle |_{R_0} \right]^T (R - R_0) \\ &= \left[\nabla_R \langle \phi_i | H_{el} | \phi_i \rangle |_{R_0} \right]^T (R - R_0) \\ &= \nabla_R V_i(R) |_{R_0}^T (R - R_0), \end{aligned} \tag{2.32}$$

where we have used the fact that the diagonal elements of the F matrix are zero for real electronic wavefunctions. One can see from this last equation that the gradients

of the adiabatic PESs at the reference geometry R_0 appear in $W_{ii}^{(1)}(R)$. In addition, the non-diagonal elements $W_{ij}^{(1)}(R)$ are related to the derivative couplings given in Eq. (2.19).

The adiabatic potential energy matrix $V(R)$ is obtained by diagonalizing the diabatic potential energy matrix $W(R)$, through the unitary transformation $S(R)$ introduced in Eq. (2.21)

$$V(R) = S(R)W(R)S^{\dagger}(R). \tag{2.33}$$

Considering a two-state system, the adiabatic PESs read

$$V_{1,2}(R) = \frac{1}{2}(W_{11}(R) + W_{22}(R)) \mp \frac{1}{2}\sqrt{(W_{22}(R) - W_{11}(R))^2 + 4W_{12}(R)^2}. \tag{2.34}$$

We now truncate the expansion of Eq. (2.29) to first order and consider R_0 to be a point of degeneracy. Introducing the following notations: $Q = R - R_0$, $W_{ii}^{(1)}(Q) = \kappa^{(i)}.Q$ and $W_{12}^{(1)}(Q) = \lambda.Q$, the adiabatic PESs read

$$V_{1,2}(Q) = \frac{1}{2}(\kappa^{(1)} + \kappa^{(2)}).Q \mp \frac{1}{2}\sqrt{(\delta.Q)^2 + 4(\lambda.Q)^2}, \tag{2.35}$$

where $\delta = \kappa^{(2)} - \kappa^{(1)}$. From this last equation, the conditions for the existence of a conical intersection between the two adiabatic PESs are:

$$\delta.Q = 0 \quad \text{and} \quad \lambda.Q = 0. \tag{2.36}$$

Therefore, at first order, the degeneracy is lifted along two directions defined by the unitary vectors

$$e_g = \frac{g}{||g||} = \frac{\nabla_Q(\delta.Q)}{||\nabla_Q(\delta.Q)||} = \frac{\delta}{||\delta||}, \tag{2.37}$$

and

$$e_h = \frac{h}{||h||} = \frac{\nabla_Q(\lambda.Q)}{||\nabla_Q(\lambda.Q)||} = \frac{\lambda}{||\lambda||}. \tag{2.38}$$

In these last equations, $g = \delta$ is the *gradient difference* vector and $h = \lambda$ is the linear *derivative coupling* vector. The space spanned by these two vectors is called the $g - h$ space or branching space whereas the space orthogonal to the branching space is the intersection space, also called conical intersection seam. Thus, a conical intersection is a subspace of the nuclear configuration space of dimension 3N-8, where N denotes the number of atoms of the system (the space of the nuclear configurations is of dimension 3N-6).

From Eq. (2.35), the adiabatic PESs form a double cone at the intersection, as illustrated in Fig. 2.1. Any infinitesimal displacement along a direction orthogonal to the branching space preserves the degeneracy. However we stress that, because
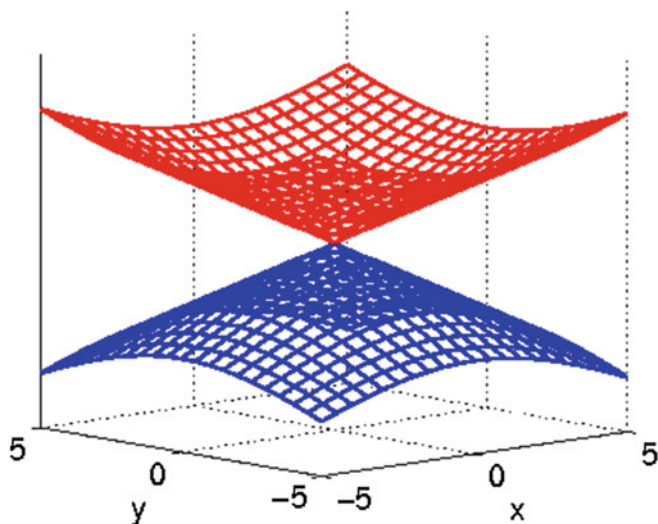
Fig. 2.1 Adiabatic PESs around a conical intersection obtained within the first-order description. The PESs are obtained from Eq. (2.34) with $W_{11} = -x$, $W_{22} = x$ and $W_{12} = y$. V_1 and V_2 are displayed in *blue* and *red*, respectively

of the first order nature of the above analysis, a finite displacement along such a direction will in general lift the degeneracy. This is a consequence of the curvature of the conical intersection seam, encapsulated in the second order terms $W^{(2)}$ in Eq. (2.29) [7–9].

2.3 Basics of Electronic Structure Theory

In the previous section, we have seen that in a vast majority of cases, the quantum mechanical description of a molecular system can be greatly simplified if the nuclear and electronic motions are separated. In this case, the electronic problem can be treated for fixed nuclei by solving the clamped nucleus or electronic TISE of Eq. (2.5). Finding accurate and efficient numerical procedures to solve the electronic TISE has been a major goal of theoretical chemistry since the beginning of the second part of the previous century [10, 11].

2.3.1 Spin Orbitals and Slater Determinants

In quantum mechanics, to completely describe an electron, the spin needs to be considered in addition to its motion in space. Electrons have a spin $s = \frac{1}{2}$,

therefore the electron spin state space is spanned by the orthonormal basis $\left\{|s = \frac{1}{2}, m_s = \frac{1}{2}\rangle, |s = \frac{1}{2}, m_s = -\frac{1}{2}\rangle\right\}$ conventionally noted $\{|\alpha\rangle, |\beta\rangle\}$. It is often convenient, for ease of notation, to introduce an unspecified spin variable, that we note σ, and to represent the eigenstates $|\alpha\rangle$ and $|\beta\rangle$ by eigenfunctions $\langle\sigma|\alpha\rangle = \alpha(\sigma)$ and $\langle\sigma|\beta\rangle = \beta(\sigma)$. It follows that an electron will be specified by four variables, the three spatial variables, gathered in the vector $\boldsymbol{r}$ and the spin variable. These will be conveniently gathered in a vector $\boldsymbol{\xi} \equiv (\boldsymbol{r}, \sigma)$. In general, the wavefunction of a single electron $\psi(\boldsymbol{\xi})$ is called a spin orbital. It is expressed as the product of a function of the spatial coordinates $\boldsymbol{r}$ named spatial orbital and one of the two spin functions

$$\psi(\boldsymbol{\xi}) = \varphi(\boldsymbol{r}) \times \begin{cases} \alpha(\sigma) \\ \text{or} \\ \beta(\sigma) \end{cases}. \tag{2.39}$$

From a set of K spatial orbitals, a set of $2K$ spin orbitals can be generated. In addition, if the spatial orbitals are orthonormal, so are the spin orbitals. In the rest of this chapter, the spin orbitals will be called molecular orbitals (MOs).

The wavefunction of a N-electron system must be antisymmetric with respect to the exchange of two electrons

$$\Psi\left(\boldsymbol{\xi_1}, \ldots, \boldsymbol{\xi_i}, \ldots, \boldsymbol{\xi_j}, \ldots, \boldsymbol{\xi_N}\right) = -\Psi\left(\boldsymbol{\xi_1}, \ldots, \boldsymbol{\xi_j}, \ldots, \boldsymbol{\xi_i}, \ldots, \boldsymbol{\xi_N}\right). \tag{2.40}$$

A wavefunction satisfying this requirement can be conveniently written in the form of a Slater determinant [12]

$$\Phi(\boldsymbol{\xi_1}, \boldsymbol{\xi_2}, \ldots, \boldsymbol{\xi_N}) = \frac{1}{\sqrt{N!}} \begin{vmatrix} \psi_1(\boldsymbol{\xi_1}) & \psi_2(\boldsymbol{\xi_1}) & \cdots & \psi_N(\boldsymbol{\xi_1}) \\ \psi_1(\boldsymbol{\xi_2}) & \psi_2(\boldsymbol{\xi_2}) & \cdots & \psi_N(\boldsymbol{\xi_2}) \\ \vdots & \vdots & \ddots & \vdots \\ \psi_1(\boldsymbol{\xi_N}) & \psi_2(\boldsymbol{\xi_N}) & \cdots & \psi_N(\boldsymbol{\xi_N}) \end{vmatrix}. \tag{2.41}$$

The factor $\frac{1}{\sqrt{N!}}$ ensures the normalization of the Slater determinant. As seen in Eq. (2.41), the coordinates of a single electron appear in a given row whereas a single MO appears in a given column. According to the general properties of determinants, the exchange of the coordinates of two electrons correspond to the permutation of two rows of the determinant, which changes its sign. Therefore the Slater determinant satisfies the antisymmetry principle, illustrated by Eq. (2.40). In addition, if two MOs are identical, two of the columns of the determinant are identical, which makes it zero. This correspond to the physical situation of two electron being in the same quantum state. Thus we see that the antisymmetry principle implies that two fermions can not be in the same quantum state. This principle is known as the Pauli exclusion principle.

2.3.2 The Hartree–Fock Approximation

The Hartree–Fock approximation [13, 14] plays a central role in the molecular electronic structure theory. In most cases, it provides a qualitatively correct description of the electronic structure of many electron atoms and molecules in their ground electronic state. In addition, it constitutes a basis upon which more accurate methods can be developed. A detailed derivation and discussion of the method can be found in textbooks such as [10, 11]. The Hartree–Fock approximation assumes the simplest possible form for the electronic wavefunction, i.e a single Slater determinant given by Eq. (2.41). Starting from the electronic TISE Eq. (2.5), the Hartree–Fock energy E^{HF} is simply

$$E^{HF} = \langle \Phi | H_{el} | \Phi \rangle. \tag{2.42}$$

The Hartree–Fock approximation relies on the variational principle, which states that any approximate wavefunction has an energy above or equal to the exact ground state energy. This principle has an important consequence: for a given system, the wavefunction of the form of Eq. (2.41) that minimizes the energy in Eq. (2.42) is the best possible wavefunction within the single determinant approximation.

Let us write the electronic Hamiltonian in atomic units

$$H_{el}(r; R) = -\frac{1}{2} \sum_i^{N_{el}} \nabla_i . \nabla_i + \sum_i^{N_{el}} \sum_{j>i}^{N_{el}} \frac{1}{|r_j - r_i|} - \sum_\alpha^{N_{nu}} \sum_i^{N_{el}} \frac{Z_\alpha}{|R_\alpha - r_i|} + \sum_\alpha^{N_{nu}} \sum_{\beta>\alpha}^{N_{nu}} \frac{Z_\alpha Z_\beta}{|R_\alpha - R_\beta|}. \tag{2.43}$$

This Hamiltonian can be written as the sum of three operators

$$H_{el}(r; R) = O^1(r; R) + O^2(r) + V^{NR}(R), \tag{2.44}$$

where

$$O^1(r; R) = \sum_i^{N_{el}} h_i \tag{2.45}$$

with

$$h_i = -\frac{1}{2} \nabla_i . \nabla_i - \sum_\alpha^{N_{nu}} \frac{Z_\alpha}{|R_\alpha - r_i|} \tag{2.46}$$

is a mono-electronic operator,

$$O^2(r) = \sum_i^{N_{el}} \sum_{j>i}^{N_{el}} g_{ij} \tag{2.47}$$

with

$$g_{ij} = \frac{1}{|r_j - r_i|} \tag{2.48}$$

is a bi-electronic operator, and

$$V^{NR}(\boldsymbol{R}) = \sum_{\alpha}^{N_{nu}} \sum_{\beta > \alpha}^{N_{nu}} \frac{Z_{\alpha} Z_{\beta}}{|\boldsymbol{R}_{\alpha} - \boldsymbol{R}_{\beta}|} \tag{2.49}$$

is the nuclear repulsion potential energy operator. This last operator does not depend on the electronic coordinates and therefore contributes to the molecular energy as a constant.

With these definitions, the Slater–Condon rules [12, 15] can be used to obtain an expression for the energy of Eq. (2.42) as a function of the MOs. The contribution of the mono-electronic operator reads

$$\langle \Phi | O^1 | \Phi \rangle = \sum_{i}^{N_{el}} \langle \psi_i(\boldsymbol{\xi_1}) | h_1 | \psi_i(\boldsymbol{\xi_1}) \rangle. \tag{2.50}$$

The contribution of the bi-electronic operators reads

$$\langle \Phi | O^2 | \Phi \rangle = \sum_{i}^{N_{el}} \sum_{j>i}^{N_{el}} \left(\langle \psi_i(\boldsymbol{\xi_1}) \psi_j(\boldsymbol{\xi_2}) | g_{12} | \psi_i(\boldsymbol{\xi_1}) \psi_j(\boldsymbol{\xi_2}) \rangle - \langle \psi_i(\boldsymbol{\xi_1}) \psi_j(\boldsymbol{\xi_2}) | g_{12} | \psi_j(\boldsymbol{\xi_1}) \psi_i(\boldsymbol{\xi_2}) \rangle \right)$$

$$= \frac{1}{2} \sum_{i}^{N_{el}} \sum_{j}^{N_{el}} \left(J_{ij} - K_{ij} \right). \tag{2.51}$$

In this last equation, J_{ij} and K_{ij} denote the Coulomb and exchange integrals, respectively. The Coulomb integral represents the repulsion between the two electronic densities $|\psi_i(\boldsymbol{\xi_1})|^2$ and $|\psi_j(\boldsymbol{\xi_2})|^2$. The exchange integral has no classical analogue and is a consequence of the Pauli principle. Using Eqs. (2.50) and (2.51), the Hartree–Fock energy reads

$$E^{HF} = \sum_{i}^{N_{el}} \langle \psi_i(\boldsymbol{\xi_1}) | h_1 | \psi_i(\boldsymbol{\xi_1}) \rangle + \frac{1}{2} \sum_{i}^{N_{el}} \sum_{j}^{N_{el}} (J_{ij} - K_{ij}) + V_{NR}(\boldsymbol{R}). \tag{2.52}$$

The above equation can be recast in a form where the Coulomb and exchange integrals are replaced by the expectation values of Coulomb and exchange operators J_i and K_i, defined such that

$$J_i | \psi_j(\boldsymbol{\xi_2}) \rangle = \langle \psi_i(\boldsymbol{\xi_1}) | g_{12} | \psi_i(\boldsymbol{\xi_1}) \rangle | \psi_j(\boldsymbol{\xi_2}) \rangle \tag{2.53}$$

and

$$K_i | \psi_j(\boldsymbol{\xi_2}) \rangle = \langle \psi_i(\boldsymbol{\xi_1}) | g_{12} | \psi_j(\boldsymbol{\xi_1}) \rangle | \psi_i(\boldsymbol{\xi_2}) \rangle. \tag{2.54}$$

The energy now reads

$$E^{HF} = \sum_i^{N_{el}} \langle \psi_i(\boldsymbol{\xi_1})|h_1|\psi_i(\boldsymbol{\xi_1})\rangle + \frac{1}{2}\sum_i^{N_{el}}\sum_j^{N_{el}} \langle \psi_j(\boldsymbol{\xi_1})|J_i - K_i|\psi_j(\boldsymbol{\xi_1})\rangle + V_{NR}(\boldsymbol{R})$$

$$\equiv \sum_i^{N_{el}} \langle \psi_i|h_1|\psi_i\rangle + \frac{1}{2}\sum_i^{N_{el}}\sum_j^{N_{el}} \langle \psi_j|J_i - K_i|\psi_j\rangle + V_{NR}(\boldsymbol{R}). \tag{2.55}$$

In this last equation, the dependence of the orbitals on the electronic coordinates is dropped since it formally depends on the coordinates of a single electron.

The objective is now to find the set of MOs that minimizes the energy of Eq. (2.55), with the additional constraint that the set of MOs remains orthonormal. This type of constrained optimization problem can be conveniently solved by the method of Lagrange multipliers. This method consists in minimizing the Lagrange function $\mathcal{L}$

$$\mathcal{L} = E - \sum_i^{N_{el}}\sum_j^{N_{el}} \varepsilon_{ij}(\langle \psi_i|\psi_j\rangle - \delta_{ij}) \tag{2.56}$$

with respect to the MOs

$$\delta\mathcal{L} = \delta E - \sum_i^{N_{el}}\sum_j^{N_{el}} \varepsilon_{ij}(\langle \delta\psi_i|\psi_j\rangle - \langle \psi_i|\delta\psi_j\rangle) = 0, \tag{2.57}$$

where the ε_{ij} are the Lagrange multipliers.

By developing this last equation, one finds the Hartree–Fock equations

$$F_i|\psi_i\rangle = \sum_j \varepsilon_{ij}|\psi_j\rangle \tag{2.58}$$

where F_i is an effective one-electron operator called the Fock operator

$$F_i = h_i + \sum_j^{N_{el}} (J_j - K_j). \tag{2.59}$$

The Fock operator is the sum of two terms: an operator h_i containing the kinetic energy operator and the electron–nuclei attraction potential operator, and an operator describing the repulsion of the electron with all the other electrons.

The matrix of the Lagrange multipliers ε is hermitian, therefore there exists a unitary transformation U that diagonalizes ε. Applying this unitary transformation to the set of MOs $\{|\psi_i\rangle\}$

$$|\psi_i'\rangle = \sum_j U_{ij}|\psi_j\rangle \tag{2.60}$$

yields a new set of MOs $\{|\psi_i'\rangle\}$ verifying

$$F_i'|\psi_i'\rangle = \varepsilon_i'|\psi_i'\rangle \tag{2.61}$$

where $\varepsilon' = \boldsymbol{U}^\dagger \boldsymbol{\varepsilon} \boldsymbol{U}$. In addition, it can be shown that $F_i' = F_i$ and that the electronic wavefunction constructed with the new MOs is equal to the original electronic wavefunction to a phase factor. This transformed set of equations is known as the *canonical Hartree–Fock equations* and the corresponding orbitals the *canonical orbitals*. The prime symbols will be dropped from now on. In this representation, the Lagrangian multiplier are interpreted as orbital energies

$$\langle\psi_i|F_i|\psi_i\rangle = \varepsilon_i\langle\psi_i|\psi_i\rangle = \varepsilon_i. \tag{2.62}$$

Equation (2.61) forms a set of pseudo-eigenvalue equations as the Fock operator depends on the MOs via the Coulomb and exchange operators, and must be solved by an iterative procedure. The unknown MOs $\{|\psi_i\rangle\}$ are expanded in a set of non-orthogonal, atom-centered basis functions $|\psi_i\rangle = \sum_\mu c_{\mu i}|\chi_\mu\rangle$. Inserting this expansion in the canonical Hartree–Fock equations Eq. (2.61) yields

$$F_i\sum_\mu c_{\mu i}|\chi_\mu\rangle = \varepsilon_i\sum_\mu c_{\mu i}|\chi_\mu\rangle. \tag{2.63}$$

Multiplying on the left by χ_ν^* and integrating, one obtains

$$\sum_\mu c_{\mu i}\langle\chi_\nu|F_i|\chi_\mu\rangle = \varepsilon_i\sum_\mu c_{\mu i}\langle\chi_\nu|\chi_\mu\rangle. \tag{2.64}$$

This last set of equations can be written in a compact matrix form

$$\boldsymbol{FC} = \boldsymbol{SC\varepsilon} \tag{2.65}$$

where $\boldsymbol{F}$ is the Fock matrix of elements $F_{\nu\mu} = \langle\chi_\nu|F_i|\chi_\mu\rangle$, $\boldsymbol{S}$ is the overlap matrix of elements $S_{\nu\mu} = \langle\chi_\nu|\chi_\mu\rangle$ and $\boldsymbol{C}$ is the vector of the coefficients of the expansion of the MOs on the basis set $c_{\mu i} = \langle\chi_\mu|\psi_i\rangle$. These equations are known as the *Roothaan–Hall equations* [16, 17]. The problem of the calculation of the MOs is now turned into the determination of the coefficients $c_{\mu i}$.

The presence of the overlap matrix $\boldsymbol{S}$ in the Roothaan–Hall equations Eq. (2.65) reflects the fact that the basis functions used to expand the orbitals are non-orthogonal. By multiplying from the left by $\boldsymbol{S}^{-\frac{1}{2}}$ and inserting the unit matrix $\boldsymbol{I} = \boldsymbol{S}^{-\frac{1}{2}}\boldsymbol{S}^{\frac{1}{2}}$, Eq. (2.65) can be recast as

$$\tilde{\boldsymbol{F}}\tilde{\boldsymbol{C}} = \tilde{\boldsymbol{C}}\boldsymbol{\varepsilon}, \tag{2.66}$$

where $\tilde{F} = S^{-\frac{1}{2}} F S^{-\frac{1}{2}}$ and $\tilde{C} = S^{\frac{1}{2}} C$. Equation (2.66) is a standard set of eigenvalue equations, the diagonalization of the matrix $\tilde{F}$ yields a set of eigenvectors $\tilde{C}$ which can be back-transformed to obtain the vectors C solutions of Eq. (2.65).

As mentioned above, since the construction of the Fock matrix F involves the calculation of integrals over the Coulomb and exchange operators which depend on the MOs that we want to calculate, the Roothaan–Hall equations must be solved iteratively. The procedure starts with the definition of an initial guess for the MOs. This can be done conveniently by using simple empirical methods such as the Hückel method [18]. Using this initial guess, the Fock matrix can be constructed and diagonalized to yield a new set of MOs which is in turn used to construct a new Fock matrix. This procedure, called the Self-Consistent Field (SCF) method, is iterated until convergence of the MOs.

For a N-electron closed-shell molecule, using a basis containing $M \geq N$ functions, the solution of the Roothaan–Hall equations generates M spatial orbitals and $2M$ spin orbitals. In the case of molecule with an even number of electrons and a singlet ground state (a closed-shell molecule), the restriction that each spatial orbital should have two electrons (one with spin α and one with spin β) is usually made. This method is called *restricted Hartree–Fock* method. In this case, among the M spatial orbitals obtained from the calculation, the $N/2$ orbitals of lowest energy are occupied and the remaining $M - N/2$ MOs are unoccupied, or virtual orbitals. The Hartree–Fock energy and the N-electron wavefunction are obtained using the $N/2$ occupied orbitals. This description defines the notion of an electronic configuration associated with a Slater determinant, which correspond to a particular repartition of the electrons in the different MOs.

In most cases, the Hartree–Fock method provides a qualitatively correct description of the electronic structure of a molecular system. Usually, the Hartree–Fock method gives 99 % of the total energy of the molecule described by the non-relativistic Schrödinger equation and the clamped nucleus Hamiltonian. The difference between the best Hartree–Fock energy, i.e the Hartree–Fock energy in the limit of an infinite basis, and the "exact" energy is called the electronic correlation energy.

2.3.3 Electronic Correlation

Taking into account the electronic correlation is mandatory if a quantitative description of the electronic structure and energy of the system of interest is required. In addition, in some cases, the inclusion of the electronic correlation effects are necessary to obtain even a qualitatively correct description of the electronic structure of the system. By definition, the mean-field approximation resulting from the approximation of the multi-electron wavefunction by a single Slater determinant is unable to account for the electronic correlation. A correlated electronic wavefunction must then be written as a linear combination of several Slater determinants
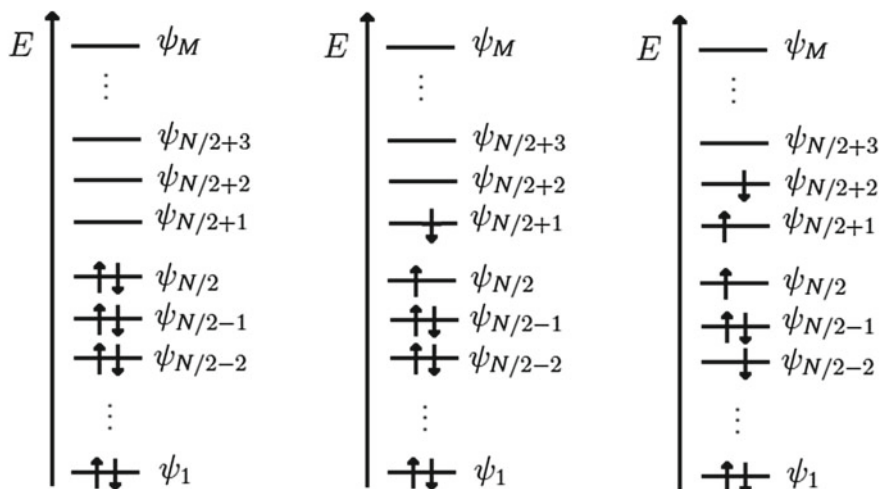
Fig. 2.2 Scheme illustrating different electronic configuration for a molecular system of N electrons described in a basis of M orbitals. The *left scheme* shows the ground state configuration, the *middle scheme* shows a singly excited configuration and the *right scheme* a doubly excited configuration

$$\Psi(\boldsymbol{\xi_1}, \boldsymbol{\xi_2}, \ldots, \boldsymbol{\xi_N}) = \sum_i c_i \Phi_i(\boldsymbol{\xi_1}, \boldsymbol{\xi_2}, \ldots, \boldsymbol{\xi_N}). \tag{2.67}$$

From a set of orbitals such as the one obtained from a Hartree–Fock calculation, many Slater determinants corresponding to excited configurations can be constructed. These are obtained by replacing one or several occupied orbitals by virtual orbitals, as illustrated in Fig. 2.2.

Usually, two different types of electronic correlation are distinguished, the *static electronic correlation* and the *dynamic electronic correlation*. Although this distinction is by no means strict, it is useful because the two types of electronic correlation have different physical origins and different methods can be used to recover one or the other type of correlation.

A strong static correlation is encountered in situations where several electronic states are degenerate, or at least close in energy. Such situations occur when electrons can be distributed in several ways in orbitals close in energy. This is the case, for instance, in bond breaking processes, or in the case of systems containing transition metal atoms with incomplete electronic shells. The electronic wavefunction will therefore include important contributions from a few configurations, and the Hartree–Fock method has to be replaced by a method capable of treating several configurations on an equal footage. This is the case of the Multi-Configuration Self-consistent field (MCSCF) method, in which the trial wavefunction is expressed as a linear combination of Slater determinants as in Eq. (2.67), and both the MOs and expansion coefficients c_i are optimized variationally.

The dynamic electronic correlation results from the Coulombic repulsion between two electrons lying close to each other. It requires the inclusion of a large number of configurations obtained by exciting electrons to high-energy virtual orbitals. However, in this case the electronic structure is still dominated by a single configuration and the other Slater determinants included in the wavefunction have small coefficients. Therefore the dynamic correlation energy can be recovered by methods starting from the Hartree–Fock wavefunction. Among the methods that are able to take into account the dynamic correlation energy, one can cite the configuration interaction methods (CI), methods based on the perturbation theory or the coupled cluster methods (CC). These methods are usually qualified as *single-reference* methods because they start from the Hartree–Fock Slater determinant.

Unfortunately, in many situation of interest, both static and dynamic electronic correlation need to be taken into account. This is particularly true for the study of processes involving excited electronic states as in UV spectroscopy or in photochemistry. In this case, methods capable of taking into account the dynamic electronic correlation on top of a multi-determinantal wavefunction of the MCSCF type are needed. These methods are usually called *multi-reference* methods. The two standard methods that are able to account for both the static and dynamic electronic correlation are the multi-reference configuration interaction (MRCI) and several variants of second-order multi-reference perturbation theory (MRPT).

2.3.3.1   The Configuration Interaction Methods

In the configuration interaction method, the wavefunction is expanded in a basis of Slater determinants. The Hartree–Fock determinant, noted Φ^{HF}, is taken as a reference zeroth-order wavefunction. Slater determinants corresponding to excited configurations are generated by swapping occupied MOs ψ_a with virtual (unoccupied) MOs ψ_r and can be classified with respect to the number of excited electrons. Singly excited Slater determinants are noted Φ_a^r, doubly excited Slater determinants Φ_{ab}^{rs}, triply excited Slater determinants Φ_{abc}^{rst}, and so on. The configuration interaction wavefunction then reads

$$\Psi = c_{HF}\Phi^{HF} + \sum_{a,r} c_{ar}\Phi_a^r + \sum_{a<b,r<s} c_{ab,rs}\Phi_{ab}^{rs} + \cdots$$

$$= \sum_I c_I \Phi_I \tag{2.68}$$

where I is a composite index accounting for all kinds of excitations. The final configuration interaction wavefunction is obtained by variationally optimizing the expansion coefficients c_I, with the normalization constraint $\langle\Psi|\Psi\rangle=1$. Again, this is done by using the Lagrange multiplier technique. The Lagrangian function

$$\mathcal{L} = \langle \Psi | H | \Psi \rangle - E(\langle \Psi | \Psi \rangle - 1)$$

$$= \sum_I \sum_J c_I^* c_J \langle \Phi_I | H | \Phi_J \rangle - E \left(\sum_I c_I^* c_I - 1 \right) \qquad (2.69)$$

is minimized with respect to the expansion coefficients

$$\frac{\partial \mathcal{L}}{\partial c_I} = 2 \sum_J c_J \langle \Phi_I | H | \Phi_J \rangle - 2 E c_I = 0. \qquad (2.70)$$

This last set of equations can be written in matrix form

$$\boldsymbol{H c = E c}. \qquad (2.71)$$

Solving this set of secular equations is equivalent to diagonalizing the configuration interaction matrix $\boldsymbol{H}$. Therefore the lowest eigenvalue of $\boldsymbol{H}$ is the ground state energy, the second lowest, the energy of the first excited state, and so on.

When all the Slater determinants that can be constructed from a set of Hartree–Fock MOs are taken into account, the method is called full configuration interaction. It provides the best possible solutions of the non-relativistic, clamped nuclei TISE within the basis set used for the calculation. The exact solutions are thus obtained from a full configuration interaction calculation at the complete basis limit. However, the number of configurations that can be built from a set of MOs grows extremely fast with the size of the system (i.e the size of the molecule and/or of the basis set).

For most systems, it is therefore necessary to reduce the number of configurations. This is usually done by truncating the expansion of Eq. (2.68) to a given level of excitation. When only singly excited configurations are included, the method is called configuration interaction with single excitations (CIS). Because, in virtue of the Brillouin's theorem [10], matrix elements between the Hartree–Fock determinant and a singly excited determinant are zero, the CIS method does not improve the description of the ground electronic state. It allows one to calculate excited states that are dominated by single excitations with an accuracy similar to that of the Hartree–Fock method for the ground state.

Including the singly and doubly excited configurations yields the configuration interaction with single and double excitations method (CISD). In contrast to the CIS method, the CISD method improves the description of the ground state because doubly excited configurations are directly mixed with the Hartree–Fock configuration

$$\langle \Phi^{HF} | H_{el} | \Phi_{ab}^{rs} \rangle = \langle \psi_a \psi_b | g_{12} | \psi_r \psi_s \rangle - \langle \psi_a \psi_b | g_{12} | \psi_s \psi_r \rangle. \qquad (2.72)$$

In addition, in the CISD method, the singly excited configurations are now indirectly mixed to the ground state, through their mixing with the doubly excited configurations. Configuration interaction methods including higher level excitations (CISDT, CISDTQ, . . .) are less commonly used.

2.3.3.2 The Multi-configuration Self-consistent Field Method

The Multi-Configuration Self-Consistent Field method combines the ideas of orbital optimization through a SCF technique as in the Hartree–Fock method, and a multi-configuration expansion of the electronic wavefunction as in the configuration interaction method. In other words, the electronic wavefunction is still expressed as a linear combination of Slater determinants $\Psi = \sum_i c_i \Phi_i$, but now both the coefficients c_i and the orbitals are optimized variationally [19–22]. This procedure being computationally more expansive than the configuration interaction method, only a limited number of configurations can be included in the MCSCF wavefunction. Therefore, the MCSCF method is usually not used to calculate a large fraction of the dynamic electronic correlation energy. On the other hand, it is well suited when the static correlation effects are important. In these cases, several configurations are quasi-degenerate and need to be included in the electronic wavefunction on an equal footing to obtain a qualitatively correct zeroth order description of the electronic structure of the system.

An important issue in MCSCF calculations is the selection of the configurations to be included in the wavefunction expansion. The most popular approach is the complete active space self-consistent field (CASSCF) method, also called full optimized reaction space (FORS). This approach starts from a zeroth order set of MOs, usually obtained via the Hartree–Fock method. The set of MOs is split into three subsets, as illustrated in Fig. 2.3. A first one containing occupied inactive orbitals, for which the occupation numbers are fixed to 2. A second one containing active orbitals, including both occupied and virtual orbitals of the reference Hartree–Fock configuration, in which all possible electron excitations are allowed. And a third one containing virtual inactive orbitals, for which the occupation numbers are fixed to 0.

Fig. 2.3 Scheme illustrating the notion of active space in the CASSCF method. In the present case, an active space of four electrons in four orbitals, noted CAS(4, 4) is depicted
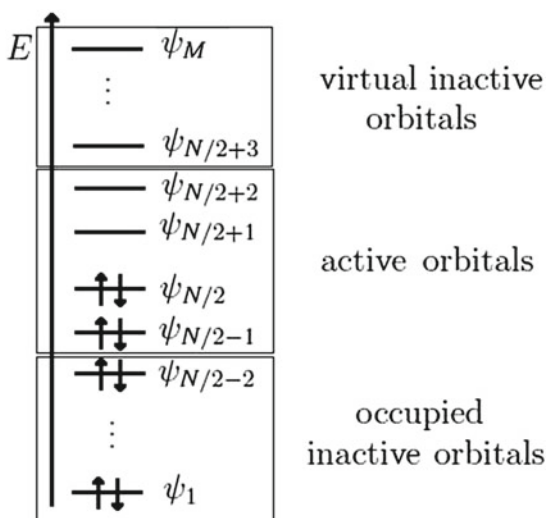
More precisely, a set of active orbitals and a number of active electrons are defined. All the configurations that can be built by excitations of the active electrons among the active orbitals are included into the wavefunction. Other, more flexible approaches for the selection of the configurations included in the MSCSF wavefunction exist, such as the *Restricted Active Space Self-Consistent Field* [23, 24] (RASSCF) and the *Occupation Restricted Multiple Active Space* (ORMAS) [25] methods.

A CASSCF wavefunction is, in general, much harder to converge than a simple SCF wavefunction. Several optimization procedures have been developed for the CASSCF wavefunction. The most popular one uses a Newton–Raphson-based method to minimize the energy. The energy is expanded to second order in the variational parameters (the orbital and configurational coefficients) around a particular set of coefficients

$$E(\boldsymbol{c}) = E(\boldsymbol{c_0}) + \boldsymbol{g}^T(\boldsymbol{c} - \boldsymbol{c_0}) + \frac{1}{2}(\boldsymbol{c} - \boldsymbol{c_0})^T \boldsymbol{H}(\boldsymbol{c} - \boldsymbol{c_0}). \qquad (2.73)$$

In this equation, $\boldsymbol{c} \equiv \begin{pmatrix} \boldsymbol{c}^{(o)} \\ \boldsymbol{c}^{(c)} \end{pmatrix}$ is a vector gathering the orbital and configurational coefficients, $\boldsymbol{c_0}$ is the vector of the current coefficients, $\boldsymbol{g} = \nabla_{\boldsymbol{c}} E(\boldsymbol{c})|_{\boldsymbol{c}=\boldsymbol{c_0}}$ is the gradient of the energy with respect to the coefficients at $\boldsymbol{c_0}$ and $\boldsymbol{H} = \nabla_{\boldsymbol{c}} \nabla_{\boldsymbol{c}}^T E(\boldsymbol{c})|_{\boldsymbol{c}=\boldsymbol{c_0}}$ the Hessian matrix. Requiring the gradient of the energy to vanish yields

$$\boldsymbol{c} = \boldsymbol{c_0} - \boldsymbol{H}^{-1}\boldsymbol{g}. \qquad (2.74)$$

Since the energy is not a quadratic function of the coefficients, several Newton steps are needed to locate a minimum. In addition, the calculation and inversion of the full Hessian matrix can be extremely time consuming for large active spaces and/or basis sets. Often, the elements of the Hessian coupling orbital and configurational coefficients (cross derivatives) are neglected and the optimization of the two sets of coefficients are decoupled.

During a CASSCF optimization near an electronic state degeneracy, problems of convergence often occur. The algorithm can swap from one state to the other. This problem is known as the root flipping problem. A way around this problem is to optimize the two states simultaneously. Specifically, a weighted average of the energies of the two states is minimized, and a same set of orbitals is optimized for the two states. This procedure is called state-averaged CASSCF (SA-CASSCF).

2.3.3.3 Methods Based on Perturbation Theory

As explained above, the dynamic electronic correlation can be taken into account by the (truncated) configuration interaction method in the case of a single reference system. Similarly, the multi-reference configuration interaction (MRCI) method can be used for multi-reference systems. In this method, a CASSCF wavefunction is used as the zeroth order description of the system. A configuration interaction matrix

containing all the configurations corresponding to single and double excitations (this is the MRCISD approach) from the configurations present in the CASSCF wavefunction is constructed and diagonalized. However this approach is computationally highly expansive and can only be used for small molecules.

Another approach is to include the effect of excited configurations through perturbation theory. This method avoids the diagonalization of a large matrix and can be accurate if the dynamic electronic correlation effects are not too large.

The Møller–Plesset perturbation theory [26] corresponds to the application of the stationary perturbation theory to the calculation of the correlation energy using the Hartree–Fock Slater determinant Φ^{HF} as the zeroth order wavefunction. These methods are denoted MPn where n is the order of the perturbative corrections included. In the Møller–Plesset method, the unperturbed Hamiltonian operator is chosen as a sum of Fock operators

$$H_0 = \sum_i^{N_{el}} F_i = \sum_i^{N_{el}} \left(h_i + \sum_j^{N_{el}} J_j - K_j \right). \tag{2.75}$$

The Hartree–Fock determinant and all Slater determinants built with Hartree–Fock orbitals are eigenfunctions of H_0. The perturbation operator W is then defined as the difference between H_0 and the exact electronic Hamiltonian H_{el} of Eq. (2.43)

$$W = H_{el} - H_0 = \sum_i^{N_{el}} \left(\sum_{j>i}^{N_{el}} g_{ij} - \sum_j^{N_{el}} J_j - K_j \right). \tag{2.76}$$

With these definitions, the zeroth order energy is a sum of MO energies

$$E_0^{(0)} = \langle \Phi^{HF} | H_0 | \Phi^{HF} \rangle = \sum_i^{N_{el}} \langle \Phi^{HF} | F_i | \Phi^{HF} \rangle = \sum_i^{N_{el}} \varepsilon_i. \tag{2.77}$$

The first order energy

$$E^{\mathrm{MP1}} = E_0^{(0)} + E_0^{(1)} = \langle \Phi^{HF} | H_0 | \Phi^{HF} \rangle + \langle \Phi^{HF} | W | \Phi^{HF} \rangle = \langle \Phi^{HF} | H_{el} | \Phi^{HF} \rangle = E^{HF} \tag{2.78}$$

is simply the Hartree–Fock energy. The general expression of the second order perturbative correction to the energy is:

$$E_0^{(2)} = \sum_{j \neq 0} \frac{|\langle \Phi^{HF} | W | \Phi_j \rangle|^2}{E_0^{(0)} - E_j^{(0)}} \tag{2.79}$$

where Φ_j denotes the excited Slater determinants. Singly excited determinants $\Phi_j \equiv \Phi_a^r$ does not contribute to the correction. Both terms in the right-hand side of the matrix elements

$$\langle \Phi^{HF}|W|\Phi_a^r\rangle = \langle \Phi^{HF}|H_{el}|\Phi_a^r\rangle - \langle \Phi^{HF}|H_0|\Phi_a^r\rangle \tag{2.80}$$

are zero, the first one because of Brillouin's theorem and the second one because H_0 is diagonal in the basis of the Slater determinants. In addition, Slater determinants corresponding to triple excitations and higher level excitations do not contribute because the W operator only contains two-electron operators. Therefore, only doubly excited Slater determinants contribute to the second order energy correction.

The energies $E_j^{(0)}$ read

$$E_j^{(0)} = \langle \Phi_{ab}^{rs}|H_0|\Phi_{ab}^{rs}\rangle = E_0^{(0)} + \varepsilon_r + \varepsilon_s - \varepsilon_a - \varepsilon_b. \tag{2.81}$$

Therefore, using Eqs. (2.72) and (2.81), the second order correction to the energy reads

$$E^{\mathrm{MP2}} = \sum_{a<b,r<s} \frac{|\langle \psi_a\psi_b|g_{12}|\psi_r\psi_s\rangle - \langle \psi_a\psi_b|g_{12}|\psi_s\psi_r\rangle|^2}{\varepsilon_a + \varepsilon_b - \varepsilon_r - \varepsilon_s}. \tag{2.82}$$

The MP2 method can be used to approximate the CISD energy of the ground state of a molecular system at a low computational cost. Higher order corrections have increasingly complicated expressions, however corrections up to fourth order (MP4) [27] are commonly available in the major quantum chemistry program packages.

As stated above, the CASSCF method is the method of choice to obtain a qualitative description of the electronic structure of a molecular system when static correlation plays a role. However, if a high accuracy is sought, the dynamic electronic correlation needs to be taken into account. Therefore, a method capable of describing accurately molecules in excited electronic states of different nature with a balanced accuracy over a wide range of geometries (in particular in regions where several electronic states become close in energy) must account for both the static and dynamics electronic correlations. The full CI and MRCISD method mentioned above can account for both types of correlation but they are extremely expansive and can only be applied to small systems. An alternative is to account for the dynamic electronic correlation energy through second-order perturbation theory on top of a CASSCF zeroth-order wavefunction. This is the idea behind the multi-reference perturbation theory methods (MRPT).

Several different methods of the MRPT2 type exist. The most popular are the multi-reference second-order Møller–Plesset (MRMP2) method of Hirao [28] and the complete active-space second-order perturbation theory (CASPT2) method of Andersson et al. [29]. In these methods, each state is perturbed separately. This can become problematic when, for instance, two states become sufficiently close in energy to interact after perturbation, these interactions will not be properly accounted for by such calculations. To solve this problem, methods based on second-order multi-state multi-reference perturbation theory (MS-MRPT2) can be used. These methods build an effective Hamiltonian between the perturbed states and diagonalize it, allowing one to treat quasi-degenerate states perturbatively. The most famous MS-MRPT2 methods are the multi-state CASPT2 method [30] and its extended version

(XMSCASPT2) [31], and the multi-configuration second-order quasi-degenerate perturbation theory (MCQDPT2) [32] and its extended version (XMCQDPT2) [33]. The XMCQDPT2 method is an approach to second order multi-state multi-reference perturbation theory recently developed by Granovsky, and implemented in the Firefly QC package [34], which is partially based on the GAMESS (US) source code [35]. It has been applied to a number of problems of biological and photochemical interest [36–43] and was shown to compare favourably with respect to experimental observations and other high-level theoretical methods [44–46]. All the excited state electronic structure calculations presented in this thesis have been performed with the CASSCF and XMCQDPT2 methods.

2.4 Potential Energy Surface Exploration

One of the most important applications of electronic structure calculations is the exploration of PESs. In particular, the theoretical description of chemical transformations requires the knowledge of the main stationary points of the relevant PESs.

For instance, a thermal reaction on the ground electronic state is, in the simplest case, characterized by the two minima corresponding to the reactants and products, and the transition state connecting them, as illustrated in the left panel of Fig. 2.4. Similarly, the characterization of stationary points is essential for the description of photochemical reactions. In this case, besides minima and transition states, conical intersections also play an important role. They provide channels connecting photo-products on the ground state with the Franck–condon region on the excited state, as illustrated in the right panel of Fig. 2.4. As for the calculation of electronic wave-functions and energies through (MC)SCF techniques, the determination of stationary points on PESs is an optimization problem.
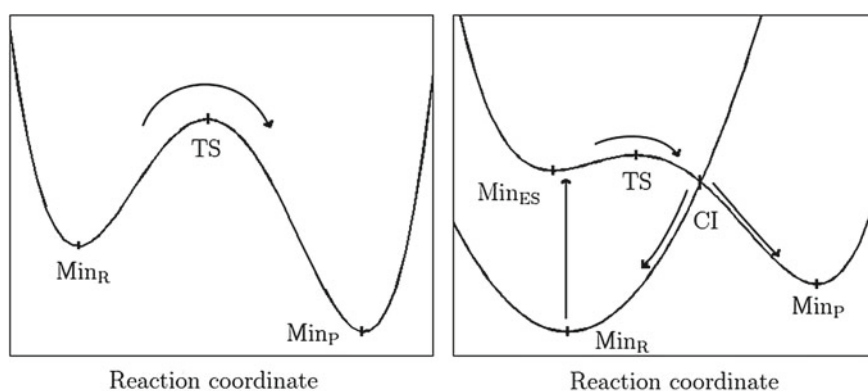
Fig. 2.4 Scheme illustrating a simple thermal reaction on the ground electronic state (*left panel*) and a photochemical reaction (*right panel*). Min_R and Min_P denote the minima corresponding to the reactants and products on the ground state PES. Min_{ES} denotes a local minimum on the excited state PES. TS denotes the transition state and CI denotes a point of conical intersection

2.4.1   Minima and Transition State Optimization

The simplest methods to find a minimum are methods based on the gradient of the energy with respect to the nuclear coordinates $g(R_0) = \nabla_R E(R)|_{R=R_0}$. The steepest descent method uses the opposite of the gradient as the search direction $d_i = -g_i$, where the subscript i denotes the current iteration. A displacement is performed in this direction to find a new estimation of the minimum. At this point, a new gradient evaluation is performed, providing the search direction for the next step. This procedure is iterated until all the components of the gradient are smaller than a predefined threshold. A slightly more efficient method is the conjugated gradient method. In this method, the search direction is defined as a mixture of the opposite of the gradient and the previous search direction $d_i = -g_i + \beta_i d_{i-1}$. Both methods are easy to implement but converge slowly towards a minimum.

A faster convergence can be obtained by using methods based on a second order expansion of the energy such as the Newton–Raphson-based methods [47]. In these methods, the search direction is defined as (see also Eq. (2.74))

$$d_i = -H_i^{-1} g_i, \tag{2.83}$$

where H is the Hessian matrix of the electronic energy with respect to the nuclear coordinates. In a coordinate system that diagonalizes the Hessian matrix, the search direction reads

$$d'_i = -(H^{(d)})_i^{-1} g'_i, \tag{2.84}$$

where $H^{(d)}$ is the diagonal Hessian matrix. If all the eigenvalues of the Hessian matrix are positive, the algorithm converges towards a minimum, whereas if the Hessian has a negative eigenvalue, the algorithm tends to converge towards a transition state.

Two problems need to be addressed to make this class of methods robust and efficient. The first one is to improve the search direction and the size of the step taken along this direction. This can be done by adding a shift parameter λ in the Newton–Raphson step

$$d'_i = -(H^{(d)} - \lambda I)_i^{-1} g'_i. \tag{2.85}$$

The shift parameter can be used to ensure that the optimization proceeds downhill even if the Hessian has negative eigenvalues. In addition, it can be chosen such that the step size is lower or equal to a predefined threshold. Popular methods using a shift parameter are the rational function optimization (RFO) [48] and Trust Radius (TR) methods [49, 50]. A finer control on the step size and direction can be achieved using an approximate line search method, which attempts to fit a polynomial function to the energies and gradients of the best previous points [51].

A second important issue is the calculation of the Hessian matrix which can be a computationally expansive task. A method to avoid such calculation is to start with an approximate Hessian, e.g. empirically determined or calculated at a lower level of theory, and to update the Hessian during the optimization using only energies and

gradients at successive optimization steps. The most popular updating scheme is the Broyden–Fletcher–Goldfarb–Shanno (BFGS) scheme [52–55]. Methods based on such an approximate Hessian matrix are called quasi-Newton methods.

The above methods can be modified to enforce convergence to a transition state. In this case, the quality of the initial geometry and Hessian are more crucial than for the optimization of a minimum.

The minimum and transition state optimizations performed in this thesis have been performed using the Berny algorithm [56] implemented in the Gaussian 03 program package [57].

2.4.2 Minimum Energy Conical Intersection Optimization

As mentioned in Sect. 2.2.3, a conical intersection is not an isolated point but a hyperline of $N - 2$ dimensions (the seam of conical intersection), where N is the number of vibrational degrees of freedom. At each point of the seam, the degeneracy is lifted upon displacement in the branching plane whereas it is conserved at first order along the N-2 directions orthogonal to the branching plane. One is often interested in finding the point of lowest energy within this seam, called the minimum energy conical intersection (MECI) in order to characterize a photochemical process.

In this thesis, the method proposed by Bearpark et al. [58], and implemented in the Gaussian 03 package [57], has been used (see Chap. 3). Considering two adiabatic electronic states of energy E_1 and E_2, the principle of the method is to minimize simultaneously the energy difference $\Delta E = E_2 - E_1$ in the branching plane and the energy of the upper state E_2 in the intersection space. To avoid confusions in the notations, the gradient difference and derivative coupling vectors will be noted x_1 and x_2. The branching plane is the space spanned by the two unitary vectors e_{x_1} and e_{x_2} defined in Sect. 2.2.3. The condition for the minimization of the energy difference in the branching plane reads

$$\nabla_R \Delta E^2 = 2\Delta E x_1. \tag{2.86}$$

The squared energy difference is used because it varies more smoothly in the vicinity of a conical intersection. The norm of x_1 has no significance, the step size should only depend on the energy difference ΔE, therefore the gradient to be used to minimize ΔE is defined as

$$f = 2\Delta E e_{x_1}. \tag{2.87}$$

The minimization of E_2 in the intersection space is done by mean of a projector

$$P = I - x_1 x_1^T - x_2 x_2^T. \tag{2.88}$$

In this case the gradient to be used is

$$g = P\nabla_R E_2. \tag{2.89}$$

Overall the MECI optimization uses the composite gradient

$$\bar{g} = f + g. \tag{2.90}$$

Far from a conical intersection, the gradient is dominated by f and the algorithm converges towards a point of conical intersection. During this phase, the energies E_1 and E_2 can rise considerably and the algorithm can reach a portion of the conical intersection seam corresponding to highly distorted geometries. Therefore, as for transition state optimizations, the quality of the starting geometry is important. As the degeneracy is approached, f tends to zero and the gradient is dominated by g. Therefore the algorithm minimizes the energy inside the conical intersection seam and converges towards the MECI.

2.4.3 Minimum Energy Paths Optimization

The knowledge of the main stationary points on the PESs of interest gives some information about the reactants, products and intermediates of a (photo)chemical reaction. However, a better insight into the mechanism behind this reaction can be obtained by computing the pathways linking these stationary points. Among the infinite number of paths connecting two points, the path requiring the least increase in energy is called the minimum energy path (MEP). The MEP usually follows the steepest descent path. However, this steepest descent path usually varies from a system of coordinates to another. When mass-weighted cartesian coordinates are used, the steepest descent path is also known as the intrinsic reaction coordinate (IRC). In this thesis, the algorithm of Gonzalez and Schlegel [59, 60], implemented in the Gaussian 03 program package [57], has been used.

From a starting geometry R_k with a gradient g_k, the IRC algorithm optimizes a new point R_{k+1} such that the path between the two points is an arc of a circle to which both gradients g_k and g_{k+1} are tangent. Defining a step size s, the algorithm first generates a pivot point R_{k+1}^* at a distance $s/2$ of R_k along the direction of the gradient g_k

$$R_{k+1}^* = R_k + \frac{s}{2}\frac{g_k}{||g_k||}. \tag{2.91}$$

The new point R_{k+1} is then obtained by a constrained optimization on the hypersphere of radius $s/2$ centered at R_{k+1}^*.

References

1. H. Köppel, W. Domcke, L.S. Cederbaum, Mol. Phys. **43**, 851 (1981)
2. H. Köppel, W. Domcke, L.S. Cederbaum, Adv. Chem. Phys. **57**, 59 (1984)
3. G.A. Worth, L.S. Cederbaum, Annu. Rev. Phys. Chem. **55**, 127 (2004)
4. M. Born, R. Oppenheimer, Ann. Phys. **84**, 457 (1927)
5. M. Born, K. Huang, *The Dynamical Theory of Crystal Lattices* (Oxford University Press, Oxford, 1954)
6. W. Domcke, D.R. Yarkony, H. Köppel, *Conical Intersections, Electronic Strucutre, Dynamics and Spectroscopy* (World Scientific, New Jersey, 2004)
7. M.J. Paterson, M.J. Bearpark, M.A. Robb, L. Blancafort, J. Chem. Phys. **121**, 11562 (2004)
8. M.J. Paterson, M.J. Bearpark, M.A. Robb, L. Blancafort, G.A. Worth, Phys. Chem. Chem. Phys. **7**, 2100 (2005)
9. F. Sicilia, L. Blancafort, M.J. Bearpark, M.A. Robb, J. Phys. Chem. A **111**, 2182 (2007)
10. A. Szabo, N.S. Ostlund, *Modern Quantum Chemistry* (Mac Graw Hill Press, New York, 1989)
11. F. Jensen, *Introduction to Computational Chemistry* (Wiley, Chichester, 2007)
12. J.C. Slater, Phys. Rev. **34**, 1293 (1929)
13. D.R. Hartree, Proc. Camb. Philos. Soc. **24**, 88 (1928)
14. V. Fock, Z. Phys. **61**, 126 (1930)
15. E.U. Condon, Phys. Rev. **36**, 1121 (1930)
16. C.C.J. Roothaan, Rev. Mod. Phys. **23**, 69 (1951)
17. G.G. Hall, Proc. R. Soc. (Lond.) **A205**, 541 (1951)
18. R. Hoffmann, J. Chem. Phys. **39**, 1397 (1963)
19. J. Olsen, D.L. Yeager, P. Jorgensen, Adv. Chem. Phys. **54**, 1 (1983)
20. H.-J. Werner, Adv. Chem. Phys. **69**, 1 (1987)
21. R. Shepard, Adv. Chem. Phys. **69**, 63 (1987)
22. M.W. Schmidt, M.S. Gordon, Annu. Rev. Phys. Chem. **49**, 233 (1998)
23. J. Olsen, B.O. Roos, P. Jorgensen, H.J.A. Jensen, J. Chem. Phys. **89**, 2185 (1988)
24. M. Klene, M.A. Robb, L. Blancafort, M.J. Frisch, J. Chem. Phys. **119**, 713 (2003)
25. J. Ivanic, J. Chem. Phys. **119**, 9364 (2003), J. Chem. Phys. **119**, 9377 (2003)
26. C. Møller, M.S. Plesset, Phys. Rev. **46**, 618 (1934)
27. R. Krishnan, J.A. Pople, Int. J. Quant. Chem. **14**, 91 (1978)
28. K. Hirao, Chem. Phys. Lett. **190**, 374 (1992)
29. K. Andersson, P.A. Malmqvist, B.O. Roos, A.J. Sadlej, K. Wolinski, J. Phys. Chem. **94**, 5483 (1990)
30. J. Finley, P.-A. Malmqvist, B.O. Roos, L. Serrano-Andrés, Chem. Phys. Lett. **288**, 299 (1998)
31. T. Shiozaki, W. Györffy, P. Celani, H.-J. Werner, J. Phys. Chem. **135**, 081106 (2011)
32. H. Nakano, J. Chem. Phys. **99**, 7983 (1993)
33. A.A. Granovsky, J. Chem. Phys. **134**, 214113 (2011)
34. A.A. Granovsky, Firefly version 7.1.G, http://classic.chem.msu.su/gran/firefly/index.html
35. M.W. Schmidt, K.K. Baldridge, J.A. Boatz, S.T. Elbert, M.S. Gordon, J.H. Jensen, S. Koseki, N. Matsunaga, K.A. Nguyen, S. Su, T.L. Windus, M. Dupuis, J.A. Montgomery, J. Comput. Chem. **14**, 1347 (1993)
36. E. Epifanovsky, I. Polyakov, B. Grigorenko, A. Nemukhin, A.I. Krylov, J. Chem. Phys. **132**, 115104 (2010)
37. I.V. Polyakov, B.L. Grigorenko, E.M. Epifanovsky, A.I. Krylov, A.V. Nemukhin, J. Chem. Theory Comput. **6**, 2377 (2010)
38. B.L. Grigorenko, A.V. Nemukhin, D.I. Morozov, I.V. Polyakov, K.B. Bravaya, A.I. Krylov, J. Chem. Theory Comput. **8**, 1912 (2011)
39. B.L. Grigorenko, A.V. Nemukhin, I.V. Polyakov, A.I. Krylov, J. Phys. Chem. Lett. **4**, 1743 (2013)
40. P.M. Kozlowski, T. Kamachi, M. Kumar, T. Nakayama, K. Yoshizawa, J. Phys. Chem. B **114**, 5928 (2010)

41. A. Udvarhelyi, T. Domratcheva, J. Photochem. Photobiol. A **87**, 554 (2011)
42. I. Ioffe, A.L. Dobryakov, A.A. Granovsky, N.P. Ernsting, J.L. Pérez, Lustres. Chem. Phys. Chem. **12**, 1860 (2011)
43. A.V. Bochenkova, L.H. Andersen, Faraday Discuss. **163**, 297 (2013)
44. K. Kornobis, N. Kumar, B.M. Wong, P. Lodowski, M. Jaworska, T. Andruni, K. Ruud, P.M. Kozlowski, J. Phys. Chem. A **115**, 1280 (2011)
45. S. Gozem, M. Huntress, I. Schapiro, R. Lindh, A.A. Granovsky, C. Angeli, M. Olivucci, J. Chem. Theory Comput. **8**, 4069 (2012)
46. S. Gozem, F. Melaccio, R. Lindh, A.I. Krylov, A.A. Granovsky, C. Angeli, M. Olivucci, J. Chem. Theory Comput. **9**, 4495 (2013)
47. H.P. Hratchian, H.B. Schlegel, in *Theory and Applications of Computational Chemistry: The First 40 Years*, ed. by C.E. Dykstra, K.S. Kim, G. Frenking, G.E. Scuseria (Elsevier, Amsterdam, 2005), p. 195
48. A. Banerjee, A. Adams, J. Simons, R. Shepard, J. Chem. Phys. **89**, 52 (1985)
49. T. Helgaker, Chem. Phys. Lett. **182**, 503 (1991)
50. P. Culot, G. Dive, V.H. Nguyen, J.M. Ghuysen, Theor. Chim. Acta **82**, 189 (1992)
51. H.B. Schlegel, J. Comput. Chem. **3**, 214 (1982)
52. C.G. Broyden, IMA J. Appl. Math. **6**, 76 (1970)
53. R. Fletcher, Comput. J. **13**, 317 (1970)
54. D. Goldfarb, Math. Comput. **24**, 23 (1970)
55. D.F. Shanno, Math. Comput. **24**, 647 (1970)
56. C. Peng, P.Y. Ayala, H.B. Schlegel, M.J. Frisch, J. Comput. Chem. **17**, 49 (1996)
57. Gaussian 03, Revision C.02, M.J. Frisch, G.W. Trucks, H.B. Schlegel, G.E. Scuseria, M.A. Robb, J.R. Cheeseman, J.A. Montgomery, Jr., T. Vreven, K.N. Kudin, J.C. Burant, J.M. Millam, S.S. Iyengar, J. Tomasi, V. Barone, B. Mennucci, M. Cossi, G. Scalmani, N. Rega, G.A. Petersson, H. Nakatsuji, M. Hada, M. Ehara, K. Toyota, R. Fukuda, J. Hasegawa, M. Ishida, T. Nakajima, Y. Honda, O. Kitao, H. Nakai, M. Klene, X. Li, J.E. Knox, H.P. Hratchian, J.B. Cross, V. Bakken, C. Adamo, J. Jaramillo, R. Gomperts, R.E. Stratmann, O. Yazyev, A.J. Austin, R. Cammi, C. Pomelli, J.W. Ochterski, P.Y. Ayala, K. Morokuma, G.A. Voth, P. Salvador, J.J. Dannenberg, V.G. Zakrzewski, S. Dapprich, A.D. Daniels, M.C. Strain, O. Farkas, D.K. Malick, A.D. Rabuck, K. Raghavachari, J.B. Foresman, J.V. Ortiz, Q. Cui, A.G. Baboul, S. Clifford, J. Cioslowski, B.B. Stefanov, G. Liu, A. Liashenko, P. Piskorz, I. Komaromi, R.L. Martin, D.J. Fox, T. Keith, M.A. Al-Laham, C.Y. Peng, A. Nanayakkara, M. Challacombe, P.M.W. Gill, B. Johnson, W. Chen, M.W. Wong, C. Gonzalez, J.A. Pople, Gaussian Inc, Wallingford (2004)
58. M.J. Bearpark, M.A. Robb, H.B. Schlegel, Chem. Phys. Lett. **223**, 269 (1994)
59. C. Gonzalez, H.B. Schlegel, J. Chem. Phys. **90**, 2154 (1989)
60. C. Gonzalez, H.B. Schlegel, J. Phys. Chem. **94**, 5523 (1990)

Chapter 3
Exploration of the Potential Energy Landscape of Aniline Using CASSCF and XMCQDPT2 Electronic Structure Calculations

In this chapter, the tools introduced in Chap. 2 are applied to the study of the photochemistry of aniline. This work has been initiated during a six-month fellowship in the group of Professor Helen Fielding in the Chemistry Department of University College London, in the framework of the FASTQUAST Initial Training Network. The excited state non-adiabatic dynamics of aniline have been studied experimentally in the Fielding group by means of time-resolved photoelectron imaging (TRPEI) [1, 2]. The goal of this work was to characterize the important regions of the potential energy surfaces of aniline relevant to its photochemistry, in order to help in the interpretation of the data generated by these experiments.

This chapter is organized as follows. In Sect. 3.1, we discuss the general features of the photochemistry of simple aromatic molecules and the current knowledge of the photochemistry of aniline obtained from previous studies. We then present our results and discuss them with respect to the available experimental data. In Sect. 3.2, the methodology used in this work is detailed. The energy and nature of the lowest singlet excited electronic states of the molecule are discussed in Sect. 3.3. The main decay pathways relevant for photochemistry of the molecule after a direct excitation to each one of the three lowest singlet excited electronic states are then presented and discussed in Sects. 3.4–3.6. Conclusions are given in Sect. 3.7.

This chapter is partly based on results and discussions published in Ref. [3] by the PCCP Owner Societies.

3.1 Introduction

3.1.1 General Trends in the Photochemistry of Simple Aromatic Organic Molecules

The photochemistry and photophysics of simple aromatic organic molecules have been investigated intensively during the last two decades. The study of these systems, ranging from simple benzene derivatives to DNA bases, aromatic amino acids

and their complexes, have revealed general trends in their photochemistry. The UV absorption spectra of these compounds are often dominated by low-lying $\pi\pi^*$ excited electronic states. However, depending on their structures, low-lying $\pi\sigma^*$ and $n\pi^*$ states are often found in the same energy range. Generally, they have very short excited state lifetimes and low fluorescence quantum yields, indicating the existence of efficient non-radiative decay channels. Theoretical studies have revealed different classes of motions, leading to low-lying conical intersections (CIs). An emblematic example is the "channel 3" phenomenon of benzene. When it is excited near the band origin corresponding to the 0–0 transition between the ground and first excited $\pi\pi^*$ electronic states, the molecule decays on a nanosecond time scale, via fluorescence and intersystem crossing to a nearby triplet state [4, 5]. However, when the molecule is excited with an excess energy of more than $3000\,cm^{-1}$, the fluorescence quantum yield suddenly drops down and an ultrafast decay, occurring on a femtosecond time scale, is observed. This photochemical behavior finds its origin in the existence of a CI between the ground and first excited $\pi\pi^*$ states. The pathway leading to this CI on the S_1 potential energy surface (PES) involves a so-called prefulvene motion of the molecule, consisting in an out-of-plane motion of one carbon atom of the benzene ring. In addition, the activation energy needed to open this ultrafast decay channel is the result of the existence of a potential energy barrier between the Franck–Condon (FC) geometry on S_1 and the prefulvene CI [6–14]. CIs between the first excited $\pi\pi^*$ state and the ground state with similar geometries have been described in many other aromatic molecules, such as for instance, pyrazine [15] and phenol [16]. Decay pathways involving out-of-plane ring deformations (also called ring puckering motions) on the second $\pi\pi^*$ excited state have also been found in a number of molecules including pyrrole [17] or the purine DNA bases adenine [18, 19] and guanine [20].

An other important class of decay pathways involves aromatic molecules containing a hydrogen atom bonded to a heteroatom such as oxygen, nitrogen or sulfur. Typical examples of such molecules are pyrrole, indole, phenol, the DNA bases, etc. These molecules are characterized by the existence of low-lying $\pi\sigma^*$ electronic states. Generally, these states have a strong Rydberg character in the FC region and a repulsive valence σ^* character at large X–H distance (where X denotes the heteroatom) where a CI with the ground state occurs, providing a highly efficient channel for deactivation to the ground electronic state [21–26]. Usually these states have low oscillator strengths, therefore they are often populated by vibronic coupling with a nearby bright $\pi\pi^*$ state.

As will be seen in this chapter, these general trends apply to the photochemistry of aniline.

3.1.2 Previous Studies on the Photochemistry of Aniline

Aniline ($C_6H_5NH_2$), composed of an amino group attached to a phenyl ring, is the simplest aromatic amine. The motif of an amino group attached to an aromatic ring is common in biological molecules. Therefore, aniline is an important model system.

The low energy part of the UV absorption spectrum of aniline is composed of two bands centered around 282 nm (4.4 eV) and 230 nm (5.4 eV) [27–29], arising from transition to the two lowest-lying singlet $\pi\pi^*$ electronic states, hereafter noted $1\pi\pi^*$ and $2\pi\pi^*$ states. The structure of the molecule in its ground and first excited electronic state has been the subject of numerous experimental [30–33] and computational [34–48] investigations. In particular, the equilibrium geometry of the $1\pi\pi^*$ state has been a subject of debate [49–57]. A pyramidal equilibrium geometry [58] was predicted by CASSCF calculations. Rotationally-resolved electronic spectra, on the other hand, suggested a quasiplanar geometry for the $1\pi\pi^*$ state; however, this structure was a vibrationally averaged structure rather than the true minimum of the PES [56].

Several high level ab initio computational investigations of the UV spectrum of aniline have been reported, including the SAC-CI calculations of Honda et al. [59], the MS-CASPT2 calculations of Hou et al. [60] and the EOM-CCSD(T) calculations of Wang et al. [61]. Honda et al. and Hou et al. predicted the three lowest singlet electronic states to be the $1\pi\pi^*$, $1\pi\sigma^*/R3s$ and $2\pi\pi^*$ states, followed by three Rydberg 3p states. Honda et al. were the first to predict the $1\pi\sigma^*/R3s$ state. This state was then observed by Ebata et al. [62] using UV–IR double-resonance spectroscopy, with an onset at 269 nm (4.60 eV). In contrast with the previous calculations, Worth et al. predicted two Rydberg 3p states to lie between the $1\pi\sigma^*/R3s$ and $2\pi\pi^*$ states. They constructed a sophisticated vibronic coupling model Hamiltonian using EOM-CCSD and EOM-CCSD(T) calculations and performed quantum dynamic simulations which reproduced the first two bands of the UV spectrum with a remarkable accuracy [61].

Early experimental investigations of the photochemistry and photophysics of aniline following excitation of the $1\pi\pi^*$ state focussed on fluorescence and intersystem crossing (ISC) [63–66], occurring on a nanosecond timescale. Surprisingly, however, it is only recently that the first studies of the ultrafast photochemistry of aniline have been reported. King et al. [67] used H (Rydberg) atom photofragment translational spectroscopy to probe the photoinduced H atom loss process in aniline. They found the N–H bond fission process to appear with a wavelength excitation threshold of 269 nm, i.e at the onset of excitation to the $1\pi\sigma^*/R3s$ state. Precisely, wavelengths of 269.513, 265.781 and 262.515 nm were found to excite resonances in the quasi-bound well formed by the $1\pi\sigma^*/R3s$ state and to yield H atoms with constant kinetic energy and anilino photofragments with low vibrational excitation. Excitation at 260 nm was found, in contrast, to populate high vibrational states of the $1\pi\pi^*$ state. In this case, the N–H bond fission process on the $1\pi\sigma^*/R3s$ state was proposed to occur after internal conversion through a $1\pi\pi^*/1\pi\sigma^*$ CI. At wavelengths below 250 nm, a bimodal H atom kinetic energy distribution appears. The high kinetic energy H atoms are produced from dissociation on the $1\pi\sigma^*/R3s$ state while the low kinetic energy H atoms were assumed to originate from the ground electronic state (GS), which is populated via vibronic coupling with either the $1\pi\pi^*$ state or the $1\pi\sigma^*/R3s$ state. Finally, as the excitation wavelength approaches 230 nm,

excitation of the $2\pi\pi^*$ state dominates. The bimodal H atom kinetic energy distribution was still observed, with an increasing relative importance of the low kinetic energy component. The high kinetic energy component was interpreted in term of internal conversion through a $2\pi\pi^*/1\pi\sigma^*$ CI or through successive $2\pi\pi^*/1\pi\pi^*$ and $1\pi\pi^*/1\pi\sigma^*$ CIs, followed by dissociation on the $1\pi\sigma^*/R3s$ state PES. Again, the low kinetic energy component was interpreted in terms of internal conversion through a $2\pi\pi^*/GS$ decay mechanism followed by dissociation on the ground state PES.

Several studies based on time-resolved pump-probe experiments have been reported. Montero et al. [68] used time-resolved photoionization spectroscopy, Roberts et al. [58] monitored the H atom rise times using femtosecond velocity map imaging while Spesyvtsev et al. [1, 2] and Thompson et al. [69] used time-resolved photoelectron imaging. These time-resolved experiments have revealed four lifetimes: $\tau_1 \gtrsim 80$ ps, $\tau_2 \sim 0.4$–3 ps, $\tau_3 \sim 100$–400 fs and $\tau_4 \lesssim 100$ fs. The fastest timescale, τ_4, is only observed following excitation to the $2\pi\pi^*$ state and has been interpreted as relaxation back to the ground electronic state [1, 2] or as decay through a series of CIs to the $1\pi\sigma^*/R3s$ state [58, 68]. τ_3 has been interpreted as population transfer through a CI between the $1\pi\sigma^*/R3s$ state and the $1\pi\pi^*$ state, from $1\pi\sigma^*/R3s$ to $1\pi\pi^*$ [1, 2], or from $1\pi\pi^*$ to $1\pi\sigma^*/R3s$ [58, 68]. τ_3 has also been proposed to arise from tunnelling through the barrier along the N–H stretching coordinate between the bound and dissociative components of the $1\pi\sigma^*/R3s$ state [69]. τ_2 was observed only in time-resolved photoelectron spectroscopy experiments [1, 2, 69] and was interpreted as motion on the $1\pi\sigma^*/R3s$ PES [1, 2] or as intramolecular vibrational energy redistribution (IVR) in the $1\pi\pi^*$ state [69]. The longest timescale, τ_1, has been interpreted as decay from the first $1\pi\pi^*$ state. More recently, new TRPEI measurements with improved signal-to-noise ratios and temporal resolution, were performed in the Fielding group [70]. Exponential decay time constants obtained from these experiments with various pump wavelengths are summarized in Table 3.1.

From the theoretical point of view, a study of the main critical points on the PESs of the ground, $1\pi\pi^*$, $1\pi\sigma^*/R3s$ and $2\pi\pi^*$ states by means of CASSCF calculations was reported by Roberts et al. in Ref. [58]. The results of this study are in line with previous theoretical studies on similar compounds, as exposed in Sect. 3.1.1, i.e minimum energy conical intersections (MECIs) corresponding to ring-puckering distortions of the phenyl ring were reported between the ground and $1\pi\pi^*$ states,

Table 3.1 Exponential decay lifetimes obtained by Kirkby et al. [70] at different pump wavelengths

Pump wavelength (nm)	τ_1 (ps)	τ_2 (fs)	τ_3 (fs)	τ_4 (fs)
272	600 ± 35	–	–	–
250	100 ± 8	571 ± 175	111 ± 20	–
245	77 ± 14	523 ± 200	145 ± 31	–
238	90 ± 5	450	134 ± 36	50 ± 10

and between the $2\pi\pi^*$ and $1\pi\pi^*$ states. A N–H dissociation pathway was found to exist on the $1\pi\sigma^*/R3s$ PES, and MECIs with the $1\pi\pi^*$ state at short N–H distance and with the ground state at large N–H distance were optimized along this pathway.

3.2 Computational Details

Minima and transition states (TSs) were optimized using the state specific complete active-space self-consistent field (SS-CASSCF) method. MECIs were optimized using state-averaged CASSCF (SA-CASSCF) [71] with equal weighting given to the two states forming the CI.

The different decay pathways relevant for the photochemistry of aniline were studied using linearly interpolated scans in internal coordinates, relaxed potential energy scans and minimum energy path (MEP) calculations using the SA-CASSCF method. Linearly interpolated scans were constructed from electronic energy calculations performed at a number of geometries obtained by linear interpolation between predefined starting and ending geometries. Internal coordinates were used to ensure a better description of pathways involving significant angular motions of the nuclei. Relaxed potential scans consist in calculations of the electronic energies along a given coordinate at geometries obtained from in optimization of the rest of the molecule. The MEP calculations were based on the intrinsic reaction coordinate (IRC) method [72, 73], exposed in Sect. 2.4.3. Although IRC calculations are often started at a transition state, the IRC calculation performed in this work (Sect. 3.6) was started at the FC geometry (the ground state equilibrium geometry) using the gradient as the initial relaxation direction.

To obtain more reliable energies, single-point extended multi-configuration quasi-degenerate second-order perturbation theory (XMCQDPT2) calculations [74] were carried out at optimised stationary points and along decay pathways calculated using the CASSCF method. This protocol is used because the XMCQDPT2 analytic gradient, required to optimize stationary points efficiently, is not available. This procedure (energies computed using a multi-reference perturbation theory method at CASSCF optimized geometries) has been used in previous investigations of the photochemistry of small organic molecule, including DNA bases [19, 20, 75, 76]. In all the XMCQDPT2 calculations reported here, the 30 lowest CASSCF states were included in the model space spanned by the XMCQDPT2 zero-order effective Hamiltonian [74, 77, 78]. An intruder state avoidance (ISA) denominator shift [74] of 0.02 was used in all the XMCQDPT2 calculations.

Two different active spaces were employed for the CASSCF calculations. CAS1 consists of 8 electrons in 7 orbitals: 3 occupied π orbitals (noted 1π, 2π and 3π) and the corresponding 3 unoccupied π^* orbitals (noted $1\pi^*$, $2\pi^*$ and $3\pi^*$) together with the occupied nitrogen lone-pair orbital (noted N_{lp}). Here, the star superscript denotes antibonding orbitals. Since it does not include the $R3s/\sigma^*$ orbital, this active space cannot describe the $^1\pi3s/\pi\sigma^*$ state. CAS2 consists of 10 electrons in 9 orbitals: CAS1 augmented with a pair of σ and $R3s/\sigma^*$ orbitals centered on the amino group.
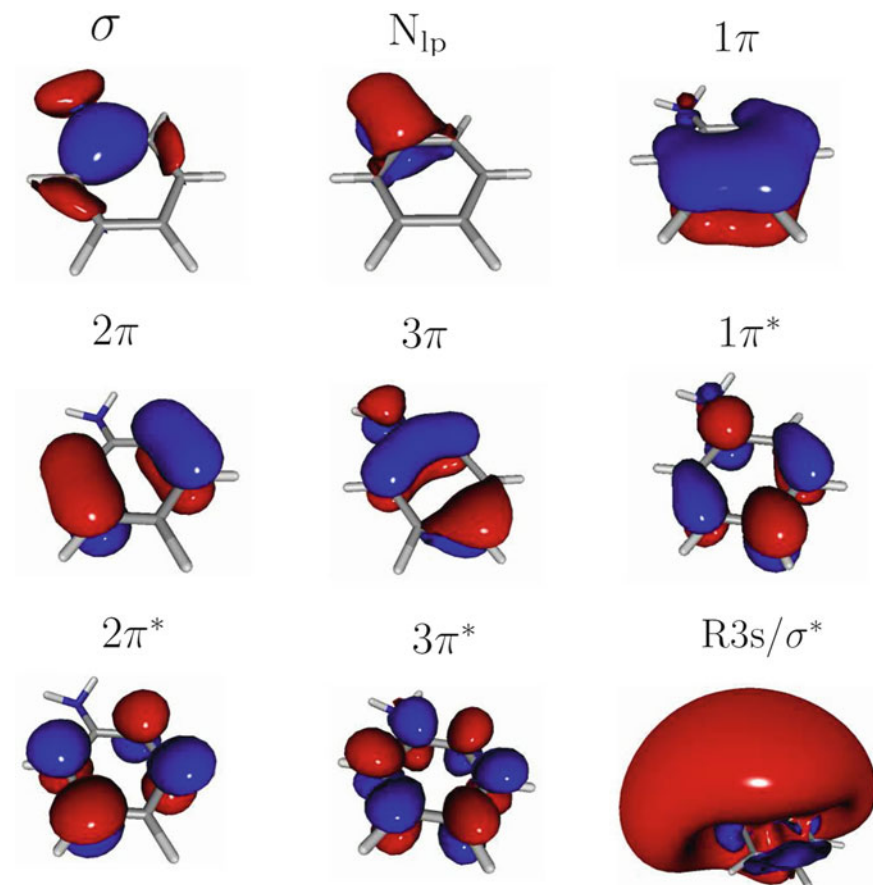
Fig. 3.1 CASSCF optimized orbitals included in CAS1 and CAS2

The orbitals included in these active spaces are represented in Fig. 3.1. Hereafter, the $1\pi\sigma^*/R3s$ state will be simply labelled as $1\pi\sigma^*$.

All the calculations performed with the CAS1 active space used the 6-311G** basis set whereas the calculations performed with the CAS2 active space used the 6-311++G** basis set augmented with two diffuse s functions and two sets of diffuse p functions on the nitrogen atom as well as a single diffuse s functions on the two hydrogen atoms of the amino group. The exponents of the supplementary diffuse functions were determined in an even tempered manner by dividing the exponent of the most diffuse s and p functions already present in the 6-311++G** basis set by a factor of 3.0. Such an extension of the basis set was found to have a significant effect on the $1\pi\sigma^*$ state vertical excitation energy and the height of the barrier to photodissociation. A similar protocol has been previously used for pyrrole [79, 80] and phenol [81].

For the MECI optimizations using the CAS1 active space, we found it necessary to use a quadratically convergent algorithm for the CASSCF wavefunction. The orbital rotation derivative contributions from the coupled perturbed multi-configurational self-consistent field (CP-MCSCF) equations (see Refs. [82–84] and the Chap. 3 of Ref. [85] for details) were neglected in the MECI optimizations using the CAS2 active space.

The notation SAn-CASSCF is used to describe a state averaged CASSCF calculation using orbitals averaged over n electronic states.

The CASSCF optimizations were performed using the Gaussian 03 program package [86] and the single point CASSCF and XMCQDPT2 calculations were performed using the Firefly QC package [87], which is based partially on the GAMESS (US) source code [88].

3.3 Vertical and Adiabatic Excitation Energies

The equilibrium geometries of the ground and $1\pi\pi^*$ states, optimized using the CAS1 active space, are shown in Fig. 3.2. Both have C_s symmetry and a pyramidal arrangement around the nitrogen atom.

We focus on the four lowest lying singlet electronic states, which we label *GS*, $1\pi\pi^*$, $1\pi\sigma^*$ and $2\pi\pi^*$, in order of increasing energy [59, 60]. The dominant configurations of each state of interest are given in Table 3.2.

The vertical excitation energies computed using the two active spaces described in Sect. 3.2 are reported in Table 3.3 and compared with previous calculations and experimental values. The CASSCF $1\pi\pi^*$ vertical excitation energy is in reasonable agreement with the experimental value. In contrast, the $2\pi\pi^*$ vertical excitation energy is grossly overestimated with an error of 1.96 eV. This large error is due to the charge transfer character of the $2\pi\pi^*$ state [58]. The XMCQDPT2 calculation using the same CASSCF wavefunction yields excitation energies in good agreement with previous calculations and experimental observations.
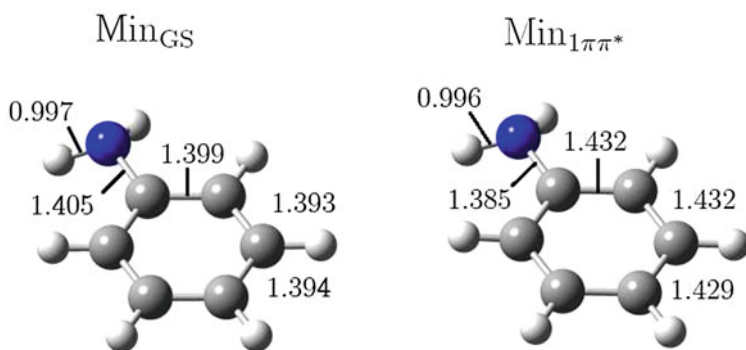
Fig. 3.2 Ground and $1\pi\pi^*$ state CASSCF optimized geometries. Figure reproduced from Ref. [3]

Table 3.2 Wavefunction expansion coefficient of the main configurations for each state obtained from a SA5-CASSCF calculation using the CAS2 active space

Symmetry	State	Coefficients
A'	GS	0.94(ref)
A''	$1\pi\pi^*$	$0.67(2\pi \rightarrow 1\pi^*) + 0.57(3\pi \rightarrow 2\pi^*)$
A'	$1\pi\sigma^*$	$0.92(3\pi \rightarrow R3s/\sigma^*)$
A'	$2\pi\pi^*$	$0.81(3\pi \rightarrow 1\pi^*) - 0.36(2\pi \rightarrow 2\pi^*)$
A''	$2\sigma^*$	$0.91(2\pi \rightarrow R3s/\sigma^*)$

Table 3.3 SA-CASSCF and XMCQDPT2 vertical excitation energies, calculated using the two active spaces described in Sect. 3.2, compared with values from previous high-level ab initio calculations and experimental values

	$A''\ 1\pi\pi^*$	$A'\ 1\pi\sigma^*$	$A'\ 2\pi\pi^*$	$A''\ 2\sigma^*$
CAS1[a]	4.81(4.59)	–	7.38	–
CAS1/XMCQDPT2[a]	4.28(4.02)	–	5.39	–
CAS2[a]	4.81(4.59)	4.90	7.36	6.19
CAS2/XMCQDPT2[a]	4.22(3.96)	4.74	5.25	6.25
SAC-CI [59]	4.20	4.53	5.34	6.39
MS-CASPT2 [60]	4.33	4.85	5.54	6.28
CR-EOM-CCSD(T) [61]	4.21	4.69	5.42	–
Exp.	4.41(4.22) [29]	4.60[b]	5.42 [29]	–

The theoretical adiabatic excitation energies and experimental 0–0 transition energy of the $1\pi\pi^*$ state are given between parenthesis

[a]This work

[b]From Ref. [62], assigned as the 0–0 transition

In addition to the $1\pi\sigma^*$ state, the CAS2 active space generates a second low-lying $R3s/\pi\sigma^*$ state, hereafter denoted $2\sigma^*$ state. Because of the large overestimation of the $2\pi\pi^*$ state, the CASSCF method wrongly predicts the $2\sigma^*$ state below the $2\pi\pi^*$ state. The correct ordering is however recovered at the XMCQDPT2 level of theory. SA5-CASSCF and XMCQDPT2 vertical excitation energies using the CAS2 active space are presented in Table 3.3. These results show that the corrections due to the inclusion of the dynamical correlation energy are less important for the $\pi\sigma^*$ states than for the $\pi\pi^*$ states. Overall, the XMCQDPT2 method provides accurate and well balanced results for the vertical excitation energies of the electronic states of interest.

Finally, we note that the CR-EOM-CCSD(T) calculations of Wang et al. [61] predicted the Rydberg $3p_z$ and $3p_y$ states to lie at 5.31 and 5.42 eV respectively, between the $1\pi\sigma^*$ and $2\pi\pi^*$ states which is in disagreement with previous high level calculations [59, 60]. We have performed a calculation at the XMCQDPT2 level of theory using the CAS2 active space augmented with the two corresponding

3p Rydberg orbitals. This calculation predicted both states to lie slightly above the $2\pi\pi^*$ state, at 5.58 and 5.62 eV respectively. Therefore these states are not further considered in this work.

3.4 Photochemistry After Excitation to the $1\pi\pi^*$ State

In this section, we study the photochemistry of aniline after excitation to the $1\pi\pi^*$ state, at energies below the vertical excitation energy of the $1\pi\sigma^*$ state. The photochemistry of aniline after excitation to the $1\pi\pi^*$ state shares many similarities with that of benzene. Following excitation to the $1\pi\pi^*$ state at wavelengths >270 nm, the fluorescence quantum yields are comparable to those of benzene and single vibronic level lifetimes ranging from 3 to 9 ns have been reported [63, 64]. In addition, CIs with the ground state, analogous to the prefulvene CI in benzene, exist in aniline. Four distinct $S_1(1\pi\pi^*)/GS$ prefulvene-like MECI points, labelled $CI^i_{1\pi\pi^*/GS}$ ($i = 1, 2, 3, 4$), where the superscript refers to the out-of-plane carbon atom (see Fig. 3.3), have been optimized. TSs were found between the $1\pi\pi^*$ equilibrium geometry and $CI^1_{1\pi\pi^*/GS}$ and $CI^4_{1\pi\pi^*/GS}$, indicating the presence of potential barriers along these pathways. The four MECI and two TS geometries, optimized using the CAS1 active space are presented in Fig. 3.4. No TSs were found on the pathways connecting the $1\pi\pi^*$ equilibrium geometry and $CI^2_{1\pi\pi^*/GS}$ or $CI^3_{1\pi\pi^*/GS}$. However, in both cases, the pathway crosses a very flat portion of the $1\pi\pi^*$ PES before reaching the MECI point. Both CASSCF and XMCQDPT2 energies of the four MECIs and two TSs are listed in Table 3.4. Because the degeneracy is lifted for XMCQDPT2 calculations at CASSCF optimized MECI points, the averaged energies of the two states and the magnitudes of the energy gaps between them are reported. These results show that, both at the

Fig. 3.3 The aniline molecule with the numbering scheme used in this work. Figure reproduced from Ref. [3]
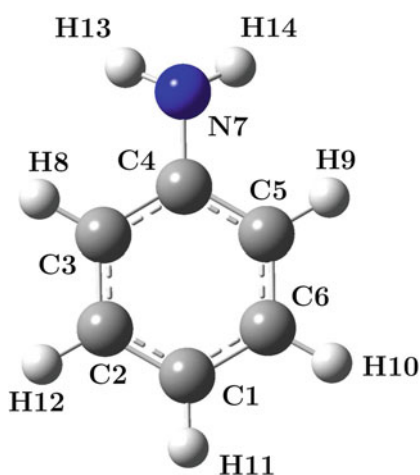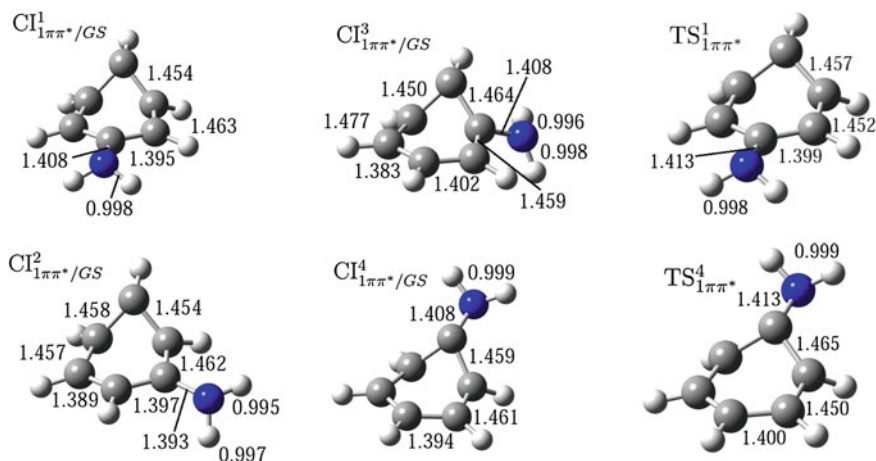
Fig. 3.4 Geometries of the four prefulvene-like MECIs and of the two TSs, $TS^1_{1\pi\pi^*}$ and $TS^4_{1\pi\pi^*}$, optimized along the pathways leading to $CI^1_{1\pi\pi^*/GS}$ and $CI^4_{1\pi\pi^*/GS}$, respectively. Optimizations were performed using the CAS1 active space. Figure reproduced from Ref. [3]

Table 3.4 SA2-CASSCF and XMCQDPT2 prefulvene MECI and TS energies in eV, relative the ground state equilibrium geometry

	CASSCF	XMCQDPT2
$CI^1_{1\pi\pi^*/GS}$	5.50	4.87(0.22)
$CI^2_{1\pi\pi^*/GS}$	5.38	4.76(0.07)
$CI^3_{1\pi\pi^*/GS}$	5.39	4.69(0.21)
$CI^4_{1\pi\pi^*/GS}$	5.26	4.55(0.46)
$TS^1_{1\pi\pi^*}$	5.57	5.10
$TS^4_{1\pi\pi^*}$	5.35	4.96

The XMCQDPT2 MECI energies are averaged over the GS and $1\pi\pi^*$ states. The values between parenthesis are the magnitude of the energy gap between the two states

CASSCF and XMCQDPT2 levels of theory, the $CI^4_{1\pi\pi^*/GS}$ MECI appears at slightly lower energy than the three others. Note that the dynamical correlation energy correction is smaller at the TSs than at the MECIs. This indicates that the XMCQDPT2 barriers are larger than the CASSCF ones. Therefore, the lack of CASSCF TS on the pathways leading to $CI^2_{1\pi\pi^*/GS}$ and $CI^3_{1\pi\pi^*/GS}$ might be a consequence of the non uniform accuracy of the CASSCF method along the pathways.

Linearly interpolated potential energy scans between the $1\pi\pi^*$ equilibrium geometry and the $CI^4_{1\pi\pi^*/GS}$ calculated at the SA2-CASSCF and XMCQDPT2 levels of theory are presented in Fig. 3.5. The scans were performed in two steps: from the $1\pi\pi^*$ equilibrium geometry to $TS^4_{1\pi\pi^*}$ and from $TS^4_{1\pi\pi^*}$ to $CI^4_{1\pi\pi^*/GS}$ MECI. Our calculation shows that the energy required to open the prefulvene decay channel is higher than the vertical excitation energy of the $1\pi\sigma^*$ state (Table 3.3) and therefore, processes taking place on the $1\pi\sigma^*$ surface are likely to compete with the prefulvene
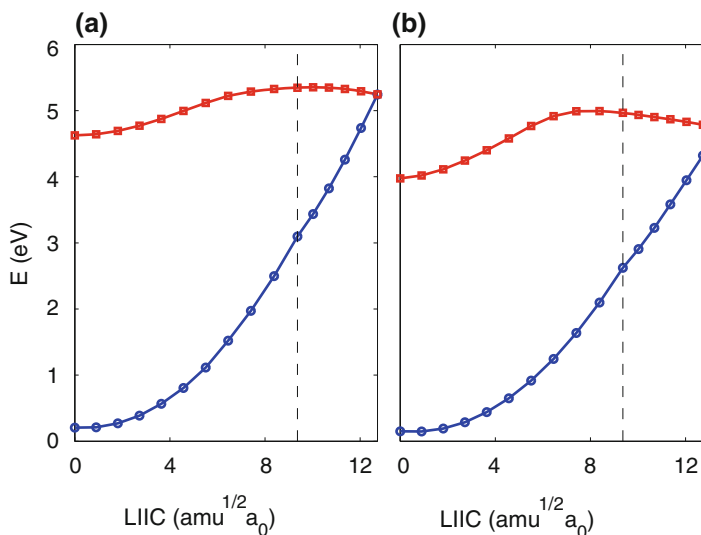
Fig. 3.5 Ground (*blue line with circles*) and $1\pi\pi^*$ (*red line with squares*) state potential energy profiles along the linearly interpolated internal coordinate (LIIC) from the $1\pi\pi^*$ equilibrium geometry to the $\text{CI}^4_{1\pi\pi^*/GS}$ MECI computed at the **a** SA2-CASSCF and **b** XMCQDPT2 levels of theory. The *vertical black dashed line* marks the $\text{TS}^4_{1\pi\pi^*}$ position (see text for details). Figure reproduced from Ref. [3]

decay channel. This explains the absence of ultrafast dynamics observed experimentally after excitations at wavelengths above 270 nm. As seen in Table 3.1, Kirkby et al. measured a decay time constant $\tau_1 = 600 \pm 35$ ps after excitation at $\lambda = 272$ nm. At this wavelength, the molecule does not have enough energy to overcome the barrier seen in Fig. 3.5. Therefore this time constant has been attributed to an intersystem crossing process to the first triplet excited state.

3.5 Photochemistry After Excitation to the $1\pi\sigma^*$ State

In this section, we study the photochemistry of aniline following excitation at wavelengths <269 nm, i.e. above the onset of the $1\pi\sigma^*$ state [62]. In the FC region, the $1\pi\sigma^*$ state PES exhibits a quasi-bound well associated with a strong Rydberg 3s character on the nitrogen atom. However, along the N–H stretching coordinate, the $1\pi\sigma^*$ state acquires a valence σ^* character and the PES becomes dissociative. The quasi-bound and dissociative components of the PES are separated by a significant potential energy barrier, the height of which has been estimated at 0.5 eV using the EOM-CCSD method [61].
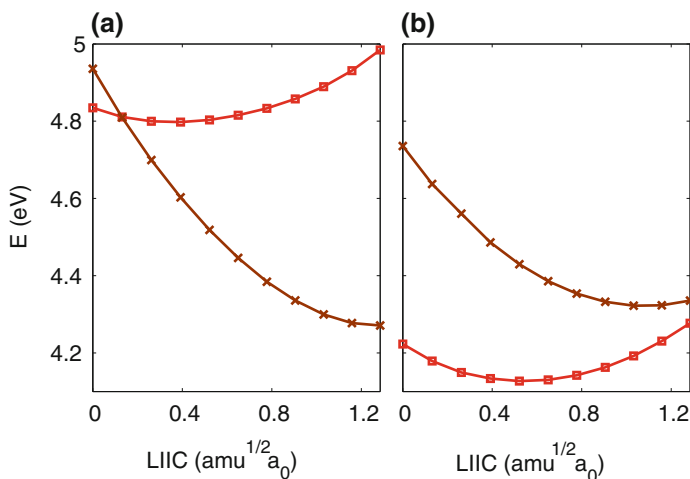
Fig. 3.6 $1\pi\pi^*$ (*red squares*) and $1\pi\sigma^*$ (*brown crosses*) potential energy curves along the linearly interpolated internal coordinate between the FC and CASSCF optimized $\text{Min}_{\pi\sigma^*}$ geometries, computed at the **a** SA5-CASSCF and **b** XMCQDPT2 levels of theory. Figure reproduced from Ref. [3]

Optimization at the SS-CASSCF level of theory predicts a planar equilibrium geometry with C_{2v} symmetry for the $1\pi\sigma^*$ state (see Fig. 3.9). Linearly interpolated scans from the FC geometry to the $1\pi\sigma^*$ equilibrium geometry, computed at the SA5-CASSCF and XMCQDPT2 levels of theory, are presented in Fig. 3.6. These calculations reveal the existence of a CI between the $1\pi\sigma^*$ and $1\pi\pi^*$ states, noted $\pi\sigma^*/1\pi\pi^*$ CI, as previously reported in Ref. [58]. At the CASSCF level of theory, the $\pi\sigma^*/1\pi\pi^*$ CI appears very close to the FC geometry, and the $1\pi\sigma^*$ state becomes the first excited electronic state at its equilibrium geometry. The corresponding MECI geometry is presented in Fig. 3.9. However, at the XMCQDPT2 level of theory, the $\pi\sigma^*/1\pi\pi^*$ CI appears much closer to the $1\pi\sigma^*$ equilibrium geometry. This result suggests that the CASSCF optimized $1\pi\sigma^*$ local minimum is not an equilibrium geometry but rather a geometry where the molecule can decay to the $1\pi\pi^*$ state. In addition, while an experimental excitation energy of 4.60 eV was attributed to the 0–0 transition to the $1\pi\sigma^*$ state in Ref. [62], the existence of the $\pi\sigma^*/1\pi\pi^*$ CI rather suggests that the spectrum of the molecule in this region should be composed of a dense set of vibronically coupled levels that cannot be attributed easily to vibrational levels of either $1\pi\pi^*$ or $1\pi\sigma^*$ states.

We now turn our attention to the H-atom loss decay pathway. We have performed a relaxed potential energy scan along the N–H stretching coordinate on the $1\pi\sigma^*$ PES. Planar geometries with C_s' symmetry were enforced during the optimizations. Here, C_s' notation is used to distinguish the planar geometry from the ground state equilibrium geometry where the symmetry plane is orthogonal to the phenyl ring. In C_s' symmetry, the $1\pi\sigma^*$ state belongs to the A'' irreducible representation whereas

the GS, $1\pi\pi^*$ and $2\pi\pi^*$ states belong to the A' irreducible representation. In these calculations, the A' and A'' states have been computed separately. The geometries on the $1\pi\sigma^*$ PES have been optimized at the SS-CASSCF level of theory using the CAS2 active space. The A' state energies at the optimized geometries have been computed at the SA3-CASSCF level of theory using the same active space. XMCQDPT2 calculations have been performed at the CASSCF optimized geometries and the results of both calculations are presented in Fig. 3.7. Consistently with the results presented above, the $1\pi\sigma^*$ state lies below the $1\pi\pi^*$ state along the CASSCF relaxed scan. A quasi-bound well is seen in the FC region, where the $1\pi\sigma^*$ state has a strong Rydberg character, separated from the dissociative part of the $1\pi\sigma^*$ PES by a potential energy barrier. The transition from the Rydberg 3s to the valence σ^* character is illustrated in Fig. 3.8, where CASSCF σ^* orbitals optimized at different N–H bond lengths are displayed.
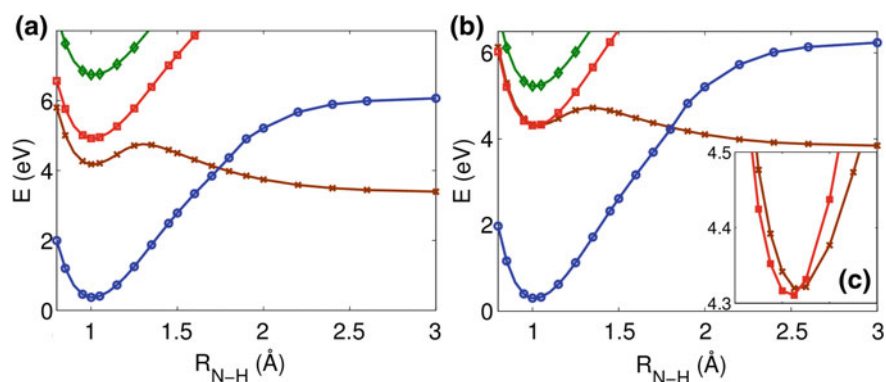
Fig. 3.7 Relaxed potential energy scan along the N–H coordinate, computed at the **a** CASSCF and **b** XMCQDPT2 levels of theory using the CAS2 active space, showing the ground-state (*blue circles*), $1\pi\pi^*$ state (*red squares*), $1\pi\sigma^*$ state (*brown crosses*), $2\pi\pi^*$ state (*green diamonds*). The geometries are optimized on the $1\pi\sigma^*$ state at the SS-CASSCF level of theory using C'_s symmetry. A zoom of the $1\pi\pi^*$ and $1\pi\sigma^*$ states potential scans around the $1\pi\sigma^*$ minimum is shown in panel (**c**). Figure reproduced from Ref. [3]

$R_{N-H} = 1.0$ Å $\quad$ $R_{N-H} = 1.25$ Å $\quad$ $R_{N-H} = 1.5$ Å $\quad$ $R_{N-H} = 3.0$ Å
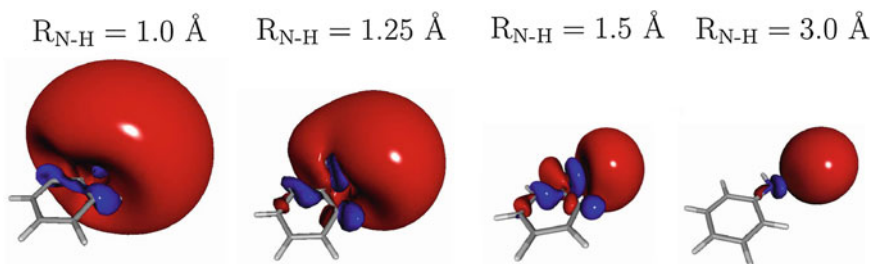
Fig. 3.8 CASSCF optimized σ^* orbital for different N–H bond lengths
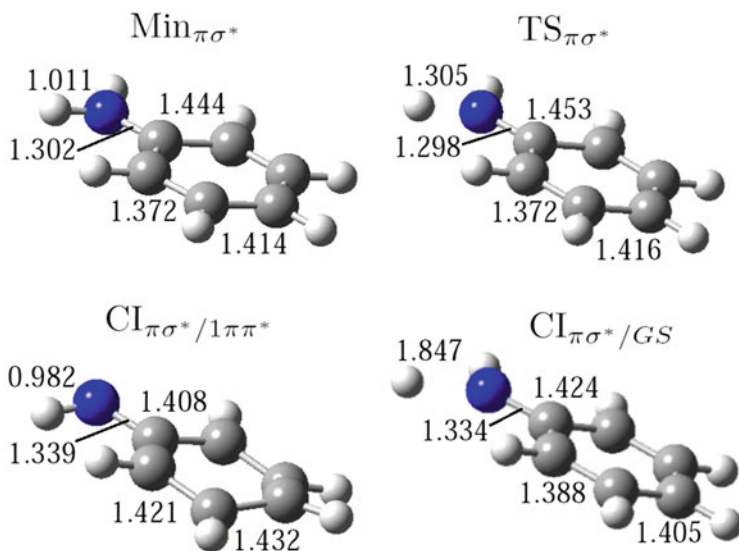
Fig. 3.9 Geometries of the $1\pi\sigma^*$ state local minimum and TS as well as of the $\pi\sigma^*/\pi\pi^*$ and $\pi\sigma^*/GS$ MECIs. Figure reproduced from Ref. [3]

A CI between the $1\pi\sigma^*$ state and the ground state occurs at a larger N–H distance. The CASSCF optimized geometries of the $1\pi\sigma^*$ TS and MECI with the ground state are presented in Fig. 3.9. Our CASSCF calculation predicted a height of 0.58 eV for the barrier separating the quasi-bound well from the dissociative part on the $1\pi\sigma^*$ curve, and an N–H bond strength of 3.37 eV, which is a significant underestimate compared to the experimental value of 3.92 eV reported by Ashfold and coworkers [67].

At the XMCQDPT2 level of theory, the $1\pi\pi^*$ and $1\pi\sigma^*$ states are almost degenerate at short N–H distance, with the $1\pi\pi^*$ state lying slightly below the $1\pi\sigma^*$ state. Consistently with the results presented in Fig. 3.6 the $1\pi\sigma^*$ curve crosses the $1\pi\pi^*$ curve close to its local minimum in the quasi-bound well. We obtain a barrier height of 0.41 eV, which is lower than the CASSCF value, and an N–H bond strength of 3.83 eV, in good agreement with the experimental value of 3.92 eV [67].

In the work of Kirkby et al. [70], two experiments at excitation wavelengths of 445 and 450 nm were performed. In both cases, three decay time constants were extracted from the photoelectron spectra, as seen in Table 3.1. The three time constants are similar for the two experiments, indicating similar dynamics following excitation at these two wavelengths. The shortest time constant τ_3 of approximately 100–150 fs could be clearly associated, through the analysis of the decay associated spectra [1, 2, 70], with a transition from the $1\pi\sigma^*$ state to the $1\pi\pi^*$ state. Therefore, this time constant can be attributed to the passage of the system through the $\pi\sigma^*/1\pi\pi^*$ CI shown above. At the CI, a competition between a transfer to the $1\pi\pi^*$ state and an ultrafast evolution on the $1\pi\sigma^*$ surface, followed by photodissociation or transfer

to the ground state at the $\pi\sigma^*/GS$ CI, occurs. The time constant τ_2 of approximately 550 fs is more difficult to interpret. Thompson et al. [69] found that a time constant of 640 fs was necessary, in addition to the larger time constant τ_1, to fit the photoelectron spectra recorded following excitation at 273 nm, thus below the onset of the $1\pi\sigma^*$ state. Consequently, they attributed τ_2 to an intramolecular vibrational energy redistribution (IVR) process occurring on the $1\pi\pi^*$ state PES. However, these results are in contrast with the experiments performed in the Fielding group [1, 2, 70], in which no evidence of a time constant of the order of τ_2 was found at 272 nm. Therefore, because in [1, 2, 70], τ_2 only appeared after excitation above the onset of the $1\pi\sigma^*$ state, it was interpreted as a mechanism occurring on the $1\pi\sigma^*$ PES. In analogy with results obtained on related systems, two different mechanisms can be proposed. The coexistence of two time scales for the evolution on the $1\pi\sigma^*$ state in pyrrole has been demonstrated using quantum dynamics simulations in Ref. [80]. In pyrrole, as in aniline, the $1\pi\sigma^*$ surface exhibits a quasi-bound well at small N–H distance, separated from the dissociative part by a potential energy barrier estimated at 0.26 eV in [80], where a crossing with the ground state occurs. The simulations performed in Ref. [80] showed that, after photoexcitation, the component of the wavepacket that has a sufficient energy to overcome the barrier evolves towards photodissociation on a very short time scale of 10 fs, whereas the component with an energy lower than the top of the barrier tunnels through the barriers and dissociates on a longer timescale of several hundreds of femtoseconds, in line with the experimental results of Ref. [89]. However, a comparison of the time-resolved photoelectron spectra of aniline and its fully deuterated analogue performed in Ref. [70] revealed no significant change of τ_2 upon deuteration. This observation rules out tunneling as an explanation for τ_2. A second interpretation for τ_2 has been proposed in [1]. It involves a trapping of the wavepacket on the upper cone of the $\pi\sigma^*/GS$ CI, in analogy with experimental observations for methylamine [90] and 5-hydroxyindole [91]. The third time constant τ_1 of approximately 80–100 ps can be associated to a decay to the ground state at the prefulvene $1\pi\pi^*/GS$ CI (see Sect. 3.4) after the fast transfer from the $1\pi\sigma^*$ state to the $1\pi\pi^*$ state, as at excitation wavelengths of 445–450 nm, the system has enough energy to overcome the potential energy barrier existing along the prefulvene decay pathway. This interpretation is further supported by the variations of τ_1 with the excitation wavelength. The diminution of τ_1 from 600 ps at $\lambda = 272$ nm to 80–100 ps at $\lambda = 250-245$ nm is consistent with the opening of the prefulvene decay channel.

3.6 Photochemistry After Excitation to the $2\pi\pi^*$ State

In this section, we study the decay pathways of aniline following excitation to the $2\pi\pi^*$ state, at excitation wavelengths $\lambda < 240$ nm. In all previous experimental studies, an ultrafast decay was observed, or inferred, and interpreted as either internal conversion to the ground state or H-atom loss on the $1\pi\sigma^*$ surface, as explained in Sect. 3.1.2. A $2\pi\pi^*/1\pi\pi^*$ MECI involving a strong out-of-plane distortion of the molecule was reported in Ref. [58]. The existence of this CI justified the interpreta-

tion of the ultrafast decay observed experimentally as the consequence of an internal
conversion to the $1\pi\pi^*$ state followed by either a transfer to the $1\pi\sigma^*$ state through
the $\pi\sigma^*/1\pi\pi^*$ CI shown in the previous section, or the transfer to the ground state
through the prefulvene CI shown in Sect. 3.4. The experiments reported in [1, 2]
show the appearance of a very short time constant of approximately 50 fs. However,
in contradiction with previous interpretations, the analysis of the experimental data
showed no evidence for a population transfer from the $2\pi\pi^*$ state to the $1\pi\pi^*$ state or
the $1\pi\sigma^*$ state associated with this time constant. Therefore, this time constant was
suggested to arise from the existence of an efficient decay pathway taking the system
straight back to its ground electronic state. In contrast, the more recent experiments
reported in [70] show evidence of population being transferred from the $2\pi\pi^*$ state
to the $1\pi\pi^*$ and $1\pi\sigma^*$ states.

Figure 3.10 presents a minimum energy path connecting the $2\pi\pi^*$ state at the FC
geometry to the ground state, computed using the IRC method. The MEP calculation
was performed in several steps and the geometry was constrained to C_s symmetry.
A first IRC calculation was initiated at the FC geometry on the $2\pi\pi^*$ state, using the
CAS1 active space and a CASSCF wavefunction averaged over the $1\pi\pi^*$ and $2\pi\pi^*$
states. The initial relaxation direction was taken to be the gradient on the $2\pi\pi^*$ PES.
The CAS1 active space was used to filter out the $\pi\sigma^*$ states, which greatly simplified
the IRC calculation. The IRC calculation was stopped at the $1\pi\pi^*/2\pi\pi^*$ crossing.
Then, a single point was calculated at a geometry obtained by extrapolating the last
IRC step. At this point, we checked that the $2\pi\pi^*$ state was lying below the $1\pi\pi^*$ state.
A second IRC calculation was then initiated at this last geometry, using the CAS1
active space and a CASSCF wavefunction averaged over the $2\pi\pi^*$ and ground states.
In the second step, in order to include the $\pi\sigma^*$ states in our calculations, we performed
single point SA5-CASSCF and XMCQDPT2 calculations at the geometries obtained
from the IRC calculations, using the CAS2 active space. Hereafter, the intrinsic
reaction coordinate will be noted q^{IRC}.
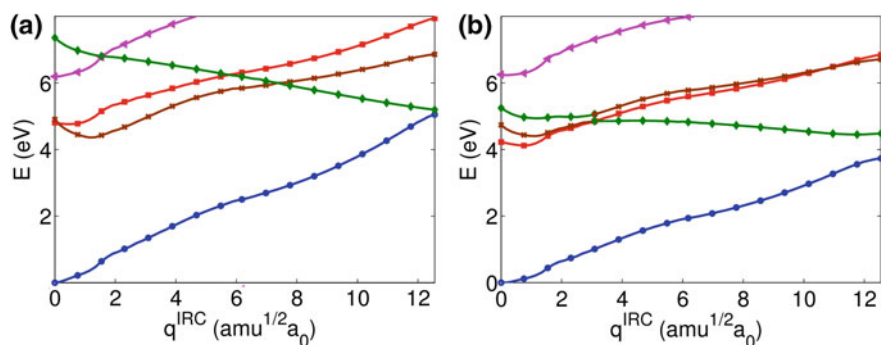
Fig. 3.10 A' Ground state (*blue circles*), $A''1\pi\pi^*$ (*red squares*), $A'1\pi\sigma^*$ (*brown crosses*), $A'2\pi\pi^*$
(*green diamonds*) and $A''2\pi\sigma^*$ (*magenta triangles*) potential energy profiles computed at the SA5-
CASSCF (**a**) and XMCQDPT2 (**b**) levels of theory along the IRC scan on the $A'2\pi\pi^*$ state. Figure
reproduced from Ref. [3]

We first consider the CASSCF IRC scan shown in Fig. 3.10a. As discussed in Sect. 3.3, the CASSCF method yields a wrong state ordering at the FC geometry, i.e. the $2\pi\sigma^*$ state lies below the $2\pi\pi^*$ state. Upon relaxation on the $2\pi\pi^*$ state, the $2\pi\pi^*$ state energy decreases and the $2\pi\sigma^*$ state energy increases until the two curves cross around $q^{\text{IRC}} = 1.8$. This $2\pi\pi^*/2\pi\sigma^*$ CI is an artefact of the CASSCF method. Overall, the CASSCF MEP shows the existence of a barrierless relaxation pathway involving a strong out-of-plane deformation of the molecule, resulting in a boat conformation of the phenyl ring at the end of the IRC scan. Along this pathway, the $2\pi\pi^*$ state crosses successively the $1\pi\pi^*$, $1\pi\sigma^*$ and ground electronic states. The XMCQDPT2 MEP computed at the CASSCF optimized geometries is shown in Fig. 3.10b. Upon relaxation, the energies of the $1\pi\pi^*$, $1\pi\sigma^*$ and $2\pi\pi^*$ states come close to one another around $q^{\text{IRC}} = 3$. In this region, the three states lie within 0.25 eV of each other, which is a strong indication for the presence of a nearby three-state CI [92–94]. In contrast to the CASSCF MEP, here the $1\pi\sigma^*$ and $2\pi\pi^*$ states, both of A' symmetry, form a narrowly avoided crossing rather than a true CI. This is, however, just an indication that the XMCQDPT2 pathway passes very close to the $1\pi\sigma^*/2\pi\pi^*$ CI seam rather than crossing it as in the CASSCF calculation. The pseudo-diabatic assignment used to distinguish between the states is of little significance in the interaction region because the electronic characters of the $1\pi\sigma^*$ and $2\pi\pi^*$ states are mixed. However, as the molecule moves away from the three-state CI region, the electronic character of both states become clear again. The same is true for the region where the $2\pi\pi^*$ state approaches the ground state at the end of the scan.

These calculations have unveiled three CIs that are relevant to the electronic relaxation of aniline following excitation to the $2\pi\pi^*$ state: $1\pi\sigma^*/2\pi\pi^*$, $1\pi\pi^*/2\pi\pi^*$ and $GS/2\pi\pi^*$ CIs. The three corresponding MECIs, labelled $\text{CI}_{1\pi\sigma^*/2\pi\pi^*}$, $\text{CI}_{1\pi\pi^*/2\pi\pi^*}$ and $\text{CI}_{GS/2\pi\pi^*}$, were optimized at the CASSCF level of theory using the CAS2 active space for $\text{CI}_{1\pi\sigma^*/2\pi\pi^*}$ and the CAS1 active space for $\text{CI}_{1\pi\pi^*/2\pi\pi^*}$ and $\text{CI}_{GS/2\pi\pi^*}$. The three resulting geometries are shown in Fig. 3.11. These three MECIs are all characterized by an out-of-plane deformation of the amino group and of the C4 carbon atom of the phenyl ring. In Fig. 3.12, we show the geometries of the molecule at four key points along the MEP: the FC geometry ($q^{\text{IRC}} = 0$), the geometry of the approximate three-state CI ($q^{\text{IRC}} = 2.89$) the geometry of the $1\pi\pi^*/2\pi\pi^*$ crossing ($q^{\text{IRC}} = 5.68$) on the CASSCF MEP and the geometry corresponding to the $GS/2\pi\pi^*$ crossing ($q^{\text{IRC}} = 12.55$). This figure shows that the IRC coordinate mainly involves a boat deformation of the phenyl ring associated with an out-of-plane motion of the amino group. However, in contrast with the $\text{CI}_{1\pi\sigma^*/2\pi\pi^*}$ and $\text{CI}_{1\pi\pi^*/2\pi\pi^*}$ geometries shown in Fig. 3.11, at the approximate three-state CI ($q^{\text{IRC}} = 2.89$), the molecule is still almost planar. It is interesting to note that similar ring puckering decay pathways have been described in other simple aromatic organic molecules such as pyrrole [17] or the purine DNA bases adenine [18, 19] and guanine [20]. In addition, the boat conformation of the phenyl ring, found at $q^{\text{IRC}} = 12.55$ (see Fig. 3.12), is reminiscent of the Dewar form of benzene, which is know to be populated after excitation to the $2\pi\pi^*$ state of benzene [95–97]. To investigate this further, we extrapolated from the CI at $q^{\text{IRC}} = 12.55$, along the IRC until a geometry where the $2\pi\pi^*$ state is the ground state was found and then performed a geometry optimization.
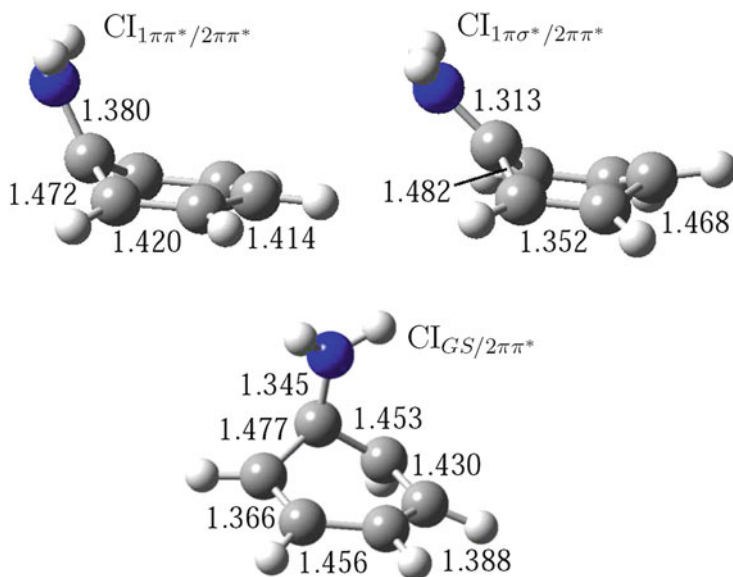
Fig. 3.11 Geometries of the three MECIs involving the $2\pi\pi^*$ state. Figure reproduced from Ref. [3]
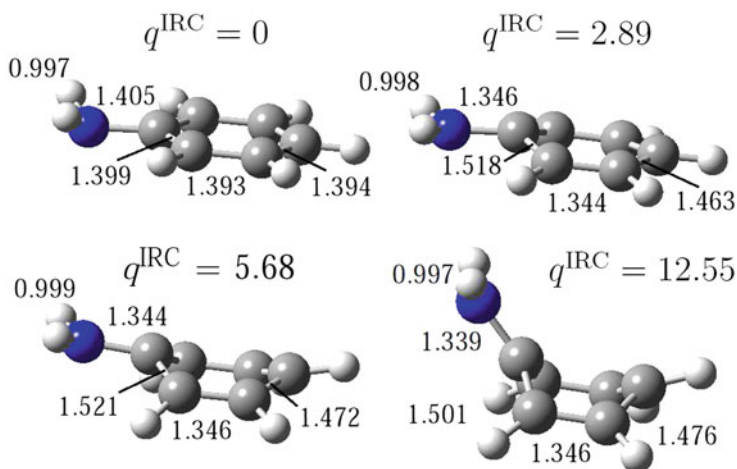
Fig. 3.12 Geometries at key points along the MEP (see text for details). Figure reproduced from Ref. [3]

The resulting local minimum on the ground state PES (Min_{Dew}) is an analogue of the Dewar benzene isomer (Fig. 3.13). We have also optimized a saddle point (TS_{Dew}) connecting this local minimum to the global equilibrium geometry of the ground electronic state (Fig. 3.13). The energies of the Dewar minimum and TS relative to the global minimum energy, computed at the SA2-CASSCF and XMCQDPT2 level of theory using the CAS1 active space, are presented in Table 3.5. The SA2-CASSCF energies of the $CI_{2\pi\pi^*/GS}$ points, are also reported. The Dewar form of aniline is local minimum on the ground state PES, separated from the global minimum by a barrier with a height evaluated at 0.57 eV. Interestingly, the Dewar form of aniline could be a possible experimental probe of the ring puckering decay pathway discussed above.

In addition to the ring-puckering decay pathway, the potential energy curves in Fig. 3.10 suggest two alternative decay pathways. At the three-state CI, the molecule can be transferred to the $1\pi\pi^*$ or $1\pi\sigma^*$ states. In both cases, it is clear that the molecule can relax to the FC region, from which the molecule can then decay to the ground state via the prefulvene $CI_{1\pi\pi^*/GS}$ shown in Fig. 3.4 or the $CI_{\pi\sigma^*/GS}$ shown in Fig. 3.9, or dissociate on the $1\pi\sigma^*$ PES. In order to find out if other direct decay pathways to the ground state exist, we performed linearly interpolated scans from
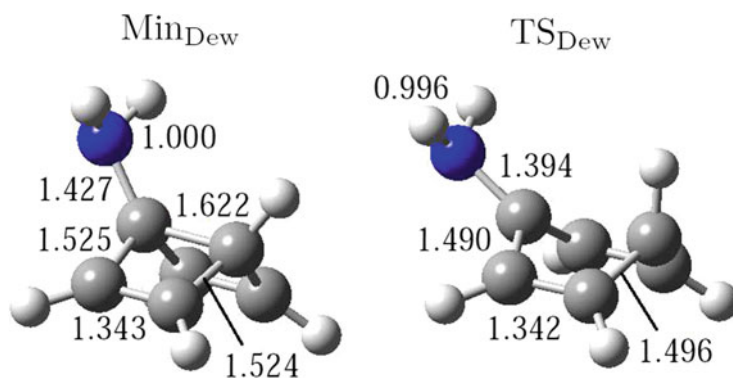
Fig. 3.13 Geometries of the Dewar minimum and TS on the ground state PES. Figure reproduced from Ref. [3]

Table 3.5 SA2-CASSCF and XMCQDPT2 energies of the Dewar minimum and TS and SA2-CASSCF energies of the $CI_{2\pi\pi^*/GS}$ points

	SA2-CASSCF	XMCQDPT2
Min_{Dew}	3.97	3.54
TS_{Dew}	4.60	4.11
$CI_{2\pi\pi^*/GS}^{MECI}$	4.79	–
$CI_{2\pi\pi^*/GS}^{IRC}$	5.21	–

$CI_{2\pi\pi^*/GS}^{MECI}$ refers to the MECI (see Fig. 3.11) and $CI_{2\pi\pi^*/GS}^{IRC}$ to the CI point reached on the IRC path at $q^{IRC} = 12.55$ (see Figs. 3.10 and 3.12)

Fig. 3.14 Linearly interpolated scans **a** from the $CI_{1\pi\pi^*/2\pi\pi^*}$ to the prefulvene $CI_{1\pi\pi^*/GS}$ and **b** from the $CI_{1\pi\sigma^*/2\pi\pi^*}$ to the $CI_{1\pi\sigma^*/GS}$ computed at the SA5-CASSCF and SA6-CASSCF level of theory, respectively, using the CAS2 active space. Figure reproduced from Ref. [3]
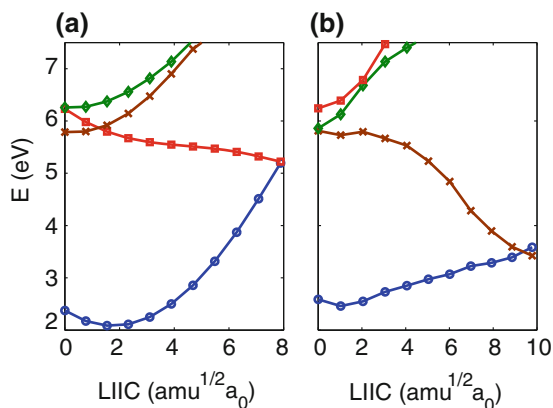
the $CI_{1\pi\pi^*/2\pi\pi^*}$ to the prefulvene $CI_{1\pi\pi^*/GS}$ and from the $CI_{1\pi\sigma^*/2\pi\pi^*}$ to the $CI_{1\pi\sigma^*/GS}$ respectively, using the CAS2 active space. For the former, the orbitals were averaged over the five lowest states while for the latter, the inclusion of a sixth state was found necessary for a well balanced description of the states of interest along the pathway. Both calculations are presented in Fig. 3.14. In both cases, the initial geometries were not taken to be the MECI structures of $CI_{1\pi\pi^*/2\pi\pi^*}$ and $CI_{1\pi\sigma^*/2\pi\pi^*}$, but rather the CI points reached in the CASSCF IRC pathway of Fig. 3.10a. The scan in Fig. 3.14a shows the existence a rather flat but barrierless pathway connecting the $CI_{1\pi\pi^*/2\pi\pi^*}$ to the prefulvene $CI_{1\pi\pi^*/GS}$. Interestingly, a similar barrierless pathway connecting the S_2/S_1 CI to the prefulvene S_1/S_0 CI in benzene has been calculated [98, 99]. However, Fig. 3.10a shows that the path connecting the $CI_{1\pi\pi^*/2\pi\pi^*}$ with the FC geometry is steeper. Therefore, it seems most likely that, if the molecule is transferred to the $1\pi\pi^*$ state at the three-state CI, it will then relax to the FC region where it can relax further via the prefulvene $CI_{1\pi\pi^*/GS}$ or via the N–H dissociation path on the $1\pi\sigma^*$ state after crossing the $CI_{\sigma^*/1\pi\pi^*}$, as was proposed previously [67, 68].

The scan of Fig. 3.14b shows a steep pathway connecting the the $CI_{1\pi\sigma^*/2\pi\pi^*}$ to the $CI_{1\pi\sigma^*/GS}$, suggesting the possibility of very efficient relaxation to the ground state or dissociation on the $1\pi\sigma^*$ PES. A barrier is seen on the $1\pi\sigma^*$ potential energy profile. However this barrier appears much smaller than the barrier on the relaxed N–H potential scan shown in Fig. 3.7, and should therefore be easily overcome by the wavepacket upon relaxation on the $1\pi\sigma^*$ state after crossing the $CI_{1\pi\sigma^*/2\pi\pi^*}$.

In this section, we have shown the existence of a decay pathway connecting the FC region on the $2\pi\pi^*$ state to a CI with the ground state in a barrierless manner. This pathway crosses a probable three-state CI involving the $1\pi\pi^*$, $1\pi\sigma^*$ and $2\pi\pi^*$ states. Experimentally, a time constant τ_4 of approximately 50 fs was extracted from the photoelectron spectra recorded after excitation at $\lambda = 238$ nm [1, 2, 70]. In [1, 2], the analysis of the decay associated spectra did not show evidence of a rise

of population in the $1\pi\pi^*$ and $1\pi\sigma^*$ states associated with the decay of population from the $2\pi\pi^*$ state, although population was observed in these states. However, in the more recent set of experiments of Kirkby et al. [70], a rise of population in the $1\pi\pi^*$ state was observed in the first tens of femtoseconds after excitation. Population of the $1\pi\sigma^*$ was also observed, although its rise could still not be correlated to the decay of the population of the $2\pi\pi^*$ state occurring in a timescale of τ_4. As noted in [70], a direct excitation to the $1\pi\pi^*$ or $1\pi\sigma^*$ states is unlikely to occur at $\lambda = 238$ nm. The results presented in this section thus provide a satisfactory explanation for the experimental observation reported in [1, 2, 70]. After excitation to the $2\pi\pi^*$ state, the molecule relaxes towards a three-state CI in an ultrashort time scale of approximately 50 fs. At the three-state CI, the molecule can further relax on the $2\pi\pi^*$ PES and decay to the ground state at the $CI_{2\pi\pi^*/GS}$, or it can be transferred to the $1\pi\pi^*$ or $1\pi\sigma^*$ state and further decay through the mechanisms described in Sects. 3.4 and 3.5. Indeed, besides the short time constant τ_4, three other time constants were found at an excitation wavelength of 238 nm. These three time constants are similar to the three time constants found at $\lambda = 245$ nm and $\lambda = 250$ nm, and can therefore be attributed to the same decay mechanisms.

3.7 Summary and Conclusions

In this work, we have explored the PESs of the low-lying electronic states of aniline using high-level electronic structure calculations. We have revealed previously unknown stationary points and decay pathways relevant for the photochemistry of the molecule, and discussed their implications in relation with the available experimental results. This work shows that aniline has an intricate photochemistry, involving a competition between several different decay mechanisms. When the molecule is excited to its $2\pi\pi^*$ state, four time constants appear experimentally, which are related to four different decay mechanisms, involving a prefulvene decay pathway on the $1\pi\pi^*$ state, a competition between photodissociation and decay to the ground state on the $1\pi\sigma^*$ state, and a direct mechanism leading to a decay to the ground state on the $2\pi\pi^*$ state. These calculations thus provide valuable information about the decay mechanisms accessible to the molecule after UV excitation, and help in the interpretation of the complex experimental signals obtained from time-resolved experiments.

Nevertheless, several questions remain open regarding the photodynamics of aniline. The τ_2 time constant of approximately 500 fs has not found a definitive interpretation. Townsend et al. have interpreted it as an IVR process on the $1\pi\pi^*$ state [69] while Kirkby et al. interpreted it as a trapping mechanism on the $1\pi\sigma^*$ PES. Wang et al. [61] suggested that two 3p Rydberg states were involved in the dynamics of the molecule after excitation to the $2\pi\pi^*$ state, however, no experimental evidence for the participation of these state has been reported. Finally, only limited insight into the relative importance of the various decay mechanisms accessible to the molecule can be obtained from the present work. It is known that nuclear dynamics around CIs

do not only depend on the location of the MECI point but also on the topography of the extended CI seam. Specifically, different decay pathways can be preferred depending on which region of the CI seam is reached [10, 100, 101]. Therefore, an extended mapping of the various CI seams connecting the electronic states of interest in this work would provide further insight on the competition between the different decay channels. Quantum dynamics simulations would also provide valuable information, however the construction of reliable coupled PESs describing large amplitude nuclear motion for a mid-size system such as aniline is an extremely difficult task which lies beyond the current state-of-the-art in this field. Indeed, although the recent quantum dynamics calculations of Wang et al. [61] could reproduce the absorption spectrum with a high accuracy, the calculations could not account for the ultrafast decay of the molecule after excitation to the $2\pi\pi^*$ state. As an alternative, direct dynamics techniques [102, 103] can also be used to study the relaxation pathways of the molecule. The conclusions drawn in this work indicate that such investigations should use high-level electronic structure calculations to reach the level of accuracy necessary for a reliable description of the relaxation of aniline after electronic excitation.

References

1. R. Spesyvtsev, O.M. Kirkby, M. Vacher, H.H. Fielding, Phys. Chem. Chem. Phys. **14**, 9942 (2012)
2. R. Spesyvtsev, O.M. Kirkby, H.H. Fielding, Faraday Discuss. **157**, 165 (2012)
3. M. Sala, O.M. Kirkby, S. Guérin, H.H. Fielding, Phys. Chem. Chem. Phys. **16**, 3122 (2014)
4. T.A. Stephenson, P.L. Radloff, S.A. Rice, J. Chem. Phys. **81**, 1060 (1984)
5. T.A. Stephenson, S.A. Rice, J. Chem. Phys. **81**, 1073 (1984)
6. I.J. Palmer, I.N. Ragazos, F. Bernardi, M. Olivucci, M.A. Robb, J. Am. Chem. Soc. **115**, 673 (1993)
7. G.A. Worth, J. Photochem. Photobiol. A **190**, 190 (2007)
8. G.A. Worth, R.E. Carley, H.H. Fielding, Chem. Phys. **338**, 220 (2007)
9. B. Lasorne, F. Silicia, M.J. Bearpark, M.A. Robb, G.A. Worth, L. Blancafort, J. Chem. Phys. **128**, 124307 (2008)
10. B. Lasorne, M.J. Bearpark, M.A. Robb, G.A. Worth, J. Phys. Chem. A **112**, 13017 (2008)
11. D.S.N. Parker, R.S. Minns, T.J. Penfold, G.A. Worth, H.H. Fielding, Chem. Phys. Lett. **469**, 43 (2009)
12. T.J. Penfold, G.A. Worth, J. Chem. Phys. **131**, 064303 (2009)
13. R.S. Minns, D.S.N. Parker, T.J. Penfold, G.A. Worth, H.H. Fielding, Phys. Chem. Chem. Phys. **12**, 15607 (2010)
14. T.J. Penfold, R. Spesyvtsev, O.M. Kirkby, R.S. Minns, D.S.N. Parker, H.H. Fielding, G.A. Worth, J. Chem. Phys. **137**, 204310 (2012)
15. A.L. Sobolewski, C. Woywod, W. Domcke, J. Chem. Phys. **98**, 5627 (1992)
16. O.P.J. Vieuxmaire, Z. Lan, A.L. Sobolewski, W. Domcke, J. Chem. Phys. **129**, 224307 (2008)
17. M. Barbatti, M. Vazdar, A.J.A. Aquino, M. Eckert-Maksić, H. Lischka, J. Chem. Phys. **125**, 164323 (2006)
18. S. Perun, A.L. Sobolewski, W. Domcke, J. Am. Chem. Soc. **127**, 6257 (2005)
19. L. Blancafort, J. Am. Chem. Soc. **128**, 210 (2006)
20. L. Serrano-Andrés, M. Merchán, A.C. Borin, J. Am. Chem. Soc. **130**, 2473 (2007)
21. A.L. Sobolewski, W. Domcke, Chem. Phys. **259**, 181 (2000)

22. A.L. Sobolewski, W. Domcke, C. Dedonder-Lardeuxc, C. Jouvet, Phys. Chem. Chem. Phys. **4**, 1093 (2002)
23. M.N.R. Ashfold, B. Cronin, A.L. Devine, R.N. Dixon, M.G.D. Nix, Science **312**, 1637 (2006)
24. M.N.R. Ashfold, G.A. King, D. Murdock, M.G.D. Nix, T.A.A. Oliver, A.G. Sage, Phys. Chem. Chem. Phys. **12**, 1218 (2010)
25. G.M. Roberts, D.J. Hadden, L.T. Bergendahl, A.M. Wenge, S.J. Harris, T.N.V. Karsili, M.N.R. Ashfold, M.J. Paterson, V. Stavros, Chem. Sci. **4**, 993 (2013)
26. G.M. Roberts, V. Stavros, Chem. Sci. **5**, 1698 (2014)
27. K. Kimura, H. Tsubomura, S. Nagakura, Bull. Chem. Soc. Jpn. **37**, 1336 (1964)
28. K. Kimura, S. Nagakura, Mol. Phys. **9**, 117 (1965)
29. B.N. Rajasekhar, A. Veeraiah, K. Sunanda, B.N. Jagatap, J. Chem. Phys. **139**, 064303 (2013)
30. D.G. Lister, J.K. Tyler, J.H. Hog, N.W. Larsen, J. Mol. Struct. **23**, 253 (1974)
31. M. Fukuyo, K. Hirotsu, T. Higuchi, Acta Crystallogr. **38B**, 640 (1982)
32. G. Roussy, A. Nonat, J. Mol. Spectrosc. **118**, 180 (1986)
33. G. Schultz, G. Portalone, F. Ramondo, A. Domenicano, I. Hargittai, Struct. Chem. **7**, 59 (1996)
34. A. Wolf, U. Voets, H.-H. Schmidtke, Theor. Chim. Acta **54**, 229 (1980)
35. Z. Niu, K.M. Dunn, J.E. Boggs, Mol. Phys. **55**, 421 (1985)
36. J.E. Boggs, Z. Niu, J. Comput. Chem. **6**, 46 (1985)
37. C.W. Bock, P. George, M. Trachtman, Theor. Chim. Acta **69**, 235 (1986)
38. A.-D. Gorse, M. Pesquer, J. Mol. Struct. (THEOCHEM) **281**, 21 (1993)
39. Y. Wang, S. Saebo, C.U. Pittman Jr, J. Mol. Struct. (THEOCHEM) **281**, 91 (1993)
40. M. Castellà-Ventura, E. Kassab, Spectrochim. Acta A **50**, 69 (1994)
41. J. Sponer, P. Hobza, Int. J. Quantum Chem. **57**, 959 (1996)
42. O. Bludský, J. Sponer, J. Leszczynski, V. Spirko, P. Hobza, J. Chem. Phys. **105**, 11042 (1996)
43. I. López-Tocón, J.C. Otero, M. Becucci, G. Pietraperzia, E. Castellucci, Chem. Phys. **249**, 113 (1999)
44. M. Alcolea Palafox, J.L. Núñez, M. Gil, J. Mol. Struct. (THEOCHEM) **593**, 101 (2002)
45. P.M. Wojciechowski, W. Zierkiewicz, D. Michalska, P. Hobza, J. Chem. Phys. **118**, 10900 (2003)
46. M.A. Palafox, M. Gill, N.J. Nunez, V.K. Rastogi, L. Mittal, R. Sharma, Int. J. Quantum Chem. **103**, 394 (2005)
47. V. Hänninen, L. Halonen, J. Phys. Chem. **126**, 064309 (2007)
48. I.V. Alabugin, M. Manoharan, M. Buck, R.J. Clark, J. Mol. Struct. (THEOCHEM) **813**, 21 (2007)
49. J.C. Jiang, C.E. Lin, J. Mol. Struct. (THEOCHEM) **392**, 181 (1997)
50. W.B. Tzeng, K. Narayanan, K.C. Shieh, C.C. Tung, J. Mol. Struct. (THEOCHEM) **428**, 231 (1998)
51. I. López-Tocón, R.G. Della Valle, M. Becucci, E. Castellucci, J.C. Otero, Chem. Phys. Lett. **327**, 45 (2000)
52. D.M. Upadhyay, M.K. Shukla, P.C. Mishra, J. Mol. Struct. (THEOCHEM) **531**, 249 (2000)
53. K. Pirowska, P. Kolek, J. Goclon, J. Najbar, Chem. Phys. Lett. **387**, 165 (2004)
54. G. Piani, M. Pasquini, I. López-Tocón, G. Pietraperzia, M. Becucci, E. Castellucci, Chem. Phys. **330**, 138 (2006)
55. E. Drougas, J.G. Philis, A.M. Kosmas, J. Mol. Struct. (THEOCHEM) **758**, 17 (2006)
56. W.E. Sainclair, D.W. Pratt, J. Chem. Phys. **105**, 7942 (1996)
57. L. Santos, E. Martinez, B. Ballesteros, J. Sanchez, Spectrochim. Acta A **56**, 1905 (2000)
58. G.M. Roberts, C.A. Williams, J.D. Young, S. Ullrich, M.J. Paterson, V.G. Stavros, J. Am. Chem. Soc. **134**, 12578 (2012)
59. Y. Honda, M. Hada, M. Ehara, H. Nakatsuji, J. Chem. Phys. **117**, 2045 (2002)
60. X.-J. Hou, P. Quan, T. Höltzl, T. Veszprémi, M.T. Nguyen, J. Phys. Chem. A **109**, 10396 (2005)
61. F. Wang, S.P. Neville, R. Wang, G.A. Worth, J. Phys. Chem. A **117**, 7298 (2013)
62. T. Ebata, C. Minejima, N. Mikami, J. Phys. Chem. A **106**, 11068 (2002)
63. H. Von Weyssenhoff, F. Kraus, J. Chem. Phys. **54**, 2387 (1971)

64. R. Scheps, D. Florida, S.A. Rice, J. Chem. Phys. **61**, 1730 (1973)
65. J.L. Knee, P.M. Johnson, J. Chem. Phys. **80**, 13 (1984)
66. B. Kim, C.P. Schick, P.M. Weber, J. Chem. Phys. **103**, 6903 (1995)
67. G.A. King, T.A.A. Oliver, M.N.R. Ashfold, J. Chem. Phys. **132**, 214307 (2010)
68. R. Montero, A.P. Conde, V. Ovejas, R. Martínez, F. Castaño, A. Longarte, J. Chem. Phys. **135**, 054308 (2011)
69. J.O.F. Thompson, R.A. Livingston, D. Townsend, J. Chem. Phys. **139**, 034316 (2013)
70. O.M. Kirkby, M. Sala, G. Balerdi, R. de Nalda, L. Bañares, S. Guérin, H.H. Fielding, Phys. Chem. Chem. Phys. **17**, 16270 (2015)
71. M.J. Bearpark, M.A. Robb, H.B. Schlegel, Chem. Phys. Lett. **223**, 269 (1994)
72. C. Gonzalez, H.B. Schlegel, J. Chem. Phys. **90**, 2154 (1989)
73. C. Gonzalez, H.B. Schlegel, J. Phys. Chem. **94**, 5523 (1990)
74. A.A. Granovsky, J. Chem. Phys. **134**, 214113 (2011)
75. L. Serrano-Andrés, M. Merchán, A.C. Borin, Chem. Eur. J. **12**, 6559 (2006)
76. M. Merchán, L. Serrano-Andrés, J. Am. Chem. Soc. **125**, 8108 (2003)
77. F. Berndt, I. Ioffe, A.A. Granovsky, R. Mahrwald, S. Tannert, S.A. Kovalenko, N.P. Ernsting, J. Photochem. Photobiol. A **234**, 164 (2012)
78. A.L. Dobryakov, I. Ioffe, A.A. Granovsky, N.P. Ernsting, S.A. Kovalenko, J. Chem. Phys. **137**, 244505 (2012)
79. V. Vallet, Z. Lan, S. Mahapatra, A.L. Sobolewski, W. Domcke, Faraday Discuss. **127**, 283 (2004)
80. V. Vallet, Z. Lan, S. Mahapatra, A.L. Sobolewski, W. Domcke, J. Chem. Phys. **123**, 144307 (2005)
81. Z. Lan, W. Domcke, V. Vallet, A.L. Sobolewski, S. Mahapatra, J. Chem. Phys. **122**, 224315 (2005)
82. D.R. Yarkony, J. Chem. Phys. **92**, 2457 (1990)
83. I.N. Ragazos, M.A. Robb, F. Bernardi, M. Olivucci, Chem. Phys. Lett. **197**, 217 (1992)
84. H. Lischka, M. Dallos, P. Szalay, D.R. Yarkony, R. Shepard, J. Chem. Phys. **120**, 7322 (2004)
85. W. Domcke, D.R. Yarkony, H. Köppel, *Conical Intersections, Electronic Strucutre, Dynamics and Spectroscopy* (World Scientific, New Jersey, 2004)
86. Gaussian 03, Revision C.02, M.J. Frisch, G.W. Trucks, H.B. Schlegel, G.E. Scuseria, M.A. Robb, J.R. Cheeseman, J.A. Montgomery, Jr., T. Vreven, K.N. Kudin, J.C. Burant, J.M. Millam, S.S. Iyengar, J. Tomasi, V. Barone, B. Mennucci, M. Cossi, G. Scalmani, N. Rega, G.A. Petersson, H. Nakatsuji, M. Hada, M. Ehara, K. Toyota, R. Fukuda, J. Hasegawa, M. Ishida, T. Nakajima, Y. Honda, O. Kitao, H. Nakai, M. Klene, X. Li, J.E. Knox, H.P. Hratchian, J.B. Cross, V. Bakken, C. Adamo, J. Jaramillo, R. Gomperts, R.E. Stratmann, O. Yazyev, A.J. Austin, R. Cammi, C. Pomelli, J.W. Ochterski, P.Y. Ayala, K. Morokuma, G.A. Voth, P. Salvador, J.J. Dannenberg, V.G. Zakrzewski, S. Dapprich, A.D. Daniels, M.C. Strain, O. Farkas, D.K. Malick, A.D. Rabuck, K. Raghavachari, J.B. Foresman, J.V. Ortiz, Q. Cui, A.G. Baboul, S. Clifford, J. Cioslowski, B.B. Stefanov, G. Liu, A. Liashenko, P. Piskorz, I. Komaromi, R.L. Martin, D.J. Fox, T. Keith, M.A. Al-Laham, C.Y. Peng, A. Nanayakkara, M. Challacombe, P.M.W. Gill, B. Johnson, W. Chen, M.W. Wong, C. Gonzalez, J.A. Pople, Gaussian Inc, Wallingford CT (2004)
87. A.A. Granovsky, Firefly version 7.1.G, http://classic.chem.msu.su/gran/firefly/index.html
88. M.W. Schmidt, K.K. Baldridge, J.A. Boatz, S.T. Elbert, M.S. Gordon, J.H. Jensen, S. Koseki, N. Matsunaga, K.A. Nguyen, S. Su, T.L. Windus, M. Dupuis, J.A. Montgomery, J. Comput. Chem. **14**, 1347 (1993)
89. H. Lippert, H.H. Ritze, I.V. Hertel, W. Radloff, Phys. Chem. Chem. Phys. **5**, 1423 (2004)
90. D.-S. Ahn, J. Lee, J.-M. Choi, K.-S. Lee, S.J. Baek, K. Lee, K.K. Baek, S.K. Kim, J. Chem. Phys. **128**, 224305 (2008)
91. J.S. Lim, S.K. Kim, Nat. Chem. **2**, 627 (2010)
92. S. Matsika, D.R. Yarkony, J. Chem. Phys. **117**, 6907 (2002)
93. S. Han, D.R. Yarkony, J. Chem. Phys. **119**, 11561 (2003)
94. M.S. Schuurman, D.R. Yarkony, J. Phys. Chem. B **110**, 19031 (2006)

95. H.R. Ward, J.S. Wishnok, J. Am. Chem. Soc. **90**, 5353 (1968)
96. D. Bryce-Smith, A. Gilbert, D.A. Robinson, Angew. Chem. Int. Ed. **10**, 745 (1971)
97. A.L. Sobolewski, J. Chem. Phys. **93**, 6433 (1990)
98. A. Toniolo, A.L. Thompson, T.J. Martínez, Chem. Phys. **304**, 133 (2004)
99. A.L. Thompson, T.J. Martínez, Faraday Discuss. **150**, 293 (2011)
100. D. Mendive-Tapia, B. Lasorne, G.A. Worth, M.J. Bearpark, M.A. Robb, Phys. Chem. Chem. Phys. **12**, 15725 (2010)
101. J.J. Serrano-Pérez, F. de Vleeschouwer, F. de Proft, D. Mendive-Tapia, M.J. Bearpark, M.A. Robb, J. Org. Chem. **78**, 1874 (2013)
102. G.A. Worth, M.A. Robb, B. Lasorne, Mol. Phys. **106**, 2077 (2008)
103. M. Barbatti, WIREs Comput. Mol. Sci. **1**, 620 (2011)

Chapter 4
Theory of Nuclear Quantum Dynamics Simulations

In Chap. 2, we have seen that the theoretical study of a molecular system is, in a vast majority of cases, separated in two steps. In a first step, the electronic structure of the system is studied by solving the electronic Schrödinger equation with fixed nuclei. This approach, combined with geometry optimization techniques, allows one to locate the important features of the various potential energy surfaces (PESs) of the electronic states of interest. In the context of photochemistry, as seen in Chap. 3, this approach allows one to characterize the various decay pathways of the molecule after photoexcitation. This information can then be used to interpret the various decay time constants obtained from time-resolved spectroscopic measurements. However, in most cases, including aniline studied in Chap. 3, various decay mechanisms are in competition, and it is often difficult to infer, from this static information, the relative importance of the various decay mechanisms. It is thus often necessary to study the dynamics of the nuclei in the manifold of the excited states of interest to obtain a deeper insight into the photophysics and photochemistry of the system of interest.

The dynamics of the nuclei in molecules is often affected by strong quantum effects [1]. One can mention, for instance, zero point energy effects or tunneling of light nuclei through potential energy barriers. In addition, in situation where strong vibronic couplings exist, the system can be transferred from one electronic state to another upon nuclear motion. This phenomenon is of purely quantum origin. Therefore, an accurate description of such phenomena requires a quantum treatment of the dynamics of the nuclei.

We have seen in Chap. 2 that, in a vast majority of case, the calculation of the electronic structure of molecular systems is performed in a time-independent formalism, through the solution of the time-independent electronic Schrödinger equation. In contrast, in nuclear quantum dynamics, a majority of problems can be treated either in a time-independent or in a time-dependent formalism [2, 3]. In this thesis, the time-dependent formalism was used. Therefore, in this chapter, the theoretical tools for the study of the quantum dynamics of the nuclei in molecular systems will be introduced from a time-dependent perspective.

4.1 Setting up the Hamiltonian Operator

4.1.1 The Choice of the Coordinates and the Nuclear Kinetic Energy Operator

The choice of the coordinates used to parametrize the motion of the nuclei is of great importance in molecular quantum dynamics simulations. In order to ensure a good convergence of the algorithm used to solve the nuclear Schrödinger equation, a set of nuclear coordinates well adapted to the problem under consideration must be chosen. A good set of coordinates is such that the correlation between the different coordinates is minimal. When only low amplitude vibrational motions, implying a nearly harmonic portion of the PES, need to be described, the rectilinear normal coordinates are a good choice because they lead to a simple and separable nuclear kinetic energy operator (KEO). However, in more floppy systems, involving, for instance, several equilibrium geometries connected by low-energy potential energy barriers, large amplitude angular motions need to be described. In such situations, rectilinear coordinates cease to be a good choice because they introduce strong, unphysical, correlations. A more natural choice is then to use a set of curvilinear coordinates because they lead to a more separable Hamiltonian operator. Unfortunately, the use of curvilinear coordinates often leads to a very complicated expression of the nuclear KEO. In general, obtaining the correct KEO is not a problem since analytic computation softwares can be used for that purpose. In addition, the action of the KEO can be computed numerically, avoiding the need for the analytic expression [4, 5]. It is nevertheless of high interest to find a general form of the KEO that is as compact as possible and well adapted to the numerical method used to solve the nuclear Schrödinger equation. The polyspherical approach (see Ref. [6] and references therein) meets both these requirements.

Consider an isolated molecule composed of N atoms. The position of the nuclei is described by N vectors or $3N$ coordinates. The global translation of the molecule is described by the three coordinates (X_G, Y_G, Z_G) of the center of mass G of the molecule. In the center of mass frame, or space-fixed frame $\{G, e_{x^{SF}}, e_{y^{SF}}, e_{z^{SF}}\}$, the configuration of the nuclei is described by $N - 1$ vectors or $3N - 3$ coordinates. The KEO T as a function of the mass-weighted cartesian coordinates of the nuclei $(x_1, \ldots, x_i, \ldots, x_{3N-3})$, obtained by multiplying the standard cartesian coordinates by $\sqrt{m_i}$, where m_i is the mass of the ith nucleus, simply reads

$$T = -\frac{1}{2} \sum_{i=1}^{3N-3} \frac{\partial^2}{\partial x_i^2}. \qquad (4.1)$$

The general expression of the KEO in terms of generalized coordinates $(q_1, \ldots, q_i, \ldots, q_{3N-3})$, which can be of any kind, has been derived by Podolsky [7]

$$T = -\frac{1}{2} \sum_{i,j}^{3N-3} \mathcal{J}^{-1} \frac{\partial}{\partial q_i} \mathcal{J} g_{ij} \frac{\partial}{\partial q_j}. \tag{4.2}$$

In this equation $\mathcal{J} = |Det(\boldsymbol{J})|$ is the absolute value of the determinant of the Jacobian matrix $J_{ij} = \frac{\partial x_i}{\partial q_j}$ and $\boldsymbol{g}$ is the metric tensor of elements

$$g_{ij} = \sum_{\alpha=1}^{3N-3} \frac{\partial q_i}{\partial x_\alpha} \frac{\partial q_j}{\partial x_\alpha}. \tag{4.3}$$

The overall rotation of the molecule can be separated from its internal deformation motion by introducing a body-fixed (BF) frame $\{G, e_{x^{BF}}, e_{y^{BF}}, e_{z^{BF}}\}$, whose orientation with respect to the SF frame is determined by three Euler angles noted α, β and γ. The shape and size of the molecule is then described by $3N-6$ internal BF-coordinates. The KEO can be expressed as a function of the three BF-components $(J_{x^{BF}}, J_{y^{BF}}, J_{z^{BF}})$ of the total angular momentum $\boldsymbol{J}$ of the molecule, and of the momentum operators $P_j = -i \frac{\partial}{\partial q_j}$ with $j = 1, \ldots, 3N-6$

$$T = \sum_{i,j}^{3N-6} \frac{P_i G_{ij} P_j}{2} + \sum_{i}^{3N-6} \sum_{\alpha=x,y,z} \frac{P_i C_{i\alpha} J_\alpha + J_\alpha C_{\alpha i} P_i}{2} + \sum_{\alpha=x,y,z} \sum_{\beta=x,y,z} \frac{J_\alpha \Gamma_{\alpha\beta} J_\beta}{2} + V_{extra}. \tag{4.4}$$

Here, V_{extra} is a purely multiplicative operator called the extra potential term. The volume elements used to normalize the wavefunction reads $dV = \sin \beta d\alpha d\beta d\gamma \, dq_1 \ldots dq_{3N-6}$. This ensures that the momentum operators P_i are Hermitian. The matrices $\boldsymbol{G}$, $\boldsymbol{C}$ and $\boldsymbol{\Gamma}$, which stand for internal vibrations, Coriolis couplings and overall rotation, respectively, are, in general, functions of the internal coordinates.

The polyspherical approach provides, for a particular class of curvilinear coordinates, general expressions for the elements of the $\boldsymbol{G}$, $\boldsymbol{C}$ and $\boldsymbol{\Gamma}$ matrices, whatever the number of atoms and the set of $N-1$ vectors (Jacobi, Radau, valence, …) used to parametrize the system. In addition, the use of a specific definition for the BF frame ensures that the KEO has the so-called product form (see Sect. 4.2.2), i.e. it is expressed as a sum of products of operators acting on a single coordinate. This definition of the BF frame is as follows: the z^{BF} axis is parallel to one of the $N-1$ vectors used to parametrize the system and the (xz) BF half-plane, with $x > 0$ is parallel to another vector. A detailed presentation of the method can be found in Ref. [6].

4.1.2 The Discrete Variable Representation

In order to solve the nuclear Schrödinger equation, a suitable representation of the wavefunction and of the operators is needed. In this section, the variational

basis representation (VBR), the finite-basis representation (FBR) and the discrete variable representation (DVR) are introduced. For convenience, a one-dimensional system, described by the Hamiltonian operator $H(x) = T(x) + V(x)$, is considered. This operator acts in a Hilbert space $\mathcal{H}$ of infinite dimension. In practice, the Schrödinger equation is solved numerically, and a finite basis of dimension N $\{|\phi_n\rangle, n = 1, \ldots, N\}$ is used. The subspace of $\mathcal{H}$ spanned by this basis is noted $\mathcal{H}_N$. In the variational approach, the unknown solution of the Schrödinger equation is represented exactly in the finite basis. In this case, the eigenvalues of the Hamiltonian are larger than or equal to the exact eigenvalues. The representation in which the Hamiltonian matrix elements $H_{mn} = \langle \phi_m | H | \phi_n \rangle$ are evaluated exactly is called the variational basis representation (VBR). In the VBR, the errors are only due to the truncation of the basis. In most cases, the matrix elements of the KEO $T_{mn} = \langle \phi_m | T | \phi_n \rangle$ are known analytically. In contrast, because the potential operator is, in general, a complicated function of the coordinate operator, its matrix elements $V_{mn} = \langle \phi_m | V | \phi_n \rangle$ are not known analytically. In addition, an accurate evaluation of these matrix elements by numerical integration is too much time consuming to be practical in most situations.

The idea behind the DVR method [8–11] is to use a representation in terms of localized functions obtained by transformation from a "global" basis [12]. Usually, bases constructed from orthogonal polynomials, noted $F_n(x)$, which are solution of one dimensional problems such as the particle in a box (Chebyshev polynomials) or the harmonic oscillator (Hermite polynomials), are used. These polynomial bases verify the general relationship

$$\int_{x=a}^{x=b} F_m(x) F_n(x) \omega(x) dx = \delta_{mn},\tag{4.5}$$

where $\omega(x)$ is a specific weight function. Choosing $\chi_n(x) = \sqrt{\omega(x)} F_n(x)$, one obtains an orthonormal basis. Standard DVRs are related to their corresponding "global representation" through Gaussian quadratures [13]. A set of N points $\{x_\alpha\}$ and of N complex constants (weights) $\{\omega_\alpha\}$ defines a quadrature relation in $\mathcal{H}_N$ if

$$\int_a^b \Phi^*(x) \Psi(x) dx = \sum_{\alpha=1}^{N} |\omega_\alpha|^2 \, \Phi^*(x_\alpha) \Psi(x_\alpha),\tag{4.6}$$

where Φ and Ψ are elements of $\mathcal{H}_N$. The overlap integrals and coordinate operator matrix elements are then given exactly by

$$\sum_{\alpha=1}^{N} |\omega_\alpha|^2 \, \chi_m^*(x_\alpha) \chi_n(x_\alpha) = \langle \chi_m | \chi_n \rangle = \delta_{mn},\tag{4.7}$$

$$\sum_{\alpha=1}^{N} |\omega_\alpha|^2 \, \chi_m^*(x_\alpha) x_\alpha \chi_n(x_\alpha) = \langle \chi_m | x | \chi_n \rangle = X_{mn},\tag{4.8}$$

for $m, n \leq N - 1$. These two relations can be recast in matrix form as

$$U^\dagger U = I \qquad (4.9)$$

and

$$U^\dagger X^D U = X, \qquad (4.10)$$

where I is the identity matrix of dimension N, X is the matrix of the coordinate operator, X^D is the diagonal matrix of the grid points $X^D_{\alpha\beta} = x_\alpha \delta_{\alpha\beta}$ and the elements of U read

$$U_{\alpha m} = \omega_\alpha \chi_m(x_\alpha). \qquad (4.11)$$

Equation (4.9) demonstrates that U is a unitary matrix. Therefore, by multiplying Eq. (4.10) by U from the left and by $U^\dagger$ from the right, one obtains that $U^\dagger$ diagonalizes the matrix of the coordinate operator X

$$U X U^\dagger = X^D. \qquad (4.12)$$

In the DVR, the Hamiltonian operator and the wavefunction are represented in the basis $\{|\xi_\alpha\rangle, \alpha = 1, \ldots, N\}$ of the eigenfunctions of the coordinate operator $x|\xi_\alpha\rangle = x_\alpha|\xi_\alpha\rangle$. This basis is related to the "global" basis $\{|\chi_n\rangle, n = 1, \ldots, N\}$ through the transformation matrix U

$$\xi_\alpha(x) = \sum_{m=1}^{N} U^*_{\alpha m} \chi_m(x). \qquad (4.13)$$

The function $\xi_\alpha(x)$ is localized around the DVR grid point x_α and is exactly zero at all the other grid points. This is seen by evaluating Eq. (4.13) at a DVR grid point x_β

$$\begin{aligned}
\xi_\alpha(x_\beta) &= \sum_{m=1}^{N} U^*_{\alpha m} \chi_m(x_\beta) \\
&= \sum_{m=1}^{N} \frac{1}{\omega_\beta} U^*_{\alpha m} U_{\beta m} \\
&= \frac{1}{\omega_\beta} \left(U U^\dagger \right)_{\alpha\beta} \\
&= \frac{\delta_{\alpha\beta}}{\omega_\beta}.
\end{aligned} \qquad (4.14)$$

An element $|\Psi\rangle$ of $\mathcal{H}_N$ can be expanded in the "global" basis $\{|\chi_n\rangle, n = 1, \ldots, N\}$ as

$$|\Psi\rangle = \sum_{m=1}^{N} \langle \chi_m|\Psi\rangle |\chi_m\rangle. \qquad (4.15)$$

Using Eqs. (4.11) and (4.13) the projection of $|\Psi\rangle$ on an element of the localized basis $\{|\xi_\alpha\rangle, \alpha = 1, \ldots, N\}$ can be expressed as

$$
\langle \xi_\alpha | \Psi \rangle = \sum_{m=1}^{N} \omega_\alpha \chi_m(x_\alpha) \langle \chi_m | \Psi \rangle
$$
$$
= \omega_\alpha \Psi(x_\alpha). \tag{4.16}
$$

As seen in this last equation, in the DVR, the wavefunction is represented by its values at the grid points x_α. The matrix elements of the KEO in the DVR are exactly given by

$$
T_{\alpha\beta}^{\text{DVR}} = \langle \xi_\alpha | T | \xi_\beta \rangle = \sum_{m,n=1}^{N} U_{\alpha m} \langle \chi_m | T | \chi_n \rangle U_{n\beta}^{\dagger}. \tag{4.17}
$$

The most attractive feature of the DVR is that the matrix of an operator that is a function of the coordinate operator, such as the potential operator, is approximately diagonal in general

$$
V_{\alpha\beta}^{\text{DVR}} = \langle \xi_\alpha | V | \xi_\beta \rangle \approx V(x_\alpha) \delta_{\alpha\beta}. \tag{4.18}
$$

This last equation would hold exactly for an infinite local basis, as in this case, the DVR would be equivalent to the continuous coordinate representation. We stress here that, because the local basis $\{|\xi_\alpha\rangle, \alpha = 1, \ldots, N\}$ and the "global" basis $\{|\chi_n\rangle, n = 1, \ldots, N\}$ are related by a unitary transformation, the operators obtained in the "global" basis contain the same approximation. Therefore, to distinguish it from the VBR, the representation in terms of the "global" basis $\{|\chi_n\rangle, n = 1, \ldots, N\}$ is called finite basis representation (FBR).

4.2   The Solution of the Nuclear Time-Dependent Schrödinger Equation

4.2.1   The Standard Method

In the standard method for the solution of the nuclear time-dependent Schrödinger equation (TDSE), the wavefunction is expanded in a basis of time-independent functions called a primitive basis. Specifically, considering a molecule with f degrees of freedom (dofs), a basis of N_κ one-dimensional functions $\chi_{j_\kappa}^{(\kappa)}(q_\kappa)$ with $\kappa = 1, \ldots, f$ can be defined for each dof and the total nuclear wavefunction is expanded in the product basis composed of Hartree products of these one-dimensional functions

$$
\Psi(q_1, \ldots q_f, t) = \sum_{j_1}^{N_1} \cdots \sum_{j_f}^{N_f} C_{j_1, \ldots, j_f}(t) \prod_{\kappa=1}^{f} \chi_{j_\kappa}^{(\kappa)}(q_\kappa), \tag{4.19}
$$

where q_κ is the nuclear coordinate for the κth mode and the $C_{j_1,\ldots,j_f}(t)$ are the time-dependent expansion coefficients. The Dirac-Frenkel time-dependent variational principle

$$\langle \delta\Psi | H - i\frac{\partial}{\partial t} | \Psi \rangle = 0 \tag{4.20}$$

can be used to derive the equation of motion for the coefficients, leading to

$$i\dot{C}_J = \sum_L H_{JL} C_L, \tag{4.21}$$

where J denotes a collective index $J = j_1\ldots j_f$ and H_{JL} is an element of the matrix representation of the Hamiltonian in the primitive basis. A number of methods exist for the integration of such systems of linear differential equations, including, for instance, the split-operator method [14–16], the Chebyshev method [17] or the short-iterative Lanczos method [18] (see also Refs. [19–21] for reviews and [22–25] for recent applications in atom-molecule, molecule-molecule and molecule-surface reactive scattering). However, because the number of configurations $\Phi_J(q_1,\ldots,q_f) = \prod_{\kappa=1}^{f} \chi_{j_\kappa}^{(\kappa)}(q_\kappa)$ grows exponentially with the number of dofs, the standard method is generally applicable to systems with less than ten dofs.

4.2.2 The Multi-configuration Time-Dependent Hartree Method

In order to treat larger systems in a quantum dynamical framework, one needs a more compact basis in which the time-dependent wavepacket can be expanded. A possibility is to consider a basis of time-dependent functions. Indeed, while in most situations of interest the wavepacket explores large portions of the PES during a propagation, at a given time, the wavepacket often has a simple and localized structure. It is thus natural to try to define a time-dependent basis set optimized to correctly describe the wavepacket at any given time during the propagation. This is the basic idea behind the multi-configuration time-dependent Hartree method [26–32]. More precisely, the MCTDH ansatz reads

$$\Psi(q_1,\ldots q_f, t) = \sum_{j_1}^{n_1} \cdots \sum_{j_p}^{n_p} C_{j_1,\ldots,j_p}(t) \prod_{\kappa=1}^{p} \varphi_{j_\kappa}^{(\kappa)}(Q_\kappa, t)$$

$$= \sum_J C_J(t) \Phi(Q_1,\ldots Q_p, t). \tag{4.22}$$

where the $\varphi_{j_\kappa}^{(\kappa)}(Q_\kappa, t)$ are time-dependent basis functions called single-particle functions (SPFs) and the $\Phi(Q_1,\ldots Q_p, t)$ are Hartree products of SPFs called

configurations. The coordinates Q_κ for each set of n_κ SPFs are composite coordinates of one or more system coordinates

$$Q_\kappa = (q_{1,\kappa}, \ldots, q_{d,\kappa}). \tag{4.23}$$

The SPFs $\varphi_{j_\kappa}^{(\kappa)}(Q_\kappa, t)$ are d-dimensional functions, i.e d system coordinates have been combined and treated as one "particle". Overall, in Eq. (4.22), the f system coordinates have been combined to form p "particles". The SPFs are expressed as linear combinations of Hartree products of primitive, time-independent, basis functions

$$\varphi_{j_\kappa}^{(\kappa)}(Q_\kappa, t) = \sum_{l_1}^{N_{1,\kappa}} \cdots \sum_{l_d}^{N_{d,\kappa}} c_{j_\kappa, l_1 \ldots l_d}(t) \chi_{l_1}^{(\kappa)}(q_{1,\kappa}) \ldots \chi_{l_d}^{(\kappa)}(q_{d,\kappa}). \tag{4.24}$$

The MCTDH ansatz Eq. (4.22) is not unique. Applying linear transformations among the SPFs

$$\tilde{\varphi}_{j_\kappa}^{(\kappa)} = \sum_{l_\kappa}^{n_\kappa} U_{j_\kappa l_\kappa}^{(\kappa)} \varphi_{l_\kappa}^{(\kappa)} \tag{4.25}$$

and the inverse transformations to the coefficients

$$\tilde{C}_{j_1, \ldots, j_f} = \sum_{l_1}^{n_1} \cdots \sum_{l_f}^{n_f} (U^{(1)})_{l_1 j_1}^{-1} \ldots (U^{(f)})_{l_f j_f}^{-1} C_{l_1, \ldots, l_f}, \tag{4.26}$$

one obtains

$$\Psi(q_1, \ldots q_f, t) = \sum_{j_1}^{n_1} \cdots \sum_{j_f}^{n_f} \tilde{C}_{j_1, \ldots, j_f} \prod_{\kappa}^{f} \tilde{\varphi}_{j_\kappa}^{(\kappa)}(Q_\kappa, t). \tag{4.27}$$

In order to ensure the uniqueness of the MCTDH equations of motion, constraints are introduced on the SPFs

$$i \langle \varphi_i^{(\kappa)} | \dot{\varphi}_j^{(\kappa)} \rangle = \langle \varphi_i^{(\kappa)} | g^{(\kappa)} | \varphi_j^{(\kappa)} \rangle = g_{ij}^{(\kappa)}. \tag{4.28}$$

From this last equation, it follows that if the constraint operator $g^{(\kappa)}$, acting on the κth particle, are chosen to be Hermitian, then a set of orthonormal SPF will remain orthonormal at all time

$$\begin{aligned}
\frac{\partial}{\partial t} \langle \varphi_i^{(\kappa)} | \varphi_j^{(\kappa)} \rangle &= \langle \dot{\varphi}_i^{(\kappa)} | \varphi_j^{(\kappa)} \rangle + \langle \varphi_i^{(\kappa)} | \dot{\varphi}_j^{(\kappa)} \rangle \\
&= -i(g_{ij}^{(\kappa)} - g_{ji}^{(\kappa)*}) = -i(\mathbf{g}^{(\kappa)} - \mathbf{g}^{(\kappa)\dagger})_{ij}.
\end{aligned} \tag{4.29}$$

Assuming the simplest choice for the constraints, i.e $g^{(\kappa)} = 0$, the MCTDH equations of motion can be derived by inserting the MCTDH ansatz of Eq. (4.22) into the Dirac-Frenkel time-dependent variational principle of Eq. (4.20). Other choices are possible for the constraints, see Ref. [28] for details. We first introduce the projector $P^{(\kappa)}$ on the space spanned by the SPFs of the κth particle

$$P^{(\kappa)} = \sum_{j=1}^{n_\kappa} |\varphi_j^{(\kappa)}\rangle \langle \varphi_j^{(\kappa)}| \tag{4.30}$$

and the single-hole functions $\Psi_l^{(\kappa)}$, defined as the wavefunction associated with the jth SPF of the κth particle

$$\begin{aligned}
\Psi_l^{(\kappa)} &= \langle \varphi_l^{(\kappa)}|\Psi\rangle \\
&= \sum_{j_1} \cdots \sum_{j_{\kappa-1}} \sum_{j_{\kappa+1}} \cdots \sum_{j_p} C_{j_1 \ldots j_{\kappa-1} l j_{\kappa+1} \ldots j_p} \varphi_{j_1}^{(1)} \cdots \varphi_{j_{\kappa-1}}^{(\kappa-1)} \varphi_{j_{\kappa+1}}^{(\kappa+1)} \cdots \varphi_{j_p}^{(p)} \\
&= \sum_{J^\kappa} C_{J_l^\kappa} \Phi_{J^\kappa}, \tag{4.31}
\end{aligned}$$

where the new composite index J^κ and J_l^κ and the single-hole configurations Φ_{J^κ} have been introduced. Using the single-hole functions, one can define the mean-field matrices

$$\mathcal{H}_{ij}^{(\kappa)} = \langle \Psi_i^{(\kappa)}|H|\Psi_j^{(\kappa)}\rangle \tag{4.32}$$

and the density matrices

$$\rho_{ij}^{(\kappa)} = \langle \Psi_i^{(\kappa)}|\Psi_j^{(\kappa)}\rangle = \sum_{J^\kappa} C_{J_i^\kappa}^* C_{J_j^\kappa}. \tag{4.33}$$

Using these definitions, the MCTDH equations can be written in matrix form

$$i\dot{C} = \mathcal{K}C \tag{4.34}$$

$$i\dot{\varphi}^{(\kappa)} = (1 - P^{(\kappa)})(\rho^{(\kappa)})^{-1}\mathcal{H}^{(\kappa)}\varphi^{(\kappa)}. \tag{4.35}$$

In these last two equations C is the vector of the coefficients and $\mathcal{K}$ is the matrix representation of the Hamiltonian in the basis of the configurations

$$\mathcal{K}_{JL} = \langle \Phi_J|H|\Phi_L\rangle. \tag{4.36}$$

Equations (4.34) and (4.35) constitute a set of non-linear coupled differential equations which is more complicated than the linear set of equations of the standard method given by Eq. (4.21). However, the ability of the MCTDH method to treat larger systems than the standard method lies in the compactness of the SPF basis.

The dimension of the SPF basis $n_1 \times \cdots \times n_p$ is much smaller than that of the primitive basis $N_1 \times \cdots \times N_f$ because $p \leq f$ and, in general, the n_κ required to achieve convergence are rather small, thanks to the variational nature of the method.

An attractive feature of the MCTDH method is that by varying the number of SPF basis functions involved in the calculations, one can simply control the degree of accuracy of the method. In addition, the natural populations, obtained as the eigenvalues of the density matrices $\rho^{(\kappa)}$, provide a measure of the accuracy of the calculation. A calculation is well converged with respect to the size of the SPF basis if, for each particle κ, the smallest natural population is small.

Provided the Hamiltonian operator can be written in a suitable form and an efficient integration scheme is used to solve the equations of motion (see Sects. 4.2.3 and 4.2.4), the MCTDH method allows one to perform accurate quantum dynamics calculations for realistic molecular systems with more than twenty degrees of freedom [33–45], and on simple model systems with up to roughly eighty degrees of freedom [46–48].

An extension of the MCTDH method, called multi-layer MCTDH [49–51], developed by Haobin Wang and Michael Thoss, allows one to treat even larger and more complex systems.

4.2.3 Product Form of the Hamiltonian Operator

The solution of the MCTDH equations of motion requires the evaluation of the Hamiltonian and mean-field matrix elements. A Hamiltonian matrix element $\mathcal{K}_{IJ} = \langle \Phi_I | H | \Phi_J \rangle$ involves integrals of the form $\langle \varphi_{i_1}^{(1)} \ldots \varphi_{i_p}^{(p)} | H | \varphi_{j_1}^{(1)} \ldots \varphi_{j_p}^{(p)} \rangle$. In general, these integrals are p-dimensional and need to be evaluated in the full primitive basis, which is precisely what needs to be avoided to break the unfavorable scaling of the standard method with respect to the size of the system. The direct evaluation of these multi-dimensional integrals can be avoided if the Hamiltonian is written in a so-called product form, *i.e* as a sum of products of operators acting on a single particle only

$$H(q_1, \ldots, q_f) = \sum_r c_r h_r^{(1)}(Q_1) \ldots h_r^{(p)}(Q_p). \tag{4.37}$$

In this case one obtains

$$\langle \varphi_{i_1}^{(1)} \ldots \varphi_{i_p}^{(p)} | H | \varphi_{j_1}^{(1)} \ldots \varphi_{j_p}^{(p)} \rangle = \sum_r c_r \langle \varphi_{i_1}^{(1)} | h_r^{(1)} | \varphi_{j_1}^{(1)} \rangle \cdots \langle \varphi_{i_p}^{(p)} | h_r^{(p)} | \varphi_{j_p}^{(p)} \rangle. \tag{4.38}$$

Here, a high dimensional integral is replaced by a sum of products of integrals of lower dimension that can be quickly evaluated.

In most cases, as mentioned in Sect. 4.1.1, the kinetic energy operator is naturally obtained in the required product form. This is, however, not the case for the potential energy operator. While many model potentials are of product form, ab initio potential energy surfaces, which are represented by a mathematical function of the nuclear coordinates adjusted to reproduce the electronic energy of the molecule at a set of calculated points, are generally not. It is therefore necessary, for an optimal performance of the MCTDH method, to bring the potential to product form. This can be done by using the *potfit* algorithm, implemented in the Heidelberg MCTDH package [32]. This method, described in Refs. [28, 30, 52, 53], allows one to bring to product form general potentials for systems with up to approximately six degrees of freedom, because the algorithm requires the full potential to be kept in memory. Recently, an extension of the potfit method, called multi-grid potfit [54] has been developed, allowing one to bring to product form potentials of systems with up to twelve degrees of freedom. Other strategies exist for even larger systems, such as the n-mode representation [55, 56], also called cut-HDMR [57, 58], which has been used, for instance, to bring to product form the 15D PES of the protonated water dimer or the 21D PES of malonaldehyde.

4.2.4 Integration of the Equations of Motion

An important aspect concerning the efficiency of the MCTDH method is the algorithm used to solve the equations of motion of Eqs. (4.34) and (4.35). In this section, two different integration schemes, the variable mean-field and constant mean-field schemes, are briefly presented.

4.2.4.1 The Variable Mean-Field Integration Scheme

The MCTDH equations of motion are a system of coupled non-linear first-order ordinary differential equations. The most straightforward way to solve these equations is to use an all-purpose integration algorithm such as the Adams-Bashforth-Moulton method or the Runge-Kutta method. This integration scheme is called the variable mean-field (VMF) scheme to distinguish it from the scheme presented in the next section. The VMF scheme is not optimal because the vector of the coefficients C and the SPFs contain components that are highly oscillatory in time. Therefore, small integration steps need to be used in order to accurately solve the MCTDH equations. In this case, the computation of the mean-field Eq. (4.32) and density matrices Eq. (4.33), at each time step of the propagation, dominates the computational effort. To avoid this problem, an integration scheme specifically tailored to the solution of the MCTDH equations of motion, the constant mean-field integration (CMF) scheme, has been developed.

4.2.4.2   The Constant Mean-Field Integration Scheme

The idea behind the CMF integration scheme [59] is to take advantage of the fact that the Hamiltonian matrix elements of Eq. (4.36) and the products of the inverse density and mean-field matrices $(\rho^{(\kappa)})^{-1}\mathcal{H}^{(\kappa)}$ appearing in Eq. (4.35), generally change much slower than the coefficients and SPFs. It is therefore possible to use larger time-steps for the evaluation of the former quantities than for the latter. More precisely, starting from an initial set of coefficients and SPFs, the Hamiltonian, mean-field and density matrices are constructed. With these matrices kept constant, the wavefunction is propagated for a given time τ. The resulting coefficients and SPFs are then used to compute new Hamiltonian, mean-field and density matrices. The CMF equations of motion, using the simple constraint operators $g^{(\kappa)} = 0$, read

$$i\dot{C} = \bar{\mathcal{K}}C \tag{4.39}$$

$$
\begin{aligned}
i\dot{\varphi}^{(1)} &= (1 - P^{(1)})(\bar{\rho}^{(1)})^{-1}\bar{\mathcal{H}}^{(1)}\varphi^{(1)} \\
&\qquad\vdots \\
i\dot{\varphi}^{(p)} &= (1 - P^{(p)})(\bar{\rho}^{(p)})^{-1}\bar{\mathcal{H}}^{(p)}\varphi^{(p)}.
\end{aligned} \tag{4.40}
$$

In these equation, the bar indicates that the corresponding matrix is held constant during the CMF integration step $t_m \leq t \leq t_{m+1}$, where $t_m = t_0 + m\tau$, m is the number of CMF steps made so far and t_0 is the initial time.

Supposing that a large update step τ can be used, the CMF scheme has several advantages. First, as explained above, it requires much less frequent computations of the Hamiltonian, mean-field and density matrices. In addition, the structure of the system of differential equations is simplified. The CMF scheme splits the MCTDH system of coupled differential equations into $p + 1$ sets of equations uncoupled from each other. In addition, the coefficients are now obtained from a set of linear differential equations of the same form than the equations of motions in the standard method given in Eq. (4.21) in Sect. 4.2.1. Therefore, integrators specifically designed for the time-dependent Schrödinger equation such as, for instance, the Short-iterative Lanczos integrator, can be used to propagate the coefficients. The set of equations for the SPFs, however, is still non-linear due to the projection operator $P^{(\kappa)}$.

It is important to note that the scheme presented above is only a simplified version of the actual CMF scheme implemented in the Heidelberg MCTDH package. In this form, the method defines a first-order integrator which would perform quite poorly. Therefore it has to be replaced by a more subtle, second-order CMF scheme, described in details in Refs. [28, 59].

4.2.5 The MCTDH Equations of Motion for Several Electronic States

In the previous sections, the Born-Oppenheimer approximation was assumed, i.e. nuclear motion on a single PES was considered. However, in many situations, the dynamics of the nuclei need to be treated on several PESs corresponding to coupled electronic state. The coupling between the electronic states can be due to the presence of an external electric field or to internal vibronic interactions. There exists two different ways of treating several coupled electronic states with the MCTDH method [60], the single-set formulation and the multi-set formulation.

In the single-set formulation, the electronic manifold is treated as one extra degree of freedom, noted κ_e. The Q_{κ_e} coordinate then labels the electronic states, taking only discrete values $Q_{\kappa_e} = 1, 2, \ldots, \sigma$, where σ is the number of electronic states. The number of SPFs for the electronic degree of freedom is set to the number of states $n_{\kappa_e} = \sigma$. In this formulation, the MCTDH equations of motions Eqs. (4.34) and (4.35) are unchanged. This formulation is called single-set formulation because a single set of SPF is used to treat the dynamics in all the electronic states.

In the multi-set formulation, in contrast, a different set of SPF is used for each electronic state. The wavefunction and the Hamiltonian is expanded in the set of electronic states $\{|\alpha\rangle, \alpha = 1, \ldots, \sigma\}$

$$|\Psi(t)\rangle = \sum_{\alpha=1}^{\sigma} \Psi(t)^{(\alpha)} |\alpha\rangle \tag{4.41}$$

where $\Psi(t)^{(\alpha)}$ has the MCTDH form of Eq. (4.22) and

$$H = \sum_{\alpha,\beta=1}^{\sigma} |\alpha\rangle H_{\alpha\beta} \langle\beta|. \tag{4.42}$$

Using again the simplest choice for the constraint operators $g^{(\alpha,\kappa)} = 0$, the equations of motion read

$$i\dot{C}_J^{(\alpha)} = \sum_{\beta=1}^{\sigma} \sum_L \langle \Phi_J^{(\alpha)} | H_{\alpha\beta} | \Phi_L^{(\beta)} \rangle C_L^{(\beta)} \tag{4.43}$$

$$i\dot{\varphi}^{(\alpha,\kappa)} = (1 - P^{(\alpha,\kappa)})(\rho^{(\alpha,\kappa)})^{-1} \sum_{\beta=1}^{\sigma} \mathcal{H}_{\alpha\beta}^{(\kappa)} \varphi^{(\beta,\kappa)}. \tag{4.44}$$

These last equations show that the MCTDH method is capable of treating the nuclear dynamics of molecular systems on several coupled electronic states. This formalism has been used, in combination with the vibronic coupling model of Köppel et al.

[61, 62], introduced more than three decades ago, and briefly presented in the next section, to study the UV absorption and photoelectron spectra of a number of molecular systems.

4.3   The Vibronic Coupling Model

The MCTDH method presented above is capable of treating high-dimensional systems and has opened new possibilities in the quantum dynamical description of midsize molecular systems. However such studies require a mathematical representation of the underlying PESs in the product form. When molecular systems exhibiting strong vibronic interactions are considered, one needs, in addition, to bring these PESs and their couplings to a quasiadiabatic representation. In general, obtaining global and accurate diabatic potentials is an extremely difficult task. However, in a number of situations, only local information on the topography of the PESs is required. This is the case when one is interested in the simulation of low-resolution absorption or photoelectron spectra, or in the simulation of ultrafast non-radiative decay processes through conical intersections that lie close to the Franck-Condon region. In the later case, the dynamics of the nuclei only implies low amplitude motions, which can be described using normal coordinates. In this case, simple model Hamiltonians can be constructed and used in quantum dynamics simulations. The vibronic coupling model of Köppel et al. [61, 62], is a well known example. In this model, the diabatic Hamiltonian for several coupled electronic states is written as the sum of a reference Hamiltonian $H_0(Q)$ and a potential energy matrix $W(Q)$, *i.e* $H(Q) = H_0(Q) + W(Q)$. The Hamiltonian is conveniently expressed in terms of dimensionless normal coordinates [62, 63], collected in the vector Q. The reference Hamiltonian $H_0(Q)$ is the ground electronic state Hamiltonian, usually expressed in the harmonic approximation

$$H_0(Q) = \sum_i \frac{\omega_i}{2} \left(-\frac{\partial^2}{\partial Q_i^2} + Q_i^2 \right) I, \qquad (4.45)$$

where the ω_i are the harmonic vibrational frequencies and I is the $n \times n$ identity matrix, n being the number of electronic states included in the model. The $W(Q)$ matrix expresses the changes in the excited state potential energy with respect to the ground state as a Taylor expansion around a reference geometry, usually chosen as the ground state equilibrium geometry, at which the diabatic and adiabatic representations are identical

$$\begin{aligned} W_{nn}(Q) &= E_n + \sum_i \kappa_i^{(n)} Q_i + \sum_{i,j} \gamma_{ij}^{(n)} Q_i Q_j + \cdots \\ W_{nn'}(Q) &= \sum_i \lambda_i^{(nn')} Q_i + \sum_{i,j} \mu_{ij}^{(nn')} Q_i Q_j + \cdots, \end{aligned} \qquad (4.46)$$

where $n \neq n'$, the E_n are the vertical excitation energies, $\kappa_i^{(n)}$ and $\gamma_{ij}^{(n)}$ are respectively the linear and quadratic intrastate coupling constants for the nth electronic state and $\lambda_i^{(nn')}$ and $\mu_{ij}^{(nn')}$ are respectively the linear and quadratic interstate coupling constants between the nth and n'th electronic states.

The vibronic coupling model has been extensively used to study the spectroscopy and the dynamics of vibronically coupled systems for more than three decades. The order at which the expansion of Eq. (4.46) can be truncated depends on the nature of the system and the level of accuracy that is sought. However, in many cases, it was found that retaining only the linear terms is sufficient to obtain a satisfying description of low-resolution spectra and of the short-time dynamics of the system. In this case, the model is called linear vibronic coupling model. In the case of highly symmetric molecules, many coupling constants vanish by symmetry. The non-vanishing terms fulfill the following condition:

$$\Gamma_n \otimes \Gamma_Q \otimes \Gamma_{n'} \supset \Gamma_A \tag{4.47}$$

where Γ_n and $\Gamma_{n'}$ refer to the electronic state symmetry, Γ_Q to the normal mode symmetry and Γ_A is the totally symmetric irreducible representation of the symmetry point group of the molecule. It follows immediately that only the totally symmetric modes lead to non-vanishing linear intrastate coupling constants. Similarly, only the modes of symmetry $\Gamma_n \otimes \Gamma_{n'}$ lead to non-vanishing linear interstate coupling constants. The linear intrastate coupling constants $\kappa_i^{(n)}$ are obtained as the derivative of the energy of the nth adiabatic electronic state with respect to Q_i at the ground state equilibrium geometry

$$\kappa_i^{(n)} = \left. \frac{\partial V_n(\boldsymbol{Q})}{\partial Q_i} \right|_{Q=0}. \tag{4.48}$$

The linear interstate coupling constants $\lambda_i^{(nn')}$ read

$$\lambda_i^{(nn')} = \left. \frac{\partial W_{nn'}(\boldsymbol{Q})}{\partial Q_i} \right|_{Q=0}. \tag{4.49}$$

To obtain an expression of the $\lambda_i^{(nn')}$ coupling constant as a function of the adiabatic potential energies, one first writes the diabatic potential energy matrix along the coordinate Q_i

$$W(Q_i) = \frac{\omega_i}{2} Q_i^2 \boldsymbol{I} + \begin{pmatrix} E_n & \lambda_i^{(nn')} Q_i \\ \lambda_i^{(nn')} Q_i & E_{n'} \end{pmatrix}, \tag{4.50}$$

where $\boldsymbol{I}$ denotes the identity matrix. The eigenvalues of this matrix give the adiabatic potential energy along the Q_i coordinate. The difference $V_{n'}(Q_i) - V_n(Q_i)$ reads

$$V_{n'}(Q_i) - V_n(Q_i) = \sqrt{(E_n - E_{n'})^2 + 4(\lambda_i^{(nn')} Q_i)^2}. \tag{4.51}$$

From this last two equations, the $\lambda_i^{(nn')}$ coupling constant can be written as

$$\lambda_i^{(nn')} = \sqrt{\frac{1}{8}\frac{\partial^2(V_{n'}(Q_i) - V_n(Q_i))^2}{\partial Q_i^2}\bigg|_{Q=0}}. \tag{4.52}$$

The accuracy of the linear vibronic coupling model can be improved by adding diagonal quadratic terms $\gamma_i^{(n)}Q_i^2$ for the non totally-symmetric modes for which the diagonal linear terms vanish [63]. In this case, the $\gamma_i^{(n)}$ constants can be conveniently obtained, together with the $\lambda_i^{(nn')}$ constants, by a least square fit to the ab initio computed adiabatic energies. In this case, one may write

$$W(Q_i) = \frac{\omega_i}{2}Q_i^2 I + \begin{pmatrix} E_n + \gamma_i^{(n)}Q_i^2 & \lambda_i^{(nn')}Q_i \\ \lambda_i^{(nn')}Q_i & E_{n'} + \gamma_i^{(n')}Q_i^2 \end{pmatrix}. \tag{4.53}$$

The corresponding adiabatic potentials read

$$\begin{aligned}
V_n(Q_i) &= \frac{1}{2}\left((\omega_i + \gamma_i^{(n)} + \gamma_i^{(n')})Q_i^2 + E_n + E_{n'}\right) \\
&\quad - \sqrt{(E_{n'} - E_n + (\gamma_i^{(n')} - \gamma_i^{(n)})Q_i^2)^2 + 4\lambda_i^2 Q_i^2} \\
V_{n'}(Q_i) &= \frac{1}{2}\left((\omega_i + \gamma_i^{(n)} + \gamma_i^{(n')})Q_i^2 + E_n + E_{n'}\right) \\
&\quad + \sqrt{(E_{n'} - E_n + (\gamma_i^{(n')} - \gamma_i^{(n)})Q_i^2)^2 + 4\lambda_i^2 Q_i^2}.
\end{aligned} \tag{4.54}$$

The vibronic coupling model Hamiltonian is well suited for a combination with the MCTDH method as it has the required product form (see Sect. 4.2.3). Usually, molecular systems affected by strong vibronic couplings have complicated spectra with very dense bands. Therefore, a detailed analysis of the spectrum in terms of individual vibronic states is in general impossible and one is more interested in the overall electronic band profiles. In this case, the use of a time-dependent framework can be advantageous since the absorption profile can be obtained from the time-dependent wavepacket propagated over relatively short times, as exposed below.

4.4 Calculation of Absorption Spectra

The absorption spectrum is a useful observable that can be simulated using either a time-independent or a time-dependent formalism. In the case of molecular systems exhibiting conical intersections, the strong vibronic couplings often have distinct signatures in the absorption spectrum. For instance, the presence of unexpected bands, or of bands with an unusually complicated and dense profile, is often observed.

Consider a molecular system described by the Hamiltonian operator H with the eigenelements $\{|\Phi_n\rangle, E_n\}$. The absorption profile is given by Fermi's golden rule

$$P(E) = 2\pi \sum_n |\langle\Phi_n|\mu|\Phi_i\rangle|^2 \delta(E - E_n), \qquad (4.55)$$

where μ is the dipole moment operator, and $|\Phi_i\rangle$ is the initial state of the system. The absorption spectrum of the system can be computed directly through Eq. (4.55) using a time-independent formalism, *i.e* via the solution of the time-independent Schrödinger equation

$$H|\Phi_n\rangle = E_n|\Phi_n\rangle. \qquad (4.56)$$

We note that a very efficient version of this method based on the Lanczos iterative eigensolver has been implemented for the specific case of vibronically coupled systems described by the vibronic coupling model Hamiltonian, allowing for the computation of absorption or photoelectron spectra for systems with bases containing up to 10^9 basis functions. This method is described in details in the Chap. 7 of Ref. [64].

In a number of cases, it can be advantageous to compute the absorption spectrum without any reference to the eigenstates of the system but rather using the time-dependent wavepacket computed through the solution of the time-dependent Schrödinger equation. Using the integral form of the Dirac delta function, Eq. (4.55) can be recast as

$$P(E) = \int_{-\infty}^{+\infty} \sum_n \langle\Phi_n|\mu|\Phi_i\rangle\langle\Phi_i|\mu^\dagger|\Phi_n\rangle e^{-iE_nt} e^{iEt} dt. \qquad (4.57)$$

The wavepacket at time t reads

$$|\Psi(t)\rangle = e^{-iHt}|\Psi(0)\rangle. \qquad (4.58)$$

The wavepacket at time $t = 0$ is obtained through the application of the dipole moment operator to the initial state $|\Psi(0)\rangle = \mu|\Phi_i\rangle$. Substituting into Eq. (4.58) yields

$$|\Psi(t)\rangle = e^{-iHt}\mu|\Phi_i\rangle. \qquad (4.59)$$

Inserting now the closure relation $I = \sum_n |\Phi_n\rangle\langle\Phi_n|$, one obtains

$$|\Psi(t)\rangle = \sum_n e^{-iE_nt}\langle\Phi_n|\mu|\Phi_i\rangle|\Phi_n\rangle. \qquad (4.60)$$

Substituting this last equation into Eq. (4.57) yields

$$P(E) = \int_{-\infty}^{+\infty} \langle \Psi(0) | \Psi(t) \rangle e^{iEt} dt. \tag{4.61}$$

This last equation shows that the absorption spectrum can be computed from the Fourier transform of the autocorrelation function $C(t) = \langle \Psi(0) | \Psi(t) \rangle$, which measures the time-dependent overlap of the evolving wavepacket with the initial wavepacket. Assuming an hemitian Hamiltonian operator, one may write

$$\begin{aligned} C(-t) &= \langle \Psi(0) | e^{iHt} | \Psi(0) \rangle \\ &= \langle \Psi(0) | (e^{-iHt})^{\dagger} | \Psi(0) \rangle \\ &= C(t)^{*}. \end{aligned} \tag{4.62}$$

Using this relation, the spectrum can be written as an integral over positive times only

$$P(E) = 2 \int_{0}^{+\infty} Re \left[C(t) e^{iEt} \right] dt. \tag{4.63}$$

To account for the homogeneous broadening of the experimental spectrum, the autocorrelation function can be pre-multiplied by a damping function $f(t) = e^{-t/\tau}$, where the damping time τ is a free parameter. This is equivalent to convoluting the spectrum by a Lorentzian function of full width at half maximum of $2/\tau$. In addition, to avoid problems arising from the finite propagation time T (the so-called "Gibbs phenomenon"), the autocorrelation function can be further pre-multiplied by a filter function $g_n(t) = \cos^n(\pi t/2T)\Theta(t - T)$, where $n = 1, 2, \ldots$ and Θ denotes the Heaviside step function.

References

1. F. Gatti, *Molecular Quantum Dynamics* (Springer, Heidelberg, 2014)
2. J.M. Bowman, T. Carrington, H.-D. Meyer, Mol. Phys. **106**, 2145 (2008)
3. D.J. Tannor, *Introduction to Quantum Mechanics, A Time-Dependent Perspective* (University Science Books, California, 2007)
4. D. Lauvergnat, A. Nauts, J. Chem. Phys. **116**, 8560 (2002)
5. A.G. Császár, C. Fábri, T. Szidarovszky, E. Mátyus, T. Furtenbacher, G. Czakó, Phys. Chem. Chem. Phys. **14**, 1085 (2012)
6. F. Gatti, C. Iung, Phys. Rep. **484**, 1 (2009)
7. G.B. Arfken, H.J. Weber, F.E. Harris, *Mathematical Methods for Physicists*, 7th edn. (Academic Press, Elsevier, New York, 2012)
8. J.V. Lill, G.A. Parker, J.C. Light, Chem. Phys. Lett. **89**, 483 (1982)
9. R.W. Heather, J.C. Light, J. Chem. Phys. **79**, 147 (1983)
10. J.C. Light, I.P. Hamilton, J.V. Lill, J. Chem. Phys. **82**, 1400 (1985)
11. J.V. Lill, G.A. Parker, J.C. Light, J. Chem. Phys. **85**, 900 (1986)
12. J.C. Light, T. Carrington, Adv. Chem. Phys. **114**, 263 (2000)

13. A.S. Dickinson, P.R. Certain, J. Chem. Phys. **49**, 4209 (1968)
14. M.D. Feit, J.A. Fleck Jr, A. Steiger, J. Comput. Phys. **47**, 412 (1982)
15. M.D. Feit, J.A. Fleck Jr, J. Chem. Phys. **78**, 301 (1983)
16. M.D. Feit, J.A. Fleck Jr, J. Chem. Phys. **80**, 2578 (1984)
17. H. Tal-Ezer, R. Kosloff, J. Chem. Phys. **81**, 3967 (1984)
18. T.J. Park, J.C. Light, J. Chem. Phys. **85**, 5870 (1986)
19. R. Kosloff, J. Phys. Chem. **92**, 2087 (1988)
20. C. Leforestier, R.H. Bisseling, C. Cerjan, M.D. Feit, R. Friesner, A. Guldberg, A. Hammerich, G. Jolicard, W. Karrlein, H.-D. Meyer, N. Lipkin, O. Roncero, R. Kosloff, J. Comput. Phys. **94**, 59 (1991)
21. R. Kosloff, Annu. Rev. Phys. Chem. **45**, 145 (1994)
22. H. Song, J. Li, M. Yang, Y. Lu, H. Guo, Phys. Chem. Chem. Phys. **16**, 17770 (2014)
23. R. Otto, J. Ma, A.W. Ray, J.S. Dalutz, J. Li, H. Guo, R.E. Continetti, Science **343**, 396 (2014)
24. Y. Wang, J. Li, H. Guo, M. Yang, Theor. Chem. Acc. **133**, 1555 (2014)
25. P.M. Hundt, B. Jiang, M. van Reijzen, H. Guo, R.D. Beck, Science **344**, 504 (2014)
26. H.-D. Meyer, U. Manthe, L.S. Cederbaum, Chem. Phys. Lett. **165**, 73 (1990)
27. U. Manthe, H.-D. Meyer, L.S. Cederbaum, J. Chem. Phys. **97**, 3199 (1992)
28. M.H. Beck, A. Jäckle, G.A. Worth, H.-D. Meyer, Phys. Rep. **324**, 1 (2000)
29. H.-D. Meyer, G.A. Worth, Theor. Chem. Acc. **109**, 251 (2003)
30. H.-D. Meyer, F. Gatti, G.A. Worth, *Multidimensional Quantum Dynamics: MCTDH Theory and Applications* (Wiley-VCH, Weinheim, 2009)
31. H.-D. Meyer, WIREs Comput. Mol. Sci. **2**, 351 (2012)
32. G.A. Worth, M.H. Beck, A. Jäckle, H.-D. Meyer, Computer Code, The MCTDH Package, Version 8.2, University of Heidelberg, Heidelberg, Germany, 2000; H.-D. Meyer, computer code, The MCTDH Package, Version 8.3 (2002), Version 8.4 (2007). [http://mctdh.uni-hd.de]
33. O. Vendrell, F. Gatti, H.-D. Meyer, Angew. Chem. Int. Ed. **46**, 6918 (2007)
34. O. Vendrell, F. Gatti, D. Lauvergnat, H.-D. Meyer, J. Chem. Phys. **127**, 184302 (2007)
35. O. Vendrell, F. Gatti, H.-D. Meyer, J. Chem. Phys. **127**, 184303 (2007)
36. O. Vendrell, H.-D. Meyer, Phys. Chem. Chem. Phys. **10**, 4692 (2008)
37. O. Vendrell, F. Gatti, H.-D. Meyer, Angew. Chem. Int. Ed. **48**, 352 (2009)
38. M.D. Coutinho-Neto, A. Viel, U. Manthe, J. Chem. Phys. **121**, 9207 (2004)
39. M. Schröder, F. Gatti, H.-D. Meyer, J. Chem. Phys. **134**, 234307 (2011)
40. T. Hammer, U. Manthe, J. Chem. Phys. **136**, 054105 (2012)
41. M. Schröder, H.-D. Meyer, J. Chem. Phys. **141**, 034116 (2014)
42. G.A. Worth, H.-D. Meyer, L.S. Cederbaum, J. Chem. Phys. **105**, 4412 (1996)
43. G.A. Worth, H.-D. Meyer, L.S. Cederbaum, J. Chem. Phys. **109**, 3518 (1998)
44. G.A. Worth, H.-D. Meyer, L.S. Cederbaum, Chem. Phys. Lett. **299**, 451 (1999)
45. A. Raab, G.A. Worth, H.-D. Meyer, L.S. Cederbaum, J. Chem. Phys. **110**, 936 (1999)
46. H. Wang, J. Chem. Phys. **113**, 9948 (2000)
47. M. Nest, H.-D. Meyer, J. Chem. Phys. **117**, 10499 (2002)
48. M. Nest, H.-D. Meyer, J. Chem. Phys. **119**, 24 (2003)
49. H. Wang, M. Thoss, J. Chem. Phys. **119**, 1289 (2003)
50. U. Manthe, J. Chem. Phys. **128**, 164116 (2008)
51. O. Vendrell, H.-D. Meyer, J. Chem. Phys. **134**, 044135 (2011)
52. A. Jäckle, H.-D. Meyer, J. Chem. Phys. **104**, 7974 (1996)
53. A. Jäckle, H.-D. Meyer, J. Chem. Phys. **109**, 3772 (1998)
54. D. Peláez, H.-D. Meyer, J. Chem. Phys. **138**, 014108 (2013)
55. J.M. Bowman, S. Carter, X. Huang, Int. Rev. Phys. Chem. **22**, 533 (2003)
56. A. Chakraborty, D.G. Truhlar, J.M. Bowman, S. Carter, J. Chem. Phys. **121**, 2071 (2004)
57. H. Rabitz, O.F. Alis, J. Math. Chem. **25**, 197 (1999)
58. O.F. Alis, H. Rabitz, J. Math. Chem. **29**, 127 (2001)
59. M.H. Beck, H.-D. Meyer, Z. Phys. D **42**, 113 (1997)
60. G.A. Worth, H.-D. Meyer, H. Köppel, L.S. Cederbaum, I. Burghardt, Int. Rev. Phys. Chem. **27**, 569 (2008)

61. H. Köppel, W. Domcke, L.S. Cederbaum, Mol. Phys. **43**, 851 (1981)
62. H. Köppel, W. Domcke, L.S. Cederbaum, Adv. Chem. Phys. **54**, 59 (1984)
63. C. Woywod, W. Domcke, A.L. Sobolewski, H.-J. Werner, J. Chem. Phys. **100**, 1400 (1994)
64. W. Domcke, D.R. Yarkony, H. Köppel, *Conical Intersections, Electronic Strucutre, Dynamics and Spectroscopy* (World Scientific, New Jersey, 2004)

Chapter 5
The Role of the Low-Lying $n\pi^*$ States on the Photophysics of Pyrazine

This chapter is partly based on results and discussions published in Ref. [1] by the PCCP Owner Societies.

5.1 Introduction

In this chapter, the theoretical tools introduced in Chaps. 2 and 4 are applied to the study of the non-adiabatic relaxation dynamics of pyrazine after ultraviolet (UV) excitation.

The low energy part of the UV spectrum of pyrazine consists in two bands, dominated by absorption to the $B_{3u}(n\pi^*)$ and $B_{2u}(\pi\pi^*)$ states, respectively [2–8]. The former presents a well resolved vibrational structure, whereas the latter is much broader, indicating a fast relaxation process. Time-resolved photoelectron spectroscopy (TRPES) studies [9–12] revealed the existence of an ultrafast ($\sim$20 fs) non-radiative decay process occuring after excitation to the $B_{2u}(\pi\pi^*)$ state, due to the existence of a conical intersection (CI) between the $B_{3u}(n\pi^*)$ and $B_{2u}(\pi\pi^*)$ states lying close to the Franck–Condon (FC) region.

From the theoretical point of view, this relaxation process has been the subject of a large number of quantum dynamics investigations, based on reduced and full dimensional models. Early works [13–17] reported three- and four-mode models and showed that a simple two-state four-dimensional model provides a qualitatively correct simulation of the UV absorption spectrum [17]. These models were used to simulate various spectroscopic signals, including time-resolved transient absorption [18–20], and ionization [21] spectra, fluorescence [22] and resonance Raman spectra [23]. Worth et al. [24–27] performed accurate quantum dynamics simulations based on a model including the twenty-four vibrational modes of the molecule using the MCTDH method. These benchmark results have then been used to test various approximate methods for the simulation of non-adiabatic dynamics of molecular systems [28–40].

More recently, theoretical studies using on-the-fly trajectory surface hopping (TSH) simulations based on time-dependent density functional theory (TDDFT) electronic structure calculations [39, 41] suggested an important participation of the dark $A_u(n\pi^*)$ and $B_{2g}(n\pi^*)$ states in the non-adiabatic relaxation dynamics after excitation to the bright $B_{2u}(\pi\pi^*)$ state.

In this chapter, we further investigate the role of the dark $A_u(n\pi^*)$ and $B_{2g}(n\pi^*)$ states in the photophysics of pyrazine using quantum dynamics simulations and model Hamiltonians obtained in the framework of the vibronic coupling model of Köppel, Domcke and Cederbaum (see Sect. 4.3 in Chap. 4). Different models including various numbers of electronic states and vibrational modes were considered. In contrast to the results of Ref. [39], our results suggest that the $B_{2g}(n\pi^*)$ state plays a negligible role in the non-adiabatic dynamics of pyrazine. However, our results suggest that the $A_u(n\pi^*)$ state is significantly populated through a low-lying $B_{2u}(\pi\pi^*)/A_u(n\pi^*)$ CI. This decay channel is found to compete with the well established decay through the $B_{2u}(\pi\pi^*)/B_{3u}(n\pi^*)$ CI. These results agree well with the recent TSH simulations of Tomasello et al. [41].

The rest of this chapter is organized as follows. The details of the electronic structure calculations performed in this work are exposed in Sect. 5.2, the model Hamiltonians used for the dynamics calculations are presented in Sect. 5.3. Our results are then presented and discussed in Sect. 5.4 and Sect. 5.5 concludes this chapter.

5.2   Ab Initio Electronic Structure Calculations

The energies and properties of the low-lying excited electronic states of pyrazine have been the subject of numerous investigations using various electronic structure calculation methods [42–52]. All the electronic structure calculations presented in this chapter were performed using the aug-cc-pVDZ basis set [53]. The ground state equilibrium geometry optimization and vibrational analysis were performed using the second-order Møller-Plesset (MP2) method with the Gaussian 03 program package [54]. The resulting equilibrium geometry and harmonic frequencies have been reported in Ref. [1]. Excited-state energies were computed using the extended multi-configuration quasi-degenerate second-order perturbation theory (XMCQDPT2) method [55] as implemented in the Firefly QC package [56] which is partially based on the GAMESS (US) source code [57]. An active space of ten electrons distributed in eight orbitals was used for the underlying state-averaged complete active space self-consistent field (SA-CASSCF) wavefunction. These active orbitals include the full π orbital subset (three occupied π orbitals noted 1π, 2π and 3π, and three virtual π^* orbitals noted $1\pi^*$, $2\pi^*$ and $3\pi^*$) and the two nitrogen lone-pair orbitals (noted $1N_{lp}$ and $2N_{lp}$), see Fig. 5.1. The orbitals were averaged over the five lowest CASSCF states.

Table 5.1 Vertical excitation energies (in eV) computed using the XMCQDPT2 method and a SA5-CASSCF reference wavefunction compared with previous theoretical results and experimental data

	$B_{3u}(n\pi^*)$	$A_u(n\pi^*)$	$B_{2u}(\pi\pi^*)$	$B_{2g}(n\pi^*)$
XMCQDPT2[a]	3.93	4.45	4.79	5.38
MRCISD [52]	4.55	5.52	5.16	5.91
CASPT2 [49]	3.86	4.52	4.81	5.48
CASPT2 [51]	4.02	4.75	4.80	5.56
CASPT2 [44]	3.85	4.63	4.76	–
CASPT2 [46]	3.83	4.36	4.79	5.50
CC2 [50]	4.26	4.95	5.13	5.92
CC3 [50]	4.24	5.05	5.02	5.74
EOM-CCSD(T) [45]	3.83	4.81	4.64	5.56
SAC-CI [48]	4.25	5.24	4.84	6.04
TDDFT/B3LYP [39]	3.96	4.6	5.46	6.3
Exp. [8]	3.83[b]	–	4.81[c](4.69[b])	–

[a]This work
[b]0–0 transition
[c]Band maximum
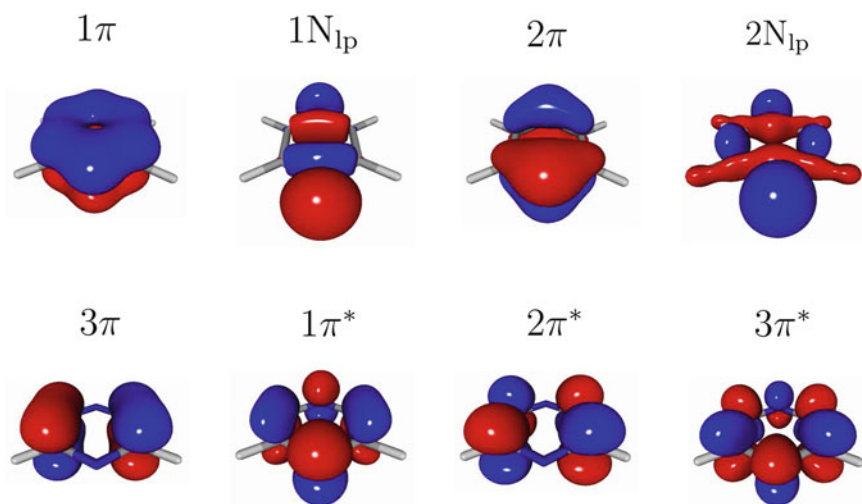
Fig. 5.1 CASSCF optimized orbitals included in the active space used in this work

Our results for the vertical excitation energies (VEEs) of the four lowest-lying singlet excited electronic states are presented in Table 5.1, in comparison with previous calculations and experimental data. Previous calculations include the complete active space second-order perturbation theory (CASPT2) calculations of

Refs. [44, 46, 49, 51], the second- and third-order approximate coupled cluster (CC2 and CC3) calculations of Ref. [50], the equation of motion coupled cluster with single, double and perturbative triple excitations calculations of Ref. [45], the symmetry adapted cluster configuration interaction calculations of Ref. [48] and the time-dependent density functional theory calculations using the B3LYP functional of Ref. [39].

Our XMCQDPT2 VEEs for the bright $B_{3u}(n\pi^*)$ and $B_{2u}(\pi\pi^*)$ are in good agreement with the experimental data [2–5, 7, 8]. A similar agreement was obtained in previous CASPT2 calculations. The results of previous calculations performed with other methods are in slightly less quantitative agreement with the experiment. The EOM-CCSD(T) and TDDFT calculations gave a good agreement for the $B_{3u}(n\pi^*)$ VEE but the former underestimated and the latter overestimated the $B_{2u}(\pi\pi^*)$ VEE. The SAC-CI calculation overestimated the $B_{3u}(n\pi^*)$ VEE but accurately reproduced the $B_{2u}(\pi\pi^*)$ VEE. The CC2, CC3 and MRCI methods overestimated both VEEs, with a larger discrepancy for the $B_{3u}(n\pi^*)$ VEE.

The VEE of the dark $A_u(n\pi^*)$ state appears more controversial. Walker and Palmer proposed an experimental value of 5.0 eV based on near-threshold energy loss spectroscopy [7]. However, other works quote a reference value of 4.72 eV [48, 49]. In addition, large discrepancies exist between the VEEs calculated with different methods. For instance, a difference of more than 1.1 eV in the $A_u(n\pi^*)$ VEE exists between the CASPT2 calculation of Ref. [46] and the MRCI calculation of Ref. [52]. Our XMCQDPT2 and previous CASPT2 calculations predicted the $A_u(n\pi^*)$ state as the second singlet excited state, i.e below the $B_{2u}(\pi\pi^*)$ state, with VEEs ranging from 4.36 to 4.75 eV. Previous CC2 and TDDFT calculations also predicted the $A_u(n\pi^*)$ state to lie below the $B_{2u}(\pi\pi^*)$ state. CC3 calculations, in contrast, predicted the $A_u(n\pi^*)$ and $B_{2u}(\pi\pi^*)$ states to be essentially degenerate whereas the SAC-CI, EOM-CCSD(T) and MRCI calculations predicted the $A_u(n\pi^*)$ state to lie above the $B_{2u}(\pi\pi^*)$ state.

A similar uncertainty exists for the position of the $B_{2g}(n\pi^*)$ state. Okuzawa et al. [6] reported a value of 5.19 eV based on UV-IR double resonance dip spectroscopy measurements. However, reference values of 5.5 eV [5, 48] and 6.10 eV [3, 49] have also been quoted in the literature. From the theoretical point of view, as for the $A_u(n\pi^*)$ state, rather large variations exists in the VEE calculated with different methods. The CASPT2 and EOM-CCSD(T) values reported in Table 5.1 are in good agreement with each other, ranging from 5.48 to 5.56 eV. The values obtained with other methods are typically higher, ranging from 5.74 eV to 6.3 eV. Our XMCQDPT2 value of 5.38 eV appears slightly underestimated with respect to previous calculations.

The interested reader is referred to the work of Weber and Reimers [46, 47] for further extensive comparisons of computational methods for the excitation energies of the low-lying singlet and triplet states of pyrazine.

5.3 Construction of the Models

The four lowest excited electronic states of the molecule, namely the $B_{3u}(n\pi^*)$, $A_u(n\pi^*)$, $B_{2u}(\pi\pi^*)$ and $B_{2g}(n\pi^*)$ states, were considered in this work. In its ground state equilibrium geometry, pyrazine is planar, with a D_{2h} symmetry. Its twenty-four normal modes can be classified as

$$\Gamma_{\text{vib}} = 5A_g + 1B_{1g} + 2B_{2g} + 4B_{3g} + 2A_u + 4B_{1u} + 4B_{2u} + 2B_{3u}. \qquad (5.1)$$

We have constructed several linear vibronic coupling model Hamiltonians augmented with diagonal quadratic terms for the non-totally symmetric modes. The total Hamiltonian of the molecule in the diabatic representation reads

$$H_m(Q) = H_0(Q) + W(Q), \qquad (5.2)$$

where $H_0(Q)$ is the ground state Hamiltonian in the harmonic approximation given in Eq. (4.45) of Sect. 4.3, Chap. 4. In our case, the elements of the potential matrix $W(Q)$ read

$$W_{nn}(Q) = E_n + \sum_i \kappa_i^{(n)} Q_i + \sum_i \gamma_j^{(n)} Q_j^2$$
$$W_{nn'}(Q) = \sum_k \lambda_k^{(nn')} Q_k. \qquad (5.3)$$

In this last equation, $n = 1, 2, 3, 4$ for the $B_{3u}(n\pi^*)$, $A_u(n\pi^*)$, $B_{2u}(\pi\pi^*)$ and $B_{2g}(n\pi^*)$ electronic states, respectively. Many of the constants appearing in this equation vanish by symmetry, according to Eq. (4.47) of Sect. 4.3, Chap. 4. The linear intrastate coupling constants $\kappa_i^{(n)}$ are only non-zero for totally symmetric modes. The B_{3g} modes give rise to non-vanishing λ_i^{12} constants, the unique B_{1g} mode gives rise to a non-vanishing λ_i^{13} constant, the B_{2g} modes give rise to non-vanishing λ_i^{23} constants and the B_{1u}, B_{2u} and A_u modes give rise to non-vanishing λ_i^{14}, λ_i^{24} and λ_i^{34} constants, respectively. Therefore, in a first-order description, the two B_{3u} modes can be neglected. Following Ref. [17], quadratic diagonal terms $\gamma_j^{(n)} Q_j^2$ were added for the non-totally symmetric modes, i.e the modes for which the diagonal linear terms vanish by symmetry. Thus, in Eq. (5.3) i runs over the totally symmetric modes, j runs over the non-totally symmetric modes and k runs over the modes of appropriate symmetry, depending on n and n', as explained above.

The values of the parameters of the vibronic coupling model Hamiltonians used for the quantum dynamics calculations reported in Sect. 5.4, obtained using our XMC-QDPT2 ab initio data, are reported below. Table 5.2 presents the values of the linear intrastate coupling constants $\kappa_i^{(n)}$, which are the derivatives of the adiabatic energies at the FC geometry. The derivatives were obtained through finite differences in this work. The dimensionless quantities $\kappa_i^{(n)}/\omega_i$, which give a better measure of the importance of the totally symmetric modes in the dynamics of the molecule after photoexcitation [58, 59], are also reported.

Table 5.2 Linear intrastate coupling constant $\kappa_i^{(n)}$ values (in eV) obtained in this work

	$B_{3u}(n\pi^*)$	$A_u(n\pi^*)$	$B_{2u}(\pi\pi^*)$	$B_{2g}(n\pi^*)$
κ_{6a}	$-0.081(-1.103)$	$-0.168(-2.283)$	$0.128(1.739)$	$-0.184(-2.500)$
κ_1	$-0.038(-0.304)$	$-0.083(-0.659)$	$-0.183(-1.452)$	$-0.117(-0.926)$
κ_{9a}	$0.117(0.762)$	$-0.071(-0.459)$	$0.045(0.295)$	$0.165(1.073)$
κ_{8a}	$-0.087(-0.436)$	$-0.465(-2.338)$	$0.026(0.132)$	$0.172(0.862)$
κ_2	$0.022(0.054)$	$0.060(0.150)$	$0.018(0.044)$	$0.030(0.074)$

The values between parenthesis are the dimensionless quantities $\kappa_i^{(n)}/\omega_i$

Table 5.3 Quadratic intrastate $\gamma_i^{(n)}$ and linear interstate coupling constant $\lambda_i^{(nn')}$ values (in eV) obtained in this work

Mode	Symm.	λ	$\gamma^{(1)}$	$\gamma^{(2)}$	$\gamma^{(3)}$	$\gamma^{(4)}$
ν_{10a}	B_{1g}	$0.195(1.684)$	-0.012	-0.048	-0.012	-0.013
ν_4	B_{2g}	$0.060(0.663)$	-0.030	-0.031	-0.031	-0.027
ν_5	B_{2g}	$0.053(0.456)$	-0.014	-0.026	-0.026	-0.009
ν_{6b}	B_{3g}	$<10^{-5}$	-0.013	-0.013	-0.005	-0.006
ν_3	B_{3g}	$0.065(0.385)$	-0.006	-0.006	0.001	-0.004
ν_{8b}	B_{3g}	$0.219(1.140)$	-0.012	-0.012	0.007	-0.043
ν_{7b}	B_{3g}	$0.020(0.050)$	0.003	0.003	0.004	0.003
ν_{16a}	A_u	$0.112(2.686)$	0.013	-0.013	-0.008	-0.008
ν_{17a}	A_u	$0.018(0.146)$	-0.016	-0.041	-0.012	-0.012
ν_{12}	B_{1u}	$0.207(1.629)$	-0.006	-0.022	-0.006	-0.006
ν_{18a}	B_{1u}	$0.090(0.632)$	-0.006	-0.002	-0.005	-0.006
ν_{19a}	B_{1u}	$0.094(0.511)$	-0.006	-0.010	-0.002	-0.006
ν_{13}	B_{1u}	$<10^{-5}$	0.004	0.004	0.004	0.004
ν_{18b}	B_{2u}	$0.044(0.332)$	-0.001	-0.003	-0.002	-0.003
ν_{14}	B_{2u}	$0.044(0.263)$	-0.019	-0.021	-0.020	-0.021
ν_{19b}	B_{2u}	$0.072(0.404)$	-0.013	-0.006	0.015	-0.006
ν_{20b}	B_{2u}	$<10^{-5}$	0.005	0.003	0.004	0.003

The values between parenthesis are the dimensionless quantities $\lambda_i^{(nn')}/\omega_i$

It is known from previous work on pyrazine [17] that the ν_{6a}, ν_1 and ν_{9a} totally symmetric modes are needed to correctly describe the dynamics at the CI between the $B_{2u}(\pi\pi^*)$ and $B_{3u}(n\pi^*)$ states and the absorption spectrum. In addition, as seen in Table 5.2, the $A_u(n\pi^*)$ state has a very large gradient along the ν_{8a} mode. Therefore, this mode needs to be included in our models in order to investigate the role of the $A_u(n\pi^*)$ state in the electronic relaxation dynamics of pyrazine. In contrast, the high frequency ν_2 mode can be safely neglected, as it gives rise to small coupling constants.

The interstate coupling constant are presented in Table 5.3, together with the diagonal intrastate quadratic coupling constants. These parameters were obtained together from least-square fitting against XMCQDPT2 adiabatic electronic energies computed along each coordinate (see Ref. [1] for more details). Our calculations

show a strong coupling of the bright $B_{2u}(\pi\pi^*)$ state with the $B_{3u}(n\pi^*)$ and $B_{2g}(n\pi^*)$ states, essentially mediated by the ν_{10a} and ν_{16a} modes, respectively. The coupling of the $B_{2u}(\pi\pi^*)$ state with the $A_u(n\pi^*)$ state, through the ν_4 and ν_5 modes, appears comparatively weaker. In addition, we predict strong couplings between the $B_{3u}(n\pi^*)$ and $A_u(n\pi^*)$ states, essentially through the ν_{8b} mode, and between the $B_{3u}(n\pi^*)$ and $B_{2g}(n\pi^*)$ states, essentially through the ν_{12} mode.

In order to single out the role of the $A_u(n\pi^*)$ and $B_{2g}(n\pi^*)$ states in the dynamics of pyrazine after excitation to the $B_{2u}(\pi\pi^*)$ state, three different models, including different numbers of electronic states and vibrational modes, were constructed. In each case, only modes that give rise to non-negligible first-order coupling constants were included.

Only the $B_{3u}(n\pi^*)$ and $B_{2u}(\pi\pi^*)$ states were included in the first model. As explained above, only the totally symmetric modes and the unique B_{1g} mode give

$Q_{6a}(A_g)$ $\omega = 593$ cm^{-1}

$Q_1(A_g)$ $\omega = 1017$ cm^{-1}

$Q_{9a}(A_g)$ $\omega = 1242$ cm^{-1}

$Q_{8a}(A_g)$ $\omega = 1605$ cm^{-1}

$Q_{10a}(B_{1g})$ $\omega = 936$ cm^{-1}

$Q_4(B_{2g})$ $\omega = 734$ cm^{-1}

$Q_5(B_{2g})$ $\omega = 942$ cm^{-1}

$Q_3(B_{3g})$ $\omega = 1352$ cm^{-1}

$Q_{8b}(B_{3g})$ $\omega = 1553$ cm^{-1}

$Q_{16a}(A_u)$ $\omega = 337$ cm^{-1}

$Q_{12}(B_{1u})$ $\omega = 1022$ cm^{-1}

$Q_{18a}(B_{1u})$ $\omega = 1148$ cm^{-1}

$Q_{19a}(B_{1u})$ $\omega = 1486$ cm^{-1}

$Q_{18b}(B_{2u})$ $\omega = 1079$ cm^{-1}

$Q_{14}(B_{2u})$ $\omega = 1364$ cm^{-1}
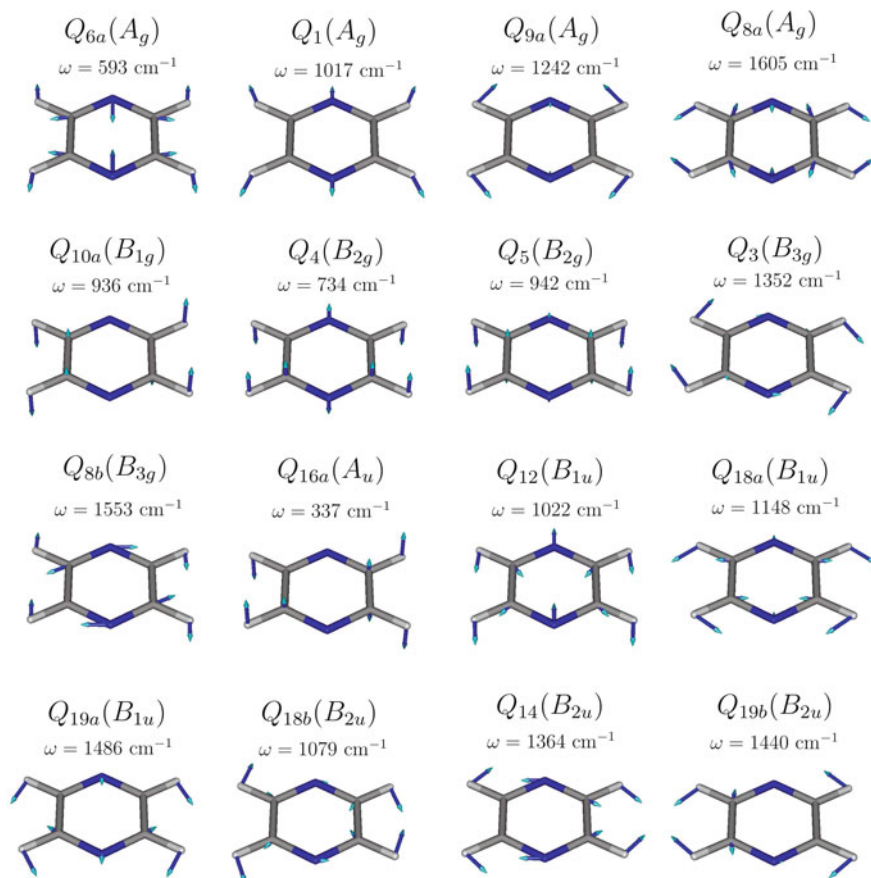
$Q_{19b}(B_{2u})$ $\omega = 1440$ cm^{-1}

Fig. 5.2 Ground state normal modes computed at the MP2/aug-ccPVDZ level of theory. The corresponding symmetry labels and harmonic frequencies are also shown

rise to non-vanishing first-order coupling constants in this case. Therefore, the ν_{6a}, ν_1, ν_{9a} and ν_{8a} totally symmetric modes, and the ν_{10a} mode, were included in the model. This model is referred to as the two-state model. Similar two-state models have been previously used [17, 23, 32] to simulate the excited state dynamics of pyrazine.

In a second model, the $A_u(n\pi^*)$ state is further included, and now the B_{2g} and B_{3g} modes give rise to non-vanishing first-order coupling constants. Besides the five modes included in the two-state model, this model includes the ν_4 and ν_5 modes of B_{2g} symmetry and the ν_3 and ν_{8b} modes of B_{3g} symmetry. This model, referred to as three-state model, includes nine vibrational modes.

Finally, in a third model, the $B_{2g}(n\pi^*)$ state is further included, and the A_u, B_{1u} and B_{2u} modes give rise to non-vanishing first-order coupling constants. Besides the nine modes included in the three-state model, the ν_{16a} mode of A_u symmetry, the ν_{12}, ν_{18a} and ν_{19a} modes of B_{1u} symmetry and the ν_{18b}, ν_{14} and ν_{19b} modes of B_{2u} symmetry were included. This model is referred to as four-state model and includes sixteen vibrational modes. The displacement vectors associated with these modes, obtained from our MP2 calculations are illustrated in Fig. 5.2.

5.4 Time-Dependent Nuclear Quantum Dynamics Simulations

Quantum dynamics simulations of the UV absorption spectrum and of the electronic state population dynamics of the molecule excited by a short laser pulse resonant with the transition to the bright $B_{2u}(\pi\pi^*)$ state, based on the models described in Sect. 5.3 were performed using the MCTDH method in the multi-set formalism (see Sect. 4.2.5 in Chap. 4). For the representation of the Hamiltonian and the wave function, a Hermite polynomial DVR scheme [60] was used for all the degrees of freedom. The number of SPF and primitive basis functions used in the calculations are listed in Table 5.4. Test calculations with both larger primitive and SPF bases have been

Table 5.4 Number of SPF and primitive basis functions used in the calculations

| Model	Combinations of modes	Numbers of SPFs	Numbers of grid points
Two-state	(ν_{6a}, ν_{10a}), ν_1, ν_{9a}, ν_{8a}	[4, 34, 14], [4, 12, 8], [4, 12, 8], [4, 10, 6]	(32, 40), 16, 14, 24
Three-state	(ν_{6a}, ν_{10a}), (ν_1, ν_4), $(\nu_{9a}, \nu_3, \nu_{8b})$, (ν_{8a}, ν_5)	[4, 30, 34, 14], [4, 12, 15, 8], [4, 13, 14, 8], [4, 20, 24, 8]	(32, 40), (16, 20), (14, 10, 14), (24, 10)
Four-state	$(\nu_{6a}, \nu_{10a}, \nu_{16a})$, $(\nu_1, \nu_4, \nu_{19b})$, $(\nu_{9a}, \nu_3, \nu_{8b})$, $(\nu_{8a}, \nu_5, \nu_{12})$ $(\nu_{18a}, \nu_{18b}, \nu_{19a}, \nu_{14})$	[4, 36, 42, 14, 6], [4, 13, 14, 8, 5], [4, 24, 28, 8, 5], [4, 18, 19, 8, 5], [4, 7, 7, 4, 4]	(32, 40, 20), (16, 20, 10), (14, 10, 14), (24, 10, 11), (7, 7, 7, 8)

performed. The results (populations and spectra) of these calculations were found
almost identical to those performed with the bases of Table 5.4, indicating a satisfac-
tory convergence of the results presented in this work.

5.4.1   Simulation of the UV Absorption Spectrum

The UV absorption spectrum in the energy range between 3.8 and 5.7 eV consists in
two distinct bands, dominated by absorption to the $B_{3u}(n\pi^*)$ and $B_{2u}(\pi\pi^*)$ states.
The theoretical framework outlined in Sect. 4.4 of Chap. 4 was used to compute
the absorption spectrum. Specifically, two wavepacket propagations, initiated on
the $B_{3u}(n\pi^*)$ and $B_{2u}(\pi\pi^*)$ states, respectively, were performed. In each case, the
initial wavepacket $\Psi(\mathbf{Q}, 0)$, obtained by projecting the ground vibronic eigenfunc-
tion on the diabatic excited state manifold, was propagated for 120 fs. From these
two propagations, autocorrelation functions were calculated and Fourier transformed
to obtain partial absorption spectra. Before the Fourier transform, the autocorrela-
tion functions were multiplied by a damping function $f(t) = e^{-t/\tau}$ to account for
the homogeneous broadening of the experimental spectrum, and by a filter function
$g(t) = \cos^2(\pi t/2T)\Theta(t - T)$, where Θ denotes the Heaviside step function, to avoid
problems arising from the finite propagation time T. The full absorption spectrum
was then obtained as the oscillator strength-weighted sum of the two partial absorp-
tion spectra. The experimentally determined oscillator strengths of 0.006 and 0.1 [5]
for the $B_{3u}(n\pi^*)$ and $B_{2u}(\pi\pi^*)$ states were used. This strategy implicitly invokes
the Franck–Condon approximation, which is known to be much more accurate in
the diabatic representation than in the adiabatic representation. In addition, the influ-
ence of the dark $A_u(n\pi^*)$ and $B_{2g}(n\pi^*)$ states on the spectrum, mediated by their
vibronic coupling with the bright states, is fully taken into account. Based on exten-
sive test calculations, an adjustment of the $A_u(n\pi^*)$ state VEE was found necessary to
obtain a reasonable agreement between simulated and experimental spectra. A value
of 4.69 eV was found to provide the most satisfactory description of the absorption
spectrum. This value is somewhat higher than our ab initio value of 4.45 eV. Neverthe-
less, the magnitude of this adjustment appears reasonable given the large deviations
existing between VEEs computed with different methods, as seen in Table 5.1. Our
simulated absorption spectra, using the three different models described in Sect. 5.3,
compared with the experimental spectrum [2] are presented in Fig. 5.3. In each case,
the whole computed spectrum was blue-shifted so that the position of the $B_{3u}(n\pi^*)$
0–0 peak matches the experimental one at approximately 324 nm.

   The spectrum computed with the two-state model is presented in Fig. 5.3b. In this
case, damping times τ of 400 and 40 fs were used for the $B_{3u}(n\pi^*)$ and $B_{2u}(\pi\pi^*)$
components, respectively. The whole spectrum was blue-shifted by 0.04 eV. The two-
state model qualitatively reproduces the shape of the $B_{2u}(\pi\pi^*)$ band. A closer look

Fig. 5.3 Comparison of **a** the experimental UV absorption spectrum taken from Ref. [2] with the spectra computed with **b** the two-state model, **c** the three-state model and **d** the four-state model. Figure reproduced from Ref. [1]
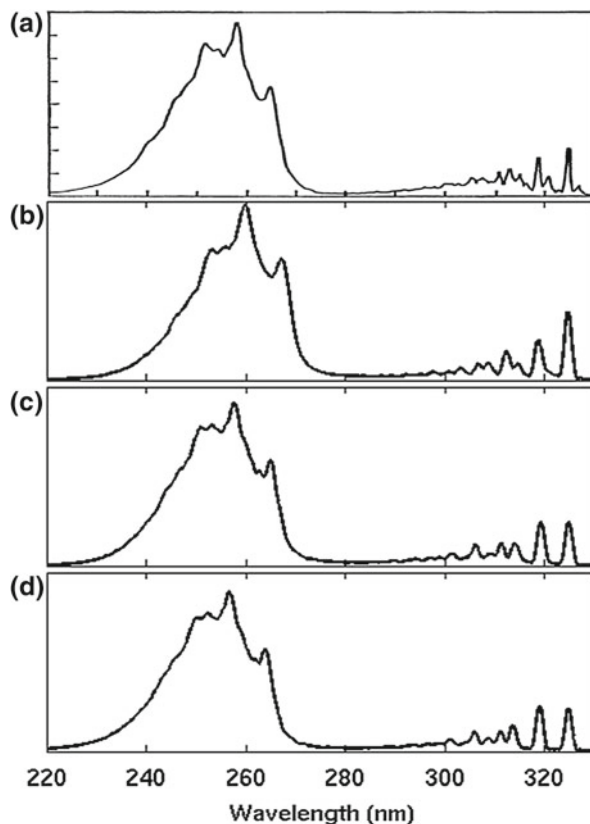
shows, however, that the portion between 245 and 255 nm is not well reproduced. In addition, the whole band appears slightly red-shifted with respect to the experimental one (the experimental spectrum is presented in Fig. 5.3a). The agreement for the $B_{3u}(n\pi^*)$ band is less satisfactory. In particular, the relative intensities of the two most intense peaks at approximately 324 and 319 nm, corresponding to the 0–0 and ν_{6a}^1 transitions respectively, disagree with experiment.

The spectrum computed with the three-state model is presented in Fig. 5.3c. Damping times τ of 400 and 100 fs were used for the $B_{3u}(n\pi^*)$ and $B_{2u}(\pi\pi^*)$ components, respectively. The spectrum was blue-shifted by 0.13 eV to approximately match the experimental $B_{3u}(n\pi^*)$ 0–0 peak. A comparison of panels b and c of Fig. 5.3 shows that the inclusion of the $A_u(n\pi^*)$ state in the simulations significantly improves the agreement between the simulated and experimental spectra. Both the shape and positions of the $B_{2u}(\pi\pi^*)$ band are improved. The relative intensity of the 0–0 and ν_{6a}^1 peaks of the $B_{3u}(n\pi^*)$ band is also better reproduced by the three-state model. Nevertheless, the agreement with experiment remains more qualitative than for the $B_{2u}(\pi\pi^*)$ band. In particular, the small peak appearing slightly above 320 nm in the

experimental spectrum, assigned to the vibronically induced ν_{10a}^1 transition, is not visible in our computed spectra. This occurs because our model overestimates the position of this peak, which overlaps with the ν_{6a}^1 peak.

The spectrum computed with the four-state model is presented in Fig. 5.3d. Damping times τ of 400 and 100 fs were used for the $B_{3u}(n\pi^*)$ and $B_{2u}(\pi\pi^*)$ components, respectively, and the spectrum was blue-shifted by 0.17 eV. The spectra obtained with the three- and four-state models are almost identical. This indicates, as will be confirmed below, that the $B_{2g}(n\pi^*)$ state is not significantly involved in the dynamics of pyrazine after excitation to the bright $B_{2u}(\pi\pi^*)$ state.

The results presented in this section allow us, by taking into account the overall energy shift and the adjustment of the $A_u(n\pi^*)$ state vertical excitation energy applied in the three-state model, to propose refined estimations of 4.06, 4.82 and 4.92 eV for the vertical excitation energies of the $B_{3u}(n\pi^*)$, $A_u(n\pi^*)$ and $B_{2u}(\pi\pi^*)$ states, respectively.

5.4.2 Electronic State Populations and Decay Mechanism

It is well known from previous experimental [9–12] and theoretical works [13, 21, 24–26] that after excitation to the bright $B_{2u}(\pi\pi^*)$ state, pyrazine undergoes an ultrafast radiationless decay process in a few tens of femtoseconds. This process was directly observed recently by TRPES using sub-20 fs pulses [11, 12]. In this section, we present quantum dynamics simulations of the excited state dynamics of pyrazine triggered by a 14 fs sine-squared shaped laser pulse resonant with the transition from the ground to the $B_{2u}(\pi\pi^*)$ state. Specifically, the total Hamiltonian operator reads

$$H(Q, t) = H_m(Q) + H_{int}(t), \tag{5.4}$$

where $H_m(Q)$ is the molecular Hamiltonian operator given in Eq. (5.2) and

$$H_{int}(t) = -\mu\varepsilon(t) \tag{5.5}$$

is the Hamiltonian operator describing the interaction of the molecule with the electric field in the dipolar approximation. In this last equation, μ denotes the matrix representation of the dipole moment operator, featuring permanent dipole moments on the diagonal and transition dipole moments as off diagonal elements. As in the previous section, the Franck–Condon approximation was used. In addition, only the transition dipole moment between the ground and $B_{2u}(\pi\pi^*)$ states was considered. This assumption relies on the fact that the transition dipole moment between the ground and $B_{3u}(n\pi^*)$ states is comparatively much smaller and that we consider a laser pulse resonant with the transition to the $B_{2u}(\pi\pi^*)$ state. Accordingly, $\varepsilon(t)$ denotes the component of the electric field parallel with the transition dipole moment between the ground and $B_{2u}(\pi\pi^*)$ states. The electric field reads

$$\varepsilon(t) = \varepsilon_0 \sin^2 \left(\frac{\pi t}{t_p} \right) \cos (\omega t) \, \Theta \left(t_p - t \right), \tag{5.6}$$

where ε_0 is the peak amplitude, t_p is the pulse duration, ω is the frequency and $\Theta \left(t_p - t \right)$ is a Heaviside step function, which ensures that the electric field is zero for $t > t_p$. These parameters were set to $\varepsilon_0 = 0.01$ a.u, $t_p = 14$ fs and $\hbar\omega = 4.7$ eV. We note that, because we treat explicitly the electronic excitation, the ground electronic state is included in our calculations. Nevertheless, for clarity, we continue to refer to the three models described in Sect. 5.3 as two-, three- and four-state models.

Our results were analyzed in term of diabatic and adiabatic electronic state populations. In what follows, the diabatic electronic states are labeled by Greek letters whereas the adiabatic electronic states are labeled by Latin letters. The diabatic population for the state $|\alpha\rangle$ is simply the norm of the corresponding wavefunction component

$$P_\alpha^d = ||\Psi^{d,(\alpha)}||^2. \tag{5.7}$$

The adiabatic populations are more difficult to obtain. Consider the transformation matrix $U(Q)$ that diagonalizes the diabatic potential matrix $W(Q)$ of Eq. (5.3)

$$U^\dagger(Q)W(Q)U(Q) = V(Q), \tag{5.8}$$

where $V(Q)$ is the diagonal matrix of the adiabatic potentials. This transformation matrix relates the adiabatic wavefunction to the diabatic one

$$\Psi^{ad}(Q) = U(Q)\Psi^d(Q). \tag{5.9}$$

The adiabatic population P_a^{ad} of the state $|a\rangle$ is obtained as the expectation value of the corresponding projection operator $\hat{P}_a^{ad}$

$$P_a^{ad} = \langle \Psi^d | \hat{P}_a^{ad} | \Psi^d \rangle, \tag{5.10}$$

with

$$\hat{P}_a^{ad} = \sum_{\beta,\gamma} |\beta\rangle U_{\beta a}^\dagger U_{a\gamma} \langle \gamma |. \tag{5.11}$$

Unfortunately, the adiabatic projection operator does not have the so-called product form (see Sect. 4.2.3 of Chap. 4). Therefore, the integrals of Eq. (5.10) have to be evaluated on the full primitive grid, which can become computationally expansive for systems with more than four or five degrees of freedom. For larger systems, as in the present work, a Monte Carlo integration algorithm, implemented in the Heidelberg MCTDH package, can be used. In addition, to reduce the size of the grid, the so-called "quick algorithm" (see the MCTDH html documentation [61]) was used. The idea behind this method is to ignore all the grid points at which the product of the one-dimensional reduced densities is lower than a given threshold. The

one-dimensional reduced density along the coordinate Q_i is the density integrated over all the degrees of freedom except Q_i

$$D_i(Q_i) = \langle \Psi | \Psi \rangle_{Q_i}. \tag{5.12}$$

Below, to distinguish them from the diabatic electronic states, the adiabatic electronic states are noted S_n with $n = 1, 2, 3, 4$. We first present the diabatic and adiabatic electronic state populations obtained from the two-state model in Fig. 5.4a, b, respectively. The electronic state populations have been analyzed in detail previously using similar two-state models [26, 27]. The population transfered to the $B_{2u}(\pi\pi^*)$ state by the laser pulse reaches a maximum of approximately 0.6 at 12 fs and quickly decays to the $B_{3u}(n\pi^*)$ state. After 50 fs, the $B_{2u}(\pi\pi^*)$ state population has dropped to 0.1. This time scale of 50 fs for an almost complete decay of the $B_{2u}(\pi\pi^*)$ state is in excellent agreement with the most recent TRPES experiments [11, 12]. A large recurrence occurs at 90 fs, as noted in previous theoretical works [26, 27]. Since the $B_{2u}(\pi\pi^*)$ state is the third excited state at the FC geometry, the two adiabatic excited states in the two-state model are labeled S_1 and S_3. In order to check the accuracy of the procedure used to calculate the adiabatic electronic state populations, two calculations using different standard deviations for the Monte-Carlo integration and thresholds for the quick algorithm, were performed. These quantities were set to 0.01 and 1.0×10^{-6}, respectively, in the first calculation and to 0.001 and 1.0×10^{-8}, respectively, in the second calculation. The resulting adiabatic state populations are presented in Fig. 5.4b. The S_1 adiabtic state population curves exhibit a noisy behavior

Fig. 5.4 Electronic state populations computed with the two-state model. **a** Populations of the diabatic $B_{3u}(n\pi^*)$ (*blue*) and $B_{2u}(\pi\pi^*)$ (*green*) states and **b** populations of the adiabatic S_1 (*black*) and S_3 (*cyan*) states using a Monte Carlo integration scheme combined with the so-called "quick algorithm" (see text for details). The *full lines* present the adiabatic populations computed using a standard deviation of 0.01 for the Monte Carlo integration and a threshold of 1.0×10^{-6} for the quick algorithm. Adiabatic populations computed using values of 0.001 and 1.0×10^{-8} for the same quantities are presented in *dashed lines*. Figure reproduced from Ref. [1]

after 40 fs. This corresponds to the vibrationally hot wavepacket propagating on the S_1 PES after the initial decay through the S_2/S_1 CI. In this case, the Monte-Carlo method can not integrate Eq. (5.10) with a high accuracy. Nevertheless, except for this noisy part, the adiabatic populations obtained from the two calculations are smooth and almost identical. This indicates that the Monte Carlo integration combined with the quick algorithm provides a sufficient accuracy for our purpose. As noted previously [26, 27], the decay of the adiabatic population is faster than in the diabatic case, and the final population of the upper state is lower.

The diabatic and adiabatic electronic state populations obtained with the three-state model are shown in full lines in Fig. 5.5a, b, respectively. The diabatic populations obtained with the four-state model are also shown in dashed lines in Fig. 5.5a. The comparison of the diabatic populations for the three- and four-state models confirms that the inclusion of the $B_{2g}(n\pi^*)$ state in the simulations has a minor effect on the non-adiabatic decay dynamics of the molecule after excitation to the $B_{2u}(\pi\pi^*)$ state. Only a very small amount of population is transfered to the $B_{2g}(n\pi^*)$ state, with a maximum of less than 0.02 at 11 fs. In addition, the populations of the $B_{3u}(n\pi^*)$, $A_u(n\pi^*)$ and $B_{2u}(\pi\pi^*)$ states are similar in the three- and four-state models. The population of the $B_{2u}(\pi\pi^*)$ state reaches a maximum of nearly 0.6 at 11 fs, and then quickly decays to almost zero at 50 fs. A recurrence is then seen at 95 fs, as in the simulation with the two-state model. Between 0 and 20 fs, both the $B_{3u}(n\pi^*)$ and $A_u(n\pi^*)$ state populations rise quickly and reach approximately 0.15 at 20 fs. Then, between 20 and 40 fs, the $B_{3u}(n\pi^*)$ state population continues to rise and reaches a
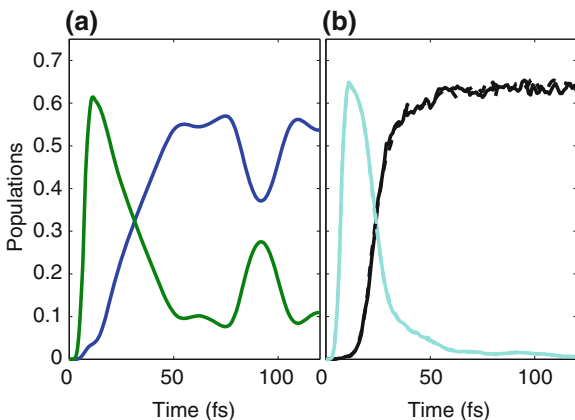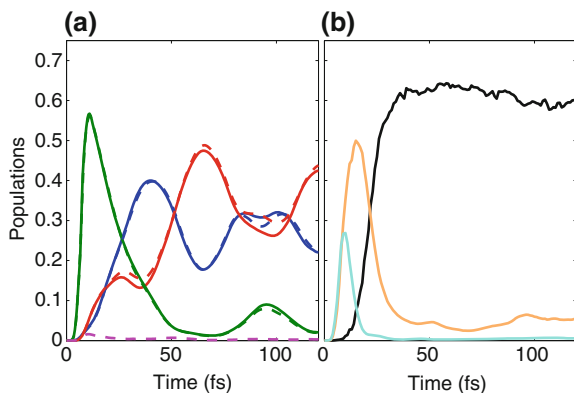

Fig. 5.5 Electronic state populations computed with the three- and four-state models. **a** Populations of the diabatic $B_{3u}(n\pi^*)$ (*blue*), $A_u(n\pi^*)$ (*red*), $B_{2u}(\pi\pi^*)$ (*green*) and $B_{2g}(n\pi^*)$ (*magenta*) states with the three-state model (*full lines*) and four-state model (*dashed lines*). The three-state model includes only the $B_{3u}(n\pi^*)$, $A_u(n\pi^*)$ and $B_{2u}(\pi\pi^*)$ states. **b** populations of the adiabatic S_1 (*black*), S_2 (*orange*) and S_3 (*cyan*) states computed using a standard deviation of 0.01 for the Monte Carlo integration and a threshold of 1.0×10^{-6} for the quick algorithm. Figure reproduced from Ref. [1]

value of 0.4 at 40 fs, while the $A_u(n\pi^*)$ state population slightly drops to 0.13. After 40 fs the $A_u(n\pi^*)$ state population increases again while the $B_{3u}(n\pi^*)$ state population starts to drop and the populations oscillate between these two states until the end of the simulation. For the calculation of the adiabatic state populations presented in Fig. 5.5b, a standard deviation of 0.01 for the Monte Carlo integration and a threshold of 1.0×10^{-6} for the quick algorithm were used. Overall, this figure shows a fast and sequential decay from the S_3 state to the S_1 state via the S_2 state. At 40 fs the S_1 population reaches a value of approximately 0.6 and remains essentially constant until the end of the simulation. In addition, a residual population of approximately 0.05 is seen to remain on the S_2 state. Note that similar adiabatic state populations were obtained in the TSH study of Tomasello et al. [41].

One-dimensional cuts of the diabatic PESs along the Q_{6a} and Q_{8a} totally symmetric coordinates are presented in Fig. 5.6a, b respectively. Both figures show $B_{2u}(\pi\pi^*)/A_u(n\pi^*)$ CI points close to the FC geometry. Upon motion along the Q_{6a} coordinate, the $B_{2u}(\pi\pi^*)$ state then crosses the $B_{3u}(n\pi^*)$ state. This $B_{2u}(\pi\pi^*)/B_{3u}(n\pi^*)$ CI is responsible for the decay of the molecule in the two-state model. The $B_{2u}(\pi\pi^*)/A_u(n\pi^*)$ CI appears much closer to the FC geometry than the $B_{2u}(\pi\pi^*)/B_{3u}(n\pi^*)$ CI. However, as seen in Table 5.3, the λ_4 and λ_5 coupling constants mediating the $B_{2u}(\pi\pi^*)/A_u(n\pi^*)$ coupling are smaller than the λ_{10a} constant mediating the $B_{2u}(\pi\pi^*)/B_{3u}(n\pi^*)$ coupling. This explains the competition between population transfer to the $B_{3u}(n\pi^*)$ and $A_u(n\pi^*)$ in the first 40 fs seen in Fig. 5.5a. Figure 5.6b shows the existence of both $B_{2u}(\pi\pi^*)/A_u(n\pi^*)$ and $A_u(n\pi^*)/B_{3u}(n\pi^*)$ low-lying CI points. The $A_u(n\pi^*)/B_{3u}(n\pi^*)$ CI explains the oscillations of population between the $B_{3u}(n\pi^*)$ and $A_u(n\pi^*)$ seen after 40 fs in Fig. 5.5a.

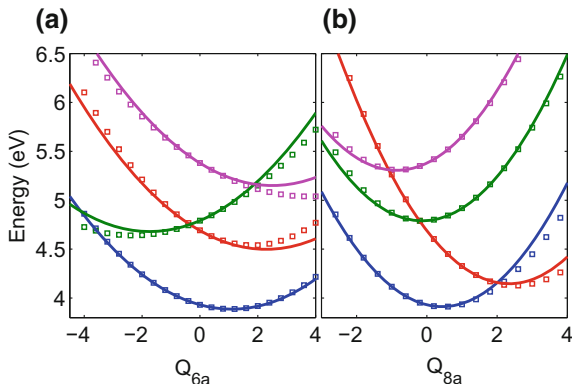**Fig. 5.6** One-dimensional cuts of the diabatic PESs of the $B_{3u}(n\pi^*)$ (*blue*), $A_u(n\pi^*)$ (*red*), $B_{2u}(\pi\pi^*)$ (*green*) and $B_{2g}(n\pi^*)$ (*magenta*) states along the **a** Q_{6a} and **b** Q_{8a} totally symmetric coordinates. The *full lines* represent the potential obtained from our model Hamiltonian whereas the *squares* are the ab initio computed points. Figure reproduced from Ref. [1]

5.5   Conclusion

During the last two decades, pyrazine has been considered as a benchmark system for the study of the radiationless decay of molecules at CIs. The ultrafast decay observed experimentally [9–12], has been interpreted within a two-state model including the vibronically coupled $B_{3u}(n\pi^*)$ and $B_{2u}(\pi\pi^*)$ states. However, recent studies based on TSH calculations [39, 41] suggested the participation of the two low-lying dark $A_u(n\pi^*)$ and $B_{2g}(n\pi^*)$ states in the photophysics of the molecule.

In this chapter, we have presented quantum dynamics simulations of the excited state non-adiabatic decay of the molecule. We have constructed linear vibronic coupling model Hamiltonians augmented with diagonal quadratic terms for the non-totally symmetric modes, including the four lowest lying excited electronic states and up to sixteen vibrational modes. In contrast to the results presented in Ref. [39], our calculations predict a negligible influence of the $B_{2g}(n\pi^*)$ state on the dynamics of the molecule. However, they suggest that the decay to the $A_u(n\pi^*)$ state, through a low-lying $B_{2u}(\pi\pi^*)/A_u(n\pi^*)$ CI, efficiently competes with the well established decay to the $B_{3u}(n\pi^*)$ state through the $B_{2u}(\pi\pi^*)/B_{3u}(n\pi^*)$ CI. In addition, we have shown the existence of a strong vibronic coupling between the $A_u(n\pi^*)$ and $B_{3u}(n\pi^*)$ states which influences the topography of the S_1 adiabatic PES. Therefore, the present work provides a significant new insight into the non-adiabatic dynamics of pyrazine after excitation to the $B_{2u}(\pi\pi^*)$ state.

Recently, we have extended the vibronic coupling model used in the present work to include all the quadratic terms and selected cubic and quartic terms in order to investigate the decay of the molecule to its ground state [62]. It is known experimentally [9] that, following the initial ultrafast decay, pyrazine further decays to its ground state on a time scale of approximately 20 ps. We found a conical intersection between the $A_u(n\pi^*)$ and the ground state. We performed quantum dynamics simulations that showed that this conical intersection explains the slow decay of the molecule to its ground state. This work gives further evidence of the important role of the $A_u(n\pi^*)$ in the non-adiabatic dynamics of pyrazine.

References

1. M. Sala, B. Lasorne, F. Gatti, S. Guérin, Phys. Chem. Chem. Phys. **16**, 15957 (2014)
2. I. Yamazaki, T. Murao, T. Yamanaka, K. Yoshihara, Faraday Discuss. Chem. Soc. **75**, 395 (1983)
3. A. Bolovinos, P. Tsekeris, J. Philips, E. Pantos, G. Anditsopoulos, J. Mol. Spectrosc. **103**, 240 (1984)
4. J. Kommandeur, W.A. Majewski, W.L. Meerts, D.W. Pratt, Annu. Rev. Phys. Chem. **38**, 433 (1987)
5. K.K. Innes, I.G. Ross, W.R. Moomaw, J. Mol. Spectrosc. **132**, 492 (1988)
6. Y. Okuzawa, M. Fujii, M. Ito, Chem. Phys. Lett. **171**, 341 (1990)
7. I.C. Walker, M.H. Palmer, Chem. Phys. **153**, 169 (1991)
8. M. Stener, P. Decleva, D.M.P. Holland, D.A. Shaw, J. Phys. B: At. Mol. Opt. Phys. **44**, 075203 (2011)

9. L. Wang, H. Kohguchi, T. Suzuki, Faraday Discuss. **113**, 37 (1999)

10. V. Stert, P. Farmanara, W. Radloff, J. Chem. Phys. **112**, 4460 (2000)

11. T. Horio, T. Fuji, Y.-I. Suzuki, T. Suzuki, J. Am. Chem. Soc. **131**, 10392 (2009)

12. Y.-I. Suzuki, T. Fuji, T. Horio, T. Suzuki, J. Chem. Phys. **132**, 174302 (2010)

13. R. Schneider, W. Domcke, Chem. Phys. Lett. **150**, 235 (1988)

14. R. Schneider, W. Domcke, Chem. Phys. Lett. **159**, 61 (1989)

15. U. Manthe, H. Köppel, J. Chem. Phys. **93**, 1658 (1990)

16. R. Seidner, G. Stock, A.L. Sobolewski, W. Domcke, J. Chem. Phys. **96**, 5298 (1991)

17. C. Woywod, W. Domcke, A.L. Sobolewski, H.-J. Werner, J. Chem. Phys. **100**, 1400 (1994)

18. G. Stock, R. Schneider, W. Domcke, J. Chem. Phys. **90**, 7184 (1989)

19. G. Stock, W. Domcke, J. Opt. Soc. Am. B **7**, 1970 (1990)

20. G. Stock, W. Domcke, Phys. Rev. A **45**, 3032 (1992)

21. M. Seel, W. Domcke, J. Chem. Phys. **95**, 7806 (1991)

22. G. Stock, W. Domcke, J. Chem. Phys. **93**, 5496 (1990)

23. G. Stock, C. Woywod, W. Domcke, T. Swinney, B.H. Hudson, J. Chem. Phys. **103**, 6851 (1995)

24. G.A. Worth, H.-D. Meyer, L.S. Cederbaum, J. Chem. Phys. **105**, 4412 (1996)

25. G.A. Worth, H.-D. Meyer, L.S. Cederbaum, J. Chem. Phys. **109**, 3518 (1998)

26. G.A. Worth, H.-D. Meyer, L.S. Cederbaum, Chem. Phys. Lett. **299**, 451 (1999)

27. A. Raab, G.A. Worth, H.-D. Meyer, L.S. Cederbaum, J. Chem. Phys. **110**, 936 (1999)

28. M. Thoss, W.H. Miller, G. Stock, J. Chem. Phys. **112**, 10282 (2000)

29. M. Santer, U. Manthe, G. Stock, J. Chem. Phys. **114**, 2001 (2001)

30. K. Ando, M. Santer, J. Chem. Phys. **118**, 10399 (2003)

31. R. Borrelli, A. Peluso, J. Chem. Phys. **119**, 8437 (2003)

32. D.V. Shalashilin, M.S. Child, J. Chem. Phys. **121**, 3563 (2004)

33. P. Puzari, R.S. Swathi, B. Sarkar, S. Adhikari, J. Chem. Phys. **123**, 134317 (2005)

34. P.S. Christopher, M. Shapiro, P. Brumer, J. Chem. Phys. **124**, 184107 (2006)

35. P. Puzari, B. Sarkar, S. Adhikari, J. Chem. Phys. **125**, 194316 (2006)

36. X. Chen, V.S. Batista, J. Chem. Phys. **125**, 124313 (2006)

37. I. Burghardt, K. Giri, G.A. Worth, J. Chem. Phys. **129**, 174104 (2008)

38. C. Lasser, T. Swart, J. Chem. Phys. **129**, 034302 (2008)

39. U. Werner, R. Mitrić, T. Suzuki, V. Bonačić-Koutecký, Chem. Phys. **349**, 319 (2008)

40. D.V. Shalashilin, J. Chem. Phys. **132**, 244111 (2010)

41. G. Tomasello, A. Humeniuk, R. Mitrić, J. Phys. Chem. A **118**, 8437 (2014)

42. W.R. Wadt, W.A. Goddard III, T.H. Dunning Jr, J. Chem. Phys. **65**, 438 (1976)

43. M.P. Fülscher, K. Andersson, B.O. Roos, J. Phys. Chem. **96**, 9204 (1992)

44. M.P. Fülscher, B.O. Roos, Theor. Chim. Acta **87**, 403 (1994)

45. J.E. Delbene, J.D. Watts, R.J.J. Bartlett, J. Chem. Phys. **106**, 6051 (1997)

46. P. Weber, J.R. Reimers, J. Phys. Chem. A **103**, 9821 (1999)

47. P. Weber, J.R. Reimers, J. Phys. Chem. A **103**, 9830 (1999)

48. Y. Li, J. Wan, X. Xu, J. Comp. Chem. **28**, 1658 (2007)

49. C. Woywod, A. Papp, G.J. Halász, A. Vibók, Theor. Chem. Acc. **125**, 521 (2010)

50. M. Schreiber, M.R. Silva-Junior, S.P.A. Sauer, W. Thiel, J. Chem. Phys. **128**, 134110 (2008)

51. M.R. Silva-Junior, M. Schreiber, S.P.A. Sauer, W. Thiel, J. Chem. Phys. **133**, 174318 (2010)

52. M. Kanno, Y. Ito, N. Shimakura, S. Koseki, H. Kono, Y. Fujimura, Phys. Chem. Chem. Phys. **17**, 2012 (2015)

53. R.A. Kendall, T.H. Dunning Jr, R.J. Harrison, J. Chem. Phys. **96**, 6796 (1992)

54. Gaussian 03, Revision C.02, M. J. Frisch, G. W. Trucks, H. B. Schlegel, G. E. Scuseria, M. A. Robb, J. R. Cheeseman, J. A. Montgomery, Jr., T. Vreven, K. N. Kudin, J. C. Burant, J. M. Millam, S. S. Iyengar, J. Tomasi, V. Barone, B. Mennucci, M. Cossi, G. Scalmani, N. Rega, G. A. Petersson, H. Nakatsuji, M. Hada, M. Ehara, K. Toyota, R. Fukuda, J. Hasegawa, M. Ishida, T. Nakajima, Y. Honda, O. Kitao, H. Nakai, M. Klene, X. Li, J. E. Knox, H. P. Hratchian, J. B. Cross, V. Bakken, C. Adamo, J. Jaramillo, R. Gomperts, R. E. Stratmann, O. Yazyev, A. J. Austin, R. Cammi, C. Pomelli, J. W. Ochterski, P. Y. Ayala, K. Morokuma, G. A. Voth, P. Salvador, J. J. Dannenberg, V. G. Zakrzewski, S. Dapprich, A. D. Daniels, M. C. Strain,

O. Farkas, D. K. Malick, A. D. Rabuck, K. Raghavachari, J. B. Foresman, J. V. Ortiz, Q. Cui, A. G. Baboul, S. Clifford, J. Cioslowski, B. B. Stefanov, G. Liu, A. Liashenko, P. Piskorz, I. Komaromi, R. L. Martin, D. J. Fox, T. Keith, M. A. Al-Laham, C. Y. Peng, A. Nanayakkara, M. Challacombe, P. M. W. Gill, B. Johnson, W. Chen, M. W. Wong, C. Gonzalez, and J. A. Pople, Gaussian, Inc., Wallingford CT, 2004
55. A.A. Granovsky, J. Chem. Phys. **134**, 214113 (2011)
56. A.A. Granovsky, Firefly version 7.1.G, http://classic.chem.msu.su/gran/firefly/index.html
57. M.W. Schmidt, K.K. Baldridge, J.A. Boatz, S.T. Elbert, M.S. Gordon, J.H. Jensen, S. Koseki, N. Matsunaga, K.A. Nguyen, S. Su, T.L. Windus, M. Dupuis, J.A. Montgomery, J. Comput. Chem. **14**, 1347 (1993)
58. F. Wang, S.P. Neville, R. Wang, G.A. Worth, J. Phys. Chem. A **117**, 7298 (2013)
59. S.P. Neville, G.A. Worth, J. Chem. Phys. **140**, 034317 (2014)
60. J.C. Light, I.P. Hamilton, J.V. Lill, J. Chem. Phys. **82**, 1400 (1985)
61. G.A. Worth, M.H. Beck, A. Jäckle, H.-D. Meyer, computer code, The MCTDH Package, Version 8.2, University of Heidelberg, Heidelberg, Germany, 2000; H.-D. Meyer, computer code, The MCTDH Package, Version 8.3 (2002), Version 8.4 (2007). http://mctdh.uni-hd.de
62. M. Sala, S. Guérin, F. Gatti, Phys. Chem. Chem. Phys. **17**, 29518 (2015)

Part II
Laser Control of Unimolecular Processes

Chapter 6
Theoretical Tools for the Description of Strong Field Laser-Molecule Interaction

In this chapter, the main theoretical tools used in the work presented in the next two chapters on the laser control of the radiationless decay in pyrazine and of the tunneling dynamics in NHD_2, are introduced. After a brief discussion of the main approximations generally made in the study of laser-molecule interactions, presented in Sect. 6.1, we introduce in Sect. 6.2 the most basic tools for the laser control of population transfer in a two-level system. The derivation of an effective Hamiltonian allowing for the description of the interaction of a molecular system with a strong non-resonant laser pulse is presented in Sect. 6.3. The Floquet theory and the adiabatic Floquet theory are finally introduced in Sects. 6.4 and 6.5.

6.1 The Semi-classical Dipolar Approximation of Laser-Matter Interaction

The quantized nature of electromagnetic fields needs to be taken into account in situations where extremely low intensity fields are considered, typically in the single photon regime. However, ordinary laser fields used in the quantum control of atomic and molecular systems contain an extremely large number of photons, and in this case, the quantum nature of the electromagnetic fields can be neglected. Therefore, in this chapter, the electric fields associated with laser light will be considered as a classical entity. Consider a pulsed linearly polarized electric field of the form

$$\varepsilon(t) = \varepsilon_0 \Lambda(t) \cos(\omega t - \boldsymbol{k}.\boldsymbol{r} + \theta) \, \boldsymbol{e}, \tag{6.1}$$

where ε_0 is the peak amplitude, $\Lambda(t)$ is the envelope of the laser pulse, ω is the pulsation, θ is the initial phase and $\boldsymbol{e}$ the unitary vector describing the direction of polarization of the electric field. In most situations, the interaction of an atomic or molecular system with a (pulsed) laser field can be described within the *dipolar approximation*. This approximation is valid if the wavelength of the laser field is large

with respect to the dimension of the system. In the case of the molecular systems considered in this thesis, this assumption holds true for wavelengths up to the deep UV domain, where the wavelength is of the order of the hundred of nanometers. In this case, one can show that the interaction of the system with the electric field dominates that with the magnetic field. In addition, the spatial variations of the electric field can be neglected ($e^{ik \cdot r} = 1$) and the electric field can be recast as

$$\boldsymbol{E}(t) = A_0 \Lambda(t) \cos(\omega t + \theta) \boldsymbol{e}. \tag{6.2}$$

The total Hamiltonian operator $H(t)$ for a molecular system described by the Hamiltonian operator H_0, in interaction with such an electric field can be written in the dipolar approximation as

$$H(t) = H_0 + H_{int}(t) \tag{6.3}$$

with

$$H_{int}(t) = -\boldsymbol{\mu} . \boldsymbol{\varepsilon}(t). \tag{6.4}$$

In this last equation, $\boldsymbol{\mu}$ is the dipole moment operator which, for a molecule constituted of N_{nu} nuclei and N_{el} electrons, reads

$$\boldsymbol{\mu} = \sum_{\alpha=1}^{N_{nu}} Z_\alpha e \boldsymbol{R}_\alpha - \sum_{i=1}^{N_{el}} e \boldsymbol{r}_i, \tag{6.5}$$

where e is the charge of the electron and Z_α the charge of the αth nucleus, $\boldsymbol{R}_\alpha$ and $\boldsymbol{r}_i$ the position operators of the ith electron and αth nucleus.

6.2 Laser Driven Two-Level System

In this section, we consider a laser driven two-level system described by the Hamiltonian operator of Eq. (6.3), in the basis $\{|1\rangle, |2\rangle\}$ of eigenstates of H_0

$$H_0|n\rangle = E_n|n\rangle, \ n = 1, 2 \tag{6.6}$$

where H_{int} describes the interaction of the system with a classical linearly polarized pulsed electric field Eq. (6.2) within the dipolar approximation. In matrix form, the total hamiltonian in the basis $\left\{ |1\rangle \equiv \begin{bmatrix} 1 \\ 0 \end{bmatrix}, |2\rangle \equiv \begin{bmatrix} 0 \\ 1 \end{bmatrix} \right\}$ reads

$$H(t) = \begin{pmatrix} \omega_1 & \Omega(t) \cos(\omega t + \theta) \\ \Omega(t) \cos(\omega t + \theta) & \omega_2 \end{pmatrix} \tag{6.7}$$

where $\omega_n = E_n/\hbar$ is the Bohr pulsation associated with the eigenstate $|n\rangle$ and

$$\Omega(t) = -\varepsilon_0 \Lambda(t) \langle 1|\boldsymbol{\mu}|2\rangle \cdot \boldsymbol{e} \tag{6.8}$$

is called the Rabi frequency. We have assumed that the permanent dipole moment is zero in the states $|1\rangle$ and $|2\rangle$, i.e $\langle 1|\boldsymbol{\mu}|1\rangle = \langle 2|\boldsymbol{\mu}|2\rangle = 0$.

6.2.1 The Resonant Wave Approximation

In this subsection, we introduce the resonant wave approximation (RWA). This approximation, which is valid when the pulsation of the electric field is close to the resonance $|\omega_2 - \omega_1 - \omega| \ll |\Omega(t)|$, allows one to derive effective Hamiltonians that are easier to manipulate than the exact Hamiltonian. We first rewrite the Hamiltonian of Eq. (6.7) in a slightly different form

$$H(t) = \begin{pmatrix} 0 & \frac{1}{2}\Omega(t)\left(e^{i\omega t}e^{i\theta} + e^{-i\omega t}e^{-i\theta}\right) \\ \frac{1}{2}\Omega(t)\left(e^{i\omega t}e^{i\theta} + e^{-i\omega t}e^{-i\theta}\right) & \omega_2 - \omega_1 \end{pmatrix} \tag{6.9}$$

where E_1 has been chosen as the origin of the energies. In this last equation, the off-diagonal elements of the Hamiltonian are expressed as the sum of a resonant and an anti-resonant term. The resonant approximation consists in neglecting the anti-resonant terms. It comes

$$H(t) = \begin{pmatrix} 0 & \frac{1}{2}\Omega(t)e^{i\omega t}e^{i\theta} \\ \frac{1}{2}\Omega(t)e^{-i\omega t}e^{-i\theta} & \omega_2 - \omega_1 \end{pmatrix}. \tag{6.10}$$

The evolution of the system is governed by the time-dependent Schrödinger equation (TDSE)

$$H(t)|\Psi(t)\rangle = i\frac{\partial}{\partial t}|\Psi(t)\rangle \tag{6.11}$$

with $|\Psi(t)\rangle = c_1(t)|1\rangle + c_2(t)|2\rangle$. We now move to a frame rotating at the angular velocity ω using the unitary transormation

$$T_1 = \begin{pmatrix} 1 & 0 \\ 0 & e^{-i\omega t} \end{pmatrix}. \tag{6.12}$$

The state of the system in the new representation is given by $|\tilde{\Psi}(t)\rangle = T_1^\dagger |\Psi(t)\rangle$. The TDSE can be recast as

$$H(t)T_1|\tilde{\Psi}(t)\rangle = i\frac{\partial}{\partial t}\left[T_1|\tilde{\Psi}(t)\rangle\right]$$
$$= i\frac{\partial T_1}{\partial t}|\tilde{\Psi}(t)\rangle + iT_1\frac{\partial|\tilde{\Psi}(t)\rangle}{\partial t}. \tag{6.13}$$

Multiplying from the left by $T_1^\dagger$ on both sides and using the fact that T_1 is unitary $(T_1^\dagger = T_1^{-1})$ yields

$$\left[T_1^\dagger H(t) T_1 - i T_1^\dagger \frac{\partial T_1}{\partial t} \right] |\tilde{\Psi}(t)\rangle = i \frac{\partial}{\partial t} |\tilde{\Psi}(t)\rangle. \tag{6.14}$$

It is seen in this last equation that the evolution of the system in the new representation is governed by a time-dependent Schrödinger equation with the transformed Hamiltonian $\tilde{H}(t) = T_1^\dagger H(t) T_1 - i T_1^\dagger \frac{\partial T_1}{\partial t}$. Using the expressions of $H(t)$ and T_1 given in Eqs. (6.10) and (6.12), one obtains

$$\tilde{H}(t) = \begin{pmatrix} 0 & \frac{1}{2}\Omega(t)e^{i\theta} \\ \frac{1}{2}\Omega(t)e^{-i\theta} & \Delta \end{pmatrix}, \tag{6.15}$$

where $\Delta = \omega_2 - \omega_1 - \omega$ is called the detuning from the resonance.

6.2.2 The Rabi Model

In this section, we consider the interaction of a two-level system with a continuous laser field. The Hamiltonian of the system in the RWA is given by Eq. (6.15) with a constant Rabi frequency $\Omega(t) = \Omega_0$. In the present case, the Hamiltonian operator is time independent. Therefore, the state of the system at time t is given by

$$|\tilde{\Psi}(t)\rangle = \exp\left(\frac{-i\tilde{H}t}{\hbar} \right) |\tilde{\Psi}(t=0)\rangle. \tag{6.16}$$

Consider the transformation

$$T_2 = \begin{pmatrix} -\sin\frac{\phi}{2}e^{-i\frac{\theta}{2}} & \cos\frac{\phi}{2}e^{-i\frac{\theta}{2}} \\ \cos\frac{\phi}{2}e^{i\frac{\theta}{2}} & \sin\frac{\phi}{2}e^{i\frac{\theta}{2}} \end{pmatrix}, \tag{6.17}$$

where ϕ is such that

$$\tan\phi = -\frac{2|\Omega_0|}{\Delta}, \quad 0 \le \phi < \pi \tag{6.18}$$

This transformation diagonalizes the Hamiltonian $\tilde{H}$

$$T_2^\dagger \tilde{H} T_2 = D = \begin{pmatrix} \lambda_- & 0 \\ 0 & \lambda_+ \end{pmatrix} \tag{6.19}$$

with

$$\lambda_\mp = \frac{\Delta}{2} \mp \frac{1}{2}\sqrt{\Delta^2 + \Omega_0^2}. \tag{6.20}$$

Transforming Eq. (6.16) yields

$$|\tilde{\Psi}(t)\rangle = T_2 \exp\left(-iDt\right) T_2^{\dagger} |\tilde{\Psi}(t=0)\rangle. \tag{6.21}$$

Considering that the system is in the state $|1\rangle$ at $t = 0$, one obtains

$$|\tilde{\Psi}(t)\rangle = \frac{1}{2} \left(\begin{matrix} \left[e^{-i\lambda_+ t} + e^{-i\lambda_- t}\right] + \cos\phi \left[e^{-i\lambda_+ t} - e^{-i\lambda_- t}\right] \\ \sin\phi e^{i\theta} \left[e^{-i\lambda_+ t} - e^{-i\lambda_- t}\right] \end{matrix} \right). \tag{6.22}$$

The state of the system a time t expressed in the basis $\{|1\rangle, |2\rangle\}$ of eigenstates of H_0 is given by

$$|\Psi(t)\rangle = T_1 |\tilde{\Psi}(t)\rangle = \frac{1}{2} \left(\begin{matrix} \left[e^{-i\lambda_+ t} + e^{-i\lambda_- t}\right] + \cos\phi \left[e^{-i\lambda_+ t} - e^{-i\lambda_- t}\right] \\ \sin\phi e^{i\theta} e^{-i\omega t} \left[e^{-i\lambda_+ t} - e^{-i\lambda_- t}\right] \end{matrix} \right). \tag{6.23}$$

From this last equation, one can express the population $P_2(t)$ of the state $|2\rangle$ at time t, i.e the probability of population transfer between the states $|1\rangle$ and $|2\rangle$ induced by the laser field

$$P_2(t) = |\langle 2|\Psi(t)\rangle|^2 = \sin^2\phi \sin^2\left(\frac{\lambda_+ - \lambda_-}{2}t\right). \tag{6.24}$$

Using Eqs. (6.18) and (6.20), one finally obtains

$$P_2(t) = \frac{\Omega_0^2}{\Omega_0^2 + \Delta^2} \sin^2\left(\sqrt{\Omega_0^2 + \Delta^2}\frac{t}{2}\right). \tag{6.25}$$

This last equation shows that, in a two-level system interacting with a monochromatic continuous laser field, the population oscillates between the two states. The amplitude of the oscillations depends on the detuning. In particular, the populations oscillate between 0 and 1 when the laser field is exactly resonant. The period of the oscillations depends both on the amplitude and on the detuning. This phenomenon is called *Rabi oscillations*.

6.2.3 The π-pulse Technique

In this section, we consider the interaction of a two-level system with a resonant $(\Delta = 0)$ pulsed laser field. The RWA Hamiltonian for this system reads

$$\tilde{H}(t) = \left(\begin{matrix} 0 & \frac{1}{2}\Omega(t)e^{i\theta} \\ \frac{1}{2}\Omega(t)e^{-i\theta} & 0 \end{matrix} \right). \tag{6.26}$$

The Hamiltonian of Eq. (6.26) is first diagonalized

$$T_3^\dagger \tilde{H}(t) T_3 = D(t) \tag{6.27}$$

with

$$D(t) = \begin{pmatrix} -\frac{1}{2}\Omega_{12}(t) & 0 \\ 0 & \frac{1}{2}\Omega_{12}(t) \end{pmatrix} \tag{6.28}$$

using the time-independent transformation

$$T_3 = \begin{pmatrix} -\frac{1}{\sqrt{2}}e^{-i\frac{\theta}{2}} & \frac{1}{\sqrt{2}}e^{-i\frac{\theta}{2}} \\ \frac{1}{\sqrt{2}}e^{i\frac{\theta}{2}} & \frac{1}{\sqrt{2}}e^{i\frac{\theta}{2}} \end{pmatrix}. \tag{6.29}$$

We note that this transformation is equivalent to T_2 with $\phi = \frac{\pi}{2}$. The evolution of the system is governed by the TDSE

$$i\frac{\partial}{\partial t}|\bar{\Psi}(t)\rangle = D(t)|\bar{\Psi}(t)\rangle, \tag{6.30}$$

with $|\bar{\Psi}(t)\rangle = T_3^\dagger|\tilde{\Psi}(t)\rangle$. Assuming that the system is in the state $|1\rangle$ at the initial time

$$|\Psi(t=0)\rangle = |\tilde{\Psi}(t=0)\rangle = \begin{pmatrix} 1 \\ 0 \end{pmatrix}, \tag{6.31}$$

one obtains

$$|\bar{\Psi}(t=0)\rangle = T_3^\dagger|\tilde{\Psi}(t=0)\rangle = \begin{pmatrix} -\frac{1}{\sqrt{2}}e^{i\frac{\phi}{2}} \\ +\frac{1}{\sqrt{2}}e^{i\frac{\phi}{2}} \end{pmatrix}. \tag{6.32}$$

The solution of Eq. (6.30) is given by

$$|\bar{\Psi}(t)\rangle = \exp\left(-i\int_0^t D(t')dt'\right)|\bar{\Psi}(t=0)\rangle. \tag{6.33}$$

Coming back to the basis $\{|1\rangle, |2\rangle\}$ of eigenstates of H_0

$$\begin{aligned}|\Psi(t)\rangle &= T_1|\tilde{\Psi}(t)\rangle = T_1 T_3|\bar{\Psi}(t)\rangle \\ &= \begin{pmatrix} \cos\left(\int_0^t \frac{\Omega(t')}{2}dt'\right) \\ -ie^{i\theta}e^{-i\omega t}\sin\left(\int_0^t \frac{\Omega(t')}{2}dt'\right) \end{pmatrix}.\end{aligned} \tag{6.34}$$

The probability to find the system in the state $|2\rangle$ at time t is given by

$$|\langle 2|\Psi(t)\rangle|^2 = \sin^2\left(\int_0^t \frac{\Omega(t')}{2}dt'\right). \tag{6.35}$$

From this last equation, one can see that a resonant pulse yielding a Rabi frequency with an area that is an odd multiple of π will induce a complete population transfer between the states $|1\rangle$ and $|2\rangle$. In particular, a pulse such that $\int_0^t \Omega(t')dt' = \pi$ is called a π-pulse. The π-pulse corresponds to the lowest pulse area which induces a complete population transfer between two quantum states. This means that when the detuning is different from zero, a Rabi frequency area larger than π is needed to achieve a complete transfer [1]. In contrast, a resonant pulse yielding a Rabi frequency with an area that is an even multiple of π will induce a complete population return to the initial state.

We note here that the TDSE associated with the effective RWA Hamiltonian of Eq. (6.26) is analytically solvable because an exactly resonant laser pulse is considered. A general, non-resonant two-level model, with an arbitrary expression for the Rabi frequency $\Omega(t)$ and the (time-dependent) detuning $\Delta(t)$, is not analytically solvable. However, there exists a number of models with specific expressions for $\Omega(t)$ and $\Delta(t)$, for with analytical solutions of the TDSE are known. Examples of such models are the Rosen–Zener [2], Allen–Eberly [3] or the Demkov–Kunike [4] models, to cite only a few.

The π-pulse technique is known to be sensitive to the parameters of the laser field or to the details of the model used to describe the system. An efficient population transfer can only been obtained with a fine tuning of the laser field pulsation, amplitude and pulse shape. This feature makes the π-pulse technique difficult to implement experimentally, because the generation of a laser pulse with predefined values for the different parameters is difficult, and because the eigenenergies and coupling strengths of the system are, in general, only known with a finite precision. It is therefore of great importance to have access to a method that is able to produce a population transfer with a high efficiency and that is robust with respect to variations of the parameters of the laser field or to errors in the Hamiltonian matrix elements. This can be achieved by different methods including adiabatic passage [5, 6], composite pulse sequences [7], or population inversion by a phase jump [8]. These methods do not require a fine tuning of the parameters of the laser field to achieve efficient population transfers. However, the price to pay for this robustness is that one needs to spend more energy to produce a population transfer, that is to say, larger Rabi frequency areas are needed.

6.3 The Non-resonant Dynamic Stark Effect

In the previous section, the basic features of the interaction of a quasi-resonant laser field with a two-state quantum system have been presented. For this purpose, the RWA allows one to derive convenient effective Hamiltonians. The RWA only describes one-photon processes, which are dominant when quasi-resonant fields of moderate intensities are considered. In this section, we consider the interaction of a molecular system with a strong, non-resonant laser pulse. In this case, the system can not be reduced to a few-level system because the high intensity of the field induces

multi-photon processes that implies all the quantum states of the system. In the non-resonant case, these multi-photon processes essentially manifest themselves as Stark shifts, that is, shifts of the energy levels of the system induced by the electric field. The Stark effect induced by a static electric field is well known and discussed in many quantum mechanics textbooks. Similar shifts can be produced by oscillating electric fields. If the field oscillates slowly, the energy shifts follow adiabatically the instantaneous electric field as in the static case. On the other hand, if the frequency is high, the energy shifts no longer follow the instantaneous electric field, but rather its intensity envelope. This effect is known as the dynamic Stark effect [9, 10].

In many quantum systems, energy levels are organized in manifolds of close-lying levels, separated by large energy gaps. For instance molecules have electronic states which support a dense manifold of vibrational and rotational energy levels. In general, one is only interested in a subset of levels, called *essential states* in the following. For instance, one is often only interested in the dynamics of the system in the ground, or in the few lowest electronic states. It is therefore convenient to work with an effective Hamiltonian including explicitly the essential states, and including the influence of the non-essential states as Stark shifts.

6.3.1 The Adiabatic Elimination Approach

The derivation given in this section follows closely that given in Ref. [10]. Consider a molecular system described by the Hamiltonian operator H_0 such that

$$H_0|j\rangle = \hbar\omega_j|j\rangle, \tag{6.36}$$

where $\hbar\omega_j = E_j$ is the energy of the state $|j\rangle$. For simplicity, in the rest of this section, atomic units are assumed ($\hbar = 1$). The Hamiltonian for the system in interaction with a laser pulse of expression

$$\varepsilon(t) = \frac{1}{2}\varepsilon_0\Lambda(t)\left(e^{i\omega t} + e^{-i\omega t}\right)\boldsymbol{e} \tag{6.37}$$

in the dipolar approximation is given by

$$H(t) = H_0 - \boldsymbol{\mu}.\varepsilon(t). \tag{6.38}$$

The state of the system can be expressed in the basis of H_0 as

$$|\Psi(t)\rangle = \sum_j c_j(t)e^{-i\omega_j t}|j\rangle. \tag{6.39}$$

Inserting this expression in the TDSE yields

$$\sum_j c_j(t)e^{-i\omega_j t}\omega_j|j\rangle - \sum_j c_j(t)e^{-i\omega_j t}\boldsymbol{\mu}|j\rangle.\boldsymbol{\varepsilon}(t) = i\sum_j \left(\dot{c}_j(t)e^{-i\omega_j t} - i\omega_j e^{-i\omega_j t}c_j(t)\right)|j\rangle.$$
(6.40)

This last equation is now projected on a state $|j'\rangle$

$$c_{j'}(t)e^{-i\omega_{j'} t}\omega_{j'} - \sum_j c_j(t)e^{-i\omega_j t}\boldsymbol{\mu}_{j'j}.\boldsymbol{\varepsilon}(t) = i\dot{c}_{j'}(t)e^{-i\omega_{j'} t} + \omega_{j'}c_{j'}(t)e^{-i\omega_{j'} t}$$
(6.41)

with $\boldsymbol{\mu}_{j'j} = \langle j'|\boldsymbol{\mu}|j\rangle$, leading to

$$i\dot{c}_{j'}(t) = -\sum_j c_j(t)e^{-i(\omega_j - \omega_{j'})t}\boldsymbol{\mu}_{j'j}.\boldsymbol{\varepsilon}(t).$$
(6.42)

Here, the index j runs over all the states of the system. Let us now split the system into a group of essential states, indexed by the letters k and k', and a group of non-essential states, indexed by the letter l. For an essential state $|k'\rangle$, one obtains

$$i\dot{c}_{k'}(t) = -\sum_k c_k(t)e^{-i(\omega_k - \omega_{k'})t}\boldsymbol{\mu}_{k'k}.\boldsymbol{\varepsilon}(t) - \sum_l c_l(t)e^{-i(\omega_l - \omega_{k'})t}\boldsymbol{\mu}_{k'l}.\boldsymbol{\varepsilon}(t).$$
(6.43)

To obtain an equation free of any explicit occurence of the non-essential states, one needs to derive an expression for the $c_l(t)$ that can be susbsituted in Eq. (6.43). Starting from Eq. (6.42), assuming that the non-essential states are not populated initially ($c_l(-\infty) = 0$) and neglecting the couplings between the non-essential states ($\boldsymbol{\mu}_{ll'}.\boldsymbol{\varepsilon}(t) = 0$), one obtains

$$i\dot{c}_l(t) = -\sum_j c_j(t)e^{-i(\omega_j - \omega_l)t}\boldsymbol{\mu}_{lj}.\boldsymbol{\varepsilon}(t)$$
(6.44)

$$c_l(t) = \frac{i}{2}\int_{-\infty}^{t}\sum_k \left(e^{-i(\omega_k - \omega_l - \omega)t'} + e^{-i(\omega_k - \omega_l + \omega)t'}\right)\boldsymbol{\mu}_{lk}.\boldsymbol{A}(t')c_k(t')dt',$$
(6.45)

where $\boldsymbol{A}(t) = \varepsilon_0\Lambda(t)\boldsymbol{e}$. This last expression can be integrated by parts repeatedly to yield

$$c_l(t) = -\frac{1}{2}\sum_{s=0}^{\infty}\sum_k (-i)^s\left(\frac{e^{-i(\omega_k - \omega_l - \omega)t}}{(\omega_k - \omega_l - \omega)^{s+1}} + \frac{e^{-i(\omega_k - \omega_l + \omega)t}}{(\omega_k - \omega_l + \omega)^{s+1}}\right)\boldsymbol{\mu}_{lk}.\frac{d^s}{dt^s}\left[\boldsymbol{A}(t)c_j(t)\right].$$
(6.46)

This last equation can be simplified if we assume that the product $A(t)c_k(t)$ varies slowly in time. In this case, the time derivatives can be neglected and only the s=0 term is retained

$$c_l(t) = -\frac{1}{2}\sum_k \left(\frac{e^{-i(\omega_k - \omega_l - \omega)t}}{\omega_k - \omega_l - \omega} + \frac{e^{-i(\omega_k - \omega_l + \omega)t}}{\omega_k - \omega_l + \omega} \right) \boldsymbol{\mu}_{lk}.\boldsymbol{A}(t)c_k(t). \qquad (6.47)$$

This expression of the $c_l(t)$ can now be inserted in Eq. (6.43). After some manipulation, one obtains

$$i\dot{c}_{k'}(t) = -\sum_k c_k(t)e^{-i(\omega_k - \omega_{k'})t}\boldsymbol{\mu}_{k'k}.\boldsymbol{\varepsilon}(t)$$

$$-\frac{1}{4}\sum_k\sum_l c_k(t)e^{-i(\omega_k - \omega_{k'})t}\boldsymbol{\mu}_{k'l}.\boldsymbol{A}(t)\boldsymbol{\mu}_{pk}.\boldsymbol{A}(t)\left(\frac{e^{2i\omega t}+1}{\omega_l - \omega_k - \omega} + \frac{e^{-2i\omega t}+1}{\omega_l - \omega_k + \omega} \right).$$
$$(6.48)$$

Considering that the field is far from any resonance between the essential and non-essential states $\omega \ll \omega_l - \omega_k$, this last equation simplifies to

$$i\dot{c}_{k'}(t) = -\sum_k c_k(t)e^{-i(\omega_k - \omega_{k'})t}\boldsymbol{\mu}_{k'k}.\boldsymbol{\varepsilon}(t)$$

$$-\sum_k\sum_l c_k(t)e^{-i(\omega_k - \omega_{k'}')t}\frac{\boldsymbol{\mu}_{k'l}.\boldsymbol{e}\boldsymbol{\mu}_{lk}.\boldsymbol{e}}{\omega_l - \omega_k}\varepsilon_0^2\Lambda^2(t)\cos^2\omega t, \qquad (6.49)$$

or in matrix form

$$i\frac{\partial}{\partial t}\boldsymbol{\Psi}(t) = \left[\boldsymbol{H_0} + \boldsymbol{H}_{int}^{eff}(t) \right]\boldsymbol{\Psi}(t) \qquad (6.50)$$

with

$$(H_{int}^{eff}(t))_{k'k} = -\boldsymbol{\mu}_{k'k}.\boldsymbol{\varepsilon}(t)\boldsymbol{e} - \sum_l \frac{\boldsymbol{\mu}_{k'l}.\boldsymbol{e}\boldsymbol{\mu}_{lk}.\boldsymbol{e}}{\omega_l - \omega_k}\varepsilon^2(t). \qquad (6.51)$$

This effective interaction Hamiltonian operator is difficult to evaluate as it requires the knowledge of the transition dipole moments between the essential states and all the non-essential states. For a general molecular system, there is an infinity of such states, including bound states but also the various continua. In practice however, one can further approximate the second term of Eq. (6.51) by neglecting the (ro)vibrational structure of the non-essential electronic states. This term can then be expressed as a function of static electronic polarizabilities, that can be computed using standard electronic structure methods available in the major quantum chemistry program packages.

6.3.2 Connection with the Static Electronic Polarizability

Let us first rewrite Eq. (6.51) including explicitly the (ro)vibrational structure of each electronic state

$$(H_{int}^{eff}(t))_{km_k k' m'_{k'}} = -\boldsymbol{\mu}_{km_k k' m'_{k'}}.\varepsilon(t)\boldsymbol{e} - \sum_l \sum_{n_l} \frac{\boldsymbol{\mu}_{km_k l n_l}.\boldsymbol{e} \boldsymbol{\mu}_{l n_p k' m'_{k'}}.\boldsymbol{e}}{\omega_{l n_l} - \omega_{k' m'_{k'}}} \varepsilon^2(t). \quad (6.52)$$

Here, m_k denotes the mth (ro)vibrational state of the kth essential electronic state. Similarly, n_l denotes the nth (ro)vibrational state of the lth non-essential electronic state. Approximating the vibronic energy differences by average electronic energy differences $\omega_{l n_l} - \omega_{k' m'_{k'}} \approx \overline{\omega_l} - \overline{\omega_k}$, this last equation can be recast as

$$\begin{aligned}
(H_{int}^{eff}(t))_{km_k k' m'_{k'}} &= \langle m_k|(H_{int}^{eff}(\boldsymbol{Q}, t))_{kk'}|m'_{k'}\rangle \\
&= -\langle m_k|\boldsymbol{\mu}_{kk'}(\boldsymbol{Q}).\varepsilon(t)\boldsymbol{e}|m'_{k'}\rangle \\
&\quad - \sum_l \sum_{n_l} \langle m_k| \frac{\boldsymbol{\mu}_{kl}(\boldsymbol{Q}).\boldsymbol{e}|n_l\rangle\langle n_l|\boldsymbol{\mu}_{lk'}(\boldsymbol{Q}).\boldsymbol{e}}{\overline{\omega_l} - \overline{\omega_{k'}}}|m'_{k'}\rangle \varepsilon^2(t) \\
&= -\langle m_k|\boldsymbol{\mu}_{kl}(\boldsymbol{Q}).\varepsilon(t)\boldsymbol{e}|m'_{k'}\rangle \\
&\quad - \sum_l \langle m_k| \frac{\boldsymbol{\mu}_{kl}(\boldsymbol{Q}).\boldsymbol{e}\boldsymbol{\mu}_{lk'}(\boldsymbol{Q}).\boldsymbol{e}}{\overline{\omega_l} - \overline{\omega_{k'}}}|m'_{k'}\rangle \varepsilon^2(t),
\end{aligned} \quad (6.53)$$

where the closure relation $\sum_{n_l} |n_l\rangle\langle n_l| = I$ has been used, and $\boldsymbol{Q}$ is a vector collecting the nuclear coordinates of the molecular system. An element of the $H_{int}^{eff}(t)$ operator in the basis of the essential electronic states reads

$$(H_{int}^{eff}(t))_{kk'} = -\boldsymbol{\mu}_{kk'}(\boldsymbol{Q}).\varepsilon(t)\boldsymbol{e} - \sum_l \frac{\boldsymbol{\mu}_{kl}(\boldsymbol{Q}).\boldsymbol{e}\boldsymbol{\mu}_{lk'}(\boldsymbol{Q}).\boldsymbol{e}}{\overline{\omega_l} - \overline{\omega_{k'}}} \varepsilon^2(t). \quad (6.54)$$

Further assuming that $\overline{\omega_l} - \overline{\omega_{k'}} \approx V_l(\boldsymbol{Q}) - V_{k'}(\boldsymbol{Q})$, where $V_{k'}(\boldsymbol{Q})$ and $V_l(\boldsymbol{Q})$ are the adiabatic electronic eigenvalues (i.e, the adiabatic PESs) of the essential and non-essential states respectively, one can rewrite Eq. (6.54) as

$$(H_{int}^{eff}(t))_{kk'} = -\boldsymbol{\mu}_{kk'}(\boldsymbol{Q}).\varepsilon(t)\boldsymbol{e} - \sum_l \frac{\boldsymbol{\mu}_{kl}(\boldsymbol{Q}).\boldsymbol{e}\boldsymbol{\mu}_{lk'}(\boldsymbol{Q}).\boldsymbol{e}}{V_l(\boldsymbol{Q}) - V_{k'}(\boldsymbol{Q})} \varepsilon^2(t). \quad (6.55)$$

Introducing the static electronic polarizability $\alpha(\boldsymbol{Q})$, one finally obtains

$$(H_{int}^{eff}(t))_{kk'} = -\boldsymbol{\mu}_{kk'}(\boldsymbol{Q}).\varepsilon(t)\boldsymbol{e} - \boldsymbol{e}.\left[\frac{1}{2}\boldsymbol{\alpha}_{kk'}(\boldsymbol{Q}) - \sum_{k'' \neq k, k'} \frac{\boldsymbol{\mu}_{kk''}(\boldsymbol{Q})\boldsymbol{\mu}_{k''k'}(\boldsymbol{Q})}{V_{k''}(\boldsymbol{Q}) - V_{k'}(\boldsymbol{Q})}\right].\boldsymbol{e}\varepsilon^2(t). \quad (6.56)$$

The first term of this last equation is the exact dipolar interaction Hamiltonian of the system in the subspace of the essential states. The second term adds the influence of all the non-essential electronic states at the second order, including Stark shifts but also two-photon transitions.

6.4   The Floquet Theory

The Floquet theory provides a general formalism that allows one to describe and analyze the dynamics of a quantum system in interaction with a periodic radiation in terms of dressed states and quasienergies, which are the eigenelements of a time-independent Floquet Hamiltonian operator. The Floquet theory connects the purely quantum description of the interaction between light and matter, where both the system and the electromagnetic field are quantized, to the semiclassical description where the electromagnetic field is described classically. The classical field corresponds to a coherent state with a very large number of available photons, from which a few can be exchanged with the matter. The Floquet theory allows one to characterize this exchange by counting the number of photons taken from or given to the classical field. Technically, in the Floquet theory, one replaces the periodic time variable by an auxilliary dynamical variable. Therefore, the Floquet theory can be viewed as a mathematical tool allowing one to transform a time-dependent problem, described by a system of linear differential equations in the Hilbert space $\mathcal{H}$, into a time-independent problem, described by an eigenvalue problem in an enlarged Hilbert space $\mathcal{K}$ which takes into account the photons of the classical field.

Consider a molecular system described by the Hamiltonian operator $H_0(\boldsymbol{r}, \boldsymbol{R})$ where $\boldsymbol{r}$ and $\boldsymbol{R}$ are vectors containing the electronic and nuclear coordinates, respectively. This Hamiltonian acts in the Hilbert space $\mathcal{H}$ spanned by the basis of eigenstates of H_0. The dynamics of the system in interaction with a periodic electric field $\varepsilon(t) = \boldsymbol{\varepsilon_0} \cos(\omega t + \theta)$ with $\boldsymbol{\varepsilon_0} = \varepsilon_0 \boldsymbol{e}$ in the semiclassical dipole approximation is described by the TDSE

$$H(\boldsymbol{r}, \boldsymbol{R}, \theta + \omega t)\psi(\boldsymbol{r}, \boldsymbol{R}, t) = i\frac{\partial}{\partial t}\psi(\boldsymbol{r}, \boldsymbol{R}, t) \tag{6.57}$$

with $H(\boldsymbol{r}, \boldsymbol{R}, \theta + \omega t) = H_0(\boldsymbol{r}, \boldsymbol{R}) - \boldsymbol{\mu}(\boldsymbol{r}, \boldsymbol{R}).\varepsilon(t)$. We use the initial 2π-periodic phase θ to introduce the Hilbert space $\mathcal{L}$ of the square integrable functions on the circle of length 2π, with the scalar product

$$\langle \xi_1|\xi_2 \rangle = \int \frac{d\theta}{2\pi}\xi_1^*(\theta)\xi_2(\theta). \tag{6.58}$$

This space is spanned by the basis $\{|\xi_k\rangle, k \in \mathbb{Z}\}$ with $\langle \theta|\xi_k \rangle = e^{ik\theta}$. We introduce a time-independent Hamiltonian, called the Floquet Hamiltonian, acting in the enlarged Hilbert space $\mathcal{K} = \mathcal{H} \otimes \mathcal{L}$ defined as

$$K(\boldsymbol{r}, \boldsymbol{R}, \theta) = -i\omega \frac{\partial}{\partial \theta} + H(\boldsymbol{r}, \boldsymbol{R}, \theta)$$

$$= -i\omega \frac{\partial}{\partial \theta} + H_0(\boldsymbol{r}, \boldsymbol{R}) - \boldsymbol{\mu}(\boldsymbol{r}, \boldsymbol{R}).\boldsymbol{\varepsilon_0} \cos(\theta). \tag{6.59}$$

Below, we show that the dynamics in $\mathcal{H}$ given by Eq. (6.57) can be recovered from the dynamics in $\mathcal{K}$ defined by the TDSE

$$K(\boldsymbol{r}, \boldsymbol{R}, \theta)\Psi_K(\boldsymbol{r}, \boldsymbol{R}, \theta, t) = i\frac{\partial}{\partial t}\Psi_K(\boldsymbol{r}, \boldsymbol{R}, \theta, t). \tag{6.60}$$

The advantage is that the Floquet Hamiltonian is time-independent, leading to the simple propagator

$$U_K(t, t_0, \theta) = e^{-iK(t-t_0)} \tag{6.61}$$

verifying

$$\Psi_K(\boldsymbol{r}, \boldsymbol{R}, \theta, t) = U_K(t, t_0, \theta)\Psi_K(\boldsymbol{r}, \boldsymbol{R}, \theta, t_0). \tag{6.62}$$

To prove the correspondance between Eqs. (6.57) and (6.60), we introduce the phase translation operator $\mathcal{T}_{\omega t} = e^{\omega t \frac{\partial}{\partial \theta}}$ acting on a wavefunction $\xi(\theta)$ of $\mathcal{L}$ as

$$\mathcal{T}_{\omega t}\xi(\theta) = \xi(\theta + \omega t), \tag{6.63}$$

and which is such that

$$\psi(\boldsymbol{r}, \boldsymbol{R}, t) = \mathcal{T}_{\omega t}\Psi_K(\boldsymbol{r}, \boldsymbol{R}, \theta, t) = \Psi_K(\boldsymbol{r}, \boldsymbol{R}, \theta + \omega t, t) \tag{6.64}$$

Inserting this last equation in Eq. (6.57), one obtains

$$H(\boldsymbol{r}, \boldsymbol{R}, \theta + \omega t)\mathcal{T}_{\omega t}\Psi_K(\boldsymbol{r}, \boldsymbol{R}, \theta, t) = i\frac{\partial}{\partial t}[\mathcal{T}_{\omega t}\Psi_K(\boldsymbol{r}, \boldsymbol{R}, \theta, t)]$$

$$= i\frac{\partial \mathcal{T}_{\omega t}}{\partial t}\Psi_K(\boldsymbol{r}, \boldsymbol{R}, \theta, t) + i\mathcal{T}_{\omega t}\frac{\partial \Psi_K(\boldsymbol{r}, \boldsymbol{R}, \theta, t)}{\partial t}$$

$$= i\omega \mathcal{T}_{\omega t}\frac{\partial}{\partial \theta}\Psi_K(\boldsymbol{r}, \boldsymbol{R}, \theta, t) + i\mathcal{T}_{\omega t}\frac{\partial \Psi_K(\boldsymbol{r}, \boldsymbol{R}, \theta, t)}{\partial t}. \tag{6.65}$$

Applying the operator $\mathcal{T}_{-\omega t}$ on both members of this last equation leads to

$$H(\boldsymbol{r}, \boldsymbol{R}, \theta)\Psi_K(\boldsymbol{r}, \boldsymbol{R}, \theta, t) = \left[i\omega\frac{\partial}{\partial \theta} + i\frac{\partial}{\partial t}\right]\Psi_K(\boldsymbol{r}, \boldsymbol{R}, \theta, t). \tag{6.66}$$

One finally obtains

$$\left[H(\boldsymbol{r}, \boldsymbol{R}, \theta) - i\omega\frac{\partial}{\partial \theta}\right]\Psi_K(\boldsymbol{r}, \boldsymbol{R}, \theta, t) = i\frac{\partial}{\partial t}\Psi_K(\boldsymbol{r}, \boldsymbol{R}, \theta, t). \tag{6.67}$$

Using the fact that the Floquet Hamiltonian is time-independent, the solution of the TDSE in $\mathcal{H}$ Eq. (6.57) can be directly expressed as a function of the eigenstates and eigenvalues obtained through

$$K(\boldsymbol{r}, \boldsymbol{R}, \theta)\Phi_\nu(\boldsymbol{r}, \boldsymbol{R}, \theta) = \lambda_\nu \Phi_\nu(\boldsymbol{r}, \boldsymbol{R}, \theta). \tag{6.68}$$

Using Eqs. (6.62) and (6.64), one may write

$$\begin{aligned}
\psi(\boldsymbol{r}, \boldsymbol{R}, t) &= \mathcal{T}_{\omega t} e^{-iK(t-t_0)} \Psi_K(\boldsymbol{r}, \boldsymbol{R}, \theta, t_0) \\
&= \mathcal{T}_{\omega t} e^{-iK(t-t_0)} \mathcal{T}_{-\omega t_0} \psi(\boldsymbol{r}, \boldsymbol{R}, t_0) \otimes 1_{\mathcal{L}}. \tag{6.69}
\end{aligned}$$

where $\psi(\boldsymbol{r}, \boldsymbol{R}, t_0) \otimes 1_{\mathcal{L}}$ denotes the initial wavefunction $\psi(\boldsymbol{r}, \boldsymbol{R}, t_0)$ lifted in $\mathcal{K}$. Expanding $\psi(\boldsymbol{r}, \boldsymbol{R}, t_0) \otimes 1_{\mathcal{L}}$ in terms of the eigenfunctions of K one may write

$$\begin{aligned}
\psi(\boldsymbol{r}, \boldsymbol{R}, t) &= \sum_\nu c_\nu e^{-i\lambda_\nu(t-t_0)} \mathcal{T}_{\omega(t-t_0)} \Phi_\nu(\boldsymbol{r}, \boldsymbol{R}, \theta) \\
&= \sum_\nu c_\nu e^{-i\lambda_\nu(t-t_0)} \Phi_\nu(\boldsymbol{r}, \boldsymbol{R}, \theta + \omega(t - t_0)). \tag{6.70}
\end{aligned}$$

The coefficients c_ν can be expressed as

$$\begin{aligned}
c_\nu &= \langle \Phi_\nu(\boldsymbol{r}, \boldsymbol{R}, \theta) | \psi(\boldsymbol{r}, \boldsymbol{R}, t_0) \otimes 1_{\mathcal{L}} \rangle_{\mathcal{K}} \\
&= \int d\boldsymbol{r} d\boldsymbol{R} \int \frac{d\theta}{2\pi} \Phi_\nu^*(\boldsymbol{r}, \boldsymbol{R}, \theta) \psi(\boldsymbol{r}, \boldsymbol{R}, t_0) \\
&= \int d\boldsymbol{r} d\boldsymbol{R} \overline{\Phi}_\nu^*(\boldsymbol{r}, \boldsymbol{R}) \psi(\boldsymbol{r}, \boldsymbol{R}, t_0) \\
&= \langle \overline{\Phi}_\nu(\boldsymbol{r}, \boldsymbol{R}) | \psi(\boldsymbol{r}, \boldsymbol{R}, t_0) \rangle_{\mathcal{H}} \tag{6.71}
\end{aligned}$$

where $\overline{\Phi}_\nu(\boldsymbol{r}, \boldsymbol{R}) = \int \frac{d\theta}{2\pi} \Phi_\nu(\boldsymbol{r}, \boldsymbol{R}, \theta)$ is the average of $\Phi_\nu(\boldsymbol{r}, \boldsymbol{R}, \theta)$ over the phase.

The eigenelements of the Floquet Hamiltonian have a periodic structure $\Phi_\nu(\boldsymbol{r}, \boldsymbol{R}, \theta) \equiv \Phi_{n,k}(\boldsymbol{r}, \boldsymbol{R}, \theta) = \Phi_{n,0}(\boldsymbol{r}, \boldsymbol{R}, \theta)e^{ik\theta}$ and $\lambda_\nu \equiv \lambda_{n,k} = \lambda_{n,0} + k\omega$, where the index n refers to the Hilbert space $\mathcal{H}$. The Floquet eigenstates can thus be classified in families labeled by n with individual elements of a given family distinguished by the index k. This property allows one to simplify the expansion in terms of the eigenstates of the Floquet Hamiltonian by considering only a single member of each family, e.g. the $k=0$ member, as shown below. Eq. (6.71) can be recast as

$$\begin{aligned}
\psi(\boldsymbol{r}, \boldsymbol{R}, t) &= \sum_{n,k} c_{n,k} e^{-i(\lambda_{n,0}+k\omega)(t-t_0)} \Phi_{n,0}(\boldsymbol{r}, \boldsymbol{R}, \theta + \omega(t - t_0))e^{ik(\theta + \omega(t-t_0))} \\
&= \sum_{n,k} c_{n,k} e^{-i\lambda_{n,0}(t-t_0)} \Phi_{n,0}(\boldsymbol{r}, \boldsymbol{R}, \theta + \omega(t - t_0))e^{ik\theta} \\
&= \sum_n \tilde{c}_n(\theta) \Phi_{n,0}(\boldsymbol{r}, \boldsymbol{R}, \theta + \omega(t - t_0)) \tag{6.72}
\end{aligned}$$

with $\tilde{c}_n(\theta) = \sum_k c_{n,k} e^{ik\theta}$. To find an expression for the coefficients, we start from Eq. (6.71)

$$\tilde{c}_n(\theta) = \sum_k \langle \Phi_{n,k}(\boldsymbol{r}, \boldsymbol{R}, \theta) | \psi(\boldsymbol{r}, \boldsymbol{R}, t_0) \otimes 1_\mathcal{L} \rangle_\mathcal{K} e^{ik\theta}$$

$$= \sum_k \int d\boldsymbol{r} d\boldsymbol{R} \int \frac{d\theta'}{2\pi} \Phi_{n,0}^*(\boldsymbol{r}, \boldsymbol{R}, \theta') e^{-ik\theta'} \psi(\boldsymbol{r}, \boldsymbol{R}, t_0) e^{ik\theta}. \quad (6.73)$$

To calculate the integral over θ', we first decompose the function $\Phi_{n,0}^*(\boldsymbol{r}, \boldsymbol{R}, \theta')$ as

$$\Phi_{n,0}^*(\boldsymbol{r}, \boldsymbol{R}, \theta') = \sum_l a_l(\boldsymbol{r}, \boldsymbol{R}) e^{il\theta'}. \quad (6.74)$$

One may then write

$$\sum_k \int \frac{d\theta'}{2\pi} \Phi_{n,0}^*(\boldsymbol{r}, \boldsymbol{R}, \theta') e^{-ik\theta'} e^{ik\theta} = \sum_k \sum_l a_l(\boldsymbol{r}, \boldsymbol{R}) \int \frac{d\theta'}{2\pi} e^{i(l-k)\theta'} e^{ik\theta}$$

$$= \sum_k \sum_l a_l(\boldsymbol{r}, \boldsymbol{R}) e^{ik\theta} \delta_{kl}$$

$$= \sum_k a_k e^{ik\theta}$$

$$= \Phi_{n,0}^*(\boldsymbol{r}, \boldsymbol{R}, \theta). \quad (6.75)$$

Plugging this last result in Eq. (6.73), one finally obtains

$$\tilde{c}_n(\theta) = \langle \Phi_{n,0}(\boldsymbol{r}, \boldsymbol{R}, \theta) | \psi(\boldsymbol{r}, \boldsymbol{R}, t_0) \rangle_\mathcal{H}. \quad (6.76)$$

6.5 The Adiabatic Floquet Theory

The formalism presented in the previous section only applies to the case of a periodic Hamiltonian, i.e to the case of a system interacting with a continuous laser field. However, the Floquet formalism can be extended to the study of the interaction of quantum systems with pulsed lasers with slowly varying envelopes, frequencies or polarisation direction [11, 12]. The corresponding time-dependent Floquet Schrödinger equation, defined as the TDSE with the Floquet Hamiltonian, only depends on time through the slowly varying field parameters. It can therefore be treated using an adiabatic approximation, by studying the instantaneous eigenelements of the Floquet Hamiltonian as a function of the slow parameters. In this context, the adiabatic Floquet theory provides an intuitive, geometric, interpretation of the laser driven dynamics.

6.5.1   The Floquet Schrödinger Equation for Pulsed Laser Fields

Consider a molecular system described by the Hamiltonian operator $H_0(\mathbf{r}, \mathbf{R})$ in inter-action with a pulsed laser field with slowly varying envelope and frequency. Below, for ease of notation, the dependence of the various operators and wavefunctions on the electronic and nuclear coordinates $\mathbf{r}$ and $\mathbf{R}$ is dropped. In the semiclassical dipolar approximation, the total Hamiltonian operator of the system reads

$$H(\theta + g(t); \omega(t), \varepsilon(t)) = H_0 - \boldsymbol{\mu}.\mathbf{e}A(t)\cos(\theta + g(t)), \qquad (6.77)$$

where $g(t) = \omega(t)t$ and $A(t) = \varepsilon_0\Lambda(t)$ and $\Lambda(t)$ is the envelope of the pulsed electric field. We introduce the translation operator $\mathcal{T}_{g(t)} = e^{g(t)\frac{\partial}{\partial\theta}}$ acting in $\mathcal{L}$ as $\mathcal{T}_{g(t)}\xi(\theta) = \xi(\theta + g(t))$, and the wavefunction of $\mathcal{K}$ $\Psi_K(\theta, t)$ such that

$$\psi(t; \theta) = \mathcal{T}_{g(t)}\Psi_K(\theta, t) = \Psi_K(\theta + g(t), t). \qquad (6.78)$$

To derive the Floquet operator associated with the Hamiltonian Eq. (6.77), we start from the TDSE

$$H(\theta + g(t); \omega(t), A(t))\psi(t; \theta) = i\frac{\partial}{\partial t}\psi(t; \theta) \qquad (6.79)$$

and insert Eq. (6.78)

$$H(\theta + g(t); \omega(t), A(t))\mathcal{T}_{g(t)}\Psi_K(\theta, t) = i\frac{\partial}{\partial t}\left[\mathcal{T}_{g(t)}\Psi_K(\theta, t)\right]. \qquad (6.80)$$

The derivation is analogous to the one given in Eqs. (6.65)–(6.67) and leads to the Floquet time-dependent Schrödinger equation

$$K(\theta; \omega(t), A(t))\Psi_K(\theta, t) = i\frac{\partial}{\partial t}\Psi_K(\theta, t) \qquad (6.81)$$

with the Floquet Hamiltonian operator

$$K(\theta; \omega(t), A(t)) = H(\theta; \omega(t), A(t)) - i\omega_{eff}(t)\frac{\partial}{\partial\theta} \qquad (6.82)$$

where

$$\omega_{eff}(t) = \frac{dg(t)}{dt} = \omega(t) + \dot{\omega}t. \qquad (6.83)$$

We note the appearance of an effective instantaneous frequency $\omega_{eff}(t)$ in the Floquet Hamiltonian, which is the derivative of the phase of the field. The correspondance between the semiclassical TDSE and its Floquet counterpart is exact and does not

relie on the slow variations of the parameters of the field. However, because the Floquet Hamiltonian only depends on time through these parameters, it is well suited to an adiabatic analysis, where the dynamics of the system can be related to the instantaneous eigenstates of the Floquet Hamiltonian.

6.5.2 The Adiabatic Approximation for the Time-Dependent Floquet Schrödinger Equation

To study the Floquet Schrödinger equation using adiabatic principles, it is convenient to consider explicitly a characteristic time τ for the slow parameters. Here τ is interpreted as the pulse duration. We introduce the following notations $A(t) = \tilde{A}(s)$ and $\omega_{eff}(t) = \tilde{\omega}_{eff}(s)$, where $s = t/\tau$ is a reduced time. Gathering the slow parameters in a vector $\boldsymbol{\eta}(s)$, the Floquet Schrödinger equation Eq. (6.81) can be recast as

$$K(\theta; \boldsymbol{\eta}(s))\Psi_K(\theta, \tau s) = \frac{i}{\tau}\frac{\partial}{\partial s}\Psi_K(\theta, \tau s). \tag{6.84}$$

Let $\{\Phi_m(\theta; \boldsymbol{\eta}(s))\}$ be an orthonormal basis of instantaneous eigenvectors of the Floquet Hamiltonian with the associated eigenvalues $\lambda_m(\boldsymbol{\eta}(s))$. We define the unitary operator

$$T(\boldsymbol{\eta}(s)) = \sum_m |\Phi_m(\theta; \boldsymbol{\eta}(s))\rangle\langle\Phi_m(\theta; \boldsymbol{\eta}(s_0))| \tag{6.85}$$

where s_0 is the initial time. This operator diagonalizes the Floquet Hamiltonian at all times in the basis $\{\Phi_m(\theta; \boldsymbol{\eta}(s_0))\}$ of the Floquet Hamiltonian taken at $s = s_0$

$$T^\dagger(\boldsymbol{\eta}(s))K(\theta; \boldsymbol{\eta}(s))T(\boldsymbol{\eta}(s)) = D(\boldsymbol{\eta}(s)). \tag{6.86}$$

Defining transformed states by

$$\tilde{\Psi}_K(\theta, s) = T^\dagger(\boldsymbol{\eta}(s))\Psi_K(\theta, \tau s) \tag{6.87}$$

the Floquet Schrödinger equation (6.84) can be recast as

$$\left[D(\boldsymbol{\eta}(s)) - \frac{i}{\tau}T^\dagger(\boldsymbol{\eta}(s))\frac{\partial T(\boldsymbol{\eta}(s))}{\partial s}\right]\tilde{\Psi}_K(\theta, s) = \frac{i}{\tau}\frac{\partial}{\partial s}\tilde{\Psi}_K(\theta, s). \tag{6.88}$$

The time-dependent wavefunction can be expanded in the basis of the instantaneous eigenfunctions of the Floquet operator

$$\Psi_K(\theta, \tau s) = \sum_m c_m(\tau s)\Phi_m(\theta; \boldsymbol{\eta}(s)). \tag{6.89}$$

Using this definition and Eq. (6.87), one may write

$$\tilde{\Psi}_K(\theta, s) = \sum_m c_m(\tau s)\Phi_m(\theta; \boldsymbol{\eta}(s_0)). \tag{6.90}$$

Inserting this definition in Eq. (6.88) yields

$$\sum_m c_m(\tau s)\lambda_m(\boldsymbol{\eta}(s))\Phi_m(\theta; \boldsymbol{\eta}(s_0))$$

$$- \frac{i}{\tau} \sum_{m',m} c_m(\tau s)\langle\Phi_{m'}(\theta; \boldsymbol{\eta}(s))|\frac{\partial}{\partial s}|\Phi_m(\theta; \boldsymbol{\eta}(s))\rangle\Phi_{m'}(\theta; \boldsymbol{\eta}(s_0))$$

$$= \frac{i}{\tau} \sum_m \frac{\partial c_m(\tau s)}{\partial s}\Phi_m(\theta; \boldsymbol{\eta}(s_0)). \tag{6.91}$$

Projecting this last equation on a transformed state

$$\tilde{\Phi}_n(\theta; \boldsymbol{\eta}(s)) = T^\dagger(\boldsymbol{\eta}(s))\Phi_n(\theta; \boldsymbol{\eta}(s)) = \Phi_n(\theta; \boldsymbol{\eta}(s_0)) \tag{6.92}$$

leads to

$$c_n(\tau s)\lambda_n(\boldsymbol{\eta}(s)) - \frac{i}{\tau} \sum_m c_m(\tau s)\langle\Phi_n(\theta; \boldsymbol{\eta}(s))|\frac{\partial}{\partial s}|\Phi_m(\theta; \boldsymbol{\eta}(s))\rangle = \frac{i}{\tau}\frac{\partial c_n(\tau s)}{\partial s}. \tag{6.93}$$

This last equation constitutes a system of coupled differential equations, with non-adiabatic coupling terms $-\frac{i}{\tau}\langle\Phi_n(\theta; \boldsymbol{\eta}(s))|\frac{\partial}{\partial s}|\Phi_m(\theta; \boldsymbol{\eta}(s))\rangle$. In the adiabatic limit $\tau \to \infty$, these terms can be neglected and one obtains

$$\left[\lambda_n(\boldsymbol{\eta}(s)) - \frac{i}{\tau}\langle\Phi_n(\theta; \boldsymbol{\eta}(s))|\frac{\partial}{\partial s}|\Phi_n(\theta; \boldsymbol{\eta}(s))\rangle\right]c_n(\tau s) = \frac{i}{\tau}\frac{\partial c_n(\tau s)}{\partial s}, \tag{6.94}$$

or equivalently

$$\left[\lambda_n(\boldsymbol{\eta}(t)) - i\langle\Phi_n(\theta; \boldsymbol{\eta}(t))|\frac{\partial}{\partial t}|\Phi_n(\theta; \boldsymbol{\eta}(t))\rangle\right]c_n(t) = i\frac{\partial c_n(t)}{\partial t}. \tag{6.95}$$

This last equation shows that, in the adiabatic limit, the dynamics is restricted to the subspace of $\mathcal{K}$ containing the initial wavefunction $\Psi_K(\theta, t_0)$. Specifically, if the system is at time $t = t_0$ in the Floquet instantaneous eigenstate $\Psi_K(\theta, t_0) = \Phi_n(\theta, \boldsymbol{\eta}(t_0))$, then, in the adiabatic limit, the wavefunction $\Psi_K(\theta, t)$ solution of Eq. (6.84) is, up to a phase, the instantaneous Floquet state whose eigenenergy is continuously connected to the initial one:

$$\Psi_K(\theta, t) = \exp\left[i\delta_n(t; \boldsymbol{\eta}(t))\right]\Phi_n(\theta, \boldsymbol{\eta}(t)). \tag{6.96}$$

From Eq. (6.95), one immediately obtains

$$\delta_n(t; \boldsymbol{\eta}(t)) = -\int_{t_0}^t du\,\lambda(\boldsymbol{\eta}(u)) + i\int_{t_0}^t du\,\langle\Phi_n(\theta; \boldsymbol{\eta}(t))|\frac{\partial}{\partial u}|\Phi_n(\theta; \boldsymbol{\eta}(t))\rangle. \quad (6.97)$$

The second term of the right hand side of the last equation can be transformed by changing the variable of integration. Precisely, noting that $\frac{\partial}{\partial t} = \dot{\boldsymbol{\eta}}(t).\boldsymbol{\nabla}_{\boldsymbol{\eta}}$, one may write

$$\langle\Phi_n(\theta; \boldsymbol{\eta}(t))|\frac{\partial}{\partial t}|\Phi_n(\theta; \boldsymbol{\eta}(t))\rangle = \dot{\boldsymbol{\eta}}(t).\langle\Phi_n(\theta; \boldsymbol{\eta}(t))|\boldsymbol{\nabla}_{\boldsymbol{\eta}}|\Phi_n(\theta; \boldsymbol{\eta}(t))\rangle. \quad (6.98)$$

Using then the fact that $\dot{\boldsymbol{\eta}}(t)dt = d\boldsymbol{\eta}$, Eq. (6.97) can be recast as

$$\delta_n(t; \boldsymbol{\eta}(t)) = -\int_{t_0}^t du\,\lambda(\boldsymbol{\eta}(u)) + i\int_{\boldsymbol{\eta}(t_0)}^{\boldsymbol{\eta}(t)} d\boldsymbol{\eta}.\langle\Phi_n(\theta; \boldsymbol{\eta}(t))|\boldsymbol{\nabla}_{\boldsymbol{\eta}}|\Phi_n(\theta; \boldsymbol{\eta}(t))\rangle.$$
$$(6.99)$$

This phase is the sum of a dynamical phase (first term of the right hand side of Eq. (6.99)), which depends on the trajectory followed in the parameter space and on its speed, and of a geometric phase, which does not depend on its speed. The geometric phase can be set to zero by an appropriate choice of phase for the eigenvectors, in absence of loop in the parameter space. This approach is called *parallel transport*. When a loop is considered, the geometric phase is zero if only one parameter is varied. If two parameters are varied, it can be π if the trajectory forms a loop enclosing a degeneracy of the eigenvalue surfaces or zero if not. In this particular case, the geometric phase is known as the Berry phase [13]. It can take any value if more than two parameters are varied.

One can see a clear analogy between the adiabatic Floquet theory for the calculation of the laser driven dynamics of a quantum system and the Born-Oppenheimer approximation for the calculation of the dynamics of the nuclei in a molecular system. In the later, one uses the eigenvalues of an electronic Hamiltonian with fixed nuclei to define adiabatic potential energy surfaces. Because the dynamics of the nuclei is slow compared to that of the electrons, one can often neglect the non-adiabatic couplings between the different electronic states. Therefore, the dynamics of the nuclei can be interpreted as the motion of a nuclear wavepacket on a single adiabatic potential energy surface, which depends on the nuclear coordinates. In the adiabatic Floquet theory, one defines quasienergy surfaces as the instantaneous eigenvalues (eigenvalues at fixed time of the slow parameters of the field) of a Floquet Hamiltonian. If the parameters of the laser field vary slowly enough in time, the non-adiabatic couplings between the different quasienergy surfaces can be neglected, and the dynamics of the system driven by a laser pulse with a given set of parameters can be interpreted as a trajectory on a single quasienergy surface, which depends on the parameters of the laser pulse. The adiabatic Floquet theory thus provides an intuitive, geometric interpretation of the laser driven dynamics of the system.

6.5.3 Calculation of the Eigenvalues
of the Floquet Operator

Consider the Floquet operator $K(r, R, \theta)$ given by Eq. (6.59), associated with a molecular system, described by the Hamiltonian $H_0(r, R)$, in interaction with a laser field. In this section, we address the problem of the calculation of the eigenvalues of this Floquet operator. The matrix representation of this operator in the basis $\{|\phi_{n,k}\rangle = |\chi_n\rangle \otimes |\xi_k\rangle\}$ of $\mathcal{K}$, where $\{|\chi_n\rangle\}$ denotes the basis of $H_0(r, R)$, has a transparent structure and can be easily constructed. Considering $k = -k_{\max}, -k_{\max} + 1, \ldots, k_{\max} - 1, k_{\max}$ with $k_{\max}$ a positive integer, this matrix is of dimension $N(2k_{\max} + 1)$, with N the dimension of the basis $\{|\chi_n\rangle\}$. Therefore, depending on the value of $k_{\max}$ needed for convergence of the quasienergies, the computational cost of the direct diagonalisation of this matrix for each value of the laser field parameters considered can quickly become prohibitive. In this case, an alternative method that can be more efficient, from the computational point of view, can be used. It is based on the construction and diagonalisation of the propagator of the Schrödinger equation $U(0, \tau)$ over one period of the field $\tau = \frac{2\pi}{\omega}$, solution of

$$H(r, R, t)U(0, \tau) = i\frac{\partial}{\partial t}U(0, \tau) \tag{6.100}$$

where

$$H(r, R, t) = H_0(r, R) - \mu.\varepsilon(t). \tag{6.101}$$

The representation of $U(0, \tau)$ in the basis $\{|\chi_n\rangle\}$ is a matrix of dimension N. In practice, the nth column of $U(0, \tau)$ is obtained by solving the time-dependent Schrödinger equation

$$H(r, R, t)\Psi(t) = i\frac{\partial}{\partial t}\Psi(t) \tag{6.102}$$

using the nth eigenstate of $H_0(r, R)$ as the initial condition. The eigenvalues of the Floquet Hamiltonian are directly related to the eigenvalues of the propagator $U(0, \tau)$. Specifically, if $|\psi\rangle$ is an eigenstate of $U(0, \tau)$ with $U(0, \tau)|\psi\rangle = \lambda|\psi\rangle$, then there exists an eigenstate $|\Phi\rangle$ of $K(r, R, \theta)$ verifying $K(r, R, \theta)|\Phi\rangle = -\frac{i}{\tau}\ln(\lambda)|\Phi\rangle$ [14]. Therefore, for each value of the laser field parameters, the computation of the quasienergy spectrum requires N solution of the TDSE over one period of the laser field and the diagonalisation of a matrix of dimension N.

References

1. U. Boscain, G. Charlot, J.-P. Gauthier, S. Guérin, H.-R. Jauslin, J. Math. Phys. **43**, 2107 (2002)
2. N. Rosen, C. Zener, Phys. Rev. **40**, 502 (1932)
3. L. Allen, J.H. Eberly, *Optical Resonance and Two-Level Atoms* (Dover, New York, 1987)

4. Y.N. Demkov, M. Kunike, Vestn. Leningr. Univ. Fiz. Khim. **16**, 39 (1969)
5. N.V. Vitanov, T. Halfmann, B.W. Shore, K. Bergmann, Annu. Rev. Phys. Chem. **52**, 763 (2001)
6. K. Bergmann, H. Theuer, B.W. Shore, Rev. Mod. Phys. **70**, 1003 (1998)
7. G.T. Genov, D. Schraft, T. Halfmann, N.V. Vitanov, Phys. Rev. Lett. **113**, 043001 (2014)
8. N.V. Vitanov, New J. Phys. **9**, 58 (2007)
9. S.H. Autler, C.H. Townes, Phys. Rev. **100**, 703 (1955)
10. B.J. Sussman, Am. J. Phys. **79**, 477 (2011)
11. S. Guérin, Phys. Rev. A **56**, 1458 (1997)
12. K. Drese, M. Holthaus, Eur. Phys. J. D **5**, 119 (1999)
13. M.V. Berry, Proc. R. Soc. A **392**, 45 (1984)
14. S. Guérin, H.R. Jauslin, Adv. Chem. Phys. **125**, 147 (2003)

Chapter 7
Laser Control of the Radiationless Decay in Pyrazine Using the Dynamic Stark Effect

This chapter is partly based on results and discussions published in [1]. This material is reproduced with permission. Copyright [2014] AIP Publishing LLC.

7.1 Introduction

In this chapter, we use quantum dynamics simulations to investigate the possibility of manipulating the excited state dynamics of polyatomic molecules using mechanisms based on the dynamic Stark effect. In this type of control scenarios, a weak resonant laser pulse is used to induce an electronic excitation and to trigger the excited state dynamics while a strong non-resonant laser pulse is used to modify the shape of the potential energy surfaces of the molecule through the dynamic Stark effect, and thus to influence the evolution of the excited wavepacket. The ability of this method to control the outcome of a photoinduced non-adiabatic molecular process has been demonstrated experimentally on the photodissociation of IBr [2, 3]. From the computational point of view, a number of investigations on diatomic [4–8] or one dimensional models of polyatomic molecules [9] have been reported. A similar control mechanism, proposed by Suominen et al. [10–13] and further developed by Solá et al. [14–18], named adiabatic passage by light-induced potentials, was shown to provide a means of manipulating the bond length and inducing selective vibronic population transfer in diatomic molecules. The applicability of similar control schemes to multidimensional models of polyatomic molecules have been investigated more recently [19, 20], and the Stark control of the photodissociation of methyl iodide (CH_3I) have been demonstrated experimentally [21].

Pyrazine is a convenient model system for the study of the laser control of radiationless decay processes occurring at conical intersections (CIs), with particular focus on the control of the lifetime of the $B_{2u}(\pi\pi^*)$ state. Studies based on optimal control theory [22–24], or local control theory [25], predicted a high level of control over the lifetime of the $B_{2u}(\pi\pi^*)$ state. Another approach, based on the concept of overlapping resonances, in conjunction with approximate computational methods

allowing for a full dimensional treatment of the problem has been reported [26–28]. Again, a significant degree of control over the lifetime of the $B_{2u}(\pi\pi^*)$ state could be achieved. More recently, the coherent control of the ionization of pyrazine after electronic excitation of the neutral molecule has been investigated [29, 30].

In Chap. 5, we showed that the dark $A_u(n\pi^*)$ state plays an important role in the photophysics of pyrazine. However, in the present work, we consider a simpler model including only the bright $B_{3u}(n\pi^*)$ and $B_{2u}(\pi\pi^*)$ states and the four most important vibrational modes of the molecule. Similar models have been considered in a number of previous investigations of the non-adiabatic dynamics of the molecule [31, 32] and its control by laser pulses [22, 25, 26]. Therefore, while this model can not fully account for the complexity of the dynamics of photoexcited pyrazine, it allows us to compare our control mechanism with alternative control mechanisms proposed in previous studies. In addition, the results presented in this chapter are of general interest for the laser control of radiationless decay processes using the dynamic Stark effect.

The rest of this chapter is organized as follows. The model and computational methodology used in this work are presented in Sect. 7.2. In Sect. 7.3, we present and analyze the mechanism behind our control strategy. Our results are presented in Sect. 7.4 and a discussion of these results in comparison with previous works on the laser control of pyrazine, together with our conclusions, is given in Sect. 7.5.

7.2   Model and Methods

7.2.1   The Hamiltonian

We consider a reduced-dimensional model of pyrazine including four vibrational degrees of freedom and three electronic states: the ground state and the vibronically coupled $B_{3u}(n\pi^*)$ and $B_{2u}(\pi\pi^*)$ states, hereafter noted S_0, S_1 and S_2. The vibrational modes included are the totally symmetric ν_{6a}, ν_1 and ν_{9a} modes and the ν_{10a} mode of B_{1g} symmetry, which couples the S_1 and S_2 electronic states at first order. The body-fixed frame used in this work corresponds to the frame of the principal axes of inertia with the following definition: at the ground state equilibrium geometry the molecule lies in the yz plane, with both nitrogen atoms on the z axis. In D_{2h} symmetry, the S_1 and S_2 states are coupled with the ground electronic state by an electric field polarized along the x and y directions, respectively. Upon displacement along the coupling mode, the S_0/S_1 transition dipole moment (TDM) acquires a non-zero y component, while the S_0/S_2 TDM acquires a non-zero x component. In addition, due to the inversion symmetry, the permanent dipole moments are zero.

We consider the interaction of the molecule with a weak laser pulse resonant with the $S_0 \rightarrow S_2$ electronic transition, hereafter denoted pump pulse, and a strong non-resonant laser pulse, denoted control pulse. The pump pulse is polarized along the y direction and the control pulse along the z direction. The total Hamiltonian in the diabatic representation reads

$$H^d(\mathbf{Q}, t) = H_m^d(\mathbf{Q}) + H_{\text{int}}^{p,d}(\mathbf{Q}, t) + H_{\text{int}}^{c,d}(\mathbf{Q}, t), \tag{7.1}$$

where $\mathbf{Q}$ denotes a vector collecting the vibrational coordinates, $H_m^d(\mathbf{Q})$ is the molecular Hamiltonian, $H_{\text{int}}^{p,d}(\mathbf{Q}, t)$ describes the interaction of the molecule with the pump pulse and $H_{\text{int}}^{c,d}(\mathbf{Q}, t)$ describes the interaction of the molecule with the control pulse.

A linear vibronic coupling model Hamiltonian [33], augmented with a diagonal quadratic term along the ν_{10a} mode [31] is adopted for the molecular Hamiltonian. Its matrix representation in the basis of the diabatic electronic states reads

$$\mathbf{H}_m^d(\mathbf{Q}) = H_0(\mathbf{Q})\mathbf{I} + \mathbf{V}^d(\mathbf{Q}), \tag{7.2}$$

where $H_0(\mathbf{Q})$ is the ground state Hamiltonian in the harmonic approximation (see Sect. 4.3 in Chap. 4), $\mathbf{I}$ is the 3×3 identity matrix, and

$$\mathbf{V}^d(\mathbf{Q}) = \begin{pmatrix} 0 & 0 & 0 \\ 0 & V_{11}^d(\mathbf{Q}) & V_{12}^d(\mathbf{Q}) \\ 0 & V_{12}^d(\mathbf{Q}) & V_{22}^d(\mathbf{Q}) \end{pmatrix} \tag{7.3}$$

is the diabatic potential energy matrix. In our case, the elements of the latter read

$$V_{nn}^d(\mathbf{Q}) = E_i + \sum_i \kappa_i^{(n)} Q_i + \gamma_{10a} Q_{10a}^2, \tag{7.4a}$$

$$V_{12}^d(\mathbf{Q}) = \lambda_{10a} Q_{10a}. \tag{7.4b}$$

with $n = 1, 2$ and $i = 6a, 1, 9a$. The $\kappa_i^{(n)}$ parameters, which are the derivatives of the adiabatic electronic energies at the Franck–Condon (FC) geometry, were computed through finite differences, whereas the $\gamma_{10a} Q_{10a}^2$ and λ_{10a} parameters were obtained together via a least-square fit to ab initio computed adiabatic electronic energies along the Q_{10a} coordinate.

In typical experiments and in the present work, the pump pulse used to trigger the electronic excitation is of low intensity in order to avoid competing multi-photon processes. Therefore the interaction of the pump pulse with the electronic polarizability can be neglected, and the corresponding interaction Hamiltonian simply reads

$$H_{\text{int}}^{p,d}(\mathbf{Q}, t) = -\mu_y^d(\mathbf{Q})\varepsilon_p(t), \tag{7.5}$$

where $\mu_y^d(\mathbf{Q})$ is the y-component of the dipole moment operator and $\varepsilon_p(t)$ is the electric field associated with the pump pulse, given by

$$\varepsilon_p(t) = A_p(t)\cos(\omega_p t). \tag{7.6}$$

In this last equation, $A_p(t) = \varepsilon_p^0 \Lambda_p(t)$ denotes an envelope function, with ε_p^0 the peak amplitude. The matrix representation of $\mu_y^d(\mathbf{Q})$ in the basis of the diabatic electronic states reads

$$\boldsymbol{\mu}_y^d(\boldsymbol{Q}) = \begin{pmatrix} 0 & \mu_{01}^d(\boldsymbol{Q}) & \mu_{02}^d(\boldsymbol{Q}) \\ \mu_{01}^d(\boldsymbol{Q}) & 0 & 0 \\ \mu_{02}^d(\boldsymbol{Q}) & 0 & 0 \end{pmatrix}, \tag{7.7}$$

where, for ease of notation, the subscript y is dropped for the matrix elements. In the spirit of the vibronic coupling model, the following simple expressions were adopted for the diabatic transition dipole matrix elements [31]

$$\mu_{01}^d(\boldsymbol{Q}) = \xi_{10a}^{(01)} Q_{10a}, \tag{7.8a}$$

$$\mu_{02}^d(\boldsymbol{Q}) = \mu^{(02)}(0) + \sum_k \xi_k^{(02)} Q_k + \frac{1}{2}\rho_{10a}^{(02)} Q_{10a}^2, \tag{7.8b}$$

where $\mu^{(02)}(0)$ is the S_0/S_2 TDM at the FC geometry and k runs over the totally symmetric modes. The constants $\xi_k^{(02)}$ were computed through finite differences of the adiabatic $\mu_{02}^{ad}(\boldsymbol{Q})$ TDM at the FC geometry

$$\xi_k^{(02)} = \left.\frac{\partial\mu_{02}^{ad}(Q_k)}{\partial Q_k}\right|_{Q=0}. \tag{7.9}$$

At D_{2h} symmetry, the non-adiabatic couplings between the S_1 and S_2 states are zero. As a result, a smooth dependence of the $\mu_{02}^d(\boldsymbol{Q})$ matrix element with respect to the totally symmetric modes is expected. Cuts of $\mu_{02}^d(\boldsymbol{Q})$ along the three totally symmetric modes considered in this work are presented in Fig. 7.1. This figure shows that the ab initio computed adiabatic TDMs along the totally symmetric modes are well approximated by linear terms.

The Q_{10a} modes couples the S_1 and S_2 states at first order. To obtain the ξ_{10a}^{01} and ρ_{10a}^{01} constants, we use the unitary matrix $\boldsymbol{S}(\boldsymbol{Q})$ that diagonalizes the diabatic potential matrix $\boldsymbol{V}^d(\boldsymbol{Q})$ to relate the diabatic and adiabatic dipole moment matrices

$$\boldsymbol{\mu}^{ad}(\boldsymbol{Q}) = \boldsymbol{S}^\dagger(\boldsymbol{Q})\boldsymbol{\mu}^d(\boldsymbol{Q})\boldsymbol{S}(\boldsymbol{Q}) \tag{7.10}$$
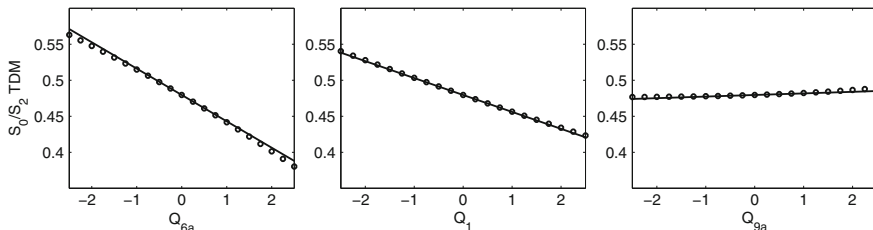

Fig. 7.1 Cuts of the $\mu_{02}^d(\boldsymbol{Q})$ TDM surface along the Q_{6a}, Q_1 and Q_{9a} totally symmetric normal coordinates. The *circles* are the ab initio computed adiabatic TDMs and the *solid lines* are the model diabatic TDMs
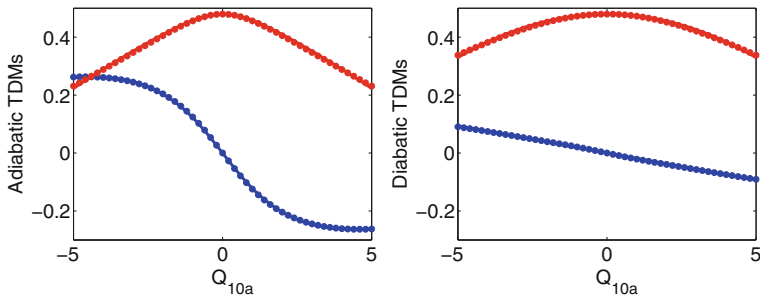
Fig. 7.2 Adiabatic (*left panel*) and diabatic (*right panel*) TDMs along the Q_{10a} normal coordinate. The μ_{01} and μ_{02} components are shown in *blue* and *red* respectively. The *circles* represent the ab initio computed adiabatic TDMs (*left panel*) and the diabatic TDMs obtained directly from Eq. (7.10). The *full lines* represent the adiabatic and diabatic TDMs obtained from our model

where

$$S(\boldsymbol{Q}) = \begin{pmatrix} 1 & 0 & 0 \\ 0 & \cos(\theta(\boldsymbol{Q})) & \sin(\theta(\boldsymbol{Q})) \\ 0 & -\sin(\theta(\boldsymbol{Q})) & \cos(\theta(\boldsymbol{Q})) \end{pmatrix} \tag{7.11}$$

and

$$\theta(\boldsymbol{Q}) \equiv \theta(Q_{10a}) = \frac{1}{2} \tan^{-1} \left(\frac{2\lambda Q_{10a}}{E_2 - E_1} \right). \tag{7.12}$$

Using Eq. (7.10), the ξ_{10a}^{01} and ρ_{10a}^{01} were fitted against the ab initio computed adiabatic TDMs. Cuts of the adiabatic and diabatic TDMs along the Q_{10a} coordinate are presented in Fig. 7.2. This figure shows that, although the adiabatic TDMs curves have rather complicated shapes that can not be well approximated by low-order polynomials, the diabatic TDMs are well approximated by linear and quadratic terms, see Eq. (7.8).

For the $H_{\text{int}}^{c,ad}(t)$ operator, the effective Hamiltonian of Eq. (6.56), was used. In addition, all the elements of the $\boldsymbol{\mu}_z^{ad}$ matrix in the subspace of electronic states considered in this work are zero by symmetry. We thus obtain

$$H_{\text{int}}^{c,d}(t) = -\frac{1}{2} \alpha_{zz}^d(\boldsymbol{Q}) \varepsilon_c^2(t) \tag{7.13}$$

where $\alpha_{zz}^d(\boldsymbol{Q})$ is the zz component of the diabatic static polarizability and $\varepsilon_c(t)$ is the electric field associated with the control pulse

$$\varepsilon_c(t) = A_c(t) \cos(\omega_c t). \tag{7.14}$$

Again $A_c(t) = \varepsilon_c^0 \Lambda_c(t)$ is an envelope function, with ε_c^0 the peak amplitude. The matrix representation of $\alpha_{zz}^d(\boldsymbol{Q})$ in the basis of the diabatic electronic states reads

$$\boldsymbol{\alpha}_{zz}^{d}(\boldsymbol{Q}) = \begin{pmatrix} \alpha_{00}^{d}(\boldsymbol{Q}) & 0 & 0 \\ 0 & \alpha_{11}^{d}(\boldsymbol{Q}) & \alpha_{12}^{d}(\boldsymbol{Q}) \\ 0 & \alpha_{12}^{d}(\boldsymbol{Q}) & \alpha_{22}^{d}(\boldsymbol{Q}) \end{pmatrix}, \tag{7.15}$$

where, for ease of notation, the subscript zz is dropped for the matrix elements. As for the potentials and TDMs the matrix elements of the diabatic static polarizability were expressed as low order Taylor expansions

$$\alpha_{nn}^{d}(\boldsymbol{Q}) = \alpha^{(n)}(0) + \sum_{k} \chi_{k}^{(n)} Q_k + \varphi_{10a}^{(n)} Q_{10a}^2, \tag{7.16a}$$

$$\alpha_{12}^{d}(\boldsymbol{Q}) = \chi_{10a}^{12} Q_{10a} \tag{7.16b}$$

where $n = 0, 1, 2$ and $\alpha^{(n)}(0)$ is the static polarizability of the electronic state n at the FC geometry. As for the TDMs, the $\chi_{k}^{(n)}$ parameters were obtained from the derivatives (computed as a finite differences) of the adiabatic static polarizability at the FC geometry

$$\chi_{k}^{(n)} = \left. \frac{\partial \alpha_{nn}^{ad}(\boldsymbol{Q})}{\partial Q_k} \right|_{\boldsymbol{Q}=0}, \tag{7.17}$$

whereas the $\varphi_{10a}^{(n)}$ and χ_{10a}^{12} parameters were obtained through a least-square fit to ab initio computed adiabatic static polarizabilities along the Q_{10a} coordinate. Again, the transformation matrix $\boldsymbol{S}(\boldsymbol{Q})$ was used to relate the diabatic and adiabatic static polarizability matrices. As seen in Fig. 7.3, the static polarizabilities along the totally symmetric modes are well approximated by linear terms, at the exception of the static polarizability of the S_1 state along the Q_{6a} mode, which clearly displays a quadratic behavior in the FC region. However, the inclusion of a quadratic term was found to have a minor effect on the results of the simulations presented in Sect. 7.4 below. Cuts of the static polarizabilities along the Q_{10a} coordinate are presented in Fig. 7.4. Again, while the adiabatic static polarizabilities have rather complicated shapes, their diabatic counterpart can be well approximated by the simple expressions of
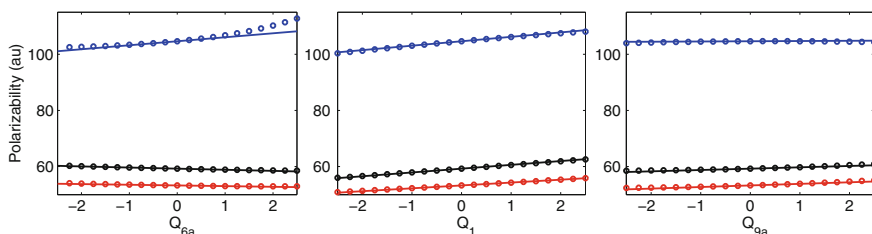

Fig. 7.3 Cuts of the S_0 (*black*) S_1 (*blue*) and S_2 (*red*) static polarizability surfaces along the Q_{6a}, Q_1 and Q_{9a} totally symmetric normal coordinates. The *circles* represent the ab initio computed static polarizabilities and the *full lines* represent the static polarizabilities obtained from our model
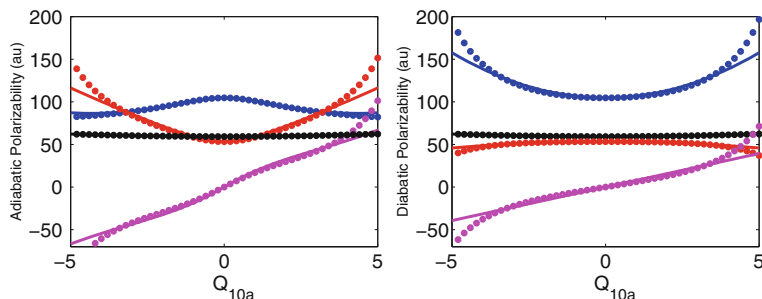
Fig. 7.4 Adiabatic (*left panel*) and diabatic (*right panel*) static polarizabilities along the Q_{10a} normal coordinate. The α_{00}^d, α_{11}^d, α_{22}^d and α_{12}^d components are shown in *black*, *blue*, *red* and *magenta*, respectively. The *circles* represent the ab initio computed adiabatic static polarizability and the diabatic static polarizability obtained from application of the transformation $S(Q)$. The *full lines* represent the static polarizabilities obtained from our model

Eq. (7.16) in the FC region. In contrast, significant deviations between the model and the ab initio data are observed for $Q_{10a} > 4$.

We note that a different strategy can be used to parametrize such a model Hamiltonian. In Ref. [20] Blancafort et al. studied photophysics of fulvene in interaction with a strong non-resonant laser field, using a four dimensional model Hamiltonian expressed in a combination of rectilinear and curvilinear coordinates. They obtained the model parameters directly from fits to ab initio calculations including explicitly static electric fields of different amplitudes. A comparison of the results obtained from this strategy could be used to assess the validity of our model. Such comparison between the two strategies has been performed in Ref. [9] in the case of a one dimensional system.

7.2.2 Electronic Structure Calculations

All the electronic structure calculations presented in this work were performed with the aug-cc-pVDZ basis set of Dunning [34]. The ground state geometry optimization and normal mode calculations were performed at the second-order Møller–Plesset (MP2) level of theory using the Gaussian 03 program package [35]. The PESs were explored with the extended multi-configuration quasi-degenerate second-order perturbation theory (XMCQDPT2) method [36] using the Firefly QC package [37] which is partially based on the GAMESS (US) source code [38]. For the underlying state-averaged complete active space self-consistent field (SA-CASSCF) wavefunction, an active space of ten electrons in eight orbitals, including the full π orbital subset and the two nitrogen lone-pair orbitals was used. The transition dipole moments

and static polarizabilities were obtained at the zero-order QDPT (ZO-QDPT) level of theory. The ZO-QDPT properties include only a part of the electron dynamic correlation corrections obtained via the XMCQDPT2 method. Therefore they are an approximation of the true XMCQDPT2 properties (more details can be found in the Firefly documentation [37]). The static polarizabilities were computed using the finite-field method, i.e as the numerical derivative of the dipole moments with respect to the amplitude of an applied static electric field. The number of states included in the SA-CASSCF stage was found to have an important impact on the result of the static polarizability calculations. Test calculations were performed with an increasing number of states included in the SA-CASSCF stage until converged values of the static polarizability were obtained. We found that including the six lowest CASSCF states allows one to obtain stable static polarizability values without significantly degrading the accuracy of the energies. For the sake of comparison, we have also computed MRCI static polarizabilities using the same basis set and SA-CASSCF guess wavefunction. Our results are presented in Table 7.1.

We observe that in most cases the CASSCF, ZO-QDPT and MRCI results are very similar. The only notable exception is for the α_{zz} component of the S_1 state, for which the ZO-QDPT and MRCI results differ by almost 10% from the CASSCF results. Our results predict the α_{zz} component to be roughly twice as large for the S_1 state as for the S_2 state. This difference is very important since it will allow for an efficient shift of the S_1 state with respect to the S_2 state by a non-resonant laser pulse (see Sect. 7.3 below). In addition, we note that this result is in line with the high resolution Stark effect measurements of Okruss et al. [39] who observed that the S_1 state polarizability was significantly higher than that of the ground state. Test calculations of the static polarizabilities at the ZO-QDPT level of theory using the aug-cc-pVTZ basis set yielded values of 59.5, 105.4 and 53.6 a.u for the α_{zz} component for the S_0, S_1 and S_2 states respectively (the values obtained for the α_{xx} and α_{yy} showed similar deviations with respect to the aug-cc-pVDZ values). These results indicate that the aug-cc-pVDZ basis set provides reasonably well converged static polarizability values. Details of the values of the parameters obtained for the potential energy, transition dipole moment and static polarizability surfaces from our XMCQDPT2 calculations can be found in Ref. [1].

Table 7.1 SA-CASSCF, ZO-QDPT and MRCI polarizabilities in atomic units at the ground state equilibrium geometry

	S_0			S_1			S_2		
	α_{xx}	α_{yy}	α_{zz}	α_{xx}	α_{yy}	α_{zz}	α_{xx}	α_{yy}	α_{zz}
CASSCF	36.3	68.1	59.3	37.7	64.3	114.4	37.5	57.7	53.3
ZO-QDPT	36.3	68.8	59.3	37.7	64.4	104.7	37.5	57.1	53.3
MRCI	36.5	70.0	61.0	38.3	66.9	104.5	38.0	60.5	56.3

7.3   An Adiabatic Picture of the Control Mechanism

Generally, control scenarios relying on the interaction of the system with a strong, non-resonant laser pulse, can be classified in two categories. The first category is based on a *dynamical* effect, i.e the control pulse is short with respect to the characteristic time of the process. This scheme can be used in the case of photoreactive processes where two or several reactive channels are in competition. Here the short control pulse imparts a "kick" to the molecule which can be used to influence the branching ratio between the different channels. This type of scenario has been recently used to manipulate the branching ratio between different photodissociation products [3, 7, 19, 21]. The second category relies on a strong *adiabatic* effect. Here the control pulse is long with respect to the characteristic time of the process. The control pulse interacts with the system during the whole process. This scheme is expected to be useful in cases where the dynamics of the photoexcited molecule is dominated by a single process, such as the non-radiative decay through a sloped CI (see e.g. [40] and references therein), as it is the case for pyrazine (see Fig. 7.5). In this case, the Stark shift induced by the control pulse can be used to shift the CI seam away from the FC geometry and thus to quench the non-radiative decay of the system as long as the control pulse is on. This type of scenario has been proposed theoretically to prevent photodissociation of a fluoroethylene derivative [9]. The second scenario is the one adopted in the present work.

The impact of a strong non-resonant laser field on the topography of the PESs of the coupled S_1 and S_2 states can be analyzed in terms of dressed PESs [9, 17], which are obtained as the instantaneous eigenvalues of the matrix:

$$W(\boldsymbol{Q}) = \frac{1}{2} \sum_i \omega_i Q_i^2 + \boldsymbol{V}^d(\boldsymbol{Q}) - \frac{1}{4} \boldsymbol{\alpha}^d(\boldsymbol{Q}) A_c(t)^2. \tag{7.18}$$
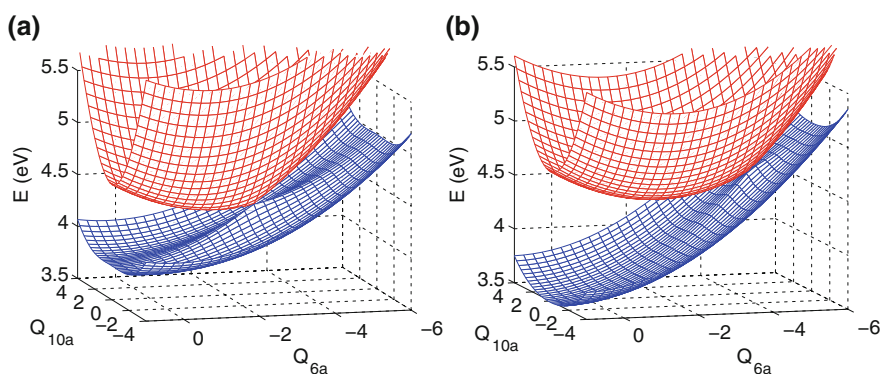

Fig. 7.5 S_1 (*blue*) and S_2 (*red*) adiabatic PESs plotted as a function of Q_{6a} and Q_{10a} **a** in the field-free case with $Q_1 = 1.83$ and $Q_{9a} = -0.15$ and **b** dressed by a control field of intensity $I = 50\,\text{TW/cm}^2$ with $Q_1 = 2.42$ and $Q_{9a} = 0.13$. Figure reproduced from Ref. [1]

Such an analysis is relevant when the control field is switched on (and off) adiabatically in a non-resonant way. In this expression, the rapidly oscillating term $\cos^2(\omega_c t)$ has been averaged over time. This approximation is valid if the control field frequency is high with respect to any two photon transition frequency between the S_1 and S_2 states. The dressed PESs of Eq. (7.18) are evaluated for fixed values of the control field amplitude (corresponding formally to the amplitude of the envelope function $A_c(t)$ at a fixed time t). They allow one to characterize the modifications of the topography of the PESs induced by the control field from an adiabatic point of view. Thus, in practice, $A_c(t)^2$ in Eq. (7.18) is treated as a constant. We stress here that this approximation is necessary for an analysis of the system in terms of dressed PESs. However, in the full time-dependent simulations presented in Sect. 7.4, the more accurate expression of Eq. (7.1) has been used.

The effect of the Stark shifts on the seam of CI connecting the S_1 and S_2 states is of particular interest. As seen in Table 7.1, the S_1 α_{zz} component is roughly twice as large as the S_2 α_{zz} component at the FC geometry. As a result, the interaction of the molecule with a strong non-resonant control pulse is expected to shift the CI away from the FC region.

Thanks to the simple mathematical expressions assumed in our model for the diabatic potential energy and polarizability matrices (Eqs. (7.4) and (7.16) respectively), the position and energies of the minima of the upper dressed adiabatic potential energy surface and CI seam are given by simple analytic expressions [33]. Specifically, in our case the position of the minimum of the upper adiabatic surface is identical to that of the diabatic $V_2(\boldsymbol{Q})$ and simply reads

$$Q_i^{\min} = -\frac{\kappa_i^{(2)}}{\omega_i}. \tag{7.19}$$

The corresponding energy is given by

$$V_2^{\min} = E_2 - \frac{1}{2} \sum_i \frac{(\kappa_i^{(2)})^2}{\omega_i}. \tag{7.20}$$

The position and energy of the minimum energy conical intersection (MECI) are given by

$$Q_i^{\text{MECI}} = \frac{(\delta_i/\omega_i)(F - \Delta)}{D} - \frac{\sigma_i}{\omega_i} \tag{7.21}$$

and

$$V^{\text{MECI}} = \frac{E_1 + E_2}{2} + \frac{(F - \Delta)^2}{2D} - \frac{1}{2} \sum_i \frac{\sigma_i^2}{\omega_i} \tag{7.22}$$

where the following quantities

$$\sigma_i = \frac{\kappa_i^{(2)} + \kappa_i^{(1)}}{2} \tag{7.23a}$$

$$\delta_i = \frac{\kappa_i^{(2)} - \kappa_i^{(1)}}{2} \tag{7.23b}$$

$$\Delta = \frac{E_2 - E_1}{2} \tag{7.23c}$$

$$D = \sum_i \frac{\delta_i^2}{\omega_i} \tag{7.23d}$$

$$F = \sum_i \frac{\sigma_i \delta_i}{2} \tag{7.23e}$$

have been introduced.

A similar analysis can be performed for the dressed potential energy surfaces. Combining Eqs. (7.4), (7.16) and (7.18), the elements of the dressed diabatic potential energy matrix corresponding to the excited states can be written as

$$W_{jj}^d(\mathbf{Q}) = \frac{1}{2} \sum_i \omega_i Q_i^2 + E_j^s + \sum_k \kappa_k^{s,(j)} Q_k + \gamma_{10a}^{s,(j)} Q_{10a}^2 \tag{7.24a}$$

$$W_{12}^d(\mathbf{Q}) = \lambda^s Q_{10a}, \tag{7.24b}$$

where

$$E_j^s = E_j - \frac{1}{4}\alpha^{(j)}(0)A_c^2(t) \tag{7.25a}$$

$$\kappa_k^{s,(j)} = \kappa_k^{(j)} - \frac{1}{4}\chi_k^{(j)} A_c^2(t) \tag{7.25b}$$

$$\gamma_{10a}^{s,(j)} = \gamma_{10a}^{(j)} - \frac{1}{4}\varphi_{10a}^{(j)} A_c^2(t) \tag{7.25c}$$

$$\lambda^s = \lambda - \frac{1}{4}\chi_{10a}^{12} A_c^2(t). \tag{7.25d}$$

One can see that the dressed potential energy matrix elements of Eq. (7.24) have the same form than the field-free diabatic potential energy matrix elements of Eq. (7.4). Thus, analytical expressions for the positions and energies of the minima of the dressed upper adiabatic PES and MECI can be obtained by replacing E_j by E_j^s and $\kappa_i^{(j)}$ by $\kappa_i^{s,(j)}$ in Eqs. (7.19)–(7.23).

In Table 7.2, we report the energy and geometry of the MECI between the dressed S_1 and S_2 PESs and of the minimum of the dressed S_2 PES as a function of the intensity of the control field. For each control field intensity considered, the reference energy is taken as the zero point energy of the dressed ground electronic

Table 7.2 Energy (in eV) and geometry of the MECI between the dressed S_1 and S_2 PESs and of the minimum of the dressed S_2 PES as a function of the intensity of the control field (in TW/cm^2)

	$I = 0$	$I = 10$	$I = 20$	$I = 30$	$I = 40$	$I = 50$
E^{MECI}	4.36	4.40	4.45	4.51	4.57	4.65
Q_{6a}^{MECI}	-2.70	-3.03	-3.35	-3.67	-3.98	-4.29
Q_{9a}^{MECI}	-0.15	-0.09	-0.04	0.02	0.08	0.13
Q_1^{MECI}	1.83	1.96	2.08	2.20	2.32	2.42
E^{min}	4.32	4.32	4.33	4.34	4.35	4.36
Q_{6a}^{min}	-1.77	-1.78	-1.78	-1.79	-1.79	-1.80
Q_{9a}^{min}	-0.30	-0.29	-0.29	-0.28	-0.27	-0.27
Q_1^{min}	1.45	1.47	1.48	1.50	1.51	1.53

For each control field intensity, the reference energy is the zero point energy of the dressed ground state

state. In the field-free case, the MECI is very close to the minimum of S_2, and lies 0.45 eV below the S_2 vertical excitation energy. In comparison, the S_2/S_1 MECI was reported in Ref. [41] at 0.16 eV below the S_2 vertical excitation energy at a position $(Q_{6a}^{\text{MECI}}, Q_{9a}^{\text{MECI}}, Q_1^{\text{MECI}}) = (-2.99, -0.02, 1.547)$, using a four mode model similar to the model considered in this work.

The S_0 and S_2 states have similar polarizabilities (see Table 7.1). Therefore, the relative energy and position of the minimum of the dressed S_2 PES are almost insensitive to the control field intensity. In contrast, because the S_1 state has a larger polarizability than the S_2 state, the MECI is shifted to higher energies as the control field intensity is increased. To further illustrate the effect of the control field on the topography of the PESs, two dimensional cuts of the S_1 and S_2 PESs as a function of Q_{6a} and Q_{10a}, both in the field-free case and in the presence of a control field of intensity $I = 50$ TW/cm^2, are presented in Fig. 7.5. In each case, the two other coordinates Q_1 and Q_{9a} have been fixed at their value at the MECI. In the field-free case, the CI is readily accessible after excitation close to the origin of the S_2 state, and a very fast radiationless decay occurs. However, the interaction with a sufficiently strong non-resonant laser pulse is seen to shift the CI away from the FC region, creating a bound potential well in the S_2 state. As a result, one can expect to trap the wavepacket in this potential well as long as the non-resonant pulse interacts with the molecule, and thus to avoid the radiationless decay to the S_1 state.

To further investigate the structure of the vibronic manifold of the molecule dressed by the control field at energies close to the onset of the S_2 state, we have calculated the absorption spectrum of the molecule in this energy range as a function of the intensity of the control field. Specifically, the time-dependent Schrödinger equation (TDSE)

$$H^{\text{dressed}}(\boldsymbol{Q})\Psi(\boldsymbol{Q}, t) = i\hbar \frac{\partial}{\partial t}\Psi(\boldsymbol{Q}, t) \tag{7.26}$$
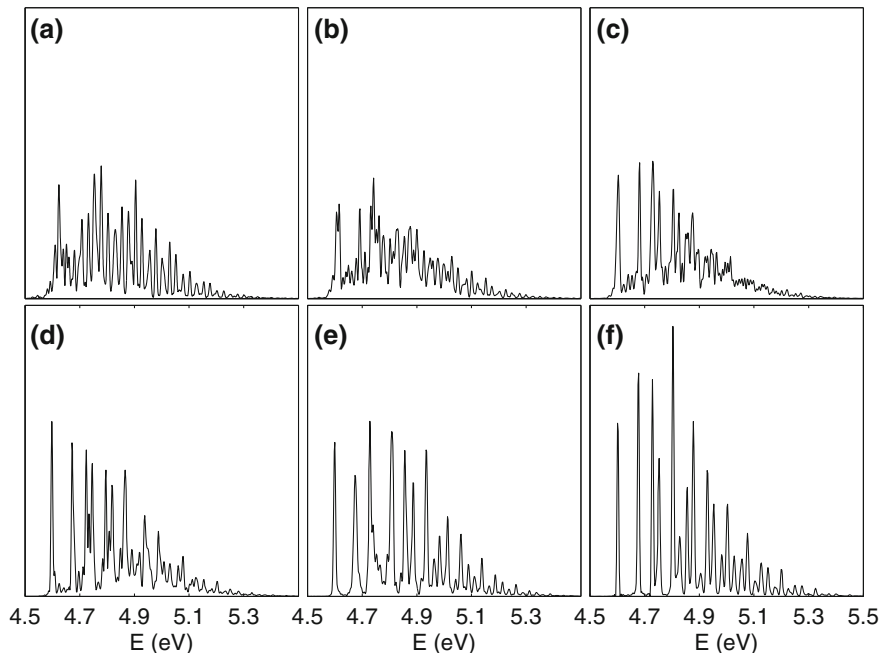
Fig. 7.6 Absorption spectra of the S_2 state in the field-free case (**a**) and in interaction with control fields of intensity $I = 10\,TW/cm^2$ (**b**), $I = 20\,TW/cm^2$ (**c**), $I = 30\,TW/cm^2$ (**d**), $I = 40\,TW/cm^2$ (**e**) and $I = 50\,TW/cm^2$ (**f**). No phenomenological broadening was applied on the spectra. Figure reproduced from Ref. [1]

with $\mathbf{H}^{\mathbf{dressed}}(\boldsymbol{Q}) = H_0(\boldsymbol{Q})\boldsymbol{I} + \boldsymbol{W}(\boldsymbol{Q})$ and $\boldsymbol{W}(\boldsymbol{Q})$ is the dressed potential energy matrix given in Eq. (7.18), was solved for different intensities of the control field, using as an initial condition the dressed ground vibronic state projected in the excited diabatic dressed S_2 manifold. For each control field intensity, the spectrum was obtained as the Fourier transform of the autocorrelation function $c(t) = \langle \Psi(0)|\Psi(t)\rangle$ obtained from a 300 fs propagation. No phenomenological broadening was applied to the spectra (see Sect. 4.4 in Chap. 4). The spectra obtained for control field intensities ranging from 0 to 50 TW/cm^2 are shown in Fig. 7.6. In all cases, the onset of absorption to S_2 occurs at a nearly constant energy of approximately 4.6 eV, in good agreement with the experimental value of 4.69 eV [42], corresponding to the field-free case. Again, this is a consequence of the fact that the S_0 and S_2 states have similar polarizabilities (see Table 7.1), and therefore experience similar Stark shifts. In the field-free case, even in the low energy range, the spectrum consists of a dense set of strongly vibronically coupled states. However, as the control field intensity is increased, the MECI is shifted to higher energies, and the low energy part of the spectra become sharper and less congested. This can be interpreted as an effective decoupling of the two electronic states in the FC region induced by the control field, i.e the control field creates pure vibrational states localized in S_2. The pure

vibrational states correspond to the lower peaks of the spectrum in Fig. 7.6 in the presence of the control field (see for instance panel (f) featuring the most favorable situation).

7.4   Results

The feasibility of the proposed control scenario was investigated by solving the TDSE

$$H^d(\boldsymbol{Q}, t)\Psi(\boldsymbol{Q}, t) = i\hbar\frac{\partial}{\partial t}\Psi(\boldsymbol{Q}, t) \tag{7.27}$$

where $H^d(\boldsymbol{Q}, t)$ is the total Hamiltonian operator given by Eq. (7.1). The envelopes $\Lambda_{p,c}(t)$ were chosen to be of sine-squared shape $\Lambda_{p,c}(t) = \sin^2\left(\frac{\pi t}{t_p^{p,c}}\right)$, where $t_p^{p,c}$ are the pulse durations. In all the simulations presented below, the values $t_p^p = 100$ fs and $t_p^c = 500$ fs have been used. The control pulse is turned on at $t = -150$ fs. The pump pulse is turned on at $t = 0$ and ends when the control pulse reaches its peak intensity, as sketched in Fig. 7.7.

An important aspect in control schemes based on the Stark effect is the choice of the frequency of the control field. It should be chosen such as to ensure a non-resonant interaction with the molecule. In our case, as mentioned in Sect. 7.2.1, all the elements of the dipole moment matrix along the z direction are zero by symmetry. However, two-photon transitions between the S_1 and S_2 states can be mediated by the non-zero $\alpha_{12}^d(\boldsymbol{Q})$ matrix element. A value of $\hbar\omega_c = 1.8$ eV, which is high with respect to any two-photon transition between the S_1 and S_2 states was chosen. Calculations with peak intensities of 0, 10, 20, 30, 40 and 50 TW/cm^2 for the control field were performed. The peak intensity of the pump pulse was set to 0.2 TW/cm^2. In order to address various parts of the spectrum, three different photon energies (4.6, 4.7 and 4.8 eV) were considered. The TDSE of Eq. (7.27), for each set of parameters was solved using the MCTDH method in the multi-set formalism. In each

Fig. 7.7 Envelope $\Lambda_p(t)$ (green full line) of the pump pulse and squared envelope $\Lambda_c^2(t)$ (brown dashed lines) of the control pulse. Figure reproduced from Ref. [1]
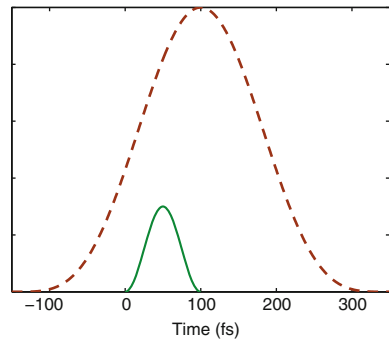
Table 7.3 Number of SPF and primitive basis functions used in the calculations

	Q_{6a}	Q_1	Q_{9a}	Q_{10a}
Primitive	42	24	16	40
SPF (S_0)	6	6	3	6
SPF (S_1)	16	10	6	12
SPF (S_2)	15	9	6	10

case, the initial wavefunction was chosen as the ground vibronic state. The wavefunction was propagated for 500 fs, between $t = -150$ fs and $t = 350$ fs. For the representation of the Hamiltonian and the wavefunction, a Hermite polynomial DVR scheme [43] was used for all the degrees of freedom. The number of SPF and primitive basis functions used in the calculations are listed in Table 7.3. The adiabatic electronic state populations were computed as outlined in Sect. 5.4 of Chap. 5 using the diabatic wavepackets obtained from the solution of the TDSE. The transformation between the diabatic and adiabatic representations   was performed exactly, i.e the integrals of Eq. (5.10) were evaluated on the full primitive grid. In Fig. 7.8 the adiabatic populations of the S_1 and S_2 states are reported for the various control pulse intensities and pump pulse photon energies considered. The populations are shown from $t = 0$, when the pump pulse is turned on while the control pulse is already intense (see Fig. 7.7). In the absence of the control field (Fig. 7.8a), the population transferred to S_2 by the pump pulse decays to S_1 before the end of the pulse at $t = 100$ fs, regardless of the pump pulse photon energy, in agreement with the ultrafast decay observed experimentally [44, 45]. The dynamics of the molecule in the presence of a control pulse of 10 TW/cm^2 peak intensity (Fig. 7.8b) is hardly different from the dynamics without control pulse. Again, the major part of the population excited to S_2 decays to S_1 before the end of the pump pulse. One can however notice that the decay rate slightly increases with the pump pulse photon energy. Already for a control pulse peak intensity of 20 TW/cm^2 (Fig. 7.8c), a significant effect of the Stark shifts on the electronic state population dynamics is observed. In the case of the lowest pump pulse photon energy (4.6 eV) considered, a fast decay occurs in the first 100 fs, i.e during the electronic excitation, as shown by the rise of the S_1 population. However at $t = 100$ fs, when the control pulse reaches its peak intensity, a substantial fraction of the population still remains in S_2 and decays at a slightly slower rate to S_1 between $t = 100$ fs and $t = 200$ fs. At a pump pulse photon energy of 4.7 eV, a significant effect is also observed, though less than at 4.6 eV. Indeed at 4.7 eV, the decay from the S_2 to S_1 is faster, however a greater amount of population is excited from the ground state by the pump pulse. For the highest pump pulse photon energy of 4.8 eV, the effect of the control pulse is almost nonexistent and a major part of the population decays before the end of the pump pulse. As the control pulse peak intensity is further increased (Fig. 7.8d–f), the trapping effect is more and more pronounced. At the highest intensities considered ($I = 40$ TW/cm^2 and $I = 50$ TW/cm^2), at the pump pulse photon energy of 4.6 eV, the most part of the population excited to the S_2
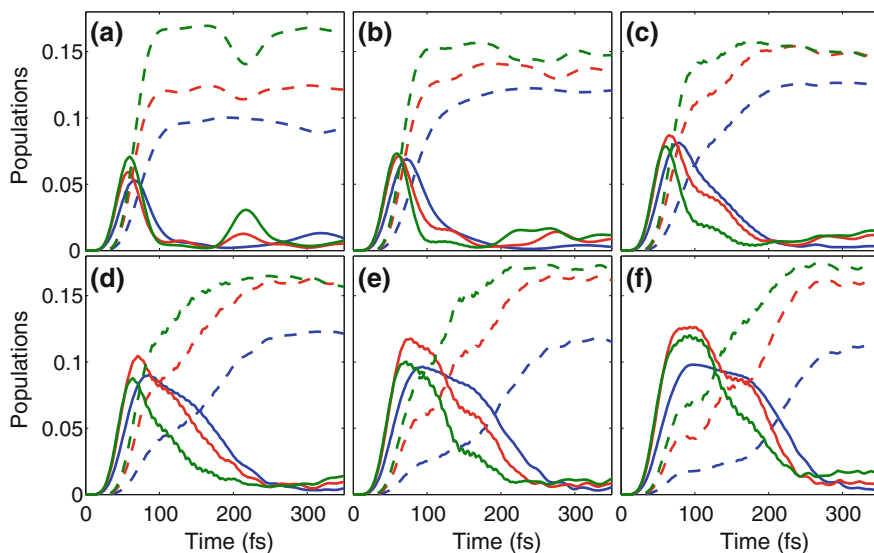
Fig. 7.8 Adiabatic populations of the S_1 (*dashed lines*) and S_2 (*full lines*) states for the pump pulse photon energies 4.6 eV (*blue*), 4.7 eV (*red*) and 4.8 eV (*green*) and for the control pulse intensities $I = 0$ (**a**), $I = 10\,\text{TW/cm}^2$ (**b**), $I = 20\,\text{TW/cm}^2$ (**c**), $I = 30\,\text{TW/cm}^2$ (**d**), $I = 40\,\text{TW/cm}^2$ (**e**) and $I = 50\,\text{TW/cm}^2$ (**f**). Figure reproduced from Ref. [1]

remains trapped up to t = 200 fs. At this time, the control pulse intensity is less than half its peak intensity (see Fig. 7.7). The decay to S_1 then occurs between $t = 200$ fs and t = 300 fs. At the pump pulse photon energy of 4.7 eV, a stepwise decay is observed, with a first decay between t = 100 fs and t = 150 fs, followed by a plateau between t = 150 fs and t = 200 fs and a second decay completed before t = 250 fs. At the highest pump pulse photon energy (4.8 eV) the population excited to S_2 has almost completely been transferred to S_1 at t = 200 fs.

Overall, these results show that, as the control pulse intensity is increased from 0 to 50 TW/cm^2, a transition between two regimes is observed concerning the excited-state dynamics of the molecule. In the absence of a control pulse or at low intensities, the dynamics of the system is dominated by the presence of the low-lying S_1/S_2 CI, readily accessed by the wavepacket after photoexcitation. The decay from the S_2 to S_1 is completed within 100 fs, i.e before the end of the pump pulse. At high intensities, the Stark shifts are strong enough to shift the CI to high energies and to create localized vibrational states in the S_2 state. As a result, after photoexcitation, the wavepacket is trapped in the S_2 state as long as the intensity of the control pulse is high enough.

7.5   Discussion and Conclusions

In this chapter, we have investigated the control of the radiationless decay between the $B_{3u}(n\pi^*)$ and $B_{2u}(\pi\pi^*)$ states of pyrazine using a strong non-resonant laser pulse. It is interesting to compare the control strategy investigated in this work with other control strategies previously studied for the control of the radiationless decay of pyrazine. Optimal control theory (OCT) was used by Wang et al. [22] and Sukharev and Seideman [23, 24]. Wang et al. used a combination of OCT with the MCTDH method and considered vibronic coupling models including three and four vibrational modes (the four mode model being equivalent to the model used in the present work). Their simulation showed the possibility of maximizing the population of either the $B_{3u}(n\pi^*)$ or $B_{2u}(\pi\pi^*)$ states at a given time using both models. In addition, the possibility of achieving more complicated control objectives such as steering the wavepacket to a desired position in a given electronic state was demonstrated. A similar study, based on local control theory was performed by Penfold et al. [25] and showed similar performances, but at the price of significantly higher field strengths. Sukharev and Seideman considered a different approach. They used a simpler two mode model and calculated all the vibronic eigenstates between 4 and 10 eV above the ground electronic state. By analyzing the projection of the calculated states on the diabatic (i.e localized) vibrational eigenstates, they showed the existence of highly excited vibronic eigenstates essentially localized in the $B_{2u}(\pi\pi^*)$ electronic state. Then they used OCT to optimize a laser field able to excite the system to a selected localized vibronic eigenstate, immune to the radiationless decay to the $B_{3u}(n\pi^*)$ state. Finally Shapiro et al. [26–28] used the concept of overlapping resonances to find specific superpositions of vibronic states designed to maximize or minimize the population of the $B_{2u}(\pi\pi^*)$ state at a given time. Significant control over the lifetime of the $B_{2u}(\pi\pi^*)$ was demonstrated. However, the problem of the preparation of the designed superpositions of states by laser pulses was not investigated.

Despite their apparent success, a common feature of these control mechanisms is their need of high selectivity. OCT and LCT are expected to be very sensitive to the details of the vibronic level pattern in the $B_{3u}(n\pi^*)$ and $B_{2u}(\pi\pi^*)$ electronic manifold. Therefore the transferability of the solutions obtained from simplified, few mode models to more realistic ones, for instance including more vibrational modes, and eventually to experiment can be questioned.

In contrast, the control mechanism presented in this chapter does not rely on a particular pulse shape designed to reach a specific target state, nor on details of the model. It is based on the topography of the PESs as well as on the relative magnitude of the static polarizabilities of the different electronic states involved. Therefore control mechanisms based on the use of the Stark effect can be expected to be more robust with respect to fluctuations of the laser pulse parameters or to an imperfect description of the system. In order to confirm this robustness, the application of the control mechanism used in this work to a model of pyrazine including the 24 vibrational modes has been investigated [46]. These calculations showed that the control mechanism investigated in the present work still applies in the full-dimensional model,

demonstrating its robustness with respect to the details of the model used to describe the system.

This attractive feature makes this class of control mechanisms a promising candidate for the laser control of non adiabatic dynamics in polyatomic molecules. Despite this, much work will be necessary to further assess the applicability of control mechanisms based on the Stark effect to a wide class of systems.

First, in the present work, rather high control pulse intensities ($I > 20\,\text{TW/cm}^2$) were shown to be necessary to produce a significant effect on the dynamics of the molecule. The technology required to produce such high intensity near infrared femtosecond laser pulses is well established and widely used in molecular alignment or strong field ionization experiments. However, in the context of laser control through the non-resonant Stark effect, competing processes such as multi-photon excitation or ionization can occur at such intensities, depending on the system. In the experimental work of Stolow et al. [2, 3] on IBr, because of the high polarizability of the molecule, significant effects could be obtained with relatively modest control pulse intensities ($<10\,\text{TW/cm}^2$), thereby minimizing such detrimental competing processes. On the other hand, in previous theoretical works [9, 19, 20], intensities similar to the ones considered in the present work were found necessary to obtain significant results. Experimental studies of the ionization of benzene, halobenzenes and azobenzenes [47, 48] using femtosecond near infrared laser pulses revealed that ionization occurs in the same range of intensities ($>10\,\text{TW/cm}^2$), mainly through resonance-enhanced multiphoton ionization.

In addition, the rotational degrees of freedom have not been considered in this work. The main detrimental effect of the rotation corresponds here to the inefficiency of the control pulse which cannot be considered as aligned with the z molecular axis, even for a cold molecule since the ground rotational state is fully delocalized. The need for aligned molecules to improve in general the efficiency of laser-control processes is a well known issue and much progress has been achieved towards this aim. In particular adiabatic alignment, that is while the field is on, and field-free post-pulse alignment have been both studied for linear or more complex polyatomic molecules (3D alignment) [49–52]. The post-pulse alignment occurs transiently when the rotational wavepacket features a rephasing while the adiabatic alignment corresponds to a non-resonant field-dressing of the rotational states. In this adiabatic case, the ground rotational dressed state features an aligned state for a sufficiently high field and one mainly recovers the vibrational structure omitting the rotational structure (see Refs. [53, 54]). The present work based on the manipulation of the vibrational structure has thus to be considered in this context of adiabatic alignment. One can even imagine that the Stark control field itself aligns the molecule if it is switched on adiabatically also with respect to the rotational structure (which generally imposes a sub-nanosecond pulse). However this general scenario cannot be applied here since the most polarizable axis, both in the ground and $B_{2u}(\pi\pi^*)$ states, is the y axis (see Table 7.1). Alternative alignment can be envisaged, for instance by confining the system in a nanostructured environment [55–57], or near a surface [58–63].

References

1. M. Sala, M. Saab, B. Lasorne, F. Gatti, S. Guérin, J. Chem. Phys. **140**, 194309 (2014)
2. B.J. Sussman, M.Y. Ivanov, A. Stolow, Phys. Rev. A **71**, 05140(R)1 (2005)
3. B.J. Sussman, D. Townsend, M.Y. Ivanov, A. Stolow, Science **314**, 278 (2006)
4. T. Dove, T.W. Schmidt, R.B. López-Martens, G. Roberts, Chem. Phys. **267**, 115 (2001)
5. H. Choi, W.-J. Son, S. Shin, B.Y. Chang, I.R. Solá, J. Chem. Phys. **128**, 104315 (2008)
6. Y.-C. Han, K.-J. Yuan, W.-H. Hu, S.-L. Cong, J. Chem. Phys. **130**, 044308 (2009)
7. C. Sanz-Sanz, G.W. Richings, G.A. Worth, Faraday Discuss. **153**, 275 (2011)
8. Y. Liu, Y. Liu, Q. Gong, Phys. Rev. A **85**, 023406 (2012)
9. D. Kinzel, P. Marquetand, L. González, J. Phys. Chem. A **116**, 2743 (2012)
10. B.M. Garraway, K.-A. Suominen, Phys. Rev. Lett. **80**, 932 (1998)
11. B.M. Garraway, K.-A. Suominen, Fortschr. Phys. **51**, 128 (2003)
12. M. Rodriguez, K.-A. Suominen, B.M. Garraway, Phys. Rev. A **62**, 053413 (2000)
13. K. Härkönen, O. Kärki, K.-A. Suominen, Phys. Rev. A **74**, 043404 (2006)
14. I.R. Solá, J. Santamaría, V.S. Malinovsky, Phys. Rev. A **61**, 043413 (2000)
15. I.R. Solá, Phys. Rev. A **69**, 033401 (2004)
16. B.Y. Chang, S. Shin, I.R. Solá, Phys. Rev. A **82**, 063414 (2010)
17. B.Y. Chang, S. Shin, J. Santamaría, I.R. Solá, J. Chem. Phys. **134**, 144303 (2011)
18. B.Y. Chang, S. Shin, J. Santamaría, I.R. Solá, J. Phys. Chem. A **116**, 2691 (2012)
19. G.W. Richhings, G.A. Worth, J. Phys. Chem. A **116**, 11228 (2012)
20. S. Ruiz-Barragan, L. Blancafort, Faraday Discuss. **163**, 497 (2013)
21. M.E. Corrales, J. González-Vázquez, G. Balerdi, I.R. Solá, R. de Nalda, L. Bañares, Nature Chem. **6**, 785 (2014)
22. L. Wang, H.-D. Meyer, V. May, J. Chem. Phys. **125**, 014102 (2006)
23. M. Sukharev, T. Seideman, Phys. Rev. Lett. **93**, 093004 (2004)
24. M. Sukharev, T. Seideman, Phys. Rev. A **71**, 012509 (2005)
25. T.J. Penfold, G.A. Worth, C. Meier, Phys. Chem. Chem. Phys. **12**, 15616 (2010)
26. P.S. Christopher, M. Shapiro, P. Brumer, J. Chem. Phys. **123**, 064313 (2005)
27. P.S. Christopher, M. Shapiro, P. Brumer, J. Chem. Phys. **125**, 124310 (2006)
28. I. Thanopulos, X. Li, P. Brumer, M. Shapiro, J. Chem. Phys. **137**, 064111 (2012)
29. Z. Hu, S. Singha, Y. Zhao, G.E. Barry, T. Seideman, R.J. Gordon, J. Phys. Chem. Lett. **3**, 2744 (2012)
30. R.J. Gordon1, Z. Hu, T. Seideman, S. Singha, M. Sukharev, Y. Zhao, J. Chem. Phys. **142**, 144311 (2015)
31. C. Woywod, W. Domcke, A.L. Sobolewski, H.-J. Werner, J. Chem. Phys. **100**, 1400 (1994)
32. T. Shiozaki, C. Woywod, H.-J. Werner, Phys. Chem. Chem. Phys. **15**, 262 (2013)
33. H. Köppel, W. Domcke, L.S. Cederbaum, Adv. Chem. Phys. **57**, 59 (1984)
34. R.A. Kendall, T.H. Dunning Jr, R.J. Harrison, J. Chem. Phys. **96**, 6796 (1992)
35. M.J. Frisch, G.W. Trucks, H.B. Schlegel, G.E. Scuseria, M.A. Robb, J.R. Cheeseman, J.A. Montgomery Jr, T. Vreven, K.N. Kudin, J.C. Burant, J.M. Millam, S.S. Iyengar, J. Tomasi, V. Barone, B. Mennucci, M. Cossi, G. Scalmani, N. Rega, G.A. Petersson, H. Nakatsuji, M. Hada, M. Ehara, K. Toyota, R. Fukuda, J. Hasegawa, M. Ishida, T. Nakajima, Y. Honda, O. Kitao, H. Nakai, M. Klene, X. Li, J.E. Knox, H.P. Hratchian, J.B. Cross, V. Bakken, C. Adamo, J. Jaramillo, R. Gomperts, R.E. Stratmann, O. Yazyev, A.J. Austin, R. Cammi, C. Pomelli, J.W. Ochterski, P.Y. Ayala, K. Morokuma, G.A. Voth, P. Salvador, J.J. Dannenberg, V.G. Zakrzewski, S. Dapprich, A.D. Daniels, M.C. Strain, O. Farkas, D.K. Malick, A.D. Rabuck, K. Raghavachari, J.B. Foresman, J.V. Ortiz, Q. Cui, A.G. Baboul, S. Clifford, J. Cioslowski, B.B. Stefanov, G. Liu, A. Liashenko, P. Piskorz, I. Komaromi, R.L. Martin, D.J. Fox, T. Keith, M.A. Al-Laham, C.Y. Peng, A. Nanayakkara, M. Challacombe, P.M.W. Gill, B. Johnson, W. Chen, M.W. Wong, C. Gonzalez, J.A. Pople, *Gaussian 03, Revision C.02* (Gaussian, Inc, Wallingford, 2004)
36. A.A. Granovsky, J. Chem. Phys. **134**, 214113 (2011)

37. A.A. Granovsky, Firefly version 7.1.G, http://www.classic.chem.msu.su/gran/firefly/index.html

38. M.W. Schmidt, K.K. Baldridge, J.A. Boatz, S.T. Elbert, M.S. Gordon, J.H. Jensen, S. Koseki, N. Matsunaga, K.A. Nguyen, S. Su, T.L. Windus, M. Dupuis, J.A. Montgomery, J. Comput. Chem. **14**, 1347 (1993)

39. M. Okruss, F. Penn, A. Hese, J. Mol. Struct. **348**, 119 (1995)

40. M. Boggio-Pasqua, M.A. Robb, M.J. Bearpark, J. Phys. Chem. A **109**, 8849 (2005)

41. A. Raab, G.A. Worth, H.-D. Meyer, L.S. Cederbaum, J. Chem. Phys. **110**, 936 (1998)

42. M. Stener, P. Decleva, D.M.P. Holland, D.A. Shaw, J. Phys. B: At. Mol. Opt. Phys. **44**, 075203 (2011)

43. J.C. Light, I.P. Hamilton, J.V. Lill, J. Chem. Phys. **82**, 1400 (1985)

44. T. Horio, T. Fuji, Y.-I. Suzuki, T. Suzuki, J. Am. Chem. Soc. **131**, 10392 (2009)

45. Y.-I. Suzuki, T. Fuji, T. Horio, T. Suzuki, J. Chem. Phys. **132**, 174302 (2010)

46. M. Saab, M. Sala, S. Guérin, B. Lasorne, F. Gatti, J. Chem. Phys. **141**, 134114 (2014)

47. T.D. Scarborough, J. Strohaber, D.B. Foote, C.J. McAcy, C.J.G.J. Uiterwaal, Phys. Chem. Chem. Phys. **13**, 13783 (2011)

48. T.D. Scarborough, D.B. Foote, C.J.G.J. Uiterwaal, J. Chem. Phys. **136**, 054309 (2012)

49. J.J. Larsen, K. Hald, N. Bjerre, H. Stapelfeldt, T. Seideman, Phys. Rev. Lett. **85**, 2470 (2000)

50. J.G. Underwood, B.J. Sussman, A. Stolow, Phys. Rev. Lett. **94**, 143002 (2005)

51. K.F. Lee, D.M. Villeneuve, P.B. Corkum, A. Stolow, J.G. Underwood, Phys. Rev. Lett. **97**, 173001 (2006)

52. A. Rouzée, S. Guérin, O. Faucher, B. Lavorel, Phys. Rev. A **77**, 043412 (2008)

53. S. Hervé, F. Le Quéré, R. Marquardt, Int. J. Quant. Chem. **99**, 439 (2004)

54. S. Thomas, S. Guérin, H.R. Jauslin, Phys. Rev. A **71**, 013402 (2005)

55. R.G. Chapman, J.C. Sherman, J. Org. Chem. **65**, 513 (2000)

56. X. Zhao, S. Liu, Y. Li, M. Chen, Spectrochim. Acta A **75**, 794 (2010)

57. T. Kiljunen, B. Schmidt, N. Schwentner, Phys. Rev. Lett. **94**, 123003 (2005)

58. P. Avouris, J.E. Demuth, J. Chem. Phys. **75**, 4783 (1981)

59. R. Dudde, K.-H. Frank, E.E. Koch, J. Electron. Spectrosc. Relat. Phenom. **47**, 245 (1988)

60. T. Omiya, H. Yokohara, M. Shimomura, J. Phys. Chem. C **116**, 9980 (2012)

61. P. Saalfrank, G.K. Paramonov, J. Chem. Phys. **107**, 10723 (1997)

62. M.J. Comstock, N. Levy, A. Kirakosian, J. Cho, F. Lauterwasser, J.H. Harvey, D.A. Strubble, J.M.J. Fréchet, D. Trauner, S.G. Louis, M.F. Crommie, Phys. Rev. Lett. **99**, 038301 (2007)

63. M.G. Reuter, M. Sukharev, T. Seideman, Phys. Rev. Lett. **101**, 208303 (2008)

Chapter 8
Laser Driven Tunneling Dynamics in NHD$_2$

This chapter is partly based on results and discussions published in Refs. [1, 2]. This material is reproduced with permission. Copyright [2012, 2014] AIP Publishing LLC.

8.1 Introduction

Tunneling plays an essential role in a number of chemical and physical phenomena including chemical [3], photochemical [4] or biological reactions [5], electron transfer between quantum dots [6], strong field ionization [7] or nuclear fission [8] and fusion [9]. In addition, the tunneling effect is a paradigmatic example of quantum coherence phenomena. Therefore, the laser control of the tunneling dynamics of quantum systems is a topic of major interest [10]. Tunneling can occur from a potential well to a continuum, or between different wells in a bound potential. In particular, the tunneling effect in systems described by a symmetric double well potential represents the simplest and most intensively studied situation. Various schemes to control the tunneling dynamics of symmetric double well quantum systems have been proposed. Enhancement of tunneling, i.e. field-induced tunneling in a time much shorter than the natural time, by a nonresonant [11–13] or resonant [14] pulse-shaped field, localization of the system in one of the two wells from the delocalized ground state by a quasi-resonant field [15], or the coherent destruction of tunneling during the field [16–19]. More recently, a scheme to induce the localization and suppression of tunneling by adiabatic passage has been proposed [20]. Control of tunneling shares some aspects with the control of superposition of states [21] and with the orientation of molecules [22]. Most of these studies have been proposed in simplified, typically one-dimensional, systems. In this chapter, we first address the laser induced enhancement of tunneling (Sect. 8.2) and next the coherent destruction of tunneling (Sect. 8.3) in a model of NHD$_2$ taking into account its six vibrational degrees of freedom.

Ammonia and its isotopomers, through their inversion motion (also called umbrella motion), are a textbook example illustrating the tunneling dynamics in a symmetric double well potential. In addition, they are simple enough to allow for an accurate, full-dimensional quantum mechanical description of their nuclear dynamics. Our choice of NHD$_2$ as a target system was motivated the possibility to use the vibrational eigenstates computed in a previous theoretical study [23], and the transition moments between them, to construct a model Hamiltonian allowing us to study the laser control of the tunneling motion of the molecule at a reduced computational cost. The main objective of this work was to assess the applicability of control schemes established for simple model systems to a realistic model of a polyatomic molecule.

8.2 Laser Induced Enhancement of Tunneling

In this section, we study the strategy of enhancement of tunneling by a pulsed resonant laser field [14] in NHD$_2$ by means of quantum dynamics simulations performed using the MCTDH method as implemented in the Heidelberg package. The MCTDH method has been previously used to investigate the laser driven vibrational dynamics of similar systems such as HCF$_3$ [24], HFCO [25], DFCO [26] or HONO [27, 28]. An effective Hamiltonian built in a basis of low-lying vibrational eigenstates of the molecule was first used to explore the influence of the laser pulse parameters on the efficiency of the control scheme at a reduced computational cost. The dynamics of the molecule driven by a suitable laser pulse was then computed using the exact vibrational Hamiltonian. Choosing a linearly polarized laser pulse of appropriate frequency, we obtained a laser driven tunneling effect in a time approximately twenty times smaller than the field-free tunneling time in rather good accordance with analytical predictions obtained from an oversimplified three-state model. This result necessitates that the molecule experiences a three-dimension alignment during the excitation process [29–34]. If the molecule experiences only a one-dimensional alignment, the tunneling enhancement obtained after averaging over the azimuthal orientation about the alignment axis was found to be much reduced. In this case, the averaged tunneling enhancement can be improved by replacing the linear-polarized field by a circular-polarized field.

In the next subsection, we present the mechanism of driven enhanced tunneling by a resonant pulse using an effective three-state model. The Hamiltonian and the coordinates used in the MCTDH calculations are derived in Sect. 8.2.2. The range of parameters considered in this work is justified in Sect. 8.2.3. In Sect. 8.2.4, quantum dynamics simulations of the control scheme investigated in this work using the exact vibrational Hamiltonian are presented. Simulations are presented and discussed both for linearly and circularly polarized fields. Conclusions are given in Sect. 8.2.5.

8.2.1 Enhancement of Tunneling by a Resonant Pulsed Field: Mechanism

In a symmetric double well potential with a low-energy barrier connecting the two wells, the low-lying eigenstates form nearly degenerate doublets, one member of the doublet being symmetric and the other being antisymmetric with respect to the tunneling coordinate. The corresponding eigenfunctions are delocalized over the two wells. To study the tunneling dynamics in a symmetric double well, it is convenient to define two localized states, noted $|L\rangle$ and $|R\rangle$, as superpositions of the delocalized eigenstates of the ground tunneling doublet, noted $|(0)^s\rangle$ and $|(0)^a\rangle$.

$$|L\rangle = \frac{1}{\sqrt{2}}\left(|(0)^s\rangle + |(0)^a\rangle\right), \quad |R\rangle = \frac{1}{\sqrt{2}}\left(|(0)^s\rangle - |(0)^a\rangle\right). \tag{8.1}$$

The wavefunctions associated with the delocalized eigenstates and the localized states are illustrated in Fig. 8.1 in the case of a generic one-dimensional double well potential. If one considers, for instance, $|L\rangle$ as initial condition, the dynamics of the system is described by the state

$$
\begin{aligned}
|\Psi(t)\rangle &= e^{-i\frac{\sigma}{2}t}\frac{1}{\sqrt{2}}\left[|(0)^s\rangle e^{i\frac{\delta}{2}t} + |(0)^a\rangle e^{-i\frac{\delta}{2}t}\right] \\
&= e^{-i\frac{\sigma}{2}t}\left[|L\rangle\cos\left(\frac{\delta}{2}t\right) + i|R\rangle\sin\left(\frac{\delta}{2}t\right)\right],
\end{aligned}
\tag{8.2}
$$

where $\sigma = (\omega_{(0)^a} + \omega_{(0)^s})$ and $\delta = \omega_{(0)^a} - \omega_{(0)^s}$ with $\hbar\omega_{(0)^s}$ and $\hbar\omega_{(0)^a}$ being the energies corresponding respectively to $|(0)^s\rangle$ and $|(0)^a\rangle$. δ is usually called the ground state tunneling splitting. From this relation, a field-free tunneling time τ can be defined as the shortest time for the system to tunnel from $|L\rangle$ to $|R\rangle$ (up to a global phase)

$$\tau = \pi/\delta. \tag{8.3}$$

The 6D model of NHD$_2$ used in this work [23] gives a splitting of $0.159\,\mathrm{cm}^{-1}$ between the two components of the ground state, in very good agreement with the experimental value of $0.171\,\mathrm{cm}^{-1}$. The corresponding field-free tunneling time is $\tau \approx 104\,\mathrm{ps}$.

Our goal is to induce a full population inversion between the two localized states by a single laser pulse in a time much smaller than the field-free tunneling time defined above. In a previous work, it was shown that this can be achieved by a 2π-pulse that selectively couples one of the two delocalized states to an intermediate excited state, noted $|\chi_e\rangle$. The 2π-pulse induces a full Rabi oscillation between the two coupled states and the required π phase to the delocalized state that has been addressed by the
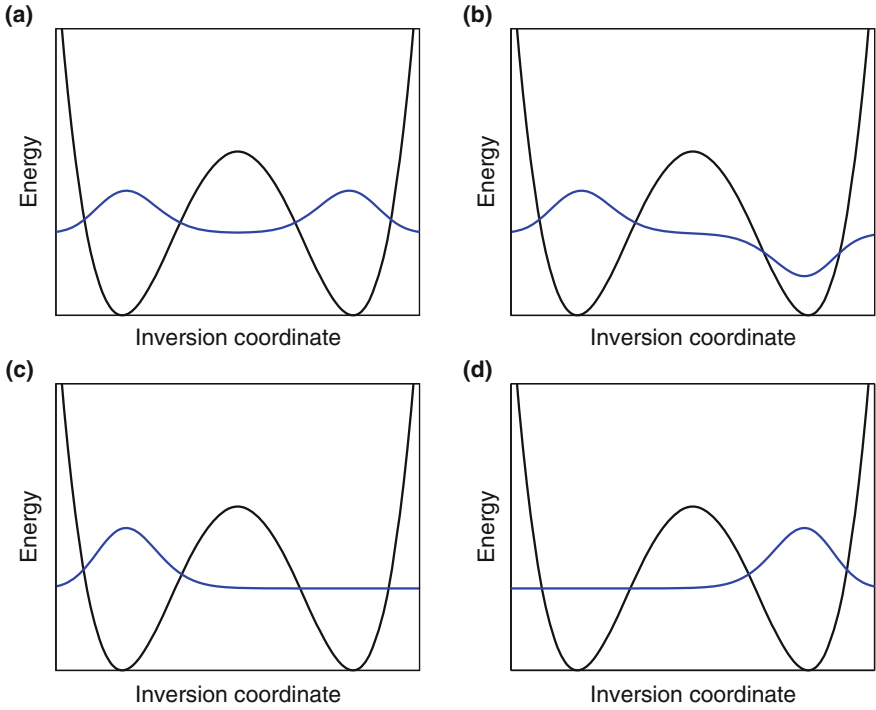
Fig. 8.1 Illustration of the wavefunctions of the delocalized states $|(0)^s\rangle$ and $|(0)^a\rangle$ (**a**) and (**b**) and of the localized states $|L\rangle$ and $|R\rangle$,(**c**) and (**d**) in the case of a generic one-dimensional double well potential

field. This result can be demonstrated analytically by assuming a simple three-state effective model. Consider a linearly polarized laser pulse of general expression

$$\boldsymbol{\varepsilon(t)} = \varepsilon_0\Lambda(t)\cos(\omega t)\boldsymbol{e}, \tag{8.4}$$

where ε_0 is the peak amplitude, $\Lambda(t)$ an envelope function, ω the carrier frequency and $\boldsymbol{e}$ the unit vector in the direction of polarization. Assuming the resonant wave approximation (RWA), the interaction of the system with the laser pulse is described by the following effective Hamiltonian operator, expressed in the dressed basis $\{|(0)^s, 0\rangle, |(0)^a, 0\rangle, |\chi_e, -1\rangle\}$, where the second label stands for the relative number of dressing photons

$$\boldsymbol{H}_{\text{RWA}}(t) = \frac{1}{2}\begin{pmatrix} 0 & 0 & \Omega(t) \\ 0 & 2\delta & 0 \\ \Omega(t) & 0 & 0 \end{pmatrix}, \tag{8.5}$$

where $\Omega(t) = -\varepsilon_0 \Lambda(t)\boldsymbol{\mu}_{(0)^s,\chi_e}.\boldsymbol{e}$, and $\boldsymbol{\mu}_{(0)^s,\chi_e}$ is the transition dipole moment vector between states $|(0)^s\rangle$ and $|\chi_e\rangle$. The time-dependent Schrödinger equation (TDSE)

$$H_{\text{RWA}}(t)\Psi(t) = i\hbar\frac{\partial}{\partial t}\Psi(t) \tag{8.6}$$

can be solved analytically, following the steps detailed in Sect. 6.2.3 of Chap. 6. Considering the system initially in the $|L\rangle$ superposition, the probability P_{tun} to find the system in the $|R\rangle$ at the end of the pulse $(t = t_p)$ is given by

$$P_{\text{tun}} = |\langle R|\Psi(t = t_p)\rangle|^2 = \frac{3}{8} + \frac{1}{8}\cos A(t_p)$$
$$- \frac{1}{4}\left[\cos\left(\delta t_p - A(t_p)/2\right) + \cos\left(\delta t_p + A(t_p)/2\right)\right], \tag{8.7}$$

with the Rabi frequency partial area $A(t) = \int_0^t |\Omega(s)|\,ds$. From this equation one can see that the tunneling inversion probability is close to unity if the conditions

$$A(t_p) \equiv \int_0^{t_p} |\Omega(t)|\,dt = 2\pi, \quad t_p \ll \pi/\delta \equiv \tau \tag{8.8}$$

are fulfilled. Thus, one requires a 2π-pulse of sufficiently short duration to enhance the tunneling. The 2π-pulse condition defines a relation between the peak amplitude and the duration of the laser pulse. Considering a sine-square shaped envelope for the laser pulse

$$\Lambda(t) = \sin^2\left(\frac{\pi t}{t_p}\right) \quad \text{for } 0 < t < t_p$$
$$\Lambda(t) = 0 \quad \text{otherwise}, \tag{8.9}$$

this relation reads

$$\left|\varepsilon_0\boldsymbol{\mu}_{(0)^a,\chi_e}.\boldsymbol{e}\right| \int_0^{t_p} \sin^2\left(\frac{\pi t}{t_p}\right) dt = 2\pi, \tag{8.10}$$

which gives

$$t_p = \frac{4\pi}{\left|\varepsilon_0\boldsymbol{\mu}_{(0)^a,\chi_e}.\boldsymbol{e}\right|}. \tag{8.11}$$

8.2.2 Hamiltonian and Coordinates

The molecule in interaction with the laser field is described by the Hamiltonian operator

$$H(\boldsymbol{q}, t) = H_0(\boldsymbol{q}) + H_{\text{int}}(\boldsymbol{q}, t), \tag{8.12}$$

where $\boldsymbol{q}$ denotes a vector gathering the six vibrational coordinates used to parametrize the motion of the nuclei (see below). $H_0(\boldsymbol{q})$ is the field-free Hamiltonian operator of the molecule

$$H_0(\boldsymbol{q}) = T(\boldsymbol{q}) + V(\boldsymbol{q}), \tag{8.13}$$

where $T(\boldsymbol{q})$ denotes the nuclear kinetic energy operator (KEO) and $V(\boldsymbol{q})$ is the potential energy surface of the ground electronic state. The $H_{\text{int}}(\boldsymbol{q}, t)$ Hamiltonian operator describes the interaction of the molecule with the laser field in the dipole approximation

$$H_{\text{int}}(\boldsymbol{q}, t) = -\boldsymbol{\mu}(\boldsymbol{q}).\boldsymbol{\varepsilon}(t), \tag{8.14}$$

where $\boldsymbol{\mu}(\boldsymbol{q})$ is the vector containing the three dipole moment surfaces and $\boldsymbol{\varepsilon}(t)$ is the electric field vector.

Following Ref. [23], the vibrational motion of the nuclei was parameterized by polyspherical Radau coordinates [35, 36]. The Radau coordinates are the spherical coordinates $(r_1, \theta_1, \varphi_1)$, $(r_2, \theta_2, \varphi_2)$ and $(r_3, \theta_3, \varphi_3)$ of the three Radau vectors, illustrated in Fig. 8.2, in the molecular frame $M = xyz$ defined as follows: the x axis is parallel to $\boldsymbol{r_3}$ and $\boldsymbol{r_2}$ lies in the (x,y) plane (see Fig. 8.3). The corresponding laboratory (or space-fixed) frame denoted $L = XYZ$ allows one to characterize the orientation of the three main axes by three Euler angles. The vibrational motion is described by the six coordinates $r_1, r_2, r_3, \theta_1, \theta_2$ and φ_1, the three remaining coordinates describe the rotation of the molecule. As a simplification, we consider the KEO of the fundamental rotational state $J = 0$ [23] and neglect the rotational motion of the molecule. This is equivalent to assuming that the molecule is ideally aligned (three-dimensional alignment) and that the Hamiltonian operator of Eq. (8.12) describes this aligned molecule. This assumption was found to be valid in the case of a diatomic molecule in Ref. [37]. The extension of this result to polyatomic molecules is a working hypothesis in the present work. Note that the actual coordinates used in the calculations are r_1, r_2, r_3, u_1, u_2 and φ_1, where $u_i = \cos(\theta_i)$. This choice allows one to work with Hermitian momentum operators [35]. The explicit expression of the $J = 0$ KEO can be found in Ref. [23]. The AMMPOT4 potential energy surface [38] and the dipole moment surfaces of Ref. [39], both developed by Marquardt and co-workers, were used in this work.

In the case of an ideal three-dimensional alignment, the M frame equals the L frame and the polarization of the laser pulse can be chosen in the molecular frame.
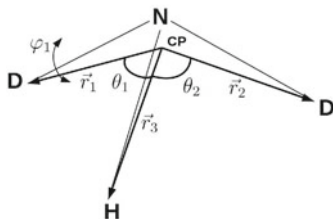
Fig. 8.2 Radau polyspherical coordinates for the NHD$_2$ molecule. CP denotes the canonical point (see Ref. [40] for a definition). Figure reproduced from Ref. [2]
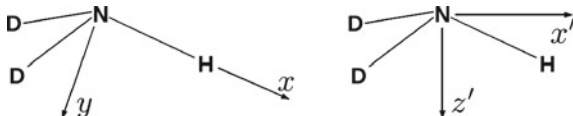

Fig. 8.3 Definition of the M and M' molecular frames. The x axis is parallel to the NH bond and the y axis lies in the NHD plane. The x' and z' axes are in the plane of the paper. The z' coordinates of the H and D atoms are mutually equal, the y' coordinate of the H atom is zero. The z and y' axes are not shown for sake of clarity. Figure reproduced from Ref. [1]

In the case of one-dimensional alignment [29] we consider the molecule as ideally aligned along the most polarizable axis of the asymmetric-top molecule, which is parallel to the dipole moment vector at the equilibrium geometry [41] (corresponding to the C_3 axis of NH$_3$), for instance during a nanosecond (non-resonant) adiabatic linearly polarized pulse. Since the most polarizable axis of the molecule does not correspond to any of the axes of the above defined molecular frame, it is convenient to introduce a second set of molecular and laboratory frames called respectively $M' = x'y'z'$ and $L' = X'Y'Z'$. The M' frame is defined as follows: The z' axis is parallel to the most polarizable axis at the equilibrium geometry while the NH bond lies in the (x', z') plane (see Fig. 8.3). The L' frame is defined as follows: the Z' axis is parallel to the z' axis; the X' and Y' axes are rotated from the x' and y' axes, respectively, by the Euler angle ϕ about the Z' axis, ϕ being the precession angle of the molecule about the alignment axis Z'.

One assumes that the field is in the plane (X, Y) of the L frame

$$\varepsilon^{(L)}(t) = \begin{pmatrix} \varepsilon_X^{(L)}(t) \\ \varepsilon_Y^{(L)}(t) \\ 0 \end{pmatrix} \tag{8.15}$$

where, for the linear polarization, we choose (see Sect. 8.2.3 for a justification of this choice)

$$\begin{cases} \varepsilon_X^{(L)}(t) = 0, \\ \varepsilon_Y^{(L)}(t) = \varepsilon_0 \Lambda(t) \cos(\omega t), \end{cases} \tag{8.16}$$

and, for the circular polarization,

$$\begin{cases} \varepsilon_X^{(L)}(t) = \frac{\varepsilon_0}{\sqrt{2}} \Lambda(t) \sin(\omega t), \\ \varepsilon_Y^{(L)}(t) = \frac{\varepsilon_0}{\sqrt{2}} \Lambda(t) \cos(\omega t). \end{cases} \tag{8.17}$$

Note that the alignment axis Z' and the direction Z of propagation of the electromagnetic field do not coincide. The electric field is then rotated in the M molecular frame, in which we know the three dipole moment surfaces, via the L' and M' frames through the series of transformations

$$\varepsilon^{(M)}(t) = \begin{pmatrix} \varepsilon_x^{(M)}(t) \\ \varepsilon_y^{(M)}(t) \\ \varepsilon_z^{(M)}(t) \end{pmatrix} = R_{M' \to M} R_{L' \to M'} R_{L \to L'} \begin{pmatrix} \varepsilon_X^{(L)}(t) \\ \varepsilon_Y^{(L)}(t) \\ 0 \end{pmatrix}. \tag{8.18}$$

The rotation matrices $R_{L \to L'}$ and $R_{M' \to M}$ depend on three constant Euler angles, $\phi_0 = 240°$, $\theta_0 = 38.677°$ and $\chi_0 = 126.465°$, determined from the definitions of the various frames given above. Following the coventions of Ref. [42], one can write

$$R_{L \to L'} = \begin{pmatrix} c\phi_0 c\theta_0 c\chi_0 - s\phi_0 s\chi_0 & -c\phi_0 c\theta_0 s\chi_0 - s\phi_0 c\chi_0 & c\phi_0 s\theta_0 \\ s\phi_0 c\theta_0 c\chi_0 + c\phi_0 s\chi_0 & -s\phi_0 c\theta_0 s\chi_0 + c\phi_0 c\chi_0 & s\phi_0 s\theta_0 \\ -s\theta_0 c\chi_0 & s\theta_0 s\chi_0 & c\theta_0 \end{pmatrix}, \tag{8.19}$$

where a short-hand notation has been used for the cos and sin functions, e.g. $c\phi_0 \equiv \cos \phi_0$. However, the matrix $R = R_{M' \to M} R_{L' \to M'} R_{L \to L'}$ was found to be independent of the angle ϕ_0. Therefore, the simpler form

$$R_{L \to L'} = \begin{pmatrix} c\theta_0 c\chi_0 & -c\theta_0 s\chi_0 & s\theta_0 \\ s\chi_0 & c\chi_0 & 0 \\ -s\theta_0 c\chi_0 & s\theta_0 s\chi_0 & c\theta_0 \end{pmatrix}. \tag{8.20}$$

can be used without loss of generality. The matrix $R_{M' \to M}$ is simply given by $R_{M' \to M} = R_{L \to L'} R_{L \to L'}^{-1} = R_{L \to L'}^{\dagger}$. Finally the $R_{L' \to M'}$ matrix defines a rotation around the alignment axis (Z') and therefore depends only on the first Euler angle ϕ

$$R_{L' \to M'} = \begin{pmatrix} c\phi & s\phi & 0 \\ -s\phi & c\phi & 0 \\ 0 & 0 & 1 \end{pmatrix}. \tag{8.21}$$

Using these definitions, one can calculate the electric field in the molecular frame M

$$\varepsilon_x^{(M)}(t) = \left(c\phi c^2 \theta_0 c\chi_0 - s\phi c\theta_0 s\chi_0 + s^2 \theta_0 c\chi_0 \right) \left(c\chi_0 \varepsilon_X^{(L)}(t) - s\chi_0 \varepsilon_Y^{(L)}(t) \right)$$
$$+ (s\phi c\theta_0 c\chi_0 + c\phi s\chi_0) \left(S\chi_0 \varepsilon_X^{(L)}(t) + c\chi_0 \varepsilon_Y^{(L)}(t) \right), \tag{8.22}$$

$$\varepsilon_y^{(M)}(t) = -\left(c\phi c^2\theta_0 s\chi_0 + s\phi c\theta_0 c\chi_0 + s^2\theta_0 s\chi_0\right)\left(c\chi_0\varepsilon_X^{(L)}(t) - s\chi_0\varepsilon_Y^{(L)}(t)\right)$$
$$+ (-s\phi c\theta_0 s\chi_0 + c\phi c\chi_0)\left(s\chi_0\varepsilon_X^{(L)}(t) + c\chi_0\varepsilon_Y^{(L)}(t)\right), \qquad (8.23)$$

$$\varepsilon_z^{(M)}(t) = c\theta_0 s\theta_0(c\phi - 1)\left(c\chi_0\varepsilon_X^{(L)}(t) - s\chi_0\varepsilon_Y^{(L)}(t)\right)$$
$$+ s\theta_0 s\phi\left(s\chi_0\varepsilon_X^{(L)}(t) + c\chi_0\varepsilon_Y^{(L)}(t)\right). \qquad (8.24)$$

8.2.3 Computational Strategy

The three-state model presented in Sect. 8.2.1 is a minimal model that provides a simple description of the control mechanism adopted in the present work. However, this model can not describe competing processes such as multi-photon excitations and vibrational Stark shifts which could impact the efficiency of the process. Therefore, it represents an oversimplification of our system and can not be used to choose the precise parameters of the laser pulse (peak amplitude, duration and frequency) which would efficiently induce the desired effect in the full system. On the other hand, simulations of the dynamics of the molecule using the exact 6D vibrational Hamiltonian are time-consuming. Therefore one can not explore the full parameter space in order to find the best possible set of parameters in a reasonable time. It is thus desirable to derive an effective but accurate model which is simple enough to allow one to perform a large number of simulations with different parameters of the field. A simple way to construct such a model is to extract all eigenstates, eigenvalues and transition dipole moments between eigenstates in a given energy window. The effective Hamiltonian reads

$$H^{eff}(t) = H_0^{eff} + H_{int}^{eff}(t), \qquad (8.25)$$

where the matrix representation of the field-free effective Hamiltonian H_0^{eff} is the diagonal matrix

$$(H_0^{eff})_{ij} = E_i\delta_{ij}, \qquad (8.26)$$

where E_i denotes the eigenvalues of the exact vibrational field-free Hamiltonian and

$$H_{int}^{eff}(t) = \boldsymbol{\mu}^{eff}.\boldsymbol{\varepsilon}(t) \qquad (8.27)$$

is the effective interaction Hamiltonian operator. The matrix elements of the effective dipole moment operator read

$$(\boldsymbol{\mu}^{eff})_{ij} = \langle\chi_i|\boldsymbol{\mu}^{(M)}|\chi_j\rangle \qquad (8.28)$$

where $|\chi_i\rangle$ denotes the ith eigenstate of the exact vibrational Hamiltonian of the molecule. We used the 142 lowest vibrational eigenstates of the molecule, spanning the energy range up to $5307\,\text{cm}^{-1}$, computed in Ref. [23] using the improved relaxation method [43, 44] as implemented in the Heidelberg MCTDH package. The package was used in this work to compute all the transition dipole moments vectors between these eigenstates. The low dimensionality and simple structure of the effective Hamiltonian of Eq. (8.25) allows for a fast integration of the associated TDSE

$$i\hbar\frac{\partial\Psi(t)}{\partial t} = H^{eff}(t)\Psi(t). \tag{8.29}$$

In this work, Eq. (8.29) was solved using a split operator-scheme, in which the propagator $U(t) = e^{-iH^{eff}t}$ is split into three terms

$$U(t) \approx e^{-\frac{i}{2}H_0^{eff}t}e^{-iH_{\text{int}}^{eff}t}e^{-\frac{i}{2}H_0^{eff}t}. \tag{8.30}$$

The propagation scheme between times t and $t + \Delta t$ reads

$$\Psi(t+\Delta t) = e^{-\frac{i}{2}H_0^{eff}\Delta t}e^{-iH_{\text{int}}^{eff}(t+\frac{\Delta t}{2})\Delta t}e^{-\frac{i}{2}H_0^{eff}\Delta t}\Psi(t) + O(\Delta t^3). \tag{8.31}$$

To avoid the calculation of the exponential of the matrix $\boldsymbol{H}_{\text{int}}^{\boldsymbol{eff}}$ at each time step of the propagation, the matrix $\boldsymbol{\mu^{eff}}.\boldsymbol{e}$ can be diagonalized before the propagation

$$\boldsymbol{\mu^{eff}}.\boldsymbol{e} = T\mu_D T^{\dagger}, \tag{8.32}$$

and the scheme (8.31) can be rewritten as

$$\Psi(t+\Delta t) = e^{-\frac{i}{2}H_0^{eff}\Delta t}Te^{-i\mu_D E(t+\frac{\Delta t}{2})\Delta t}T^{\dagger}e^{-\frac{i}{2}H_0^{eff}\Delta t}\Psi(t) + O(\Delta t^3). \tag{8.33}$$

Using this scheme, the computation of the dynamics of the system over a few picoseconds does not take more than a few seconds on a standard computer.

In order to apply the mechanism described in Sect. 8.2.1 to the enhancement of tunneling in NHD$_2$, one has first to choose a suitable intermediate excited vibrational state which can be efficiently and selectively coupled to one state of the fundamental tunneling doublet. More precisely, one needs to induce a full Rabi oscillation between one of the delocalized $|(0)^s\rangle$ and $|(0)^a\rangle$ eigenstates and the intermediate excited state without inducing any population transfer between the other delocalized eigenstate and any excited vibrational state. The vibrational eigenvalues computed in Ref. [23] compared with experimental values, and the transition dipole moments computed in this work are presented in Tables 8.1 and 8.2. As seen in Table 8.2, a field polarized along the z molecular axis couples states with different parity with

Table 8.1 Comparison of selected low-lying 6D vibrational eigenvalues calculated in [23] with available experimental values (in cm^{-1})

Level	Sym. (MS_4)	E_{MCTDH}	Exp.
$(0)^s$	A^+	0.00	0.00
$(0)^a$	A^-	0.16	0.171 [45]
$(2^1)^s$	A^+	808.81	810.23 [45]
$(2^1)^a$	A^-	817.68	819.56 [45]
$(4_a^1)^s$	A^+	1235.67	1233.27 [46]
$(4_a^1)^a$	A^-	1238.11	1235.89 [46]
$(2^2)^s$	A^+	1450.38	–
$(4_b^1)^s$	B^+	1461.55	1461.79 [46]
$(4_b^1)^a$	B^-	1461.72	1461.99 [46]
$(2^2)^a$	A^-	1575.56	–
$(2^3)^s$	A^+	1957.55	–
$(2^3)^a$	A^-	2360.99	–
$(3_a^1)^s$	A^+	2435.87	2430.80 [46]
$(3_a^1)^a$	A^-	2437.49	2434.62 [46]
$(3_b^1)^s$	B^+	2564.05	2559.81 [46]
$(3_b^1)^a$	B^-	2564.16	2559.96 [46]
$(1^1)^s$	A^+	3406.08	3404.24 [46]
$(1^1)^a$	A^-	3406.15	3404.32 [46]

The spectroscopic notation to used to label the levels is explained in Ref. [46]. Symmetry labels in the MS$_4$ permutation-inversion symmetry group are given

respect to the inversion motion. This coupling is particularly strong for states of a same tunneling doublet (see for instance the value of $\langle(0)^s|\mu_z^{(M)}|(0)^a\rangle$ in Table 8.2). These strong transition dipole moments are expected to produce significant Stark shifts which could destroy the efficiency of the process. Conversely, a field polarized in the orthogonal plane (x, y) only couples states of the same parity with respect to the inversion motion.

As illustrated in Fig. 8.4, the $|(2^2)^a\rangle$ state seems to be the best choice for the intermediate excited state, as it is well isolated in energy from both its tunneling doublet partner and other vibrational states. It has furthermore a sufficiently strong transition dipole moment with the antisymmetric component of the fundamental state $|(0)^a\rangle$. Within these conditions, the mechanism to enhance the tunneling described in the previous section is applicable with a sufficiently short pulse of non-ionizing intensity linearly polarized along the y direction.

Table 8.2 Calculated transition dipole moments (in ea_0 where e is the elementary charge and a_0 is the bohr) of the selected low-lying vibrational eigenstates with the two tunneling components of the fundamental eigenstate

Level	$\mu_x^{(0)s}$	$\mu_x^{(0)a}$	$\mu_y^{(0)s}$	$\mu_y^{(0)a}$	$\mu_z^{(0)s}$	$\mu_z^{(0)a}$
$(0)^s$	0.3278	–	0.5562	–	–	0.3028
$(0)^a$	–	0.3279	–	0.5561	0.3028	–
$(2^1)^s$	−0.0151	–	0.0448	–	–	−0.0381
$(2^1)^a$	–	−0.0150	–	0.0448	−0.0375	–
$(4_a^1)^s$	−0.0270	–	0.0086	–	–	0.0188
$(4_a^1)^a$	–	0.0275	–	−0.0094	−0.0188	–
$(2^2)^s$	−0.0065	–	0.0079	–	–	0.0046
$(4_b^1)^s$	–	–	−0.0114	–	–	0.0199
$(4_b^1)^a$	–	–	–	0.0114	−0.0199	–
$(2^2)^a$	–	0.0045	–	−0.0058	−0.0045	–
$(2^3)^s$	−0.0017	–	0.0019	–	–	0.0001
$(2^3)^a$	–	–	–	0.0005	−0.0021	–
$(3_a^1)^s$	0.0058	–	−0.0247	–	–	−0.0150
$(3_a^1)^a$	–	0.0061	–	−0.0253	−0.0153	–
$(3_b^1)^s$	–	–	0.0084	–	–	−0.0147
$(3_b^1)^a$	–	–	–	0.0085	−0.0147	–
$(1^1)^s$	–	0.0382	–	−0.0030	−0.0014	–
$(1^1)^a$	0.0381	–	−0.0031	–	–	−0.0014

For each state listed, transition dipole moment corresponding to transition from the $|(0)^s\rangle$ and $|(0)^a\rangle$ are given. Values smaller than 10^{-4} ea_0 are not given

8.2.4   Results and Discussion

8.2.4.1   Linearly Polarized Field and Three-Dimension Alignment

Here we consider the ideal case of three-dimensionally aligned molecule in interaction with a linearly polarized laser pulse. We compare the results obtained with the effective model Hamiltonian described in Sect. 8.2.3 to those obtained with the exact vibrational Hamiltonian described in Sect. 8.2.2.

Results Obtained with the Effective Hamiltonian

The TDSE of Eq. (8.29) was solved using the scheme of Eq. (8.33) for a wide range of parameters of the laser pulse, with frequencies close to the resonance between the $|(0)^a\rangle$ and the $|(2^2)^a\rangle$ states, using the $|L\rangle$ localized state as initial condition. Contour plots of the population of the target state $|R\rangle$ at the end of the interaction of the system with a laser pulse of polarization in the y direction are given in Fig. 8.5 as a function of the pulse parameters. On the left panel, the population of the target
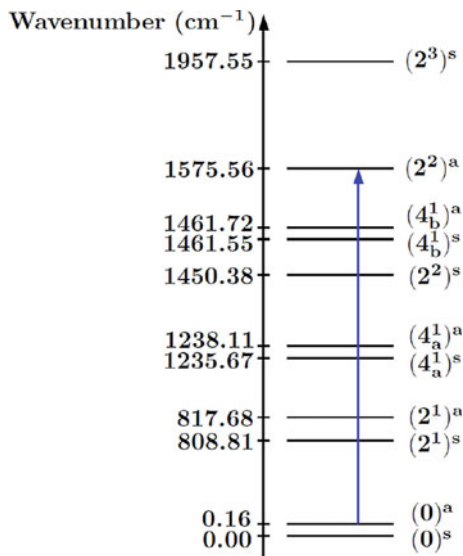
Fig. 8.4 Energy diagram illustrating our control strategy. The *blue arrow* features the resonant 2π-pulse. Figure reproduced from Ref. [1]
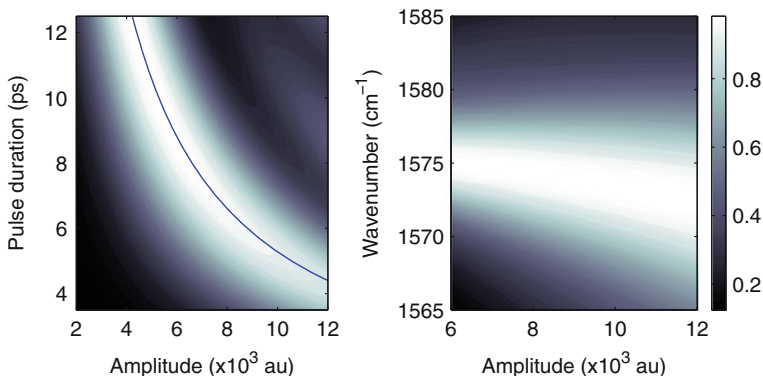

Fig. 8.5 Two dimensional contour plots of the population of the $|R\rangle$ localized superposition at the end of the pulse ($t = t_p$) as a function of the peak amplitude ε_0 and of the pulse duration t_p (*left panel*) and as a function of the peak amplitude ε_0 and the field wavenumber (*right panel*). The frequency of the field has been set at resonance ($\omega = 1575.56\,\text{cm}^{-1}$) in the *left panel*. The pulse duration t_p is chosen such that the 2π condition given by Eq. (8.11) is fulfilled in the *right panel*. The *blue curve* of *left panel* is the hyperbola defined by Eq. (8.11). Figure adapted from Ref. [1]

state is given as a function of the peak amplitude ε_0 and duration of the pulse t_p. The blue curve is the hyperbola of Eq. (8.11) defining a constant Rabi frequency area of 2π. These results confirm the mechanism suggested by the three-state system invoked in Sect. 8.2.1. The probability of population transfer to the target state is

close to unity for a Rabi frequency area close to 2π. On the right panel, the final population of the target state $|R\rangle$ is displayed as a function of the peak amplitude ε_0 and the frequency ω of the pulse. The Rabi frequency area is fixed at 2π which means that for a given peak amplitude, the pulse duration was set according to Eq. (8.11). Figure 8.5 shows that for amplitudes of the electric field strength below 8×10^{-3} au, the population transfer reaches its maximum probability for an exactly resonant laser pulse, i.e. when the field frequency matches the transition frequency between the $|(0)^a\rangle$ and the intermediate excited $|(2^2)^a\rangle$ states. However, it appears clearly that for higher amplitudes, the frequency for which the process is the most efficient is slightly detuned from the transition frequency. This effect is due to the vibrational Stark shifts which begin to play a non-negligible role as the amplitude of the laser field is increased.

In order to find a satisfactory set of parameters, we first set the peak amplitude at $\varepsilon_0 = 10^{-2}$ au. This amplitude is high enough to lead to a relatively short duration of the tunneling, and low enough to avoid detrimental effects such as ionization and to guarantee a negligible influence of the electronic polarizability (not included in our model). With this constraint, the best parameters found within our model are $\varepsilon_0 = 10^{-2}$ au, $\omega = 1574 \, \mathrm{cm}^{-1}$ and $t_p = 5280 \, \mathrm{fs}$. Results of the dynamics of the system with these parameters are shown in Fig. 8.6. Again, the mechanism is found to be consistent with the one suggested by the three-state system invoked in Sect. 8.2.1. The left panel displays the population of bare states $|(0)^s\rangle$, $|(0)^a\rangle$ and $|(2^2)^a\rangle$ during the interaction with the laser pulse. States $|(0)^a\rangle$ and $|(2^2)^a\rangle$ are selectively coupled by the pulse and the system undergoes a full Rabi oscillation between them. As stated before, during this process the state $|(0)^a\rangle$ experiences a phase change of π and as seen on the right panel, a nearly full population transfer occurs between the two localized superpositions $|L\rangle$ and $|R\rangle$ defined in Eq. (8.1). Indeed the final population of the target superposition $|R\rangle$ is approximately 0.995. Thus, given the duration of the pulse used in this calculations, we predict a full tunneling inversion in a time which is almost twenty times faster than the field-free tunneling time.

MCTDH Dynamics Calculation

In order to confirm the results obtained in the previous section, we have solved the TDSE

$$i\hbar \frac{\partial \Psi(t)}{\partial t} = H(\boldsymbol{q}, t)\Psi(t) \tag{8.34}$$

where $H(\boldsymbol{q}, t)$ is the full Hamiltonian operator of Eq. (8.12), using the parameters of the field used for the calculations presented in Fig. 8.6. This calculation was performed using the Heidelberg MCTDH package. For the representation of the Hamiltonian and the wave function, a Hermite polynomial DVR scheme [47] was used for all the degrees of freedom. Details of the primitive basis used for each degree of freedom are given in Table 8.3. The combined modes and numbers of SPF basis functions used in this calculation are described in Table 8.4.
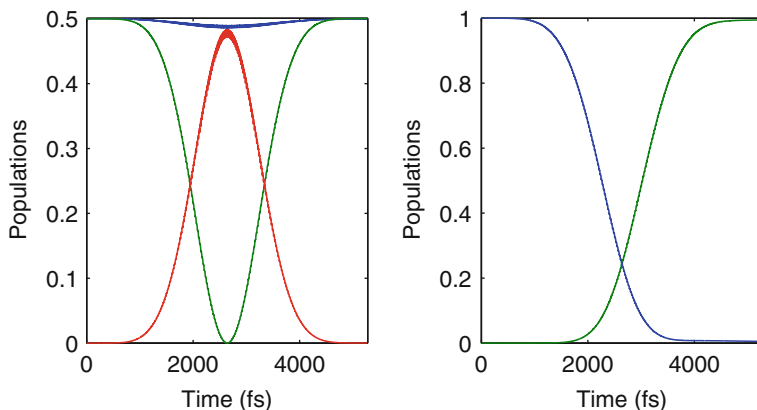
Fig. 8.6 Population of states $|(0)^s\rangle$ (*blue*), $|(0)^a\rangle$ (*green*) and $|(2^2)^a\rangle$ (*red*) during the interaction with the laser pulse (*left panel*). Population of the initial $|L\rangle$ (*blue*) and target $|R\rangle$ (*green*) superpositions (*right panel*). Figure adapted from Ref. [1]

Table 8.3 Primitive basis, numbers of grid points and grid range used for each degree of freedom

	r_1	r_2	r_3	$\cos(\theta_1)$	$\cos(\theta_2)$	φ_1
Grid range	1.3–2.6 a_0	1.3–2.6 a_0	1.3–2.8 a_0	−0.94–0.40	−0.94–0.40	−3.10–3.10 rad
Primitive basis	14	14	12	30	30	60

Table 8.4 Primitive basis, numbers of grid points and grid range used for each degree of freedom

Combined modes	(r_1, r_2)	$(\cos\theta_1, \cos\theta_2)$	(r_3, φ_1)
Number of SPF functions	25	30	30

The results obtained are shown in Fig. 8.7. The populations of the three eigenstates $|(0)^s\rangle$, $|(0)^a\rangle$ and $|(2^2)^a\rangle$ and of the two localized superpositions $|L\rangle$ and $|R\rangle$ defined in Eq. (8.1) show a good agreement with the results obtained with the effective Hamiltonian shown in Fig. 8.6. The slight differences between the two sets of results are most probably due to the approximate nature of the effective Hamiltonian described in the preceding section. The final population of the target superposition $|R\rangle$ is approximately 0.971. The full dimensional dynamics calculation confirms the global picture of the process that can be understood by considering the oversimplified three-state system described in Sect. 8.2.1. The main reason comes from the fact that the process under consideration takes place in the low-energy part of the spectrum were the density of states is rather low, allowing for a selective coupling between individual quantum states, even if the nature of the inversion motion, explained by the tunneling effect and resulting in a splitting of the vibrational states looks complicated at first sight.
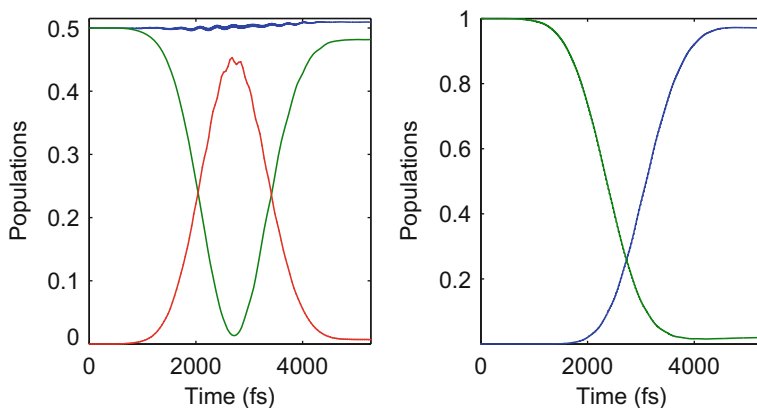
Fig. 8.7 Population of states $|(0)^s\rangle$ (*blue full line*), $|(0)^a\rangle$ (*green dashed line*) and $|(2^2)^a\rangle$ (*red dotted line*) during the interaction with the laser pulse (*left panel*) in a complete 6D MCTDH simulation. Population of the initial $|L\rangle$ (*blue full line*) and target $|R\rangle$ (*green dashed line*) superpositions (*right panel*). Figure adapted from Ref. [1]

8.2.4.2   Linearly Polarized Field and One-Dimension Alignment

Here we consider the less restrictive situation where the molecule is aligned along its most polarizable axis (one-dimensional alignment) corresponding to the direction of inversion. To analyze how the enhancement of tunneling survives with respect to this simpler one-dimensional alignment, we calculate the tunneling probability as a function of the precession angle ϕ, for the field given in Eqs. (8.15) and (8.16), using the effective Hamiltonian described in Sect. 8.2.3. The results of these calculations are shown in Fig. 8.8 (left panel) along with the projections of the unit vector along the Y axis of the laboratory frame L (which is the polarization direction of the electric field) on the unit vectors along the three directions x, y and z of the molecular M frame (right panel).

When ϕ equals zero, the system is in the situation explored in the previous section (the electric field polarization is along the y axis) and the tunneling probability is close to one. The second peak observed at $\phi \approx 0.6\pi$ corresponds to the situation where the electric field polarization direction is very close from the x direction of the M frame. As seen in Table 8.2, the $\langle(0)^a|\mu_x^{(M)}|(2^2)^a\rangle$ transition dipole moment has a smaller value than that of the $\langle(0)^a|\mu_y^{(M)}|(2^2)^a\rangle$ transition dipole moment, thus the parameters of the laser field used here do not induce a full tunneling inversion. Figure 8.8 also shows that for specific values of ϕ, namely $\phi \approx 0.4\pi$ and between $\phi \approx 1.05\pi$ and $\phi \approx 1.45\pi$ the tunneling probability drops to values close to zero. At $\phi \approx 0.4\pi$ the electric field interacts almost equally with the x and y components of the dipole moment. Since the $\langle(0)^a|\mu_x^{(M)}|(2^2)^a\rangle$ and $\langle(0)^a|\mu_y^{(M)}|(2^2)^a\rangle$ have close absolute values but different signs, they cancel out and the tunneling probability is close to zero. Between $\phi \approx 1.05\pi$ and $\phi \approx 1.45\pi$ the z component of the dipole moment dominates. The $\langle(0)^a|\mu_x^{(M)}|(2^2)^a\rangle$ and $\langle(0)^a|\mu_z^{(M)}|(2^2)^a\rangle$ transition dipole
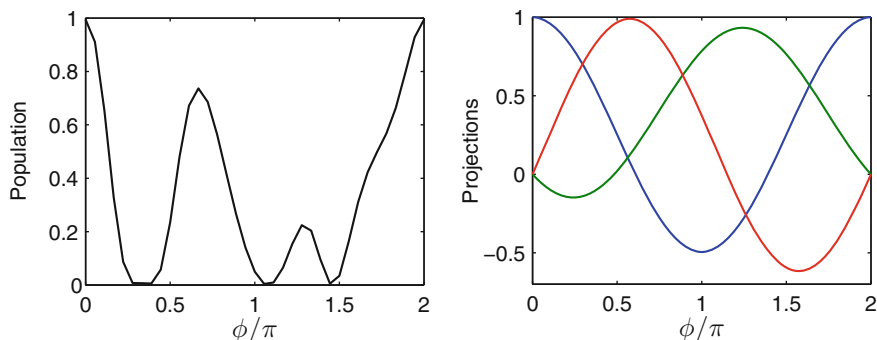
Fig. 8.8 Probability of tunneling as a function of ϕ for a molecule aligned along the Z axis of the L frame. The parameters of the laser pulse used in these calculations are $\varepsilon_0 = 10^{-2}$ au, $\omega = 1574$ cm^{-1} and $t_p = 5280$ fs, as in the previous sections (*left panel*). Projections $P_x = \vec{e}_Y \cdot \vec{e}_x$ (*blue*), $P_y = \vec{e}_Y \cdot \vec{e}_y$ (*green*) and $P_z = \vec{e}_Y \cdot \vec{e}_z$ (*red*) of the unit vector along the field polarization direction on the three directions x, y and z of the molecular frame M (*right panel*). Figure adapted from Ref. [1]

moments have almost identical values, thus one could expect to observe a full tunneling inversion for a field polarized along the z axis. However, as mentioned in Sect. 8.2.3, transition dipole moments between the symmetric and antisymmetric components of a same tunneling doublet are very large along the z direction. These large transition dipole moments induce strong vibrational Stark shifts that destroy the efficiency of the process.

The tunneling probability induced by the laser field when the molecule experiences an ideal one-dimensional alignment can be estimated by the value of the tunneling probability averaged over the angle ϕ. In the present case, we found a rather low tunneling probability of 0.35. We conclude that the enhancement of tunneling by a linearly polarized laser pulse can only be efficiently induced on a three-dimensionally aligned molecule.

8.2.4.3   Circularly Polarized Field and One-Dimension Alignment

We expect that a field circularly polarized in the plane orthogonal to the axis of 1D alignment should in principle much improve the enhancement of tunneling with respect to a linearly polarized field as the circular polarization matches with the delocalization of the two molecular axes that are not aligned. However such a field has no actual coupling with the molecule since the dipole moment is here parallel to the most polarizable axis (corresponding to the axis of 1D alignment). We thus alternatively test a circularly polarized field in the (XY) plane, see Eq. (8.16). Figure 8.9 shows the tunneling with the circularly polarized field (8.16) as a function of the angle ϕ. The enhancement of tunneling is achieved with a higher probability than with the linearly polarized pulse, with an average value with respect to ϕ of 0.68.

Fig. 8.9 Same as Fig. 8.6 but for the circularly polarized pulse (8.16) with $E_0 = 0.01$ au, $t_p = 5900$ fs and $\omega = 1574$ cm^{-1}. Figure adapted from Ref. [1]
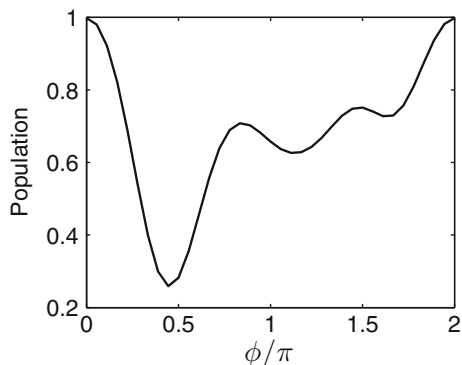
8.2.5   Conclusion

We have presented a computational study of the enhancement of tunneling induced by a resonant laser pulse using an accurate six-dimensional model of NHD$_2$. Our aim was to investigate the possibility of applying a control strategy established for a simple model system to a more complex system using accurate quantum dynamics simulations. The control strategy was first analyzed using a simple three-state model, providing an analytical formulation of the tunneling probability as a function of the parameters of the field. An effective Hamiltonian was then introduced and used to explore the influence of the parameters of the field on the efficiency of the process in a more accurate framework. These calculations allowed us to find suitable parameters of the field allowing to induce a nearly full tunneling inversion in a time much shorter than the natural tunneling time of the molecule. Finally, the parameters were used in a complete simulation of the laser induced dynamics of the molecule using an accurate Hamiltonian composed of an exact vibrational KEO, and a set of accurate potential end dipole moment surfaces.

As discussed in Chap. 6, strategies based on π-pulse techniques require a rather fine tuning of the laser parameters to achieve a high-degree of control. Further studies will be needed to overcome this major drawback and to be able to propose robust control strategies, e.g. based on adiabatic passage, in complex realistic systems such as polyatomic molecules.

Based on a static description of the relative orientation of the molecule and the polarization of the laser pulse, we found that the control strategy can only produce a high degree of control on a three-dimensionally aligned molecule, which from the experimental point of view, represents a rather strong restriction. Considering the less restrictive situation of a one-dimensionally aligned molecule, we have found that a circularly polarized laser pulse would induce a higher degree of tunneling inversion than a linearly polarized laser pulse. Further optimization of the field (such as an elliptically polarized one) that would produce a significant tunneling enhancement of the molecule experiencing a one-dimensional alignment should be investigated.

8.3 Coherent Destruction of Tunneling

The phenomenon of coherent destruction of tunneling (CDT) was first discovered by Grossmann et al. [16, 48–51]. They considered a particle moving in a one-dimensional quartic double-well potential driven by a monochromatic laser field and showed numerically that for specific values of the frequency and amplitude of the radiation, the particle is forced to stay in one of the two wells as long as the laser field is on. Since then, this intriguing phenomenon has been the object of further theoretical analysis [17, 18, 52–58], extended in various forms [20, 59–70], and demonstrated experimentally in different physical systems [71–74]. The role of CDT in processes such as the strong field ionization of diatomic molecules [75] or the proton transfer dynamics in tropolone [76] has also been discussed.

In this section, we explore theoretically the possible application of the CDT in our accurate six-dimensional model of NHD_2. As in the previous section, various effective models were used to analyse the sensitivity of the process to variations of the laser field parameters, and accurate quantum dynamics simulations using the MCTDH method were then performed in order to confirm the results obtained with the effective model.

Two different regimes were considered for the laser field frequency, as sketched in Fig. 8.10. A non-resonant regime, where the frequency of the laser field (featured by the blue arrow in Fig. 8.10) is much larger than the ground state tunneling splitting, but much smaller than the transition frequency between the $|(0)^a\rangle$ and $|(2^1)^s\rangle$ states, corresponding to an excitation of the inversion motion. This regime corresponds to the frequency regime considered in the original CDT papers [16, 48–51]. In this regime, the phenomenon of CDT is analogous to the phenomenon of dynamical localization in a high-frequency driven two-level system. In the second regime considered, referred to as quasi-resonant regime, the frequency of the laser field (featured by the red arrow in Fig. 8.10) is close to the transition frequency between the $|(0)^a\rangle$ and $|(2^1)^s\rangle$ states. In this case, the phenomenon of CDT is a consequence of the different Stark shifts induced by the laser field on the two tunneling components $|(0)^s\rangle$ and $|(0)^a\rangle$ of the ground vibrational state.

In each case, we first studied the laser driven dynamics of the system in the framework of the Floquet formalism, described in Sect. 6.5 of Chap. 6, which provides a geometrical interpretation of the laser driven dynamics and its dependence on the frequency and amplitude of the laser field, through the analysis of the eigenvalues of the Floquet operator, called quasienergies. Various effective models were used for that purpose. This analysis allowed us to explain the shape of the relevant quasienergy curves as a function of the laser parameters, and to obtain the parameters of the laser field that induce the CDT. We then used the MCTDH method to solve the TDSE for the molecule in interaction with the laser field and compare these results with those obtained from the effective Hamiltonian described in Sect. 8.2.3 above.

The models and methods used in this section are briefly outlined in Sect. 8.3.1. Section 8.3.2 presents our results and Sect. 8.3.3 concludes this chapter.
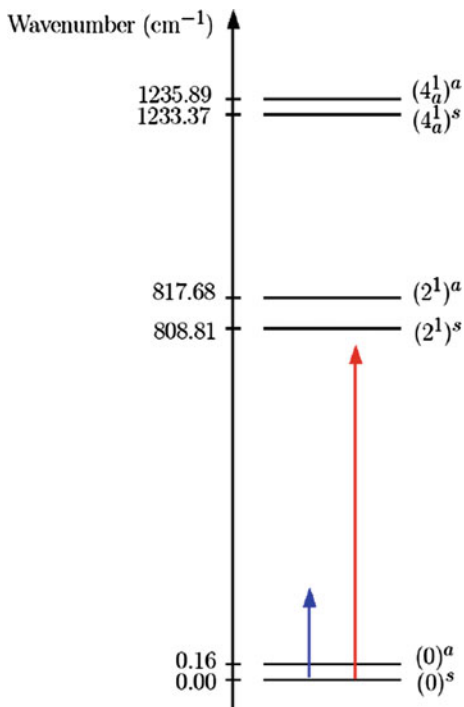
8.3.1 Model and Methods

We assumed an ideally aligned molecule [29–34] (three-dimensional alignment) in
interaction with a laser field linearly polarized along the z axis of the molecular frame.
The total angular momentum was fixed at $J = 0$. The interaction of the molecule with
a monochromatic laser field of amplitude ε_0 and frequency ω

$$\varepsilon(t) = \varepsilon_0 \cos(\omega t + \theta) \tag{8.35}$$

was studied in the framework of the Floquet formalism [77–82]. Again, we used the
142 lowest vibrational eigenstates of the molecule, computed in Ref. [23], and the
transition dipole moments between them, to construct an effective Floquet Hamil-
tonian [82]

$$K^{eff}(\theta) = -i\omega \frac{\partial}{\partial \theta} + H_0^{eff} - \mu_z^{eff} \varepsilon_0 \cos(\theta) \tag{8.36}$$

where H_0^{eff} is the diagonal matrix of the vibrational eigenenergies, μ_z^{eff} is the matrix of
the z-component of the dipole moment (see Sect. 8.2.3 above) and ε_0 is the amplitude
of the electric field of phase θ at $t = 0$, taken as a dynamical variable for the laser field.
The construction of quasienergy diagrams allows us to determine the parameters of

the laser field that lead to the CDT. The TDSE for the molecule in interaction with the laser field was then solved using both the effective Hamiltonian

$$H^{eff}(t) = H_0^{eff}(t)\mu_z^{eff}\varepsilon(t) \tag{8.37}$$

and the exact vibrational Hamiltonian

$$H(\boldsymbol{q}, t) = T(\boldsymbol{q}) + V(\boldsymbol{q}) + H_{int}(\boldsymbol{q}, t), \tag{8.38}$$

where $T(\boldsymbol{q})$ is the $J = 0$ KEO in Radau coordinates, $V(\boldsymbol{q})$ is the AMMPOT4 PES [38] and $H_{int}(t) = -\mu_z(\boldsymbol{q})\varepsilon(t)$, where $\mu_z(\boldsymbol{q})$ denotes the z-component of the dipole moment surfaces of Marquardt et al. [39] (see Sect. 8.2.2 above). The TDSE involving the effective Hamiltonian was solved using the split-operator scheme detailed in Sect. 8.2.3. The TDSE involving the exact vibrational Hamiltonian was solved using the MCTDH method. The comparison of the results obtained with the exact and effective Hamiltonians allowed us to check the accuracy of the later, as in the preceding section.

8.3.2 Results

8.3.2.1 The Non-resonant Regime

Quasienergy Diagram

Assuming the system in the $|L\rangle$ state at $t = 0$, the CDT is achieved if the system remains localized in the $|L\rangle$ state as long as the laser field is on. We consider the Floquet Hamiltonian K_2 in the basis $\{|(0)^s, k\rangle, |(0)^a, k\rangle\}$, where k is the quantum number describing the number of photons exchanged between the laser field and the molecule, describing the molecule in interaction with a periodic time-dependent laser field

$$K_2(\theta) = -i\omega\frac{\partial}{\partial\theta} + \begin{pmatrix} E_{(0)^s} & \Omega\cos\theta \\ \Omega\cos\theta & E_{(0)^a} \end{pmatrix} \tag{8.39}$$

where $\Omega = -\varepsilon_0\langle(0)^s|\mu_z|(0)^a\rangle$ and $E_{(0)^s}$ and $E_{(0)^a}$ are the energies of the $|(0)^s\rangle$ and $|(0)^a\rangle$ states, respectively. In the limit of high frequencies, i.e. when the frequency of the laser field is much higher than the tunneling splitting $\omega \gg E_{(0)^a} - E_{(0)^s}$, the quasienergies $\Xi_{(0)^a,k}$ and $\Xi_{(0)^s,k}$ as a function of the parameters of the field Ω and ω are given by simple analytic expressions, as shown below.

The operator $K_2(\theta)$ of Eq. (8.39) can be written as the sum of a zeroth-order Floquet Hamiltonian K_0 and a perturbation W. Here, the field-free Hamiltonian of the two-level system is considered as a perturbation of the field and the coupling

$$K_0(\theta) = -i\omega \frac{\partial}{\partial \theta} + \begin{pmatrix} 0 & \Omega \cos \theta \\ \Omega \cos \theta & 0 \end{pmatrix} \tag{8.40}$$

and

$$W = \begin{pmatrix} E_{(0)^s} & 0 \\ 0 & E_{(0)^a} \end{pmatrix}. \tag{8.41}$$

First we rewrite $K_2(\theta)$ in the basis where K_0 is diagonal by mean of a unitary transformation

$$S_1 = \frac{1}{\sqrt{2}} \begin{pmatrix} 1 & 1 \\ 1 & -1 \end{pmatrix}. \tag{8.42}$$

The transformed Floquet Hamiltonian $K_2' = S_1^\dagger K_2 S_1$ then reads

$$K_2'(\theta) = -i\omega \frac{\partial}{\partial \theta} + \begin{pmatrix} \Omega \cos \theta & 0 \\ 0 & -\Omega \cos \theta \end{pmatrix} + \frac{1}{2} \begin{pmatrix} \Sigma & \Delta \\ \Delta & \Sigma \end{pmatrix}, \tag{8.43}$$

where $\Sigma = E_{(0)^s} + E_{(0)^a}$ and $\Delta = E_{(0)^s} - E_{(0)^a}$. One can note here that this is equivalent to rewriting the Hamiltonian in the basis $\{|R, k\rangle, |L, k\rangle\}$ of the (dressed) localized states. We now apply a second unitary transformation

$$S_2 = \begin{pmatrix} e^{-i\frac{\Omega}{\omega} \sin \theta} & 0 \\ 0 & e^{i\frac{\Omega}{\omega} \sin \theta} \end{pmatrix}, \tag{8.44}$$

which diagonalises the operator given by the two first terms of Eq. (8.43)

$$\begin{aligned} K_2'' &= S_2^\dagger K_2' S_2 \\ &= -i\omega \frac{\partial}{\partial \theta} + \frac{1}{2} \begin{pmatrix} \Sigma & \Delta e^{2i\frac{\Omega}{\omega} \sin \theta} \\ \Delta e^{-2i\frac{\Omega}{\omega} \sin \theta} & \Sigma \end{pmatrix}. \end{aligned} \tag{8.45}$$

The exponential terms appearing in the last equation can be expanded as a sum of Bessel functions

$$e^{2i\frac{\Omega}{\omega} \sin \theta} = J_0 \left(\frac{2\Omega}{\omega} \right) + 2 \sum_{n=1}^{\infty} J_n \left(\frac{2\Omega}{\omega} \right) \zeta_n(\theta) \tag{8.46}$$

where

$$\zeta_n(\theta) = \begin{cases} \cos(n\theta), & n \text{ even} \\ i \sin(n\theta), & n \text{ odd} \end{cases} \tag{8.47}$$

In the high frequency regime, $\omega \gg E_{(0)^a} - E_{(0)^s}$, this expansion can be averaged over θ which leaves only the first term

$$e^{2i\frac{\Omega}{\omega}\sin\theta} \approx J_0\left(\frac{2\Omega}{\omega}\right), \tag{8.48}$$

where J_0 is the zero-order Bessel function. It follows

$$K_2''(\theta) = -i\omega\frac{\partial}{\partial\theta} + \frac{1}{2}\begin{pmatrix} \Sigma & \Delta J_0\left(\frac{2\Omega}{\omega}\right) \\ \Delta J_0\left(\frac{2\Omega}{\omega}\right) & \Sigma \end{pmatrix}. \tag{8.49}$$

Now coming back to the initial basis $\{|(0)^s, k\rangle, |(0)^a, k\rangle\}$

$$\begin{aligned} K_2'''(\theta) &= S_1 K_2'' S_1^\dagger \\ &= -i\omega\frac{\partial}{\partial\theta} + \frac{1}{2}\begin{pmatrix} \Sigma + \Delta J_0\left(\frac{2\Omega}{\omega}\right) & 0 \\ 0 & \Sigma - \Delta J_0\left(\frac{2\Omega}{\omega}\right) \end{pmatrix}. \end{aligned} \tag{8.50}$$

From this last equation it is clear that the quasienergies read

$$\Xi_{(0)^s,k} = \frac{1}{2}\Sigma + \frac{1}{2}\Delta J_0\left(\frac{2\Omega}{\omega}\right) + k\omega \tag{8.51}$$

$$\Xi_{(0)^a,k} = \frac{1}{2}\Sigma - \frac{1}{2}\Delta J_0\left(\frac{2\Omega}{\omega}\right) + k\omega \tag{8.52}$$

and their difference

$$\Xi_{(0)^a,k} - \Xi_{(0)^s,k} = \Delta J_0\left(\frac{2\Omega}{\omega}\right). \tag{8.53}$$

In Sect. 8.2.1, the natural tunneling time of the system was defined as a function of the field-free tunneling splitting, see Eq. (8.3). In analogy, the quasienergy difference $\Xi_{(0)^a,k} - \Xi_{(0)^s,k}$ of Eq. (8.53) defines a field-dependent tunneling splitting, and thus provides a field-dependent tunneling time. As a result, when the quasienergy difference tends towards zero, the tunneling time become infinite and the CDT is achieved. This condition $J_0\left(\frac{2\Omega}{\omega}\right) = 0$ defines a straight line in the field parameter space [17]. The connection of the quasienergies $\Xi_{(0)^s,k}$ and $\Xi_{(0)^a,k}$ to the respective field-free energies $E_{(0)^s}$ and $E_{(0)^a}$, is achieved in a continuous way by an adiabatic switching of the field until the value satisfying $J_0\left(\frac{2\Omega}{\omega}\right) = 0$.

This model gives a simple, analytic description of the phenomenon of CDT. However, it does not account for the possible effect of the higher vibrational states on the laser driven dynamics. In the present case, the frequency of the laser field is far from any resonance. Therefore, one does not expect it to induce population transfers among the vibrational states. Nevertheless, the presence of higher vibrational states can influence the dynamics through vibrational Stark shifts. These Stark shifts can

approximately be accounted for by applying second-order stationary perturbation theory.

We start by rewriting the effective Floquet operator K^{eff} of Eq. (8.36) as the sum of a zeroth order Floquet Hamiltonian K_0^{eff} and a perturbation operator W

$$K^{eff}(\theta) = K_0^{eff}(\theta) + W(\theta) \tag{8.54}$$

with

$$K_0^{eff}(\theta) = -i\omega\frac{\partial}{\partial\theta} + H_0^{eff} \tag{8.55}$$

and

$$W(\theta) = -\mu_{z_{BF}}^{eff}\varepsilon_0\cos(\theta). \tag{8.56}$$

The eigenstates and eigenenergies of the $K_0^{eff}(\theta)$ operator are simply

$$K_0^{eff}|\phi_{n,k}\rangle = \Xi_{n,k}^{(0)}|\phi_{n,k}\rangle, \quad \Xi_{n,k}^{(0)} = E_n + k\omega, \tag{8.57}$$

where $|\phi_{n,k}\rangle = |\chi_n\rangle \otimes |\xi_k\rangle$ (see Sect. 6.4 of Chap. 6), $|\chi_n\rangle$ and E_n are the eigenelements of the molecular effective Hamiltonian H_0^{eff}

$$H_0^{eff}|\chi_n\rangle = E_n|\chi_n\rangle, \tag{8.58}$$

and $|\xi_k\rangle$ are the eigenvectors of the operator $-i\omega\frac{\partial}{\partial\theta}$

$$-i\omega\frac{\partial}{\partial\theta}|\xi_k\rangle = k\omega|\xi_k\rangle. \tag{8.59}$$

The first-order correction to the energy is zero

$$\begin{aligned}
\Xi_{n,k}^{(1)} &= \langle\phi_{n,k}|W(\theta)|\phi_{n,k}\rangle \\
&= -\varepsilon_0\langle\chi_n|\mu_z|\chi_n\rangle\langle\xi_k|\cos(\theta)|\xi_k\rangle \\
&= 0.
\end{aligned} \tag{8.60}$$

The second-order correction to the energy reads

$$\begin{aligned}
\Xi_{n,k}^{(2)} &= \sum_p\sum_l\frac{\left|\langle\phi_{p,l}|W(\theta)|\phi_{n,k}\rangle\right|^2}{\Xi_{n,k}^{(0)} - \Xi_{p,l}^{(0)}} \\
&= \sum_p\varepsilon_0^2|\mu_{pn}|^2\left(\frac{|\langle\xi_{k-1}|\cos(\theta)|\xi_k\rangle|^2}{E_n - E_p + \omega} + \frac{|\langle\xi_{k+1}|\cos(\theta)|\xi_k\rangle|^2}{E_n - E_p - \omega}\right) \\
&= -\frac{1}{4}\varepsilon_0^2\sum_p|\mu_{pn}|^2\left(\frac{1}{E_p - E_n + \omega} + \frac{1}{E_p - E_n - \omega}\right),
\end{aligned} \tag{8.61}$$

where $\mu_{pn} = \langle \chi_p | \mu_z | \chi_n \rangle$. One can now define an effective Floquet Hamiltonian in the basis $\{ |(0)^s, k \rangle, |(0)^a, k \rangle \}$ including the effect of the higher dressed vibrational states through second-order perturbation theory

$$K_2^{PT}(\theta) = -i\omega \frac{\partial}{\partial \theta} + \begin{pmatrix} E'_{(0)^s} & \Omega \cos \theta \\ \Omega \cos \theta & E'_{(0)^a} \end{pmatrix} \tag{8.62}$$

with

$$E'_{(0)^s} = E_{(0)^s} - \frac{1}{4}\varepsilon_0^2 \sum_p |\mu_{p(0)^s}|^2 \left(\frac{1}{E_p - E_{(0)^s} + \omega} + \frac{1}{E_p - E_{(0)^s} - \omega} \right) \tag{8.63}$$

$$E'_{(0)^a} = E_{(0)^a} - \frac{1}{4}\varepsilon_0^2 \sum_p |\mu_{p(0)^a}|^2 \left(\frac{1}{E_p - E_{(0)^a} + \omega} + \frac{1}{E_p - E_{(0)^a} - \omega} \right) \tag{8.64}$$

and where p runs over all the vibrational states except the $|(0)^s\rangle$ and $|(0)^a\rangle$ states. Applying the high-frequency approximation, one obtains for the quasienergies

$$\Xi_{(0)^s, k} = \frac{1}{2}\Sigma' + \frac{1}{2}\Delta' J_0 \left(\frac{2\Omega}{\omega} \right) + k\omega \tag{8.65}$$

$$\Xi_{(0)^a, k} = \frac{1}{2}\Sigma' - \frac{1}{2}\Delta' J_0 \left(\frac{2\Omega}{\omega} \right) + k\omega \tag{8.66}$$

and their difference

$$\Xi_{(0)^a, k} - \Xi_{(0)^s, k} = \Delta' J_0 \left(\frac{2\Omega}{\omega} \right). \tag{8.67}$$

with $\Sigma' = E'_{(0)^s} + E'_{(0)^a}$ and $\Delta' = E'_{(0)^s} - E'_{(0)^a}$.

The quasienergies $\Xi_{(0)^s, 0}$ and $\Xi_{(0)^a, 0}$ associated with the dressed states continuously connected with the $|(0)^s\rangle$ and $|(0)^a\rangle$ states, as a function of the amplitude of the electric field for three different frequencies of $\omega = 50$, 80 and $100 \, \text{cm}^{-1}$ are presented in Fig. 8.11. The results obtained from the two-level model using Eqs. (8.51) and (8.52) are shown in red dotted lines, the results obtained from the perturbative model using Eqs. (8.65) and (8.66) are shown in blue dashed lines and the results obtained numerically from the effective Floquet Hamiltonian of Eq. (8.36) are shown in black full lines. Figure 8.11 panels (a), (b) and (c) shows that the shape of the quasienergy curves is explained by two different factors. The quasienergy curves obtained from the two-level model show multiple crossings at field amplitudes determined by the zeros of the Bessel function $J_0 \left(\frac{2\Omega}{\omega} \right)$. The quasienergy curves obtained numerically using the effective Floquet Hamiltonian of Eq. (8.36) show a similar behavior, superimposed with an amplitude-dependent red-shift induced by the vibrational Stark effect. A comparison with the quasienergy curves obtained from the perturbative model using Eqs. (8.51) and (8.52) shows that these Stark shifts are well accounted
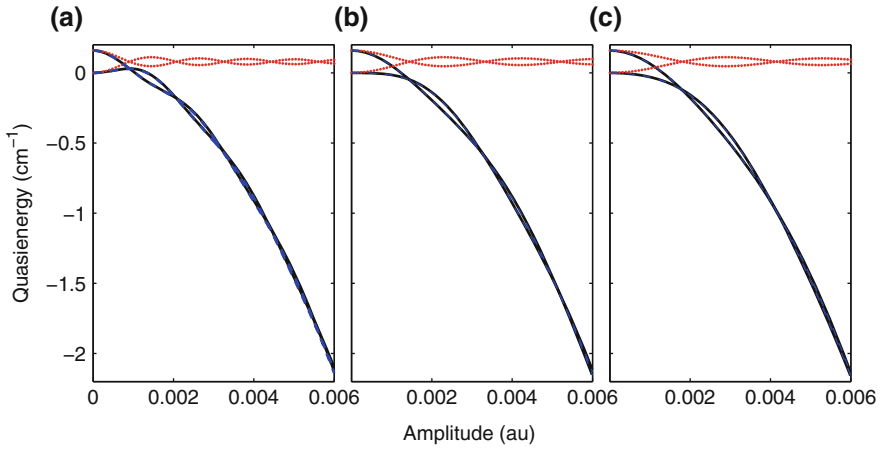
Fig. 8.11 Quasienergies $\varepsilon_{(0)^s,0}$ and $\varepsilon_{(0)^a,0}$ plotted as a function of the laser field amplitude for three different frequencies **a** $\omega = 50\,\text{cm}^{-1}$, **b** $80\,\text{cm}^{-1}$ and **c** $100\,\text{cm}^{-1}$. The results obtained from the two-level model using Eqs. (8.51) and (8.52) are shown in *red dotted lines*, the results obtained from the perturbative model using Eqs. (8.65) and (8.66) are shown in *blue dashed lines* and the results obtained numerically using the effective Floquet Hamiltonian of Eq. (8.36) are shown in *black full lines*. The *blue dashed lines* and *black full lines* are almost superimposed. Figure adapted from Ref. [2]

Fig. 8.12 Amplitudes and frequencies of the field which lead to CDT. The *full lines* represent the parameters obtained from the two-level model of Eq. (8.53) and the crosses represent the parameters obtained with the effective Floquet Hamiltonian of Eq. (8.36). The parameters given by the first, second, third and fourth crossing for each frequency are plotted in *blue*, *red*, *green* and *magenta*, respectively. Figure adapted from Ref. [2]
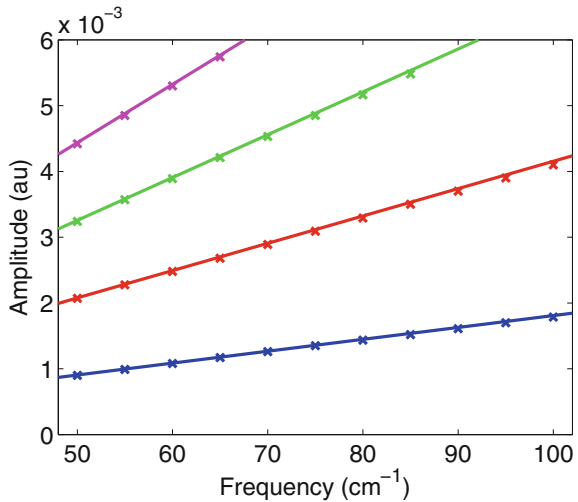
for by second-order perturbation theory. The parameters required to achieve the CDT obtained from the two-level model and the effective Floquet Hamiltonian are displayed in Fig. 8.12. One can see that the effective Floquet Hamiltonian reproduces the linear relationship between the frequencies and amplitudes of the laser field required to achieve the CDT predicted by the simple two-level model.

Time-Dependent Simulations

In order to demonstrate numerically the relation between the CDT and the crossing of the quasienergy curves shown in Fig. 8.11, we have solved the TDSE

$$H^{eff}(t)\Psi(t) = i\hbar\frac{d\Psi(t)}{dt} \tag{8.68}$$

starting from one of the $|L\rangle$ localized superposition. For the electric field, we considered a monochromatic radiation smoothly turned on of expression

$$\varepsilon(t) = \begin{cases} \varepsilon_0 \sin^2\left(\frac{\pi t}{2t_{ramp}}\right)\cos(\omega t) & \text{for } t \leq t_{ramp} \\ \varepsilon_0 \cos(\omega t) & \text{for } t > t_{ramp} \end{cases}, \tag{8.69}$$

where ε_0 and is the amplitude, ω the frequency and t_{ramp} the duration of the ramp of the electric field. A ramp of four optical cycles is considered, i.e. $t_{ramp} = 8\pi/\omega$. Calculations with $\omega = 50, 80$ and $100\,cm^{-1}$ were performed. For each of these values, the amplitudes $\varepsilon_0 = 9.00 \times 10^{-4}$, 1.43×10^{-3} and 1.78×10^{-3} au, given by the first crossing of the two quasienergy curves $\Xi_{(0)^s,0}$ and $\Xi_{(0)^a,0}$, were used. The dynamics of the system in interaction with the laser field was calculated for 105 ps, which is the approximate field-free tunneling time for NHD_2. Figure 8.13 shows the population of the $|L\rangle$ localized state as a function of time. These results show that, in the three cases, the CDT is achieve with a high efficiency, as the system is seen to remains
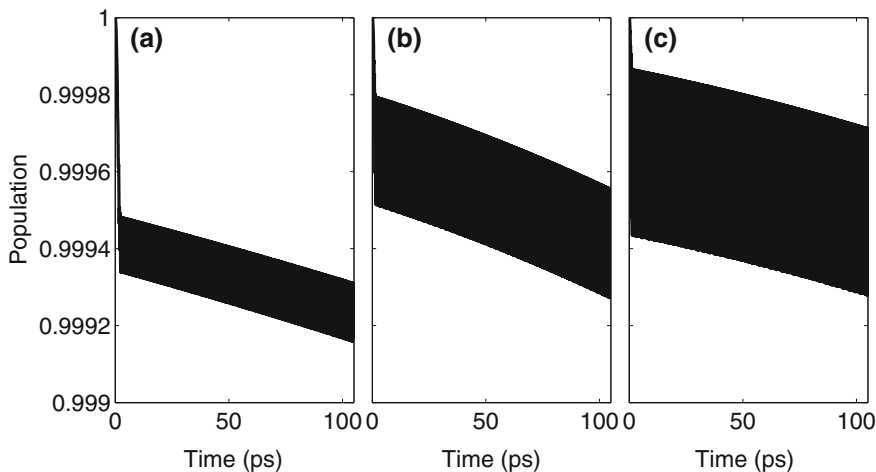

Fig. 8.13 $|L\rangle$ localized state populations obtained from the solution of the TDSE of Eq. (8.68) for the laser field frequencies and amplitudes $\omega = 50\,cm^{-1}$ and $\varepsilon_0 = 9.00 \times 10^{-4}$ au (**a**), $\omega = 80\,cm^{-1}$ and $\varepsilon_0 = 1.43 \times 10^{-3}$ au (**b**) and $\omega = 100\,cm^{-1}$ and $\varepsilon_0 = 1.78 \times 10^{-3}$ au (**c**). Figure adapted from Ref. [2]

Table 8.5 Single particle
function bases used in the
calculations

Combined modes	(r_1, r_2)	(u_1, u_2)	(r_3, φ_1)
SPF basis 1	6	10	10
SPF basis 2	10	15	15
SPF basis 3	15	20	20
SPF basis 4	25	30	30

localized in the initial well with a probability of more than 99.9 %. In addition, the
populations show fast oscillations that are not resolved in Fig. 8.13, originating from
small amplitude Rabi oscillations between the $|(0)^s\rangle$ and $|(0)^a\rangle$ states induced by the
laser field.

As in Sect. 8.2, the accuracy of the effective model was checked by solving the
TDSE with the exact 6D vibrational Hamiltonian using the MCTDH method. The
combined modes and sizes single-particle function (SPF) bases used in the calcula-
tions are presented in Table 8.5.

To study the convergence of the calculations with respect to the size of the SPF
basis, calculations with SPF bases of increasing sizes, were performed. Because
of their relatively high computational cost, these calculations were performed over
10 ps only. The frequency and amplitude of the laser field were set to $\omega = 50\,\mathrm{cm}^{-1}$
and $\varepsilon_0 = 9.0 \times 10^{-4}$ au, respectively. The populations of the initial localized state
$|L\rangle$ obtained from the MCTDH calculations, compared with that obtained with the
effective Hamiltonian, are presented in Fig. 8.14. The $|L\rangle$ state population obtained
from the calculation with the small SPF basis 1 (magenta curve) is almost identical
to that obtained from the effective Hamiltonian. However, when the size of the SPF
basis is increased, one observes a deviation of the MCTDH result compared to the
effective model. Specifically, the $|L\rangle$ state population obtained from the SPF basis 2
(green curve) follows closely the population obtained with the effective model up to
approximately $t = 2.5\,\mathrm{ps}$, and then suddenly drops down. Surprisingly, when the
size of the SPF basis is further increased, the MCTDH results still deviate from the
effective model, but to a lesser extent. The difference between the $|L\rangle$ state population
computed with the SPF basis 4 and that computed with the effective Hamiltonian is
only of roughly 0.1 % at $t = 10\,\mathrm{ps}$. These calculations reveal the approximate nature
of the effective Hamiltonian, despite the relatively high number of vibrational states
included. Nevertheless, it allows to obtain the parameters of the field required to
achieve an efficient CDT, at least for relatively short times.

8.3.2.2   The Quasi-resonant Regime

Quasienergy Diagram

In the quasi-resonant regime, the frequency of the laser field is close to the transi-
tion frequency between the $|(0)^a\rangle$ and $|(2^1)^s\rangle$ states, as featured by the
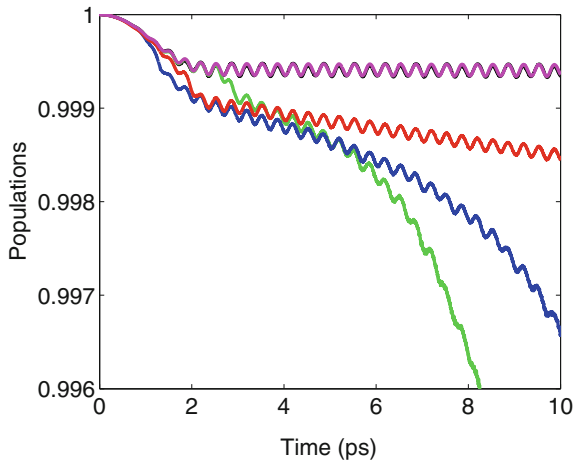
Fig. 8.14 $|L\rangle$ localized state populations obtained from the solution of the TDSE using the exact vibrational Hamiltonian, the laser field frequency and amplitude $\omega = 50\,\text{cm}^{-1}$ and $\varepsilon_0 = 9.00 \times 10^{-4}$ au and the SPF basis 1 (*magenta*), SPF basis 2 (*green*), SPF basis 3 (*blue*) and SPF basis 4 (*red*). The population computed with the effective Hamiltonian of Eq. (8.25) is shown in *black* for comparison. Figure adapted from Ref. [2]

red arrow in Fig. 8.10. A minimal model Hamiltonian in the dressed state basis $\{|(0)^s, 0\rangle, |(0)^a, 0\rangle, |(2^1)^s, -1\rangle, |(2^1)^a, -1\rangle\}$, can be written in the framework of the resonant wave approximation (RWA)

$$H^{RWA} = \begin{pmatrix} E_{(0)^s} & 0 & 0 & \Omega_{(0)^s,(2^1)^a} \\ 0 & E_{(0)^a} & \Omega_{(0)^a,(2^1)^s} & 0 \\ 0 & \Omega_{(0)^a,(2^1)^s} & E_{(2^1)^s} - \omega & 0 \\ \Omega_{(0)^s,(2^1)^a} & 0 & 0 & E_{(2^1)^a} - \omega \end{pmatrix}, \tag{8.70}$$

where, in this case, the Rabi frequencies read, e.g.

$$\Omega_{(0)^s,(2^1)^a} = -\frac{1}{2}\varepsilon_0 \langle (0)^s | \mu_z | (2^1)^a \rangle, \tag{8.71}$$

and identical expressions for $\Omega_{(0)^a,(2^1)^s}$, $\Omega_{(0)^a,(2^1)^s}$ and $\Omega_{(0)^s,(2^1)^a}$. Here, because the frequency of the laser field is much higher than in the previous section, the transition dipole moment between the $|(0)^s\rangle$ and $|(0)^a\rangle$ states can be simply neglected. Diagonalizing this Hamiltonian, one obtains

$$\Xi_{(0)^s,0} = \frac{1}{2}(E_{(0)^a} + E_{(2^1)^s} - \omega) - \frac{1}{2}\sqrt{(E_{(2^1)^s} - \omega - E_{(0)^a})^2 + 4\Omega^2_{(0)^a,(2^1)^s}} \tag{8.72}$$

$$\Xi_{(0)^a,0} = \frac{1}{2}(E_{(0)^s} + E_{(2^1)^a} - \omega) - \frac{1}{2}\sqrt{(E_{(2^1)^a} - \omega - E_{(0)^s})^2 + 4\Omega^2_{(0)^s,(2^1)^a}} \tag{8.73}$$
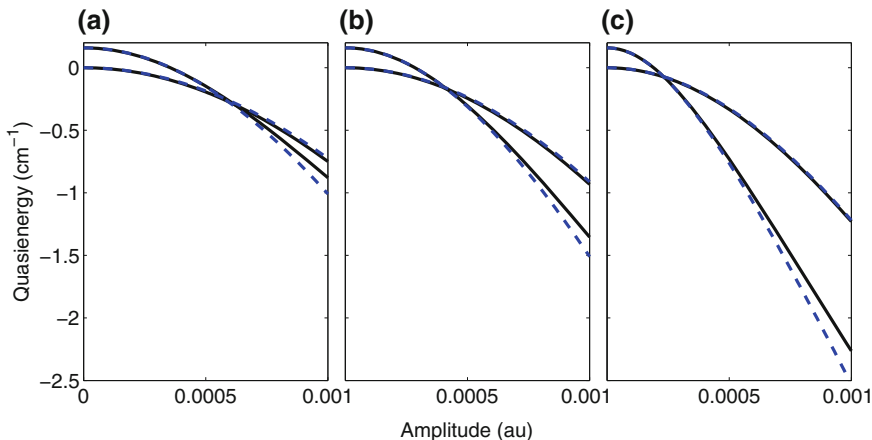
Fig. 8.15 Quasienergies $\Xi_{(0)^s,0}$ and $\Xi_{(0)^a,0}$ plotted as a function of the laser field amplitude for three different frequencies **a** $\omega = 795\,\mathrm{cm}^{-1}$, **b** $800\,\mathrm{cm}^{-1}$ and **c** $805\,\mathrm{cm}^{-1}$. The results obtained from the minimal model using Eqs. (8.72) and (8.73) are shown in *blue dashed lines* and the results obtained from the effective Floquet Hamiltonian of Eq. (8.36) are shown in *black full lines*. Figure adapted from Ref. [2]

The quasienergies $\Xi_{(0)^s,0}$ and $\Xi_{(0)^a,0}$ associated with the dressed states continuously connected with the $|(0)^s\rangle$ and $|(0)^a\rangle$ states as a function of the amplitude of the electric field for three different field frequencies of 795, 800 and 805 cm^{-1} are presented in Fig. 8.15. These frequencies are close to the resonance between the $|(0)^a\rangle$ and the $|(2^1)^s\rangle$ states at 808.65 cm^{-1}. The results obtained from the minimal model using Eqs. (8.72) and (8.73) are shown in blue dashed lines and the results obtained from the effective Floquet Hamiltonian of Eq. (8.36) are shown in black full lines.

The mechanism at the origin of the CDT in the quasi-resonant regime is different than in the case of the non-resonant regime described in Sect. 8.3.2.1 above. In the non-resonant regime, the CDT can be well understood in a two-level system because the frequency of the field is low with respect to the transition frequency to vibrationally excited states. The CDT originates from the fact that the frequency, on the other hand, is high with respect to the ground state tunneling splitting. As seen in Fig. 8.11, $\Xi_{(0)^s,0}$ and $\Xi_{(0)^a,0}$ the quasienergy curves show multiple crossings at amplitude determined by the zeros of the Bessel functions. Although the vibrational Stark shifts were found to have a non-negligible effect on the shape of the quasienergy curves, these effects were found to be very similar for the two $\Xi_{(0)^s,0}$ and $\Xi_{(0)^a,0}$ quasienergy curves. As a result, the vibrational Stark effect was found to have a negligible impact on the amplitude required to achieve the CDT for a given frequency. In addition, it is seen in Fig. 8.11 that the amplitude of the first crossing increases as the frequency of the field increases. In the quasi-resonant regime, the frequency of the field is chosen to be much higher than in the non-resonant regime, therefore the amplitude of the first crossing obtained in a simple two-level model would be extremely high. In addition, such a two-level model would obviously not be

a suitable model as the frequency of the field is chosen to be close to the transition frequency between the two ground state tunneling components and the two first excited state tunneling components. This choice has two important consequences. First, the vibrational Stark shifts experienced by the $|(0)^s\rangle$ and $|(0)^a\rangle$ are dominated by the contributions originating from the $|(2^1)^a\rangle$ and $|(2^1)^s\rangle$ states, respectively. This justify the use of the effective four-level model described above. In addition, the frequency of the laser field is closer to the transition frequency between the $|(0)^a\rangle$ and $|(2^1)^s\rangle$ states ($808.65\,\text{cm}^{-1}$) than that between the $|(0)^s\rangle$ and $|(2^1)^a\rangle$ states ($817.68\,\text{cm}^{-1}$). Therefore the Stark shift induced by the laser field on the $|(0)^a\rangle$ state is larger than the one induced on the $|(0)^s\rangle$. As a result, in the quasi-resonant regime, the quasi-energies $\Xi_{(0)^s,0}$ and $\Xi_{(0)^a,0}$ associated with the dressed states continuously connected with the $|(0)^s\rangle$ and $|(0)^a\rangle$ states only show a single crossing. The amplitude of the laser field required to induce the quasienergy crossing gets smaller as the frequency of the field approaches that of the resonance between the $|(0)^a\rangle$ and $|(2^1)^s\rangle$ states. The quasienergies given by the analytical expressions of Eqs. (8.72) and (8.73) follow closely the quasienergies obtained from the effective Floquet Hamiltonian of Eq. (8.36) at low field amplitudes. However, as the field amplitude is increased, the minimal model becomes less accurate. This indicates that, at higher amplitudes, the Stark shifts induced by the higher vibrational states become non negligible.

The parameters of the laser field required to achieve the CDT, obtained from the minimal RWA Hamiltonian and with the effective Floquet Hamiltonian are displayed in Fig. 8.16. One can see that the results obtained with the minimal four-level RWA Hamiltonian and with the effective Floquet Hamiltonian are in good agreement for laser field frequencies close to the resonance between the $|(0)^a\rangle$ and $|(2^1)^s\rangle$ states, whereas at lower frequencies, the minimal RWA Hamiltonian yields less accurate

Fig. 8.16 Amplitudes and frequencies of the field which lead to CDT. The *blue circles* represent the parameters obtained from the minimal model using Eqs. (8.72) and (8.73) and the crosses represent the parameters obtained with the effective Floquet Hamiltonian of Eq. (8.36). Figure adapted from Ref. [2]
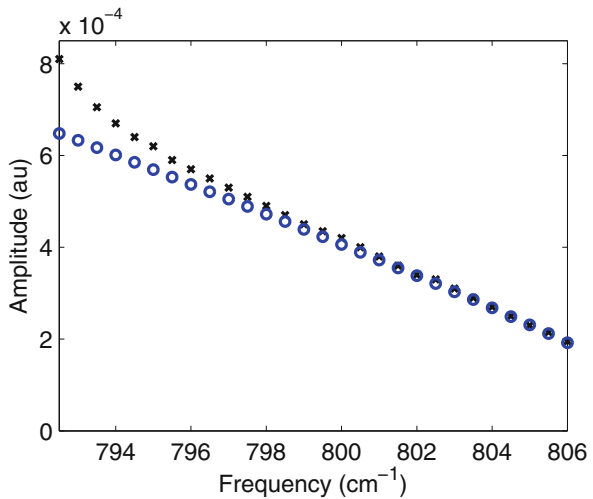
results. This discrepancy occurs because, at lower frequencies, the Stark shifts are less strongly dominated by the contributions originating from the $|(2^1)^s\rangle$ and $|(2^1)^a\rangle$ states.

Time-Dependent Simulations

Again, the TDSE of Eq. (8.68) associated with the effective Hamiltonian $H^{eff}(t)$ was solved using the field amplitudes required to achieve the CDT determined by the Floquet analysis of the previous section. Three frequencies $\omega = 795, 800$ and $805\,\mathrm{cm}^{-1}$ were considered with the corresponding amplitudes $\varepsilon_0 = 6.2 \times 10^{-4}, 4.17 \times 10^{-4}$ and 2.3×10^{-4} au, respectively. The electric field is given by Eq. (8.69) with a ramp of 50 optical cycles. The population of the $|L\rangle$ localized state for the three set of field parameters are presented in Fig. 8.17. As in the non-resonant regime, the $|L\rangle$ state populations show oscillations. The amplitude of these oscillations increases as the frequency of the laser field approaches the resonance between the $|(0)^a\rangle$ and $|(2^1)^s\rangle$ states. In the present case, these are Rabi oscillations between the $|(0)^a\rangle$ and $|(2^1)^s\rangle$ states induced by the laser field. In addition, a comparison between Figs. 8.15 and 8.11 shows that, in the quasi-resonant regime, the amplitude of the laser field required to achieve the CDT is smaller than in the non-resonant regime, which would be of interest for a practical implementation.

The accuracy of the 142 state effective Hamiltonian was then checked by solving the TDSE involving the exact vibrational Hamiltonian $H(t)$ using the MCTDH method. The frequency and amplitude of the laser field were set to $\omega = 800\,\mathrm{cm}^{-1}$ and
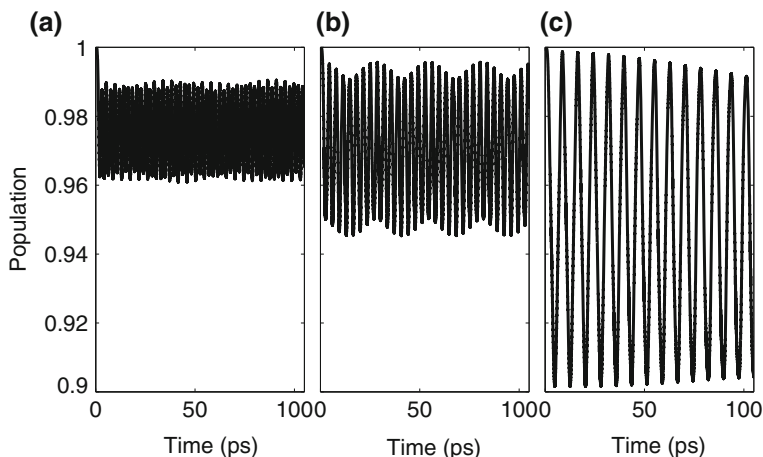

Fig. 8.17 $|L\rangle$ localized state populations obtained from the solution of the TDSE of Eq. (8.68) for the laser field frequencies and amplitudes $\omega = 795\,\mathrm{cm}^{-1}$ and $\varepsilon_0 = 6.2 \times 10^{-4}$ au (**a**), $\omega = 800\,\mathrm{cm}^{-1}$ and $\varepsilon_0 = 4.17 \times 10^{-4}$ au (**b**) and $\omega = 805\,\mathrm{cm}^{-1}$ and $\varepsilon_0 = 2.3 \times 10^{-4}$ au (**c**). Figure adapted from Ref. [2]
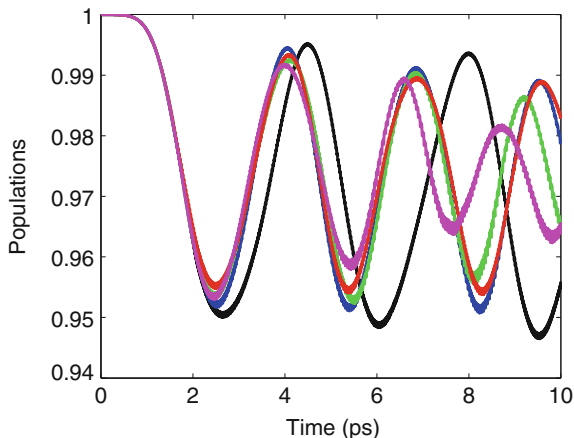
Fig. 8.18 $|L\rangle$ localized state populations obtained from the solution of the TDSE using the exact vibrational Hamiltonian, the laser field frequency and amplitude $\omega = 800\,\mathrm{cm}^{-1}$ and $\varepsilon_0 = 4.17 \times 10^{-4}$ and the SPF basis 1 (*magenta*), SPF basis 2 (*green*), SPF basis 3 (*blue*) and SPF basis 4 (*red*). The population computed with the effective Hamiltonian of Eq. (8.25) is shown in *black* for comparison. Figure adapted from Ref. [2]

$\varepsilon_0 = 4.17 \times 10^{-4}$ au respectively. Calculations using the four SPF bases presented in Table 8.5 were performed. The populations of the $|L\rangle$ localized state obtained from these calculations, and compared with the population obtained using the effective Hamiltonian are presented in Fig. 8.18. In agreement with the result obtained using the effective Hamiltonian, the populations of the $|L\rangle$ state obtained from the MCTDH calculations using the four different SPF bases stay above 0.95 during the first 10 ps. This indicates that the laser field parameters that lead to the CDT are accurately predicted by the effective Hamiltonian. The calculations with the SPF bases 1, 2 and 3 yield rather different populations, especially for $t > 6$ ps. In contrast, the populations computed with the SPF bases 3 and 4 are very similar over the 10 ps of the simulation, indicating that the SPF basis 3 is sufficient to obtain converged results. The period of the Rabi oscillations between the $|(0)^a\rangle$ and $|(2^1)^s\rangle$ states obtained from the MCTDH calculations are shorter than the ones obtained with the effective Hamiltonian. This indicates that the details of these Rabi oscillations are highly dependent on the details of the model. Indeed, Fig. 8.18 shows that the $|L\rangle$ localized state populations obtained from the full MCTDH calculations only match that obtained from the 142 state effective Hamiltonian during the first Rabi oscillation.

8.3.3   Summary

The phenomenon of coherent destruction of tunneling was investigated in a six dimensional, rotationless model of NHD_2. Two different regimes were considered for the

frequency of the laser field. A non-resonant regime, where the frequency of the laser field is much larger than the ground state tunneling splitting, but much smaller than excitation frequency of the inversion mode. This regime corresponds to the frequency regime considered in the original CDT papers [16, 48–51]. In this regime, the CDT is analogous to the phenomenon of dynamical localization in a driven two-level system and can be understood using simple analytical formulas. In the second regime considered, the quasi-resonant regime, the frequency of the laser field is close to the frequency of the transition between the $|(0)^a\rangle$ and $|(2^1)^s\rangle$ states. In this case, the CDT originates in the difference between the Stark shifts induced on the $|(0)^s\rangle$ and $|(0)^a\rangle$ states. In both case, the system was studied in the framework of the Floquet formalism, using effective models. This analysis allowed us to explain the shape of the quasienergy curves corresponding to the dressed states continuously connected to the $|(0)^a\rangle$ and $|(0)^s\rangle$ vibrational states and to determine, for each field frequency considered, the field amplitude required to achieve the CDT. The TDSE was then solved for the molecule in interaction with an adiabatically turned on continuous wave field using both an effective Hamiltonian written in a basis containing the lowest 142 vibrational states and the exact full dimensional vibrational Hamiltonian. Our results show that, in the quasi-resonant regime, the CDT can be achieved with less intense laser fields than in the non-resonant regime, which would be advantageous experimentally.

8.4 Conclusion

The results presented in this chapter show that the use of proper effective models, in combination with calculations based on the exact vibrational Hamiltonian, constitutes a promising approach to study the laser driven vibrational dynamics of polyatomic molecules. In this context, the MCTDH method is an invaluable tool as it allows to compute the laser driven dynamics of polyatomic molecules with a high accuracy,

However, our models still contain simplifications that prevent a direct comparison of our results with potential experiments. First, the rotational motion of the molecule was not explicitly described in the present work. The inclusion of the rotation in the description of the dynamics of the molecule is expected to be important in several ways. First, even at low energies, the inclusion of the rotational structure would result in a more complicated system with different selection rules. In addition, the orientation of the molecule with respect to the laser field polarization would make the control less efficient because of the rotational averaging of the laser-molecule interaction and the possible existence of competing processes. On the other hand, the combination of the laser control of the molecular alignment/orientation with the vibrational control proposed in this work could allow for a more complete control of the dynamics of the molecule. A second simplification of our models concerns the initial state chosen for the simulations. We have considered a molecule in a localized coherent superposition of vibrational eigenstates but we have not studied the preparation of this state. We note here that a control scheme for the localiza-

tion of the dynamics of a particle in a symmetric double well potential, starting from the ground delocalized eigenstate and using a three-photon process, has been proposed [20].

References

1. M. Sala, S. Guérin, F. Gatti, R. Marquardt, H.-D. Meyer, J. Chem. Phys. **136**, 194308 (2012)
2. M. Sala, F. Gatti, S. Guérin, J. Chem. Phys. **141**, 164326 (2014)
3. R.J. McMahon, Science **299**, 833 (2003)
4. O.M. Kirkby, M. Sala, G. Balerdi, R. de Nalda, L. Bañares, S. Guérin, H.H. Fielding, Phys. Chem. Chem. Phys. **17**, 16270 (2015)
5. J.P. Klinman, A. Kohen, Annu. Rev. Biochem. **82**, 471 (2013)
6. C. Livermmore, C.H. Crouch, R.M. Westervelt, K.L. Campman, A.C. Gossard, Science **274**, 1332 (1996)
7. D. Shafir, H. Soifer, B.D. Bruner, M. Dagan, Y. Mairesse, S. Patchkovskii, MYu. Ivanov, O. Smirnova, N. Dudovich, Nature **485**, 343 (2012)
8. B.S. Bhandari, Phys. Rev. Lett. **66**, 1034 (1991)
9. A.B. Balantekin, Rev. Mod. Phys. **70**, 77 (1998)
10. M. Grifoni, P. Hänggi, Phys. Rep. **304**, 229 (1998)
11. W.A. Lin, L.E. Ballentine, Phys. Rev. Lett. **65**, 2927 (1990); Phys. Rev. A **45**, 3637 (1992)
12. A. Lin, L.E. Ballentine, Phys. Rev. Lett. **65**, 2927 (1990); Phys. Rev. A **45**, 3637 (1992)
13. M. Holthaus, Phys. Rev. Lett. **69**, 1596 (1992)
14. S. Guérin, H.R. Jauslin, Phys. Rev. A **55**, 1262 (1997)
15. R. Bavli, H. Metiu, Phys. Rev. Lett. **69**, 1986 (1992); Phys. Rev. A **47**, 3299 (1993)
16. F. Grossmann, T. Dittrich, P. Jung, P. Hänggi, Phys. Rev. Lett. **67**, 516 (1991)
17. J.M. Gomez Llorente, J. Plata, Phys. Rev. A **45**, R6958 (1992)
18. C.E. Creffield, Phys. Rev. B **67**, 165301 (2003)
19. S. Ya Kilin, P.R. Berman, T.M. Maevskaya, Phys. Rev. Lett. **76**, 3297 (1996); E. Paspalakis, Phys. Lett. A **261**, 247 (1999)
20. N. Sangouard, S. Guérin, M. Amniat-Talab, H.R. Jauslin, Phys. Rev. Lett. **93**, 223602 (2004)
21. E.A. Shapiro, V. Milner, M. Shapiro, Phys. Rev. A **79**, 023422 (2009); S. Zhdanovich, E.A. Shapiro, J.W. Hepburn, M. Shapiro, V. Milner, ibid. **80**, 063405 (2009)
22. S. Guérin, L.P. Yatsenko, H.R. Jauslin, O. Faucher, B. Lavorel, Phys. Rev. Lett. **88**, 233601 (2002)
23. R. Marquardt, M. Sanrey, F. Gatti, F. Le Quéré, J. Chem. Phys. **133**, 174302 (2010)
24. C. Iung, F. Gatti, H.-D. Meyer, J. Chem. Phys. **120**, 6992 (2004)
25. G. Pasin, F. Gatti, C. Iung, H.-D. Meyer, J. Chem. Phys. **124**, 194304 (2006)
26. G. Pasin, F. Gatti, C. Iung, H.-D. Meyer, J. Chem. Phys. **126**, 024302 (2007)
27. F. Richter, F. Gatti, C. Léonard, F. Le Quéré, H.-D. Meyer, J. Chem. Phys. **127**, 164315 (2007)
28. M. Sala, F. Gatti, D. Lauvergnat, H.-D. Meyer, Phys. Chem. Chem. Phys. **14**, 3791 (2012)
29. H. Stapelfeldt, T. Seideman, Rev. Mod. Phys. **75**, 543 (2003)
30. T. Seideman, E. Hamilton, Adv. At. Mol. Opt. Phys. **52**, 289 (2006)
31. J.G. Underwood, B.J. Sussman, A. Stolow, Phys. Rev. Lett. **94**, 143002 (2005)
32. A. Rouzée, S. Guérin, O. Faucher, B. Lavorel, Phys. Rev. A **77**, 043412 (2008)
33. J.J. Larsen, K. Hald, N. Bjerre, H. Stapelfeldt, T. Seideman, Phys. Rev. Lett. **85**, 2470 (2000)
34. S.S. Viftrup, V. Kumarappan, S. Trippel, H. Stapelfeldt, E. Hamilton, T. Seideman, Phys. Rev. Lett. **99**, 143602 (2007)
35. F. Gatti, C. Iung, Phys. Rep. **484**, 1 (2009)
36. C. Iung, F. Gatti, Int. J. Quant. Chem. **106**, 130 (2006)
37. S. Hervé, F. Le Quéré, R. Marquardt, J. Chem. Phys. **116**, 3300 (2002)

38. R. Marquardt, K. Sagui, J. Zheng, W. Thiel, D. Luckhaus, S. Yurchenko, F. Mariotti, M. Quack, J. Phys. Chem. A **117**, 7502 (2013)
39. R. Marquardt, M. Quack, I. Thanopoulos, D. Luckhaus, J. Chem. Phys. **119**, 10724 (2003)
40. B.R. Johnson, W.P. Reinhardt, J. Chem. Phys. **85**, 4538 (1986)
41. G.D. Zeiss, W.J. Meath, Mol. Phys. **33**, 1155 (1977)
42. We use the notations following R. N. Zare, *Angular momentum* (Wiley, New-York, 1988)
43. H.-D. Meyer, F. Le Quéré, C. Léonard, F. Gatti, Chem. Phys. **329**, 179 (2006)
44. L.-J. Doriol, F. Gatti, C. Iung, H.-D. Meyer, J. Chem. Phys. **129**, 224109 (2008)
45. S.B. Kartha, K. Singh, V.A. Job, V.B. Kartha, J. Mol. Spectrosc. **129**, 86 (1988)
46. M. Snels, H. Hollenstein, M. Quack, J. Chem. Phys. **119**, 7893 (2003)
47. J.C. Light, I.P. Hamilton, J.V. Lill, J. Chem. Phys. **82**, 1400 (1985)
48. F. Grossmann, P. Jung, T. Dittrich, P. Hänggi, Z. Phys. B **84**, 315 (1991)
49. F. Grossmann, T. Dittrich, P. Hänggi, Phys. B **175**, 293 (1991)
50. T. Dittrich, F. Grossmann, P. Jung, B. Oelschlägel, P. Hänggi, Phys. A **194**, 173 (1993)
51. F. Grossmann, T. Dittrich, P. Jung, P. Hänggi, J. Stat. Phys. **70**, 229 (1993)
52. F. Grossmann, P. Hänggi, Europhys. Lett. **18**, 571 (1992)
53. Y. Kayanuma, Phys. Rev. A **50**, 843 (1994)
54. I. Vorobeichik, N. Moiseyev, Phys. Rev. A **59**, 3 (1999)
55. J.C.A. Barata, D.A. Cortez, J. Math. Phys. **44**, 1937 (2003)
56. M. Frasca, Phys. Rev. B **71**, 073301 (2005)
57. S. Ashhab, J.R. Johansson, A.M. Zagoskin, F. Nori, Phys. Rev. A **75**, 063414 (2007)
58. Y. Kayanuma, K. Saito, Phys. Rev. A **77**, 010101(R) (2008)
59. R.G. Unanyan, S. Guérin, H.R. Jauslin, Phys. Rev. A **62**, 043407 (2000)
60. J.M. Villas-Bôas, E.Sergio, N. Studart, Phys. Rev. B, **70**, 041302(R) (2004)
61. S. Longhi, Phys. Rev. A **71**, 065801 (2005)
62. C.E. Creffield, Phys. Rev. Lett. **99**, 110501 (2007)
63. X. Luo, Q. Xie, B. Wu, Phys. Rev. A **76**, 051802(R) (2007)
64. J. Gong, L. Morales-Molina, P. Hänggi, Phys. Rev. Lett. **103**, 133002 (2009)
65. G. Lu, W. Hai, Q. Xie, Phys. Rev. A **83**, 013407 (2011)
66. S. Longhi, Phys. Rev. A **83**, 034102 (2011)
67. X. Luo, J. Huang, C. Lee, Phys. Rev. A **84**, 053847 (2011)
68. S. Longhi, Phys. Rev. A **86**, 044102 (2012)
69. S. Longhi, G. Della Valle, Phys. Rev. A **86**, 042104 (2012)
70. X. Luo, L. Li, L. You, B. Wu, New J. Phys. **16**, 013007 (2014)
71. G. Della Valle, M. Ornigotti, E. Cianci, V. Foglietti, P. Laporta, S. Longhi, Phys. Rev. Lett. **98**, 263601 (2007)
72. H. Lignier, C. Sias, D. Ciampini, Y. Singh, A. Zenesini, O. Morsch, E. Arimondo, Phys. Rev. Lett. **99**, 220403 (2007)
73. E. Kierig, U. Schnorrberger, A. Schietinger, J. Tomkovic, M.K. Oberthaler, Phys. Rev. Lett. **100**, 190405 (2008)
74. A. Eckardt, M. Holthaus, H. Lignier, A. Zenesini, D. Ciampini, O. Morsch, E. Arimondo, Phys. Rev. A **79**, 013611 (2009)
75. T. Seideman, M. Yu, Ivanov and P. B. Corkum, *Phys. Rev. Lett.* **75**, 2819 (1995)
76. S. Takada, H. Nakamura, J. Chem. Phys. **102**, 3977 (1995)
77. J.H. Shirley, Phys. Rev. **138**, B979 (1965)
78. S.I. Chu, Adv. At. Mol. Phys. **21**, 197 (1985)
79. S.I. Chu, Adv. Chem. Phys. **73**, 739 (1987)
80. K. Drese, M. Holthaus, Eur. Phys. J. D **5**, 119 (1999)
81. S. Guérin, Phys. Rev. A **56**, 1458 (1997)
82. S. Guérin, H.R. Jauslin, Adv. Chem. Phys. **125**, 147 (2003)

Chapter 9
Conclusion

In the work presented in the first Part of this thesis, we have used high-level electronic structure and nuclear quantum dynamics calculation techniques to study the photochemistry of simple aromatic organic molecules. In a first application, initiated during a six-month fellowship in the experimental group of Helen Fielding in the Chemistry Department of University College London, we have studied the photochemistry of aniline through a systematic exploration of the potential energy surfaces of the low-lying $1\pi\pi^*$, $1\pi\sigma^*$ and $2\pi\pi^*$ states of the pmolecule using CASSCF and XMCQDPT2 calculations. Several previously unknown minimum energy conical intersections and the associated decay pathways have been reported. These include a prefulvene conical intersection between the $1\pi\pi^*$ and the ground states, characterized by an out-of-plane distortion of the carbon atom of the phenyl ring holding the amino group. The presence of a relatively high potential energy barrier along the prefulvene decay channel prevents the molecule from accessing this channel after photoexcitation close to the onset of the $1\pi\pi^*$ state. The top of the barrier being at a higher energy than the vertical excitation energy of the higher $1\pi\sigma^*$ state, the decay of the molecule at the prefulvene CIs is only observed as a secondary channel, following the transfer of the system from a higher state to the $1\pi\pi^*$ state. This prefulvene MECI occurs at a lower energy than the three other, previously known, prefulvene MECIs and its structure is close to the structure of the $1\pi\pi^*/2\pi\pi^*$ MECI responsible for a transfer of the molecule to the $1\pi\pi^*$ state after excitation to the $2\pi\pi^*$ state. Therefore the decay of the molecule through the prefulvene pathway is likely to be dominated by this newly characterized prefulvene CI. A relaxed potential energy scan describing the dissociation of one of the N–H bonds of the amino group has been presented, which supports the experimental observation of an ultrafast decay involving the previously known $1\pi\pi^*/1\pi\sigma^*$ CI. Finally, a new decay pathway, connecting in a barrierless manner the FC region of the $2\pi\pi^*$ potential energy surface to a low-lying conical intersection with the ground state has been found. This pathway, featuring a probable three-state CI involving the $1\pi\pi^*$, $1\pi\sigma^*$ and $2\pi\pi^*$ states, supports the interpretation, previously proposed by Fielding et al., that the shortest time constant of approximately 50 fs, measured after photoexcitation to the $2\pi\pi^*$ state, is associated with an efficient decay process, transferring directly

the system to its ground state. While these results provide a significant new insight into the intricate photochemistry of aniline, some experimental observations will require further efforts to find a definitive interpretation. In particular, the role of the tunneling of the dissociating H atom through the potential energy barrier separating the quasi-bound and dissociative parts of the $1\pi\sigma^*$ surface is difficult to analyse from static electronic structure calculations. Nevertheless, our work has stimulated new experiments, undergone in the Fielding group, involving a comparison of the photochemistries of aniline and its deuterated analogue, in order to provide a deeper understanding of the role of tunneling in the photochemistry of aniline.

In a second application, we have studied the photophysics of pyrazine, with a particular focus on the role of the low-lying dark $n\pi^*$ states. While the existence of these dark states is well established from previous ab initio investigations of the excited electronic states of the molecule, and despite the very large number of previous theoretical investigations of its non-adiabatic dynamics, the possible role of these states has only been highlighted in previous trajectory surface-hopping dynamics studies [1, 2]. We have used XMCQDPT2 calculations to design a vibronic coupling model Hamiltonian and performed MCTDH quantum dynamics simulations of the absorption spectrum and the ultrafast radiationless decay process occuring after excitation to the bright $\pi\pi^*$ state of the molecule. Our results show the existence of a competition between the well known ultrafast decay to the bright $B_{3u}(n\pi^*)$ state and a decay to the dark $A_u(n\pi^*)$ state, establishing the important role of the latter in the ultrafast photophysics of the molecule. More recently, in a work not presented in this thesis [3], we have extended our model to investigate the further decay of the molecule to its ground state. Our quantum dynamics simulations show that this decay occurs through a conical intersection between the $A_u(n\pi^*)$ and the ground state, and predict a time scale in agreement with experimental observations. Therefore this work gives further evidence of the important role of the $A_u(n\pi^*)$ state in the photophysics of pyrazine.

These studies illustrate the fact that, thanks to the enormous progress in the methodological development of highly accurate and efficient computational techniques, reliable electronic structure and quantum dynamics calculations can now be performed on photoexcited mid-size molecular systems. These calculations are able to provide a deep insight into the structure and dynamics of such molecules and constitute invaluable tools to help in the interpretation of increasingly sophisticated experimental investigations of their photochemistry. Nevertheless, the application of these techniques to a broader range of systems of interest for our understanding of the photochemistry of important biological molecule and for the design of innovative photoresponsive materials will require further efforts. For instance, the quantum dynamical study of the photophysics of pyrazine is facilitated by the fact that it is dominated by decay processes involving only low amplitude vibrational motions of the molecule. Therefore, model potential energy surfaces and coupling terms that are only accurate around the equilibrium geometry are sufficient to provide a reliable description of these processes by quantum dynamics simulations. However, our study of aniline shows that, despite its simple structure, its photochemistry is more intricate and involves several decay pathways characterized by large amplitude motions of

the nuclei, which can not be described by simple coupled harmonic potentials. This is illustrated by the recent quantum dynamics study of Wang et al. [4]. They have constructed a sophisticated vibronic coupling model based on an extensive mapping of the potential energy surfaces using high-level electronic structure calculations. Their model provided a remarkably accurate simulation of the absorption spectrum of the molecule. However, despite its quality, it could not account for the ultrafast decay observed experimentally after excitation to the $2\pi\pi^*$ state. This illustrates the considerable challenge posed by the development of accurate model potentials for use in quantum dynamics simulations of photochemical processes involving large amplitude motions of the nuclei. This challenge is currently an active area of research, and several significant advances towards this goal have been reported recently. One can mention for instance, the model Hamiltonian describing the ring opening of benzopyrane, developed by Joubert-Doriol et al. [5], the model Hamiltonian of Jornet Somoza et al. [6], describing the excited state dynamics of ethylene, the recent work of Köppel et al. on the exited state dynamics of butadiene [7] and the ring-opening of furan [8], or the recent set of full-dimensional potential energy surfaces for phenol of Zhu and Yarkony [9].

An other important topic for the future development of quantum dynamics for photochemistry is the inclusion of the environment of the molecular system in the models. Indeed, while the study of isolated molecular system applies to gas phase processes, most photochemical systems of interest are embedded in an environment. For instance, a large number of industrial reactions used to synthesize chemical compounds of interest are catalyzed at metal surfaces. Many technological devices based on molecular materials, including for instance, new generations of solar cells, involve molecular system adsorbed at the surface of nanomaterials. Biological molecules of interest are dissolved in water, and often embedded in a protein environment. This environment often has a significant influence on the dynamics of the molecular systems of interest. A well known example, that is the subject of intensive investigations, is the fluorescent proteins. These systems involve organic chromophores embedded in a protein environment. Taking the example of the Green Fluorescent Protein (GFP), it is know that the isolated chromophore, or the chromophore in solution, undergoes an ultrafast non-radiative decay after photoexcitation, and has therefore a low fluorescence quantum yield. However, when it is embedded in its protein environment, this ultrafast decay process is quenched by the influence of this environment and the protein is fluorescent. Therefore, the development of computational protocols able to describe the effect of this environment on the dynamics of the molecular system is of high interest. Examples of such methodologies are quantum dissipative dynamics, based on the propagation of density operators [10] or hybrid QM/MM methods allowing for a quantum treatment of the molecular system and a classical treatment of its environment [11].

As seen in second part of these thesis, the development of efficient quantum dynamical computational methods also opened the door to the study of the laser control of polyatomic molecular systems. In a first application, we used a simplified model Hamiltonian describing the excited state dynamics of pyrazine to investigate the laser control of its ultrafast radiationless decay by a strong non-resonant laser

pulse. We found that a strong non-resonant pulse can significantly alter, through the dynamic Stark effect, the topography of the conically intersecting potential energy surfaces of the molecule and thus influence its decay dynamics. In particular, we have found that, because of the difference of polarizability between the $B_{3u}(n\pi^*)$ and $B_{2u}(\pi\pi^*)$ states, the strong non-resonant pulse can trap the wavepacket in the upper $B_{2u}(\pi\pi^*)$ state, and can suppress the radiationless decay to the $B_{3u}(n\pi^*)$ state for a time much longer than the natural time scale of the process. In a subsequent work, the same control mechanism was investigated in a model including the twenty-four vibrational modes of the molecule, in the basis of our work. These full-dimensional calculations, employing the multi-layer MCTDH method, performed by Saab et al. [12], showed that the control could still be achieved, despite the fact that the natural decay process is more efficient in the full-dimensional model, than in the simpler model used in the present work. This work therefore established the robustness of the proposed control mechanism with respect to the details of the model used to describe the system.

In a second application, we have investigated the laser control of the tunneling dynamics in NHD_2 using a model including the six vibrational degrees of freedom of the molecule. Both the laser induced enhancement of tunneling by a resonant pulse and the coherent destruction of tunneling were considered. Our computational strategy involved the use of different models of increasing complexity in order to understand the general properties of the control mechanisms and to find sets of parameters of the laser field allowing for an efficient implementation of the control schemes studied. MCTDH quantum dynamics simulation using the exact vibrational Hamiltonian operator were then performed in order to confirm the applicability of these control schemes to the full system.

These studies established the MCTDH method as a powerful tool for the theoretical study of the laser control of molecular processes involving polyatomic molecules. However, several issues will need to be addressed in order to be able to design and propose laser control schemes that can be readily implemented experimentally. First, a number of control schemes developed so far rely on the knowledge of the individual quantum states of the system. However, the calculation of the rovibrational states of realistic molecular system is, in most cases, an extremely difficult task, especially when several coupled excited electronic states are considered. It is thus important to develop control schemes that rely on more accessible features of the system, such as the topography of the potential energy surfaces. The control schemes based on the dynamic Stark effect are interesting examples of such control schemes that do not require the knowledge of the individual quantum states of the system. However, their applicability to the control of a given molecular system, and the variety of targets that can be reached, depends on the topography of the polarizability surfaces of the molecule. An alternative approach, in this context, would involve resonant control schemes based on the creation of dressed electronic potential energy surfaces with an adiabatically controlled topography. A similar approach has been tested by Garraway and Suominen [13] and Solá et al. [14] for simple diatomic systems.

In addition, the rotational motion of the molecules was not explicitly included in our models. It is well established that, because of the necessary random orientation

of the individual molecules in a sample with respect to the polarization of the laser feld, the rotational motion has a detrimental effect on the efficiency with which the system can be controlled. Therefore, a systematic inclusion of the rotational motion in the models used to study the laser control of molecular systems would provide a valuable insight into the applicability of a given control scenario. In addition, it would allow one to combine a given control scenario with the well established techniques of laser induced molecular alignment and orientation, and thus to design more efficient control scenarios that could be implemented experimentally. In this context, the recent implementation of the theoretical machinery required to include the interaction of a rotating molecule with a laser field into the Heidelberg MCTDH program package will open exciting possibilities in the theoretical study of the laser control of complex molecular processes.

References

1. U. Werner, R. Mitrić, T. Suzuki, V. Bonačić-Koutecký, Chem. Phys. **349**, 319 (2008)
2. G. Tomasello, A. Humeniuk, R. Mitrić, J. Phys. Chem. A **118**, 8437 (2014)
3. M. Sala, S. Guérin, F. Gatti, Phys. Chem. Chem. Phys. **17**, 29518 (2015)
4. F. Wang, S.P. Neville, R. Wang, G.A. Worth, J. Phys. Chem. A **117**, 7298 (2013)
5. L. Joubert-Doriol, B. Lasorne, D. Lauvergnat, H.-D. Meyer, F. Gatti, J. Chem. Phys. **140**, 044301 (2014)
6. J. Jornet Somoza, B. Lasorne, M.A. Robb, H.-D. Meyer, D. Lauvergnat, F. Gatti, J. Chem. Phys. **137**, 084304 (2012)
7. A. Komainda, B. Ostojić, H. Köppel, J. Phys. Chem. A **117**, 8782 (2013)
8. E.V. Gromov, V. Sivaranjana Reddy, F. Gatti, H. Köppel, J. Chem. Phys. **139**, 234306 (2013)
9. X. Zhu, D.R. Yarkony, J. Chem. Phys. **140**, 024112 (2014)
10. A. Raab, H.-D. Meyer, Theor. Chem. Acc. **104**, 358 (2000)
11. T.J. Martinez, Acc. Chem. Res. **39**, 119 (2006)
12. M. Saab, M. Sala, S. Guérin, B. Lasorne, F. Gatti, J. Chem. Phys. **141**, 134114 (2014)
13. B.M. Garraway, K.-A. Suominen, Phys. Rev. Lett. **80**, 932 (1998)
14. I.R. Solá, J. Santamaría, V.S. Malinovsky, Phys. Rev. A **61**, 043413 (2000)